NEURAL INTERFACE SYSTEMS FOR LONG-TERM BEHAVIORAL EXPERIMENTS WITH SMALL FREELY MOVING ANIMALS

A Dissertation
Presented to
The Academic Faculty

by

Yaoyao Jia

In Partial Fulfillment
of the Requirements for the Degree
Doctor of Philosophy in the
School of Electrical and Computer Engineering

Georgia Institute of Technology
August 2019

NEURAL INTERFACE SYSTEMS FOR LONG-TERM BEHAVIORAL EXPERIMENTS WITH SMALL FREELY MOVING ANIMALS

Approved by:

Dr. Maysam Ghovanloo, Advisor
School of Electrical and Computer Engineering
Georgia Institute of Technology

Dr. Omer T. Inan, Co-advisor
School of Electrical and Computer Engineering
Georgia Institute of Technology

Dr. Wen Li
Department of Electrical and Computer Engineering
Michigan State University

Dr. Hua Wang
School of Electrical and Computer Engineering
Georgia Institute of Technology

Dr. Farrokh Ayazi
School of Electrical and Computer Engineering
Georgia Institute of Technology

Dr. Benjamin D. B. Klein
School of Electrical and Computer Engineering
Georgia Institute of Technology

Date Approved: June 17, 2019

ACKNOWLEDGEMENTS

I would like to express my sincere gratitude and appreciation to my advisor, Dr. Maysam Ghovanloo, and my co-advisor, Dr. Omer Inan, for their generous guidance and strong support. I really have learned a lot from them about not only research but also enthusiasm, dedication, and professionalism in their work. It was my greatest luck and pleasure to work with them during my Ph.D. studies. Their advisorship gave me a significant and positive impact on my future career and even life.

Besides, I would like to thank Dr. Wen Li for her never-ending help, patience, understanding, and encouragements through a hard time in my life. Dr. Li's creativity, enthusiasm, and problem-solving acumen inspired me on pursuing innovative, efficient solutions to various research challenges.

Then, I would like to extend my appreciation to the rest of my thesis committee members, Dr. Hua Wang, Dr. Farrokh Ayazi, and Dr. Benjamin Klein, for their time and consideration in reviewing my Ph.D. thesis, but also for being generous in sharing their expertise and valuable advice. Their valuable comments and feedback have been really helpful to further improve my research.

My sincere thanks also go to all the GT-Bionics lab members for their full contributions. They have truly inspired me in all the good and bad times and supported me in every stage of my research. In particular, I am grateful to Dr. Byunghun Lee, Dr. Abdollah Mirbozorgi, and Dr. Ulkuhan Guler for the stimulating discussions, for the late nights we were working together, and for all the fun we have had during the five years in

Georgia Tech. Indeed, they were sincere friends and great collaborators who have fully motivated me.

Many valuable collaborations and teamwork during my Ph.D. studies were not only within our group but also with other groups. I would also like to thank my collaborators Dr. Bin Fan from Michigan State University and Dr. Chia-Chun Hsu from Emory University for their technical assistance on microfabrication, neuroscience study, and data analysis. My Ph.D. work cannot be inseparable from our excellent teamwork.

Last, but the most important, I would like to express my deepest gratitude to my parents. Their endless love and support make me complete this long trip. I am grateful to them for pulling me through difficult times with their unconditional love. I would never complete my Ph.D. thesis without their support, encouragement, and love.

TABLE OF CONTENTS

LIST OF TABLES

LIST OF FIGURES

LIST OF SYMBOLS AND ABBREVIATIONS

IMD	Implantable medical device
CNS	Central nervous system
PNS	Peripheral nervous system
TBSI	Triangle BioSystems International
MEA	Microelectrode array
WPT	Wireless power transmission
PDL	Power delivery to the load
PTE	Power transfer efficiency
SAR	Specific absorption rate
EM	Electromagnetic
Tx	Transmitter
Rx	Receiver
DSP	Digital signal processing
GUI	Graphical user interface
COTS	Commercial off-the-shelf
BLE	Bluetooth low energy
UWB	Ultra-wideband
DBS	Deep brain stimulation
SoC	System-on-a-chip
BBB	Blood-brain barrier
IR	Infrared
WOENI	Wireless opto-electro neural interface

PCB	Printed circuit board
ADC	Analog-to-digital converter
MCU	Microcontroller unit
AFE	Analog front-end
BJT	Bipolar junction transistor
GPIO	General-purpose I/O
POT	Potentiometer
LFP	Low-pass filter
AR	Artifact rejection
SNR	signal-to-noise ratio
RMS	Root mean square
THD	Total harmonic distortion
IACUC	Institutional Animal Care and Use Committee
V1	Virtual cortex
ChR2	Channelrhodopsin-2
VA	Visual angle
E/S ratio	Evoked-to-spontaneous ratio
PSD	Power spectral density
FCC	Federal Communications Commission
ISM	Industrial, scientific, and medical
SRF	Self-resonance frequency
CLPC	Closed-loop power control
GPi	Globus pallidus
RPi	Raspberry Pi
PA	Power amplifier

DAC	Digital to analog converter
UART	Universal Asynchronous Receiver/Transmitter
VNA	Vector Network Analyzer
AP	Anteroposterior
ML	Mediolateral
DV	Dorsoventral
HRA	head rotation angle
WINeRS	Wirelessly-powered implantable neural recording and stimulation
SDR	Software defined radio
OOK	On-off keying
HDD	Hard disk drive
FPGA	Field programmable gate array
FFT	Fast Fourier transform
SFDR	Spurious-free dynamic range
ENoB	Effective number of bits
CCS	Current-controlled stimulation
LDO	Low drop-out
MUX	Multiplexer
LNA	Low noise amplifier
SAR	Successive approximation register
PLL	Phase-locked loop
P2S	Parallel-to-series
CB	Charge balance
PPM-CDR	Pulse-position-modulated clock/data recovery
LSK	Load-shift-keying

SCS	Switched-capacitor-based stimulation
VGA	Variable gain amplifier
SMD	Surface-mounted device
NEF	Noise efficiency factor
NOL	Normalized output light
TRx	Transceiver
FF-WIOS	Free-floating, wirelessly-powered, implantable optical stimulation
PDMS	Polydimethylsiloxane
S2P	Serial-to-parallel
PCE	Power conversion efficiency
AAV	Adeno-associated virus
FEM	Finite element method
FoM	Figure of merit
NHP	Non-human primates

SUMMARY

The objective of my research is to advance the neural interface systems for long-term behavioral experiments with small freely moving animals. Several innovative system- and circuit-level techniques are proposed towards the development of wireless power transmission (WPT) systems, inductively-powered implantable neural recording and stimulation interface, wireless data acquisition system, and distributed architecture consisting of multiple tiny implants.

Implantable medical devices (IMDs), which establish a direct communication pathway with the target neurons, are the tools for applying neuromodulation, while sensing neural signals to provide feedback on the evoked neural activities. This technique is known as closed-loop neuromodulation. Head-mounted devices, furnished with both neural recording and electrical stimulation and/or optical stimulation, have been developed to offer unprecedented flexibility for end-users. In addition, tiny implant design, with miniaturized footprint and minimized power consumption, has been proposed, aiming to develop the architecture of distributed tiny implants.

For untethered and battery-free operation of the IMDs, supporting systems have been developed. Two WPT systems are presented in particular: EnerCage-HC and dual-band EnerCage-HC to wirelessly power and control head-mounted devices and tiny implants, respectively. A data acquisition system is also described to collect a large amount of recording data and analyze the recovered data in real time. In collaboration with researchers in bioMEMS and biomedical science, the functionality and robustness of the IMDs and the supporting systems have been demonstrated with *in vivo* experiments.

CHAPTER 1. INTRODUCTION

Up to one billion people, nearly one in six of the world's population, suffer from neurological disorders, e.g. Parkinson's disease, epilepsy, Alzheimer's disease, stroke, brain tumor, multiple sclerosis, and Huntington's disease [1], [2]. Neurological disorders have become the leading cause of death and disability in the world today [1], [2]. Since neurological disorders cannot be treated adequately by medication alone, new therapies as an addition to the traditional medication treatment are required [3]-[5]. This is where neuromodulation-based therapies can potentially have great impact [3]-[5]. Implantable medical devices (IMDs), known as neural interfaces, which can provide a direct communication pathway between the central/peripheral nervous system (CNS/PNS) and external electronics, are tools that can implement neuromodulation [3]-[5].

Electrical stimulation is a traditional method of initiating functional response in neurons by injecting current to depolarize their cell membranes [6], [7]. However, electrical stimulation suffers from indiscriminate stimulation of cell components, large electrical artifacts, and poor spatial resolution due to unpredictable and time-variant current pathways within the neural tissue [6], [7].

Optogenetics, on the other hand, is becoming popular as an important technique in neuromodulation. This technique using light at certain wavelengths activates or inhibits genetically-modified neurons that express light-sensitive opsin proteins. In comparison with traditional electrical stimulation, optical stimulation provides several distinct advantages, such as cell-type specificity, millisecond temporal precision, and rapid reversibility [7]. Moreover, because of its much smaller electrical disturbance, this

technique enables simultaneous monitoring of neural response by electrical recording, in the vicinity of stimulation sites [7].

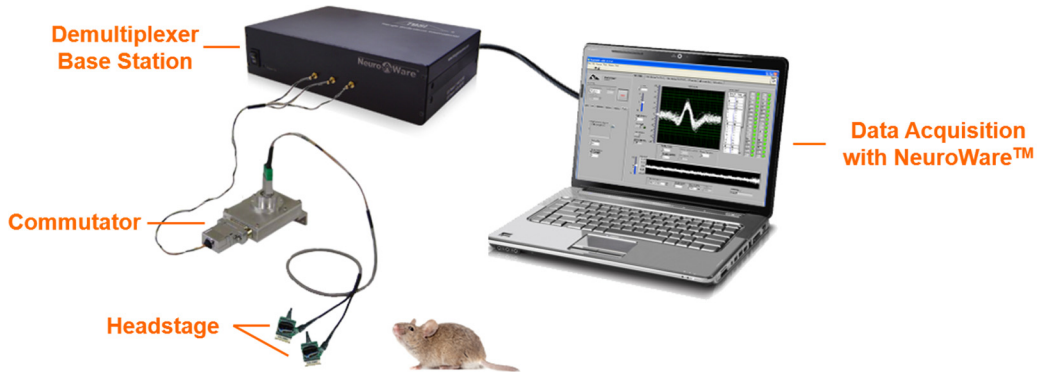

Figure 1.1. Tethered biomedical system from Triangle BioSystems International (TBSI) [15].

In the case of neural interfacing, IMDs are also expected to be capable of recording from and stimulating the neural tissue for closed-loop neuromodulation [6], [8]. Analyzing neural signals helps researchers to observe and interpret the changes in neural activities in response to various interventions, such as stimulation patterns [6], [8]. The recorded data also provides feedback on the evoked neural activity to help adjust various parameters of electrical stimulation to optimize it in terms of efficacy, safety, side effects, and power efficiency in what is known as closed-loop neuromodulation [6], [8].

Before using any IMDs in clinical applications, a significant number of *in vivo* experiments have been conducted on rodents, for evaluating IMDs, learning brain functions, and exploring therapies for neurological disorders [9], [10]. Traditionally, the IMDs have been developed in the form of a passive high-density connector or a central hub with all the electronics, which are tethered via cabling to microelectrode arrays (MEA) inserted at the target location in the brain [11]-[14], as shown in Figure 1.1. Additional cabling is needed to connect this hub/connector to external instruments, often through a

commutator. However, the cable connection may induce stress, bias the natural behavior of the animal, and restrict the experiments to one subject at a time due to the risk of wire tangling or damage by other animals.

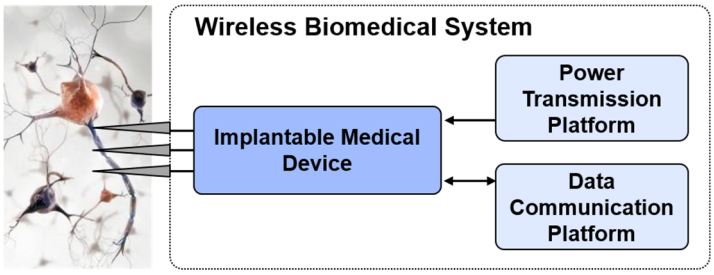

Figure 1.2. Key components involved in a wireless biomedical system for *in vivo* studies on small freely moving animals.

To support behavioral experiments conducted on freely moving rodents, a biomedical system facilitating untethered operation of the IMD is required [3], [4]. As shown in Figure 1.2, such wireless biomedical system includes three key components: IMD, wireless power transmission (WPT), and wireless data communication [3], [4]. Each component still faces several challenges and requires further research. The following text explains the main issues that remain in each component and the research pursued in this dissertation to address them.

1.1 Battery-Powered IMDs

Battery-powered biomedical system could be the most direct solution. Figure 1.3 shows a wireless biomedical system from TBSI [15]. The IMD is mounted on the animal subject's head, and is often referred to as a headstage device. The headstage is battery-powered, and a wireless data link is built for bi-directional data transmission between the headstage and the external data base. However, this biomedical system still suffers from several limitations.

Figure 1.3. Wireless biomedical system from TBSI [15].

The lifetime of batteries restricts the period of behavioral experiments, particularly when neuromodulation or other power-hungry intervention is involved [6], [7]. If the battery selected is too small, the headstage would not be suitable for long-term experiments or high-power or high-channel-count applications. The battery also needs to be changed frequently, which becomes a chronic stressor for the animal, and would impact the quality and repeatability of the experimental results. If the battery selected is too large, its weight and size may still interfere with animal behavior.

Several headstage devices have been developed at various levels of complexity, some of which are even commercially available [16]-[23], as shown in Figure 1.4. The Thomas Dual Stimulator from TREC has a total weight of 3.9 g and provides a high-density circuitry [20]. The stimulator, however, is powered by a battery (7.2 g), the weight of which is higher than the headstage itself. Plexon and EiCom provide extra light head-mounted optical devices at approximately 3 g each including the battery [21], [22]. The trade-off for these systems for providing this light weight is greatly limited features of the headstage. Multichannel Systems provides battery-powered headstages, equipped with 2-ch optical stimulation and 4-ch neural recording [23]. Although the headstage can support both neural

stimulation and recording, the headstage needs to connect with a battery board with the size large than the headstage.

A trade-off between the overall weight/size of the headstage and the capability of the headstage should be considered in design of such devices. Therefore, a new headstage design that can achieve better trade-off between size/weight and capability is required.

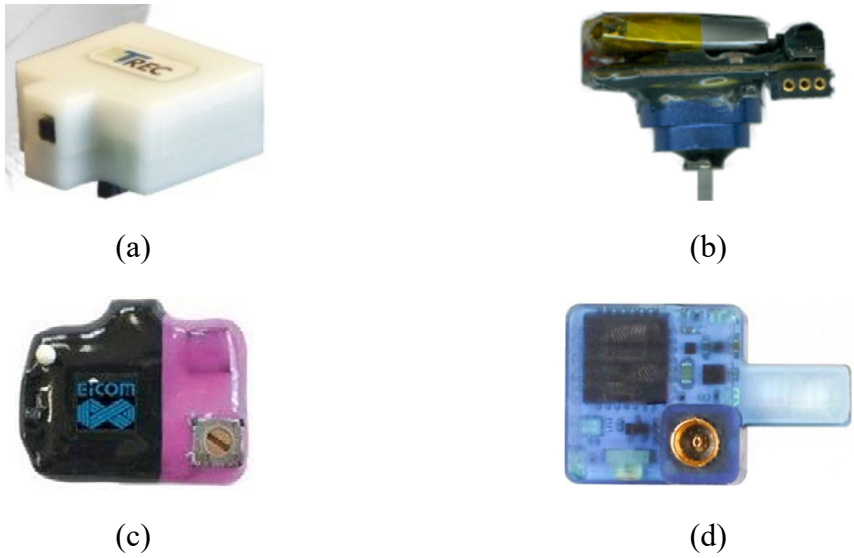

(a) (b)

(c) (d)

Figure 1.4. Examples of battery-powered headstage devices from (a) TREC [20], (b) Plexon [21], (c) EiCom [22], and (d) Multichannel Systems [23].

1.2 Inductive Power Transmission for IMDs

To overcome the limitations in the battery-powered neural interface solution, inductive power transmission systems have been developed, which can either recharge small batteries wirelessly or power the headstage indefinitely [24]-[26]. A common requirement for inductive power transmission to IMDs is sufficient power delivery to the load (PDL) at high power transfer efficiency (PTE) without surpassing the specific absorption rate (SAR) limit, particularly when a power-hungry intervention e.g. optogenetic stimulation is involved [27]-[32].

Inductive power transmission has been utilized in a wide range of applications, such as cochlear and retinal implants. Electromagnetic (EM) energy can easily penetrate through bone soft tissue with negligible loss, especially at low frequencies (e.g. kHz to MHz) [33]-[35]. In addition, these approaches stay well below the SAR limit with sufficient PDL [33]-[35]. Many effects have been undertaken to develop inductive power transmission systems, as shown in Figure 1.5 [36]-[43]. An inductively-powered homecage along with a compatible neural recording headstage from TBSI is shown in Figure 1.5a [26]. It is a 2-coil inductive link design with the transmitter (Tx) coil wrapped around the cage and the receiver (Rx) coil built in the headstage. Considering the significant size difference between the Rx and Tx coils, the PTE of the inductive link significantly drops from the perimeter area to the center area of the homecage. Because of low PTE, a large amount of power is delivery into the entire homecage, resulting in excessive heat dissipation and large EM interference with adjacent instruments.

The PTE of the inductive links proposed in [36] and [37] is maximized by locating the Tx coil, either electronically or mechanically, in the best position to power the Rx coil. These systems, however, require real-time animal tracking and additional electrical or mechanical devices to control the Tx coil, which add to the system complexity and cost.

In the experiments with freely moving rodents, the subjects' free motion constantly causes misalignments between the power Tx and Rx. Therefore, an additional requirement on the WPT design is supporting homogeneous PDL within the entire volume of a large experimental arena in the presence of misalignments. To improve the WPT robustness against misalignments, the design of four triangular slanted Tx resonators encompassing four corners of the homecage [38] and the method with multiple Tx coils located on both

top and bottom surfaces of the homecage [39] are reported. The two systems, however, fail to deliver sufficient power to the headstage at the worst scenario of 90° headstage rotation.

To achieve omnidirectional WPT, several inductive link configurations have been proposed [40]-[43]. Each approach has its pros and cons. One approach has the configuration of triple orthogonal Tx coils and a single Rx coil [40]. However, placing multiple Tx coils surrounding the cage limited the access to the animal and blocked the field of view of imaging modalities that are often used for recording animal behavior. The configuration with triple orthogonal Rx coils and a single Tx coil [41], on the other hand, blocks the access to the electronics inside the headstage, making it difficult to repair or to have electrode feed-through. In [42] and [43], a complex control circuity with phase-, time-, and/or frequency- domain modulation should be implemented to control the Tx coils.

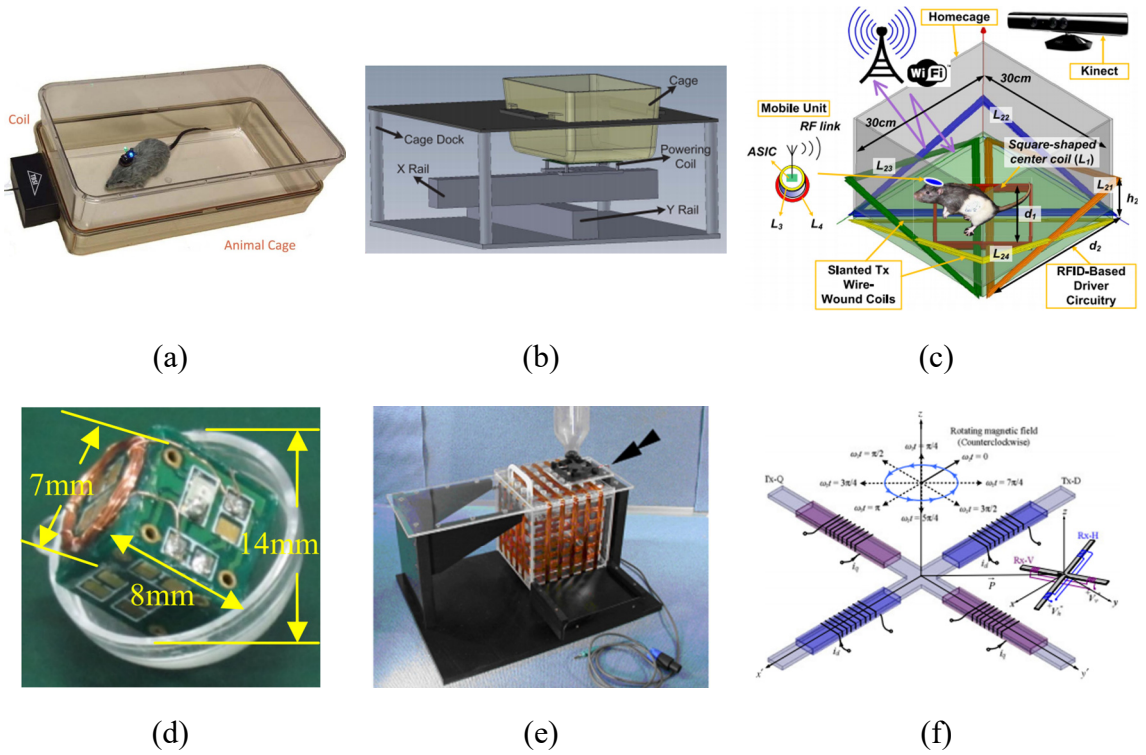

(a) (b) (c)

(d) (e) (f)

Figure 1.5. Examples of inductive power transfer systems proposed in (a) [26], (b) [37], (c) [38], (d) [40], (e) [41], and (f) [43].

Therefore, the inductive power transmission system still requires innovative system- and circuit-level techniques to achieve omnidirectional wireless powering, without substantially increasing the system complexity and requiring frequent repairs.

1.3 Wireless Data Communication with IMDs

It is well understood that most neural functions arise from a large population of neurons over a large tissue area [44]. Therefore, researches have focused on developing IMDs with high-density recording and stimulation front-ends [45], [46]. To achieve untethered and battery-free operation of the IMDs, a new challenge is wireless data transmission of large amount of recording data from a high-density neural interface, which can easily reach tens of Mbps [47]. Therefore, it is necessary to have a wireless data Rx, including blocks of the RF front-end, data demodulator, PC interface, digital signal processing (DSP), storage, external control, feedback, and graphical user interface (GUI).

One challenge of developing wireless data Rx is the wide bandwidth needed to support a large number of simultaneously recorded channels in a high density interface [47]. In behavioral experiments involving freely moving rodents, the animal subject's free movements cause constant variation in the Tx position and orientation, resulting in degradation of the RF signal strength at the position of stationary Rx antenna [48]. Another challenge is keeping the Tx size and weight as low as possible to reduce the subject burden in carrying the device, as well as the risk of biasing the animal behavior [48]. This would in turn impose a limit on the Tx power consumption and the size of its antenna, which combined with the other challenges make it difficult to maintain wireless data integrity and continuity by preventing blind spots anywhere within the experimental arena [48].

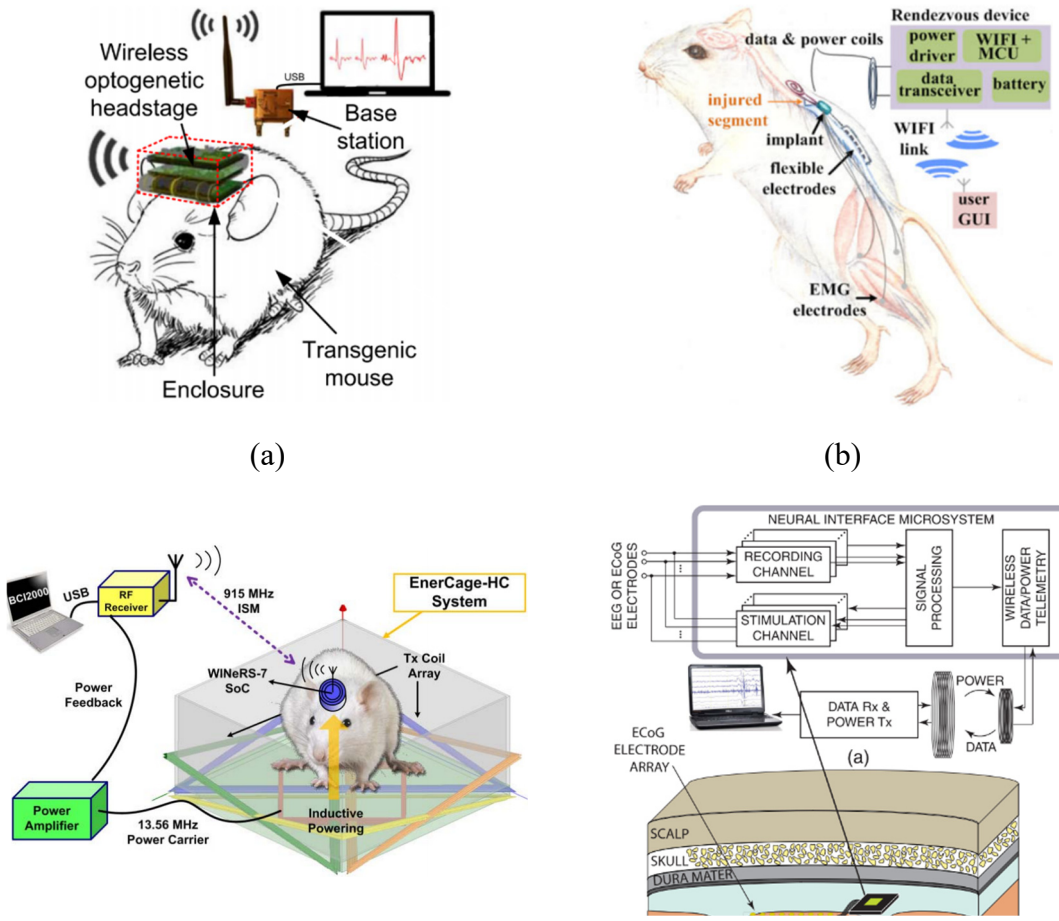

Figure 1.6. Examples of wireless data communication methods used in (a) [16], (b) [52], (c) [48], and (d) [57].

Despite a few attempts with a small number of simultaneously active channels, such as the example shown in Figure 1.6a, the abovementioned requirements have ruled out utilization of the most popular commercial off-the-shelf (COTS) solutions, such as Bluetooth low energy (BLE), ZigBee, or Wi-Fi, because of limited bandwidth or high power consumption [16], [49].

The rule of thumb in designing such wireless data Rx is to reduce the complexity and power consumption on the Tx side, often at the cost of more complexity on the Rx side, which is not under the abovementioned constraints [48]. Several customized data Rx

systems have been developed, as shown in Figure 1.6. In [50]-[52], the IMDs have on-chip Tx-Rx, which send recording data via an inductive link with modulation. In [53] and [54], the on-chip Tx encodes the recording data onto the carrier signal of the antenna. In [55]-[57], the ultra-wideband (UWB) technique is used to send data out. However, there is not enough information on the wireless coverage of the link and elimination of blind spots. In our prior work [48], we introduced a custom-designed Rx with the dual-antenna structure to extend the wireless coverage over a large experimental arena. Developing and fine-tuning the custom Rx was complicated, and operating two of them simultaneously required manual synchronization, which reduced the system scalability.

Therefore, it is still required to develop a wireless data Rx, which has advantages of scalability, flexibility of implementation, and ease of use to not only provide coverage over a standard-sized rodent homecage but also eliminate the RF blind spots.

1.4 Wirelessly-Powered Neural Recording and Stimulation

IMDs capable of injecting a designated amount of charge into the target neural tissue have been proven as effective therapeutic tools for modulating the activity of neurons in patients that do not respond to pharmaceutical treatment [6]. Deep brain stimulation (DBS), for instance, is one of the most effective treatments for Parkinson's disease and dystonia [6]. To meet the requirements of achieving closed-loop neuromodulation, several IMDs capable of neural recording and electrical stimulation have been developed [57], [58], such as the closed-loop neural-prosthetic system-on-a-chip (SoC) in Figure 1.7a. However, they suffer from inevitable limitations of electrical stimulation, e.g. non-specificity, unpredictable current pathway, electrical artifact, and electrode degradation.

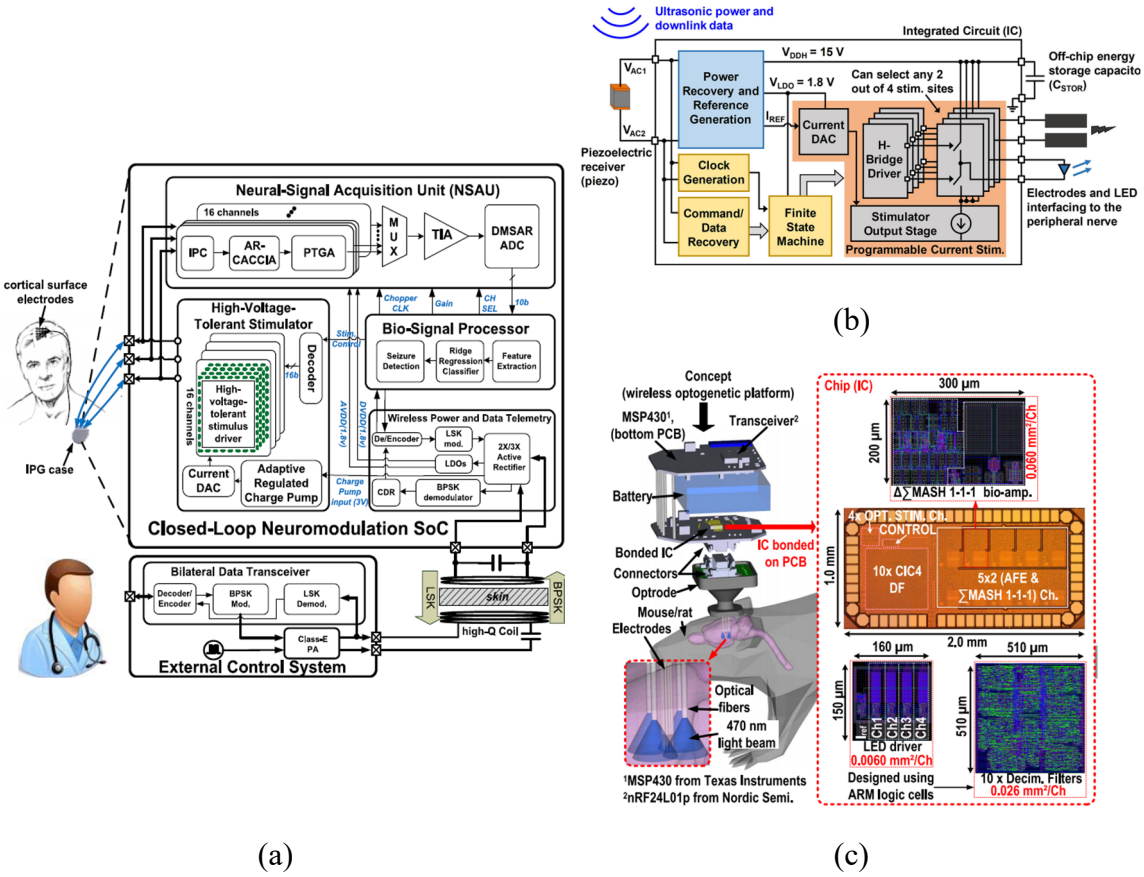

Figure 1.7. Examples of neural interface SoC designs presented in (a) [58], (b) [59], and (c) [60].

As of 10 years ago, a new method of neuromodulation has rapidly become popular among neuroscientists, known as optogenetics, which offers distinct advantages over electrical stimulation. Recent demand on neural interfaces for optogenetics application has resulted in the development of IMDs with optical stimulation capability [59], [60]. Figure 1.7b and 7c respectively show the SoC design for both optical and electrical stimulation of peripheral nerves proposed in [59] and the SoC design for simultaneous multichannel optogenetics and neural recording proposed in [60]. A weakness of these devices from a translational standpoint towards clinical application, however, is their high power consumption, which is inevitable because of the high threshold of light intensity needed to elicit selective neuromodulation, which is for instance 1 mW/mm^2 at 460 nm [61].

Therefore, it is hypothesized that a hybrid combination of both electrical and optical stimulation can offer the best of both worlds, the power efficiency of electrical and the selectivity of optical stimulation.

A comprehensive neural interface furnished with both optical and electrical stimulation capabilities, plus neural recording of the evoked activity for closing the loop is expected to offer unprecedented flexibility for end-users to execute sophisticated hybrid neuromodulation paradigms in semi- or fully-automated closed-loop fashion. Yet another key feature, which brings such a trimodal neural interface closer to clinical usability is wireless operation both in terms of power delivery and bidirectional data communication. However, such a comprehensive solution is still not available.

1.5 Distributed Tiny Implants

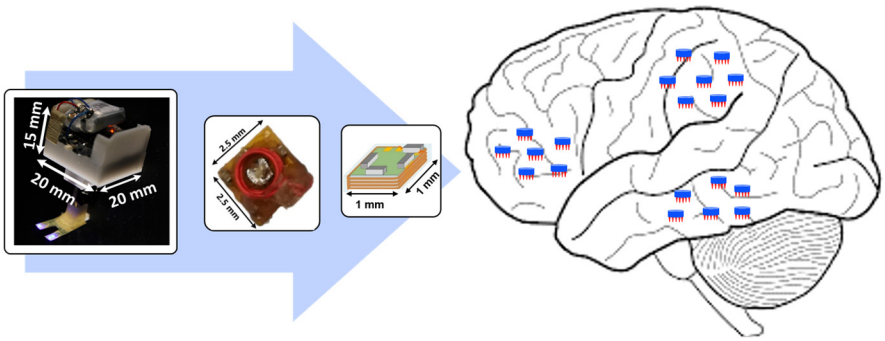

Figure 1.8. Distributed architecture consisting of multiple tiny implants as the implant size reduces.

Headstage devices always need transcutaneous hardwire connections to an implantable module (e.g. MEAs, LEDs, and etc), which is inserted into the target neural tissue. The transcutaneous hardwire connections cause infection and damage to the soft cortical tissue around the implantable module due to micromotions and breaching the blood-brain barrier (BBB), reducing the longevity of the neural interface [62], [63]. A

viable solution is the use of fully-implantable tiny IMDs. Recently, a few implant designs have been reported with impressive reduction in the device size [64]-[69]. Because of their small footprint, the tiny implant can float along with the brain in the cranial space, causing less damage to the surrounding tissue.

The neural interface has been traditionally designed as a centralized device connecting to multiple electrodes with maximum cm-sized coverage area [3]-[5]. It is well understood that neural function in the brain arises from a large distributed network [70], [71]. To meet the requirement of interfacing with large-scale cortical neuronal ensembles over large brain area, the traditional architecture will have scalability issues, including unacceptable physical size, concentrated heat generation, and high susceptibility to a local failure [64]. To address these issues, an innovative framework, which consists of a large number of tiny implants distributed over a large brain area, can be a viable solution [64].

The smaller the device, the more devices that can potentially be implanted. Finally, we can develop the framework of distributed tiny implants, as shown in Figure 1.8. Therefore, the main constraints for each implant in the distributed architecture are space, power budget, and functionality. Novel circuit topologies and system architectures should be explored to break conflicting space-power-functionality trade-offs.

1.6 Wireless Power Transmission for Distributed Tiny Implants

In the distributed architecture, each implant has an extremely small size. Neither battery nor large storage element, such as super-capacitors, is feasible to be integrated into the implant. Energy harvesting from glucose fuel cell [72], thermoelectric [73], or piezo transducers [74] have been proposed, but unlikely to provide sufficient power for the

desired functionality [75]. Another three WPT methods have been proposed: ultrasonic, optical, and EM, each of which has its own pros and cons [33]-[35].

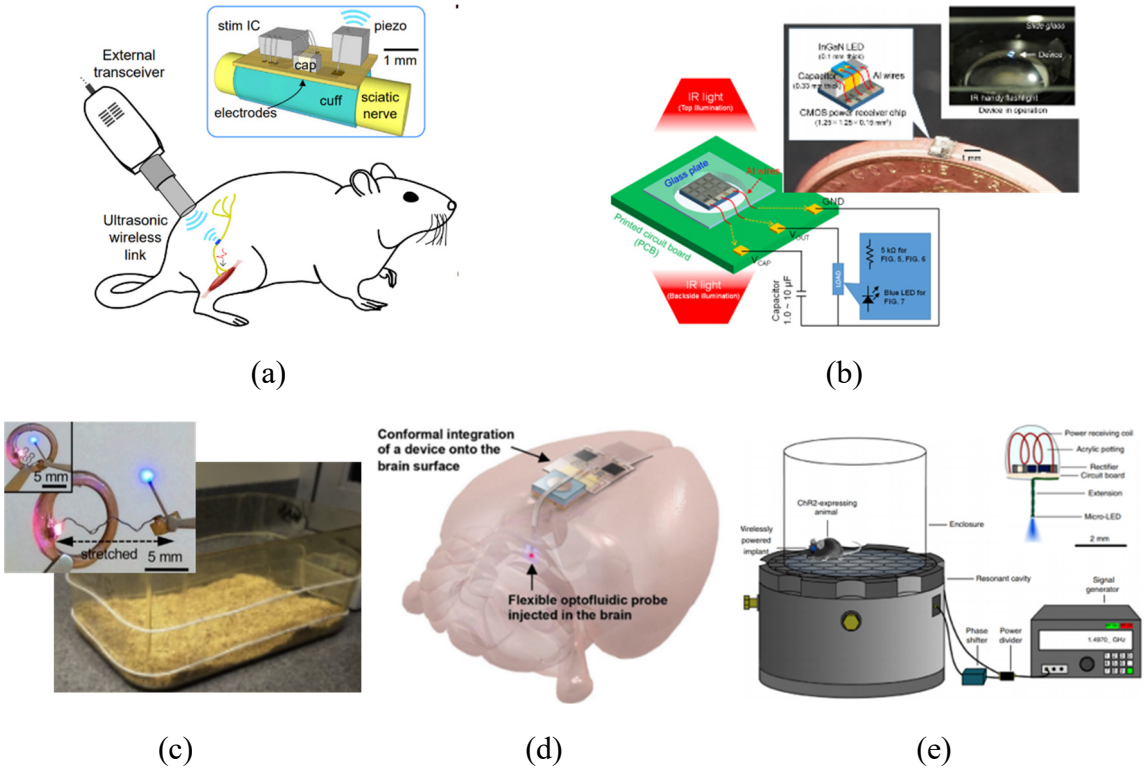

(a) (b)

(c) (d) (e)

Figure 1.9. Examples of wirelessly powered tiny implants proposed in (a) [65], (b) [66], (c) [67], (d) [68], and (e) [69].

Ultrasonic power transmission offers high PTE in deeper tissue and is immune to EM interference, but it cannot penetrate bone/skull [33]-[35]. This either limits its usage to interfacing with peripheral nerves or requires conversion from EM to ultrasonic WPT at the brain surface [64], [65], [76]. In Figure 1.9a, a 2.2 mm^3 stimulator with ultrasonic power and communication for peripheral nerve application is proposed in [65]. A hybrid inductive-ultrasonic link is proposed in [76], which enables WPT through the bone. However, the PTE of the hybrid link is low, and the experimental arena covered by sufficient PDL is limited. Ultrasonic power transmission is also prone to significant loss of PTE as a result of misalignments between Tx and Rx transducers in depth, orientation, and

horizontal displacement [33]-[35]. The work in [66] uses optical power transmission, as shown in Figure 1.9b. Photovoltaic cells integrated into the small IMD generate electric power from the light source, often infrared (IR). However, IR light has considerable heating effect due to light absorption in the tissue. Optical WPT is quite sensitive to Tx and Rx misalignments and suffers from low penetration depth in the tissue [33]-[35].

EM power transmission is another popular method. It can easily penetrate through bone soft tissue with negligible loss, especially at low frequencies [33]-[35]. However, the traditional EM power transmission in the near-field regime cannot focus the EM field to help reduce the Rx size [42], [67]. In [67], a 2-coil inductive link operating at 13.56 MHz is utilized to wirelessly power the device in a rodent homecage. However, to harvest enough power, the Rx coil needed to be ~1 cm in diameter, as shown in Figure 1.9c. EM power transmission at high frequency in the GHz range facilitates the Rx size reduction due to shorter wavelength, but they suffer from difficulties in creating homogeneous WPT in a large experimental arena [33]-[35]. At high frequency, it also increases the risk of unsafe personnel exposure to EM radiation and interference with nearby instruments [33]-[35]. In Figure 1.9d and 1.9e, the EM power transmission solutions in [68] and [69] use carrier signals in the GHz range significantly reduce the Rx size. However, in [68], the range of safe RF operation is limited to 10 cm from the Tx antenna. In [69], WPT is achieved only above a small resonant cavity. The power delivered to the small IMD depends on the physical size of the animal, in this case a mouse, but its extension to larger animals, such as rats or guinea pigs, without surpassing SAR limits might be difficult.

Therefore, a WPT approach, which can accommodate robust and sufficient power delivery to the tiny implant at high PTE without surpassing the SAR limit within the entire

volume of the experimental arena, is highly required. For the experiments with small freely moving animals, the WPT approach is also required to withstand any spatial and angular misalignments between the Tx and Rx.

1.7 Dissertation Outline

This dissertation has been organized as follows: Chapter 2 presents a wireless opto-electro interface device, as a versatile tool in the studies that involve long-term optogenetic neuromodulation. Chapter 3 proposes a wireless platform, called EnerCage-HC2, which can not only wirelessly power but also communicate with a variety of sensors, actuators, and other electronic devices that are attached to or implanted in the animal body. Chapter 4 describes a wirelessly-powered implantable neural recording and stimulation system, which is fully compatible with the EnerCage-HC2 system, a data acquisition system, which collects and analyzes the recording data, and a trimodal neural interface device furnished with both optical and electrical stimulation capabilities, plus neural recording. Chapter 5 introduces a mm-sized neuromodulation device, its supporting system for wireless optical stimulation, and a mm-sized opto-electro stimulation SoC design equipped with both optical and electrical stimulation capabilities. Chapter 6 details another wireless platform, called dual-band EnerCage-HC, for wirelessly powering tiny implants through two inductive links operating at different carrier frequencies. Chapter 7 discusses the conclusion and future work.

CHAPTER 2. WIRELESS NEURAL RECORDING AND OPTICAL STIMULATION SYSTEM

Lasers and LEDs are commonly-used light sources in optogenetics. In laser-based optical systems [77]-[80], optical fibers, microwave guides, or tapered optrodes are always used to deliver light to target neurons. For behavioral studies, these light conduits are limiting factors affecting the natural behavior of animal subjects and may cause complications in surgery [9], [10].

LEDs have much smaller size, and can be directly integrated in the optical devices that are small enough to be carried by animal subjects [81], [82]. Various LED-based optical devices eliminate the tethering effect of a stationary light source, facilitating *in vivo* experiments on freely behaving subjects [16]-[19]. The implantable module, under control of the external headstage, is implemented as a probe with integrated LEDs, penetrating deep into the brain or placed on the brain surface [17], [19]. In some cases, optical fibers are used to guide the light from LEDs embedded in the headstage to the target brain area [16], [18]. The devices in [17]-[19], however, lack neural recording capability, which is necessary as a neural response to optical stimulation or feedback for closed-loop neuromodulation. The device in [16] has features of optical stimulation and neural recording. However, these features were only tested in an acute experiment on a single animal subject. Therefore, the device stability for long-term experiments is still unclear.

To address the requirements of neural interfaces for long-term experiments with small freely behaving animals, we have developed a wireless opto-electro neural interface

(WOENI) device, capable of optical stimulation and ECoG recording [83]. As a proof of concept prototype, the WOENI device is designed to control a polyimide-based substrate, which includes four μLEDs and two epidural microelectrodes. The functionality of the WOENI device has been demonstrated *in vivo* by applying cortical optical stimulation and visual stimulation on freely behaving rats. Moreover, the consistency of *in vivo* results observed in four consecutive experiments, evenly distributed over 21-days post-implantation, can validate the stability and utility of the WOENI device.

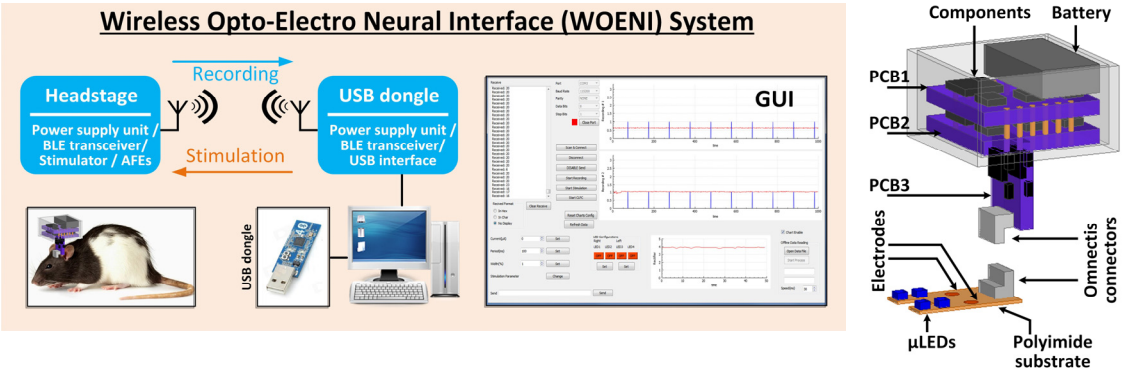

(a) (b)

Figure 2.1. (a) Conceptual representation of the WOENI system. (b) WOENI device prototype.

2.1 System Overview

In Figure 2.1a, the entire system consists of: 1) a detachable headstage, 2) an implantable polyimide-based substrate, 3) a custom-designed USB dongle, and 4) a PC that runs the GUI for parameter setting, data representation, processing, and storage. The headstage can wirelessly receive stimulation parameters set by the user in the GUI via the BLE link between the headstage and USB dongle, to selectively drive the μLEDs, and send the amplified, filtered, and digitalized ECoG data to the USB dongle. Data samples are plotted in the GUI in real time to monitor the functionality of the system and ongoing state

of the animal subject brain, and also saved locally for offline data processing. The headstage, which is shown with more details in Figure 2.1b, includes a 3.7 V, 45 mAh rechargeable battery, and COTS electronics mounted on three printed circuit boards (PCBs). One of the PCBs is mounted vertically and holds an Omnetics connector (PZN-08-AA), which provides 8 electrical contacts to the implanted polyimide-based substrate through a mating Omnetics (PZN-08-DD) connector, while supporting four addressable μLEDs and two epidural recording microelectrodes.

2.1.1 Circuit Details

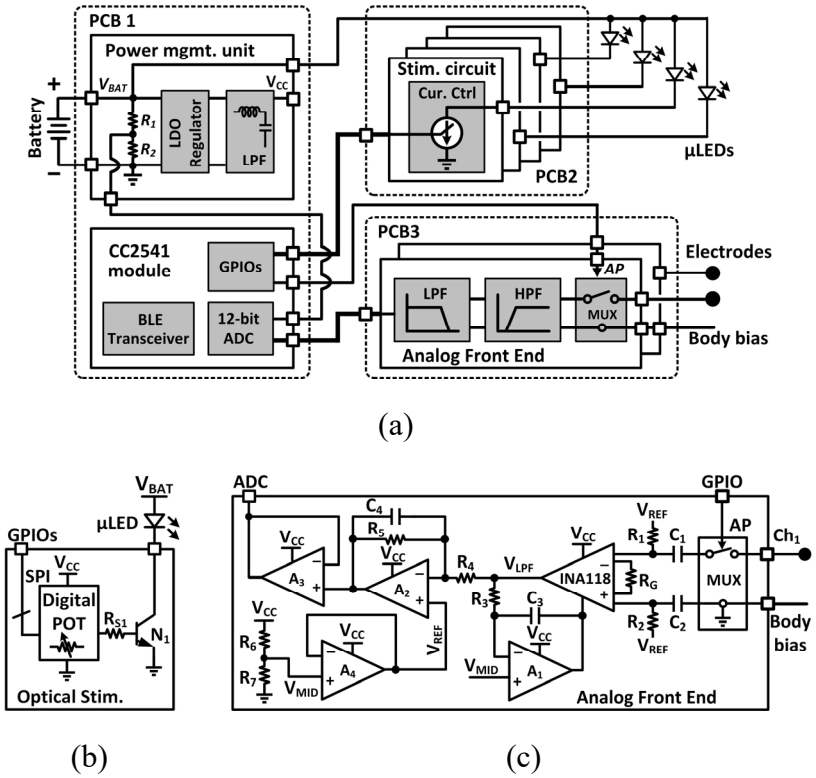

Figure 2.2. (a) A simplified block diagram of the key building blocks involved in the headstage. Schematic diagram of a single channel of (b) the optical stimulation and (c) the AFE.

The headstage circuit schematic is shown in Figure 2.2a. An adjustable regulator (TPS79901) stabilizes the battery output, V_{BAT}, to generate V_{CC} = 3.3 V, which is also low-

pass filtered. The built-in analog-to-digital converter (ADC) of the CC2541 microcontroller unit (MCU) takes samples of V_{BAT} to allow users monitor the battery voltage. The optical stimulation circuitry drives four μLEDs with adjustable current (5-30 mA), stimulation period (100-900 ms with 100 ms step, or 1-10 s with 1 s step), and stimulation pulse duty cycle (0.1-0.9% with 0.1% step, or 1-10% with 1% step). The two-channel analog front-end (AFE) amplify and filter ECoG signals by a factor of 49 dB within 1-200 Hz band, respectively, from two microelectrodes. The MCU also digitalizes the two AFE outputs at 1 kHz sampling rate, packetizes, and transmits data to the USB dongle via the BLE link. Figure 2.2b shows a single channel optical stimulation circuitry. A bipolar junction transistor (BJT) is driven by general-purpose I/O (GPIO) ports through a digital potentiometer (POT) (AD5160BRJZ100), which variable resistance adjusts the current flowing through the selected μLED in 256 steps (8-bits) [84].

Figure 2.2c shows a single channel AFE, which mainly includes three stages, referring to [85]. C_1 and C_2 eliminate the DC offset at the electrode-electrolyte interface at the instrumentation amplifier (INA118) inputs, which are further biased by R_1 and R_2. In the 1st stage, INA118 output, V_{LPF}, is low pass filtered by an amplifier (AD8603), R_3, and C_3, and subtracted from the input signal to provide a high-pass filtered version of the input signal with a cut-off frequency of $1/(2\pi \cdot R_3 \cdot C_3)$. The 2nd stage, formed by A_2, R_4, R_5, and C_4, is used as a low-pass filter (LPF) with the gain set by $-R_5/R_4$. AFE connects to the built-in ADC of CC2541 through a buffer stage. The common-mode voltage, V_{REF}, is set at half of the supply voltage. To protect AFEs from photoelectric artifacts [7], [8], an artifact rejection (AR) signal is generated during stimulation to briefly disconnect the INA118 inverting input from the microelectrode and short it to ground.

2.1.2 Data Communication Algorithm

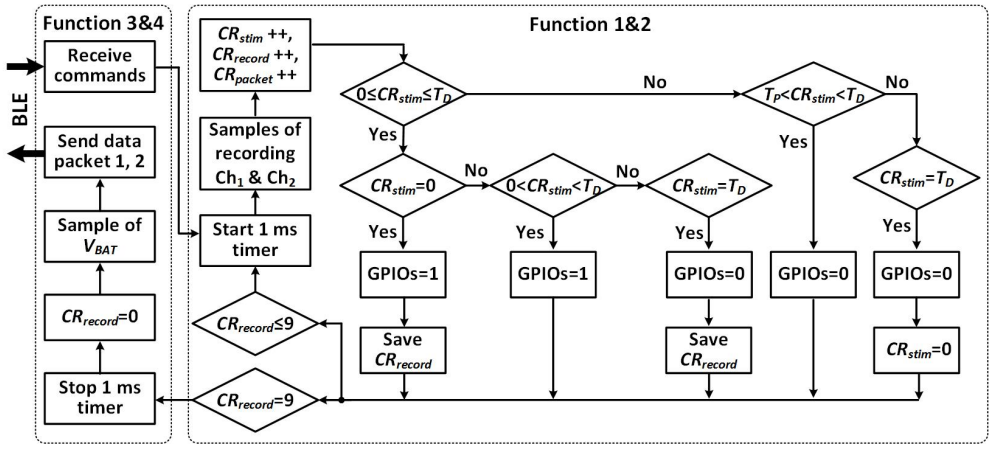

Figure 2.3. Simplified control flowchart of the MCU firmware.

The headstage firmware has four functions: 1) precisely timed stimulation, 2) continuous recording, 3) command data reception, and 4) neural data transmission. Once the BLE connection is established, the user can lunch functions 1 and 2 by triggering a 1 ms timer in a loop, as shown in Figure 2.3. Four tasks of function 2 are executed in each sequence. First, the built-in ADC captures a sample of the neural data from each AFE channel. Second, recording (CR_{record}), stimulation (CR_{stim}), and data packet (CR_{packet}) counters are added by one. CR_{stim} is then compared with 0, duty cycle (T_D), and stimulation period (T_P) to turn on/off the selected μLEDs and decide whether to save the current CR_{record}. To synchronize stimulation with recording for offline data analysis, CR_{record} will be saved if CR_{stim} = 0 and CR_{stim} = T_D, corresponding to the start and end of a stimulation pulse, respectively. Finally, CR_{record} is compared with 10 to decide whether to repeat the loop or move forward to functions 3 and 4. When functions 3 and 4 trigger, the MCU takes one sample from V_{BAT}, and packetizes it with the other 10 samples from AFE, and wirelessly transmits the packaged data to CC2540 on the USB dongle. If the BLE connection is lost, the two MCUs try to reconnect automatically.

2.1.3 *Interface Sensor Fabrication*

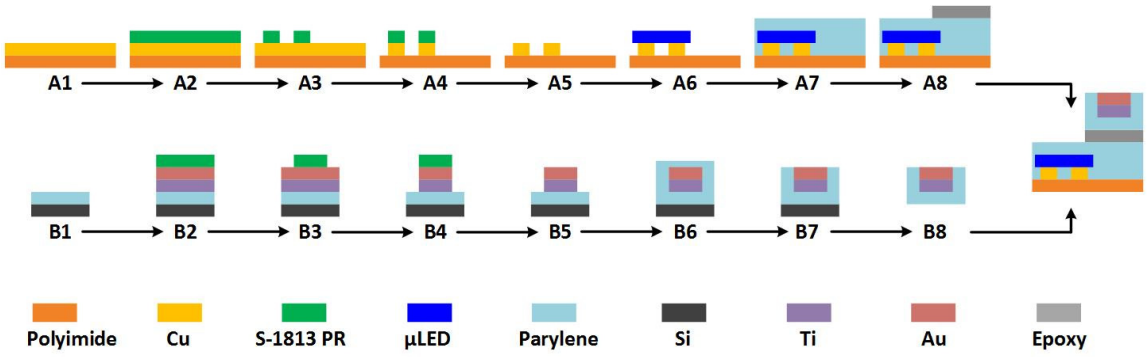

Figure 2.4. The fabrication procedure of the polyimide-based substrate.

The optical stimulation and recording electrodes are fabricated on separate polyimide films[1], as shown in Figure 2.4, which are flexible and bio-compatible. Stimulation channels are divided into two sub-arrays, each with two μLEDs separated by 1 mm to ensure enough illumination fields distinction. A 9 μm thick double-sided copper clad polyimide film was used as the substrate. Cu was patterned to create interconnections and pads for μLED bonding. Commercial surface mounted μLEDs (270 μm×220 μm×50 μm, TR2227TM) from Cree (Durham, NC) with peak wavelength of 460 nm were bonded on the interconnect pads by applying low melting point solder (~62 °C, 144 Alloy Field's Metal from Rotometals) [86]. This flexible stimulator was then packaged using Parylene-C, a polymer that has shown superior biocompatibility, good flexibility, optical transparency in the visible spectrum, colorless behavior, chemical inertness, and low permeability [87], [88]. The recording electrodes are positioned 5 mm from the closest μLED to not only record strong light-evoked ECoG signal but also reduce photoelectric artifacts, therefore, ensuring recorded ECoG signals with high signal-to-noise ratio (SNR). Our design allows the stimulation and/or recording from multiple sites of the cortex. Fabrication of the recording array initiated with chemical vapor deposition of 12 μm

[1] I would like to thank Dr. Wen Li for her technique support on the interface sensor fabrication.

Parylene on a silicon wafer, followed by thin films of titanium and gold deposition using an Edward Auto306 thermal evaporator. Au and Ti were patterned by potassium iodide and hydrofluoric acid, respectively, to create 500 μm diameter recording electrodes. The array was then packaged by Parylene-C, followed by oxygen plasma etching to selectively expose the recording sites. Finally, the flexible array was released from the silicon wafer and bonded with the stimulation array using medical grade epoxy.

2.2 Experimental Measurements

The headstage, connected to the polyimide-based substrate, executed user commands to drive a single μLED with pulse width of 10 ms at 1 Hz. The digital POT value is determined by (256-*D*)/256×100 kΩ+0.06 kΩ, where *D* is the decimal equivalent of the binary code loaded in its 8-bit register (max resistance = 100 kΩ). The μLED current at each *D* was measured from the voltage across a 10 Ω current-sensing resistor in series with the selected μLED. The emitted light during a pulse was collected from the μLED surface by an optical power meter (Newport 1835-C). Details of μLED optical properties tested with brain tissue can be found in [86].

The AFE was characterized after immersing the polyimide-based substrate in 0.9% saline solution. The noise spectrum, harmonic distortion, and frequency response of the AFE channels were measured with a dynamic signal analyzer (Agilent, 35670A). The electrochemical impedance of the recording microelectrode was analyzed using a potentiostat (Electrochemical Analyzer, CH Instruments) in a three-electrode cell, with the Au microelectrode as the working electrode, an Ag/AgCl electrode as the reference electrode, and a platinum electrode as the counter electrode.

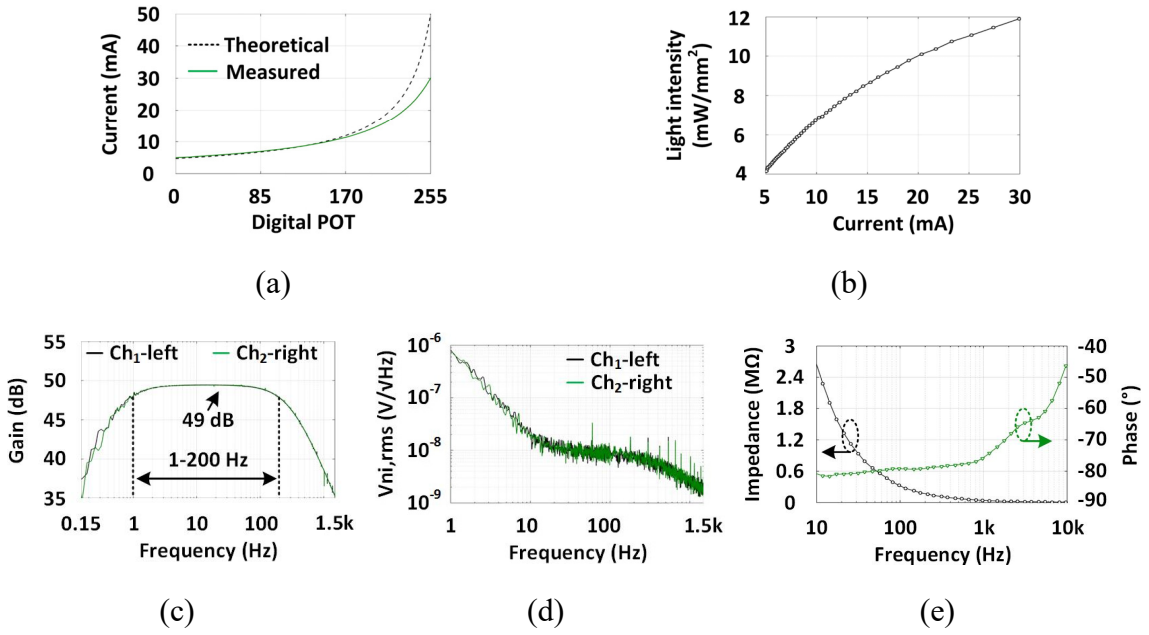

Figure 2.5. (a) Theoretical estimate and measured current through one µLED vs. the digital POT input. (b) Light intensity of the µLED vs. current. (c) 2-ch AFE frequency response. (d) Input-referred voltage noise spectral density of 2-ch AFEs. (e) Changes in the gold microelectrode impedance magnitude & phase vs. frequency.

Figure 2.5a shows how the µLED current increments from 5 to 30 mA as a function of *D*. Parasitic resistance of the battery limits the µLED current, preventing it from following the theoretical value as *D* exceeds 170. Figure 2.5b shows the measured light intensity of a single µLED as a functional of its current. At the minimum current of 5 mA, the light intensity is 4 mW/mm^2, which is above the threshold for effective optical modulation of neural activities [61]. Figure 2.5c shows the measured AFE frequency response from 0.15 Hz to 1.5 kHz. It can be seen that the midband gain of ~49 dB was relatively constant within important 1 Hz to 200 Hz band of interest, resulting in low distortion. Figure 2.5d shows the measured AFE input-referred voltage noise spectrum. The thermal noise level is 10 nV/√Hz and 1/f noise corner occurs at 10 Hz. Integration under this curve from 1 Hz to 1.5 kHz yields a root mean square (RMS) noise voltage of 8.47 µVrms and 8.64 µVrms for channels 1 and 2, respectively. Distortion stays below 1%

total harmonic distortion (THD) for input below 11.3 mV_{PP}, resulting in a dynamic range of ~53.4 dB. In Figure 2.5e, the frequency-dependent impedance magnitude and phase were measured from 10 Hz to 100 kHz when a 5 mV_{RMS} sinusoid waveform was applied to the working electrode. The impedance magnitude at 1 kHz was ~36.2 kΩ, which is suitable for ECoG recording [89]. The WOENI specifications are summarized in Table 2.1.

Table 2.1. Measured specifications of the WOENI system.

ECoG recording		**Optical stimulation**	
# of channels	2	# of channels	4
Mid-band gain	49 dB	Stim. current	5~30 mA, 8 bits
Bandwidth	1~200 Hz	Light intensity	4~12 mW/mm^2
Input-referred noise	8.47 μV_{rms}, 8.64 μV_{rms}	Stim. period	0.1~0.9 s in 10 steps, 1~10 s in 10 steps
THD (11.3 mV_{PP} input)	1%	Duty cycle	0.1~0.9% in 10 steps, 1~10% in 10 steps
Dynamic range (1% THD)	53.5 dB, 53.3 dB	**Data transmission**	
Input impedance/ 1 kHz	36.2 kΩ	Data throughput	32 kbps
CMRR	>110 dB/1 kHz	Dara error rate	< 0.3%
PSRR	>80 dB/1 kHz	Transmission range	~3 m
Power consumption	1.5 mW/channel	ENOB	11 bits
Recovery time	5 ms	Sampling rate	1 kS/s

2.3 *In Vivo* Experiments

In vivo experiments[2] were conducted on five freely behaving adult Long Evans rats (female, 300-400 g) to establish the surgical procedure and verify the functionality of the prototype WOENI device. All procedures were approved by the Institutional Animal Care and Use Committee (IACUC) at Michigan State University. Prior to device implantation, four of them received virus injection (AAV-hSyn-hChR2 (H134R)-m Cherry; UNC Vector Core) in their virtual cortex (V1) to express neurons with light-sensitive channelrhodopsin-2 (ChR2) while one non-transfected rat was used as a negative control. After recovery from

[2] I would like to thank Dr. Wen Li, Dr. Arthur Weber, and Wasif Khan for their great collaborations on the device fabrication and *in vivo* experiments, and Dr. Bin Fan for his help on the data analysis.

anesthesia, the transfected rats were housed separately, and given pain medication and antibiotics to minimize discomfort and infection until they recovered from the injection surgery. The four transfected rats and one non-transfected rat were anesthetized and placed on the stereotaxic frame for device implantation. Two small pieces of bone were removed to expose the left and right V1 cortices, respectively, with the coordinates of the skull openings (P=6.3 mm, L=3.6 mm) over V1, while the dura remained intact. The polyimide-based substrate was surgically implanted over V1 and firmly attached onto the skull using dental cement. The grounding wire was inserted under the skin. The skin was sutured closed, leaving only the Omnetics connector exposed for the detachable headstage. These experiments were performed 4 weeks after virus injection to ensure that the cortical neurons are expressing ChR2 opsin.

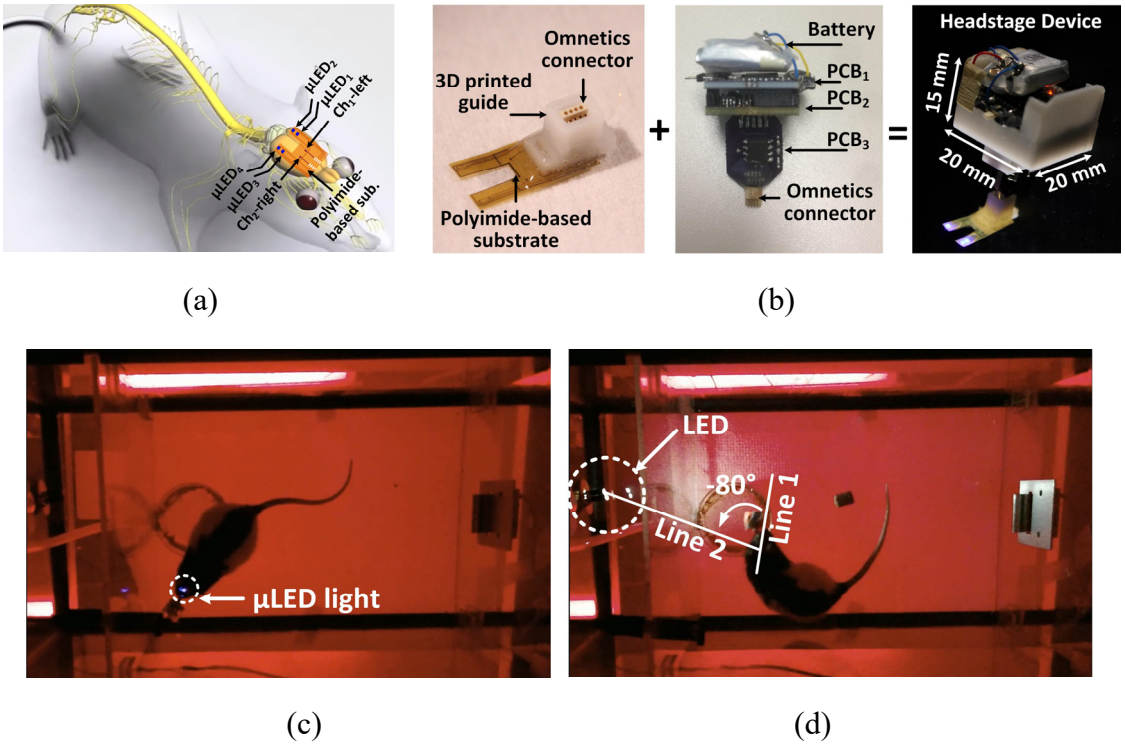

Figure 2.6. (a) Anatomical location of the polyimide-based substrate on rat brain. (b) WOENI device implementation. *In vivo* experimental setup for (c) optical stimulation on V1 and (d) visual stimulation.

Figure 2.6a shows μLED_1, μLED_2, and channel-1 left (Ch_1-left) microelectrode above the left V1 lobe, and μLED_3, μLED_4, and channel-2 right (Ch_2-right) microelectrode above the right V1 lobe of the rat brain. Figure 2.6b shows the fabricated WOENI device prototype with four optical stimulation and two ECoG recording channels. A small 3D-printed guide is glued on to the back-end of the flexible substrate around the Omnecitcs connector to facilitate insertion, prevent blockage with dental cement, and provide additional mechanical support for the headstage. The headstage electronics and rechargeable battery are housed in a 3D-printed box ($15\times20\times20$ mm^3) to avoid moisture and mechanical damage by the animal actions. The headstage weighs 5.5 g, well below the level that would cause any discomfort or interference with the natural behavior of rats. Prior to *in vivo* experiments, the rats were handled to attach the headstage and habituated to the homecage for 5 minutes. In Figure 2.6c, the top view of the experiment setup is shown when the optical stimulation on V1 was performed by turning on/off a subset of μLEDs. In Figure 2.6d, a commercial white LED (Chanzon) with diffuse white light was placed in the middle of the left wall at a height of 8 cm from the bottom of homecage to apply visual stimulation. The angle between two straight lines, one connecting the midpoint between two ears to the rat nose, and the other one connecting the ears midpoint to the LED is defined as the visual angle (VA) to indicate the relative positioning of the external LED to rats' eyes. Clockwise rotation from line 1 to 2 is considered as positive VA, while anticlockwise rotation is considered as negative VA.

2.3.1 Optical Stimulation on V1

C-Fos was used as a biomarker to validate neuronal activity induced by optical stimulation. Experiments were performed on one transfected rat (rat #1) and one non-

transfected control. Both received 45-min optical stimulation on the left V1 with 10 ms light exposure and 5 mA current at 1 Hz. After the stimulation, tissue sections with a thickness of 50 μm were cut in chilled 0.1 M phosphate buffer and stored in 24 well tissue culture dishes for post immunohistology chemical processing. The processed sections were then mounted on microscope glass slides and covered by coverslips with an anti-fade solution for c-Fos expression imaging under a fluorescent microscope.

To evaluate the device performance, the ECoG signals from both the stimulated and unstimulated V1 of other two transfected rats, rat #2 and rat #3, were recorded and compared. For each rat, four experiments were conducted on days 0, 7, 14, and 21, post polyimide substrate implantation. During each experiment, the headstage was attached to drive the remotely selected μLEDs with current of 5 mA, while recording ECoG from both channels, simultaneously. Each experiment included 150 successive optical stimulations on the left V1 lobe and 150 successive optical stimulations on the right V1 lobe. Each optical stimulation trial started with a 10 ms light exposure and lasted 1 s. Experiments were repeated on the non-transfected control using the same protocol and the ECoG signals were compared to the data recorded from the transfected rats.

The immunostained tissue analysis of rat #1 and the non-transfected control are shown in Figure 2.7a and 2.7b, respectively. Fluorescent images were taken under 10× magnification. The green fluorescence indicates cells expressing c-Fos. For the cortical tissues expressing ChR2 (Figure 2.7a), there was a significant up-regulation of the c-Fos expression in the left V1, implying that the stimulation resulted in an increase in neuronal activity. In contrast, the right V1 showed only a mild increase in the c-Fos immunostaining. This mild increase in the c-Fos expression of the control is mainly attributed to the baseline

level of the cortical neuron activity and the normal visual stimulation of cortex since the rats had their eyes open. In Figure 2.7b, there is no significant difference of c-Fos expression between the left and right V1 of the non-transfected rat. The results of the immunohistochemical analysis demonstrate the efficacy of the optogenetic stimulation on the transfected cortical tissue.

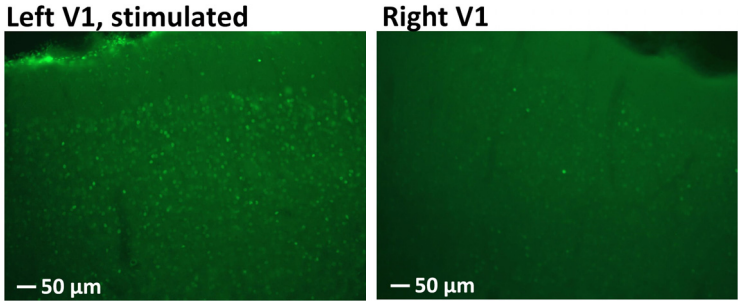

(a)

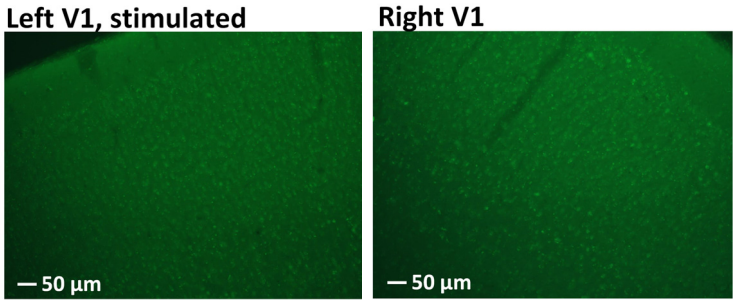

(b)

Figure 2.7. C-Fos expression in the left and right V1 of (a) rat #1 and (b) the non-transfected rat with optical stimulation on the left V1.

Figure 2.8a and 2.8b illustrate ECoG recordings from rat #2 and rat #3, respectively. The optical stimulation on the left V1 induced larger ECoG variation in Ch_1-left. Similarly, larger ECoG variation was observed in Ch_2-right with optical stimulation on the right V1. However, for the non-transfected rat, there is no significant difference in the ECoGs between the stimulated left V1 and unstimulated right V1, as shown in Figure 2.8c. Figures 2.8d and 2.8e show the RMS amplitudes of the ECoG signal during a single trial in each

of the four consecutive experiments on days 0, 7, 14, and 21 after polyimide substrate implantation on rats #2 and #3, respectively. The RMS amplitudes of the ECoG signal during a single trial (day-0) on the non-transfected rat is shown in Figure 2.8f. The independent two-sample t-test (significance level, $\alpha = 0.05$) was applied, where the RMS values of the left and right lobe ECoGs in each trial were calculated to obtain two sets of 150 RMS samples of each experiment, one from each of the two sets being compared. The significant effect of the optical stimulation on the ECoG signal from the stimulated V1 was confirmed by $p<0.05$ in all four experiments only for rats #2 and #3, and not for the non-transfected rat. We defined evoked-to-spontaneous ratio (E/S ratio) as the RMS amplitude of the ECoG signal of the stimulated V1 divided by that of the unstimulated V1. The E/S ratios of both rats #2 (Figure 2.8g) and #3 (Figure 2.8h) decayed by ~15% over four experiments, but still remained > 3.9 during 21 days, which demonstrated that the ECoG signals from stimulated and unstimulated V1 were distinguishable. In Figure 2.8i, the E/S ratio of the non-transfected rat is ~1, implying the negligible difference between the ECoG signals from the stimulated and unstimulated V1.

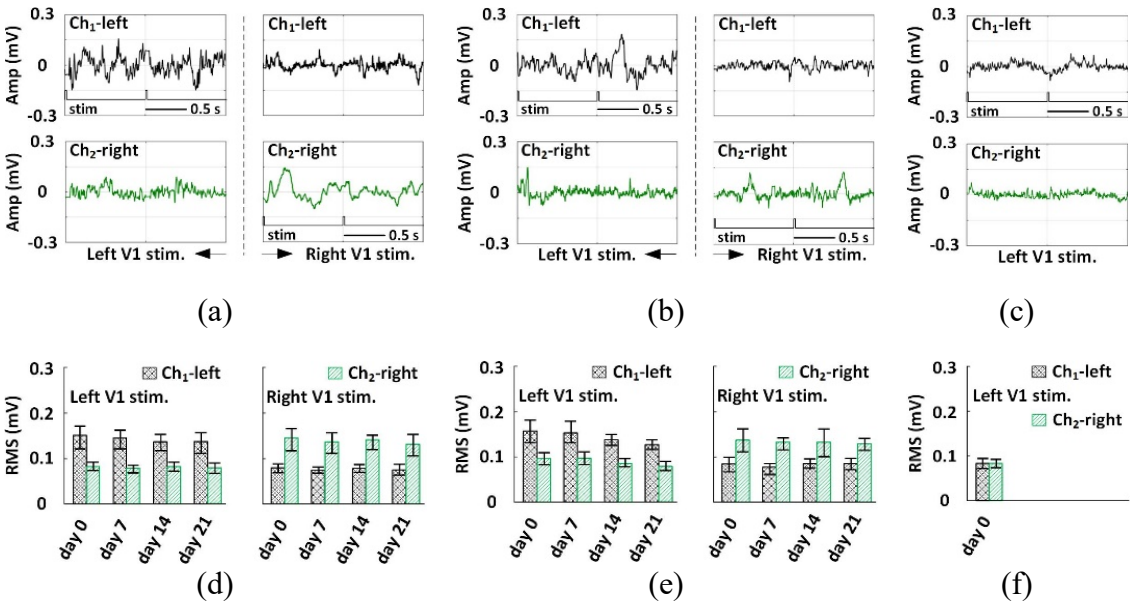

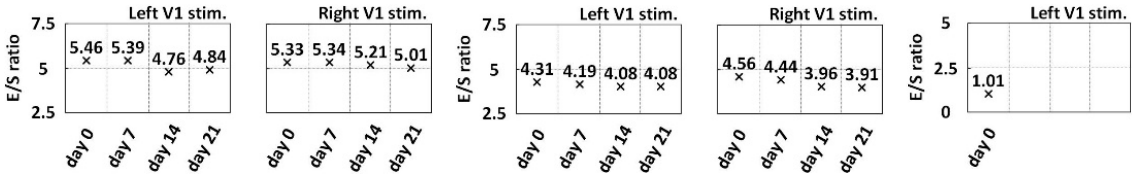

(g) (h) (i)

Figure 2.8. Examples of 2 s long ECoG data recorded from the left and right V1 of (a) rat #2, (b) rat #3, and (c) the non-transfected rat, with V1 optical stimulation flags on the stimulated side. RMS values of the ECoG recorded from Ch_1-left and Ch_2-right in each experiment performed on (d) rat #2, (e) rat #3, and (f) the non-transfected rat, indicating the optically stimulated V1. Evoked-to-spontaneous (E/S) ECoG RMS ratios of the experiments on (g) rat #2 and (h) rat #3, and (i) the non-transfected rat.

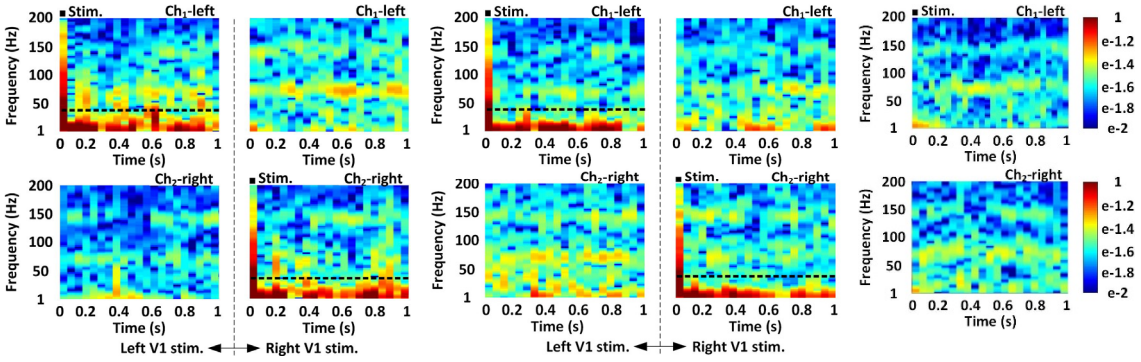

(a) (b) (c)

Figure 2.9. Time-frequency maps of the averaged and normalized PSD from 2-ch ECoG of (a) rat #2, (b) rat #3, and (c) the non-transfected rat, within 1-200 Hz frequency range and 1 s time window, with stimulation markers.

Each channel ECoG signal was averaged over four consecutive experiments and mapped onto a time-frequency map of the color-coded normalized power spectral density (PSD) distribution in 1-200 Hz frequency range [90]. In Figure 2.9a and 2.9b, the ECoG signal from stimulated V1 show significant increase in PSD, which is concentrated within a relatively narrow 1-40 Hz band. In Figure 2.9c, there was no significant difference of PSD between the stimulated and unstimulated V1 of the non-transfected rat. Integrating the normalized PSD within 1-40 Hz at each time point yields the time-varying power of the ECoG signal. The ECoG power of the experiment (day-0) was compared between one

channel to the other. In Figure 2.10a and 2.10b, higher ECoG power from the stimulated V1 was observed on the transfected rats #2 and #3, which were validated by the independent two-sample t-test (α=0.05) with $p < 0.05$. In Figure 2.10c, no significant ECoG power increase was observed on the stimulated V1 of the non-transfected rat.

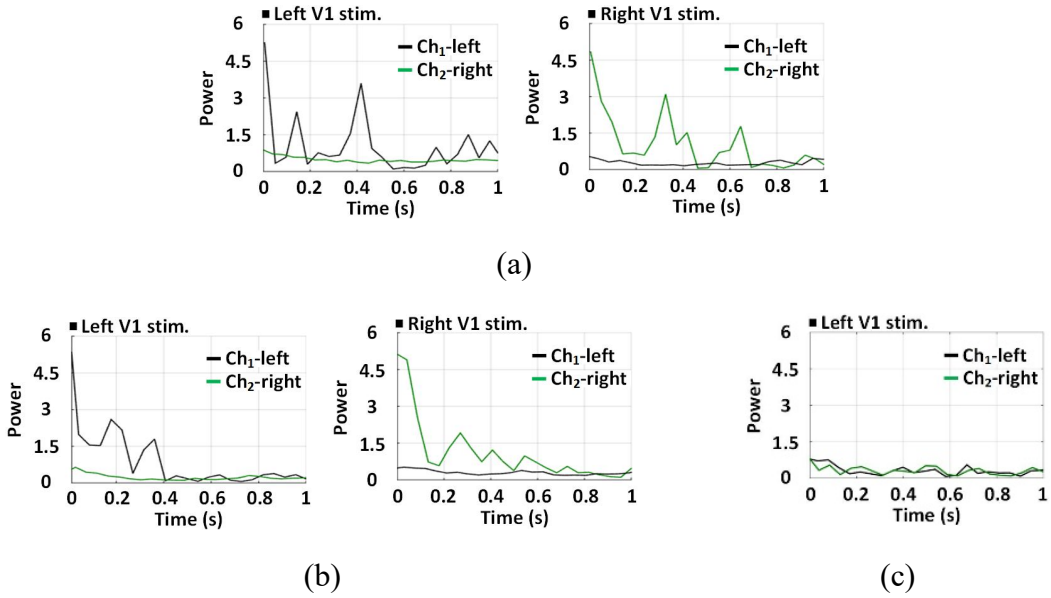

Figure 2.10. (a) Averaged time-varying ECoG power for Ch_1-left and Ch_2-right channels of (a) rat #2, (b) rat #3, and (c) the non-transfected rat, within 1-40 Hz band and 1s time window, with stimulation markers.

Figure 2.11 shows the Hilbert transformation of instantaneous phases of day-0 ECoG recordings within 1-40 Hz [91]. Colors indicate the instantaneous phase of each trial, aligned based on the stimulus ON time, and stacked. For the transfected rat #2 and #3, the ECoG signal from the stimulated V1 showed longer phase synchronization following each stimulus, while almost no phase synchrony is observed in the control lobe. The neural modulation was reliable across over 150 trials. The optical stimulation generated close to deterministic phase-locked neuronal oscillations without any latency for ~0.25 s (Ch_1-left) and ~0.2 (Ch_2-right) of rat #2 and ~0.3 s (Ch_1-left) and ~0.2 s (Ch_2-right) of rat #3, as validated by the nonparametric Wilcoxon signed rank test (α=0.05) with $p < 0.05$.

However, in Figure 2.11c, the ECoG signal from the stimulated and unstimulated V1 of the non-transfected rat did not show phase synchrony.

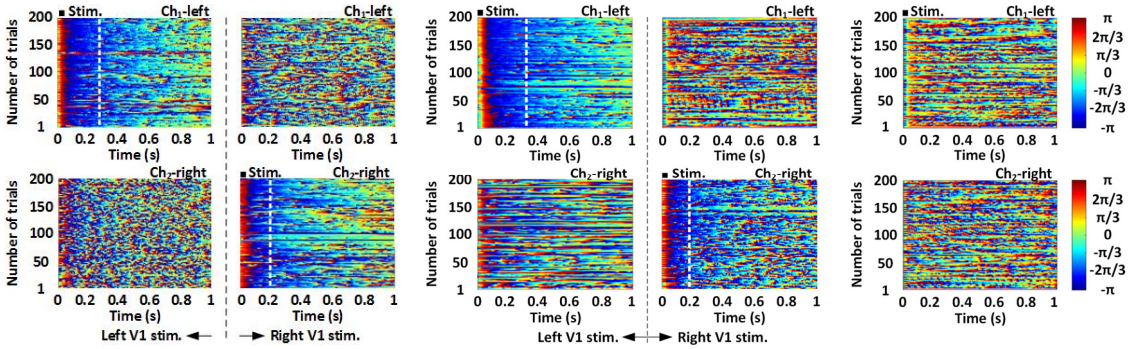

(a) (b) (c)

Figure 2.11. Instantaneous phase of the ECoG from Ch_1-left and Ch_2-right channels of (a) rat #2, (b) rat #3, and (c) non-transfected rat, within 1-40 Hz band and 1s time window, with stimulation markers.

2.3.2 Visual Stimulation

Previous studies have reported that a given side of the V1 lobe responded to the visual stimuli from the opposite half of the field of view [92]. We hypothesized that we will observe a similar result by applying visual stimulation on rat #4 on days 0, 7, 14, and 21 after implantation. The external LED was controlled by pulses of 1 s duration and 10 s intervals (0.1 Hz), while recording ECoG from the implanted microelectrodes. Each experiment included 30 trials, each of which started with 1 s visual stimulation and lasted 10 s. Similar to optogenetic stimulation, the ECoG data was transmitted to the external PC in real time and saved locally for data processing, using MATLAB Chronux toolbox [93]. Two-channel ECoG recordings in each trial were converted to the corresponding time-varying power by integrating the normalized PSD in 1-40 Hz band at every time point, compared against one another. Figure 2.12 shows the ECoG power of each channel when rat #4 had VA of 0°, 180°, -90°, and 90° to visualize all possible comparisons between

ECoG power results from the two channels. The relative positioning of the rat's eyes to the external LED is almost unchanged during the 1s stimulation pulse. The inter-channel difference of ECoG power is not visible at 0° (Figure 2.12a) and 180° (Figure 2.12b). The ECoG signals of both channels at 0° VA show higher power than that at 180° VA. At VA = -90° in Figure 2.12c, the ECoG power of Ch_2-right V1 is stronger than that of Ch_1-left, while the ECoG power of Ch_1-left is higher than Ch_2-right at VA = 90° in Figure 2.12d.

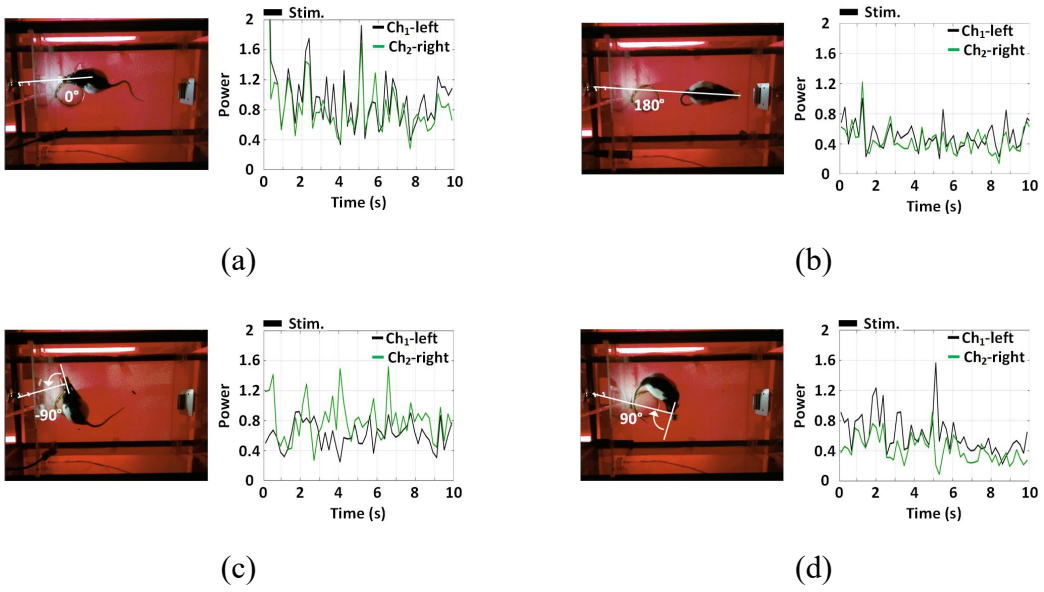

Figure 2.12. Time-varying ECoG power from Ch_1-left and Ch_2-right channels in a single trial at visual angles of (a) VA = 0°, (b) VA = 180°, (c) VA = -90°, and (d) VA = 90°, within 1-40 Hz band and 10 s time window, with stimulation markers.

In Figure 2.13, we have divided the ECoG from four consecutive experiments into four categories based on their power variances and labeled by different colors, grey: low ECoG power in both channels, orange: high ECoG power in both channels, blue: higher ECoG power in Ch_1-left, green: higher ECoG power in Ch_2-right. For each experiment, the color-coded comparison for each trial placed on a circular map, which orientation and radius correspond with the manually observed VA from the homecage top view (see Figure 2.6d) and trial number, respectively. By applying the nonparametric Wilcoxon signed rank

test (α=0.05), it was observed that blue and green were found mainly in the VA ranges of 30°-150° and -30°- -150°, respectively, with both $p < 0.05$. Orange was not observed within VA range of -165°-165°, while gray did not appear within VA range of -15°-15°. Our conclusion is that the difference between ECoG power levels from left and right channels could be caused by different amounts of light entering the subject eyes. Expectedly, the difference between ECoG power levels become smaller and less predictable when VA falls within -165°-165° and -15°-15°, in which both eyes are likely receive similar amounts of light when the LED is on.

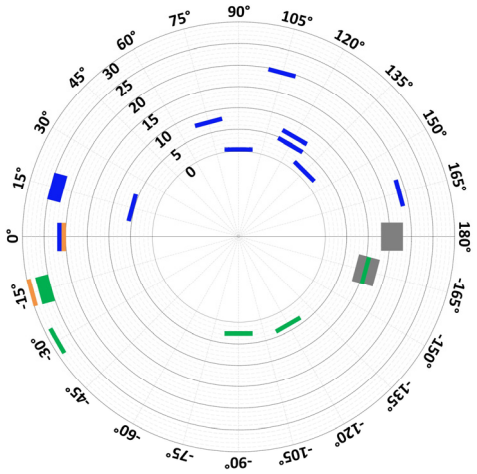

Experiment 1

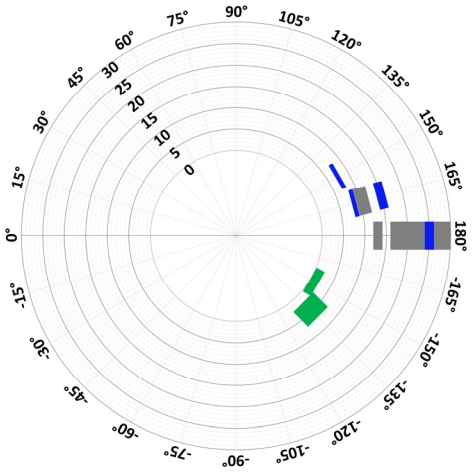

Experiment 2

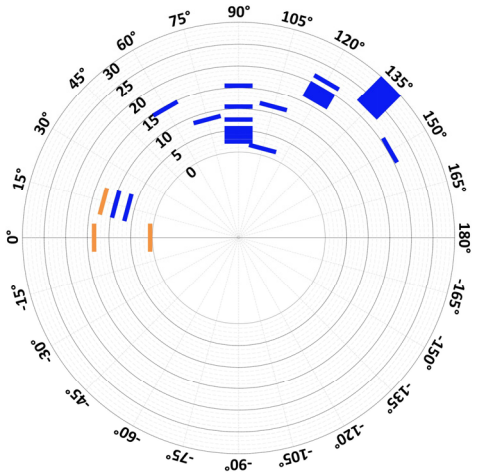

Experiment 3

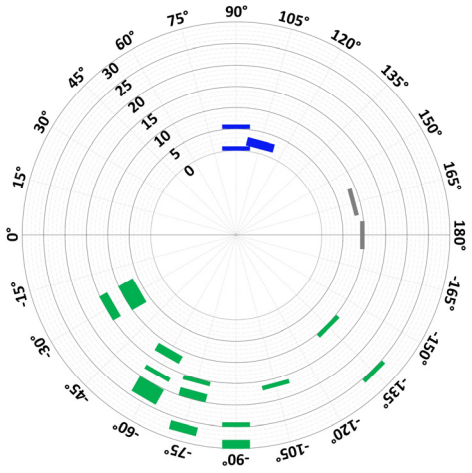

Experiment 4

Figure 2.13. Comparing ECoG power in each trial in experiments 1-4, marked based on VA (orientation) and trial number (radius). Grey: low ECoG power in both channels, Orange: high ECoG power in both channels. Blue: higher ECoG power in Ch_1-left. Green: higher ECoG power in Ch_2-right.

2.4 Summary and Discussion

To reduce the constraint imposed by conventional laser-based optical systems, particularly on small freely behaving animals, we have developed the WOENI device. While this work is primarily focused on the neural excitation, the wide selection of the μLEDs at various wavelengths makes it easy to switch to red, yellow, or a mix of these colors for applications in neural inhibition.

Table 2.2. Benchmarking of wireless LED-based neural interface systems.

Publication	2015 [17]	2015 [18]	2015 [19]	2017 [16]	**This work**
Standby power	-	-	-	119 mW	**42 mW**
# of stim.	2-ch	1-ch	4-ch	32-ch, 1-ch (test)	**4-ch**
Stim. current	20 mA	25 mA	-	150 mA	**30 mA**
# of recording	-	-	-	32-ch, 8-ch (test)	**2-ch**
Data link	2.4 GHz RF TRx	2.4 GHz RF TRx	Infrared interrogation	2.4 GHz RF TRx	**2.4 GHz RF TRx**
Device size (mm^3)	14×17×5 w/ BAT	12×11×7 w/ BAT	-	18×17×10 w/o BAT	**15×20×20 w/ BAT**
Device weight	2.9 g w/BAT	1.6 g w/BAT	1.8 g w/BAT	4.9 g w/ BAT	**5.5 g w/BAT**
Animal subject	Mouse	Mouse	Mouse	Rat	**Rat**
Freely moving	Yes	Yes	Yes	No	**Yes**
Implant duration	41 days	>5 days	>1 week	NA	**21 days**

Other efforts on developing wireless LED-based optical system are summarized in Table 2.2. Compared to them, the key advantage of this proposed design is the ability to simultaneously apply optical stimulation and continue electrophysiological recording as feedback, allowing for bi-directional optical neuromodulation. While the system in [16]

can apply multichannel neural recording and optical stimulation, it was only tested on an anesthetized rat, and its feasibility experiments on freely behaving animals is still unclear. The functionality of the WOENI device was evaluated *in vivo* on freely behaving rats.

In the case of optical stimulation on V1, immunostained tissue-based and ECoG signal-based proofs were achieved from the comparison between the transfected and non-transfected rats, and between the stimulated and unstimulated V1. Significant increases in c-Fos expression, ECoG variation, ECoG power, and phase synchronization were observed on the stimulated V1 of the transfected rats. The light-evoked phenomenon did not occur on the non-transfected rat and the difference between the left and right V1 in terms of c-Fos expression and ECoG signals were also negligible. In the case of visual stimulation on a freely behaving rat, a well-documented study [92] was also repeated, where ECoG signal from a given side of V1 was evoked when the opposite half of visual field receives stimuli. The *in vivo* experimental results match with expectations and therefore can prove the functionality of the proposed device.

The highly replicable ECoG analysis results, under two types of optical stimulation, during four conservative experiments within 21 days demonstrate the stability of the proposed device, which is critical for chronic studies. The evoked-to-spontaneous ECoG ratio reduced by ~15% in both rats over four experiments, which could be linked to glial cell and scar formation, inflammation, and mechanically induced trauma as a result of impedance mismatch between implanted devices and soft brain tissue [94]-[96]. The light-evoked ECoG, however, was still distinguishable from the spontaneous ECoG, implying the efficacy of the optical stimulation and ECoG recording up to 21 days after implantation.

CHAPTER 3. WIRELESS POWER TRANSMISSION SYSTEM FOR EVALUATING HEADSTAGE

The environment within homecage has the potential to significantly affect brain neurochemistry in rats and the resulting behavior, suggesting its influence on the quality of the collected data [97]-[100]. To conduct experiments involving small freely behaving animals, researchers must follow a labor intensive routine, such as: 1) transferring the animals from their homecages to the experimental arena, which can be an operant conditioning chamber, 2) grabbing the animals to attach cables, connectors, or wireless headstages, 3) closely observing the animal behavior during the intervention and video recording for subsequent data analysis, 4) grabbing the animals to detach cables and connectors, and 5) returning the animals back to their homecages and eventually to the animal facility [101]. This routine is repeated for every subject, which accumulates to become a chronic stressor for animals and a laborious task for researchers [97]. If any portion of the aforementioned procedure can be reduced or automated, it would have a significant impact on the quality of the experimental results, due to the more normative behavior of the animals.

Researchers have proposed wirelessly-powered and -communicated systems that create less stressful environments for longitudinal experiments on small freely moving animals [36]-[43]. In the case of inductive power transmission, angular and horizontal misalignments and distance variation between the Tx and Rx coils happen quite frequently in practice as the animal subject moves in the cage, as shown in Figure 3.1. This will result

in significant reduction in PTE and PDL, to the extent that it may cause malfunction if the condition persists beyond the built-in temporary energy storage of the headstage.

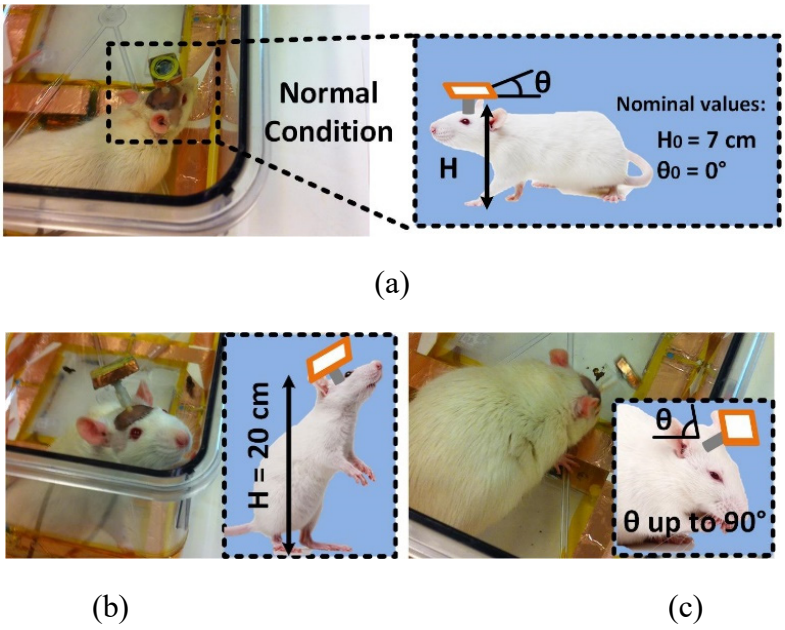

Figure 3.1. (a) Definition of normal height and orientation of the headstage when the rat is walking. (b) Problem of Tx-Rx increased distance when the animal rear on its hind limbs. (c) Angular misalignment of the headstage attached in a freely behaving animal when the head is turned downward.

We have developed a WPT system, which is built around a standard homecage [102] to wirelessly power and communicate with a stimulating headstage in this prototype, with a new 4-coil inductive link design [103]-[106]. We call it EnerCage-HC2. Wireless power is delivered in the near-field domain at 13.56 MHz, a Federal Communications Commission (FCC) approved operating frequency for industrial, scientific, and medical (ISM) applications. The novel coil arrangement around the homecage enhances the magnetic flux density, mutual coupling, and PTE in the entire 3D space of the homecage. To achieve high Q-factor in the Tx resonators at 13.56 MHz without reducing their self-resonance frequency (SRF), they are optimally segmented to achieve a homogeneous PTE. Four slanted High-Q Rx resonators encompass four diagonal planes of the headstage and

direct the Tx EM field, which is already homogenized by the Tx resonators [104], towards the Rx load to ensure sufficient PDL at any arbitrary headstage orientation. A closed-loop power control (CLPC) mechanism is established to ensure stable PDL at a user-defined level, > 40 mW in this prototype, despite animal movements. Three freely behaving rats were implanted with electrodes in the globus pallidus (GPi) to observe the well-documented effects of electrical stimulation in this region of the brain.

3.1 System Overview

3.1.1 Circuit Details

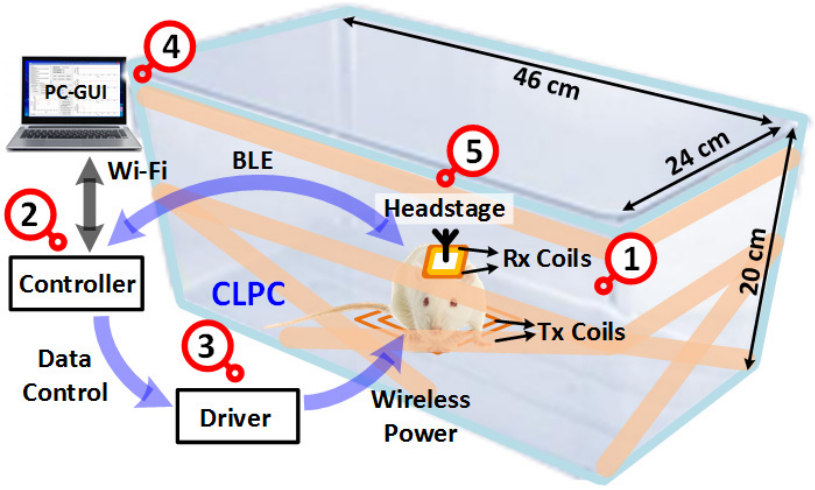

Figure 3.2. A simplified conceptual representation of the proposed EnerCage-HC2 system.

Figure 3.2 shows a simplified block diagram of the EnerCage- HC2 system, which is built around a standard rodent homecage. It is equipped with 1) a 4-coil inductive link, 2) an embedded controller based on a customized Raspberry Pi (RPi), 3) a driver block that includes a Class-C power amplifier (PA), and 4) a PC in charge of data storage and GUI. EnerCage- HC2 system wirelessly powers 5) a headstage, carried by the animal subject, which includes the Rx coils, and stabilizes its received power in a closed-loop fashion by

wirelessly communicating with the controller block through a BLE link. The BLE link combined with the Wi-Fi connection between the PC and controller are designed to enable remote control of the EnerCage-HC2 system and facilitate automatic data acquisition.

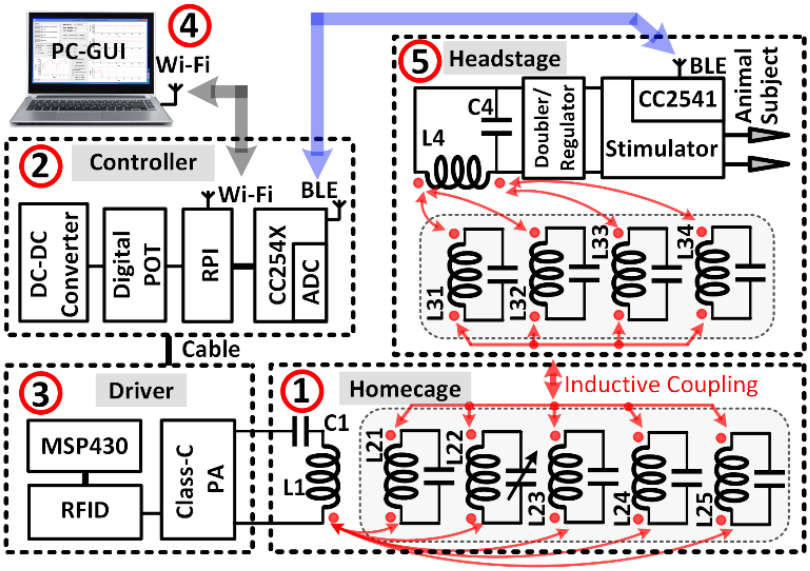

(a)

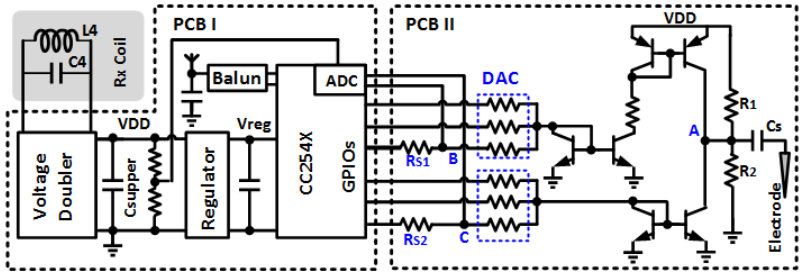

(b)

Figure 3.3. Schematic diagram of (a) the key circuits involved in the power delivery path and (b) the stimulator circuit implemented on two PCBs in the headstage.

Figure 3.3a shows a simplified schematic of wireless power and data delivery between different components of the EnerCage- HC2 system. Red arrows indicate mutual coupling among a driver coil (L_1) and five primary resonators (L_{21}-L_{25}) around the homecage on the Tx side and four resonators (L_{31}-L_{34}) around the headstage and a load coil (L_4) on the Rx side. L_1 is the only coil driven by the Class-C PA in the driver block, which

follows a RFID reader (TRF7960A, Texas Instruments). L_4 on the Rx side is the only coil connected to the headstage, which is followed by a voltage doubler and regulator, as shown in Figure 3.3b. The PA output power is controlled by its supply voltage, V_{PA}, which is generated by a DC-DC converter in the controller block and delivered through a cable. All high Q-factor resonators in this design, L_{21}-L_{25} and L_{31}-L_{34}, are simply floating and primality meant to homogenize the magnetic field and strengthen the Tx-Rx coupling to achieve better PTE all across the homecage.

Figure 3.3b shows a simplified schematic diagram of the stimulator circuit in the headstage, which involves two stacked PCBs. In PCB-I, the voltage doubler that follows L_4 generates a DC voltage, V_{DD}, from the 13.56 MHz power carrier, which is divided in half and sampled by the built-in ADC of the headstage MCU. The MCU is a CC2541 from Texas Instruments, which also establishes a bidirectional BLE link with the CC2540 MCU in the controller to deliver this information as feedback in the CLPC mechanism that continuously stabilizes V_{DD}, which also sets the stimulator compliance voltage, at a desired user-defined level. The CLPC prevents waste of power in the voltage doubler and the PA when the coupling is too strong by adjusting the PA output power to be just enough to stabilize the V_{DD} despite Tx-Rx coupling variations due to animal movements [107]. To minimize the effects of V_{DD} variations on the MCU and BLE link, it is further regulated onboard to generate V_{reg} = 3.3 V, before supplying the MCU. In PCB II, a structure involving a complementary current source/sink with a series capacitor, C_S, enable charge-balanced bipolar current stimulation. A discrete 3-bit current steering digital to analog converter (DAC) controlled by the MCU GPIO ports adjusts the stimulus current in anodic and cathodic phases. User-adjustable stimulation parameters in the GUI include

stimulation frequency, (40-200 Hz with 40 Hz resolution), pulse width in cathodic phase (100-300 μs with 50 μs resolution), and stimulation current in cathodic phase (75-525 μA with 75 μA resolution). To monitor the actual status of the stimulation, the headstage MCU also takes a burst of eight consecutive samples from every biphasic pulse (2 during cathodic phase and 6 during anodic phase) from 1 kΩ current sense resistors, R_{S1} and R_{S2}, and sends them to the controller via BLE.

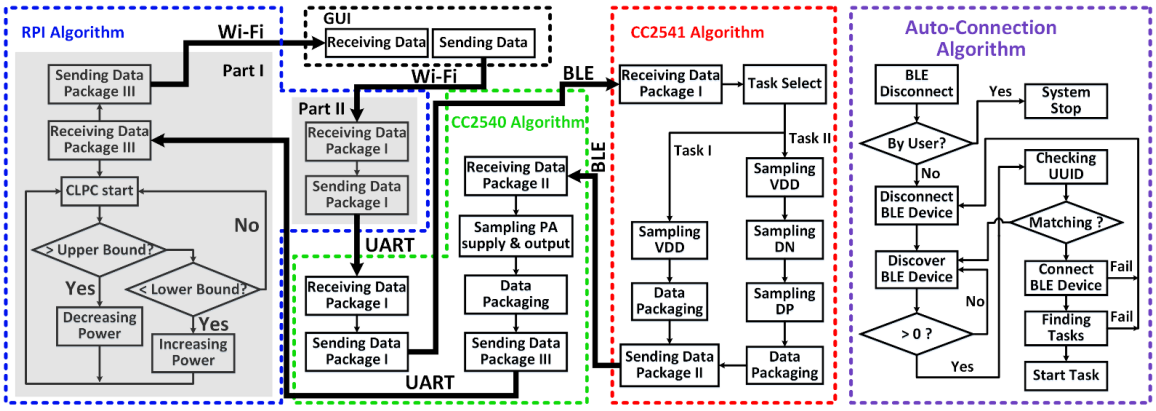

Figure 3.4. Simplified flowchart of the data communication algorithm in the proposed EnerCage-HC2 system, as implemented in the algorithm among CC2541 MCU, CC2540 MCU, and RPi.

3.1.2 Data Communication Algorithm

Figure 3.4 depicts the communication and control flowchart in EnerCage-HC2 between the two aforementioned CC254x MCUs in the headstage and controller via BLE, between RPi and the CC2540 MCU in the controller via Universal Asynchronous Receiver/Transmitter (UART), and between the PC and RPi via Wi-Fi. Upon receiving user commands from the GUI in Data Package-I via the Wi-Fi and UART connections, the CC2540 MCU (master) in the controller automatically establishes a BLE link with CC2541 MCU (slave) in the headstage. Once the BLE link is in place, CC2541 delivers the V_{DD} and stimulus current samples to the CC2540 MCU in Data Package-II. The built-in ADC

in CC2540 MCU samples the PA supply voltage (DC-DC output) and envelope of the output voltage, which are merged with Data Package-II from the headstage to form Data Package-III. Once RPi receives Data Package-III from CC2540 MCU, it dynamically sets the PA supply voltage based on the CLPC algorithm, which compares V_{DD} and a desired user-defined window. The DC-DC converter output voltage is then adjusted to keep V_{DD} within the desired range despite subject movements and headstage loading variations (e.g. stimulator on/off). If the BLE connection is lost, the CC2540 MCU will reconnect through an auto-connection algorithm.

3.2 Design of the 4-Coil Inductive Link

3.2.1 Tx Coil Design

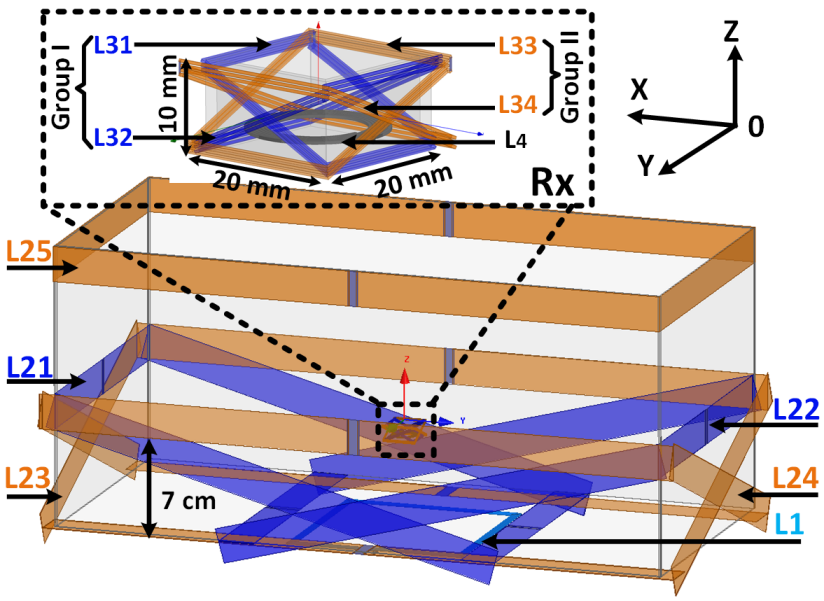

Figure 3.5. 3D model of the 4-coil inductive link constructed in the HFSS.

Figure 3.5 shows the configuration of the 4-coil inductive link[3] with multiple resonators on the Tx and Rx sides in a model constructed in the HFSS environment. Table 3.1 presents detailed specifications of each coil based on dimensions of the homecage and

[3] I would like to thank Dr. Abdollah Mirbozorgi for his great collaboration on the 4-coil inductive link design and optimization.

headstage. On the Tx side we have a wire-wound coil, L_1, which is located under the center of the homecage, driven by the Class-C PA, four High-Q resonators made of copper coil (L_{21}-L_{24}), which are covering four sides of the homecage, and an additional High-Q resonator, L_{25}, wrapped around the rim of the homecage. L_{21}-L_{24} are tilted to elevate the EM field at the nominal height and deliver sufficient power to the headstage even with maximum angular misalignment (90º). The height of L_{21}-L_{24} on one side is 7 cm, which is the nominal height of the headstage on the rat head, H_0, and extended on the other side to fully overlap with L_1 and maximize mutual coupling.

Table 3.1. Measured specifications of the 4-coil inductive link at 13.56 MHz.

Parameter	L_1	L_{21}, L_{22}	L_{23}, L_{24}	L_{25}	L_{31}-L_{34}	L_4
Inductance (µH)	5.46	0.88	0.94	1.01	0.68	0.96
Q-Factor	116	166	160	162	125	142
d_o (cm)	13	-	-	-	-	1.8
d_i (cm)	12.8	-	-	-	-	1.3
Length (cm)	-	32	44	44	2.4	-
Width (cm)	-	22	22	24	2	-
Conductor width (mm)	-	25	25	25	-	-
Thickness (µm)	-	89	89	89	-	
Diameter (mm)	1.45	-	-	-	0.4	0.4
Number of turns	3	1	1	1	3	6
Type of coil	AWG15	Foil tape	Foil tape	Foil tape	AWG26	AWG26

The key factor in determining the Tx resonator (L_{21}-L_{25}) geometries in EnerCage-HC2 system is the compatibility with standard homecage dimensions that are used for rodents, particularly within a rack, and maximum overlap with L_1. Optimizing the 4-coil inductive link means increasing the minimum PTE within the homecage to ensure PDL is enough to keep the headstage on when the CLPC adjusts the Tx power, as opposed to maximizing PTE in the perfectly aligned regions in traditional coil optimization. The optimal size of L_1 is directly related to the separation distance (H) and the headstage (Rx)

dimension and can be calculated for maximum coupling between driver (L_1) and load (L_4) coils using $A_T = A_R + \pi \times H^2$, where A_T and A_R are the areas of L_1 and L_4, respectively.

The subject often climbs the walls of the cage, as shown in Figure 3.1b, resulting in a large distance between the headstage and Tx coils, creating an unfavorable case power transmission scenario. We solved this problem by adding a fifth resonator, L_{25}, to the original design of the Tx coils in [104] at the height of 20 cm from the bottom, to enhance the magnetic flux density on top of the homecage. L_{25}, wrapping around the rim of the homecage, compensates for dropping PTE and PDL due to reduced coupling with L_{21}-L_{24}, as the height of the headstage increases. Considering the large dimension of L_{21}-L_{25}, all Tx resonators were segmented to create a more homogeneous magnetic field inside the homecage. Each segment has equal length and links to other segments by small capacitors in a way that the length of each segment is less than $\lambda/10$, where λ is the wavelength of the power carrier [108], [109]. The cage made of polycarbonate, which is the substrate for L_{21}-L_{25}, has a relative permittivity of $\varepsilon r = 3$. Therefore, for the current induced in Tx resonators, λ is 13 m. To ensure the length of each segments is less than $\lambda/10$, L_{21}-L_{25} were segmented into two identical pieces to prevent phase-inversion in the current distribution along L_{21}-L_{25}, which causes EM field cancellation at the location of L_4 [110].

3.2.2 Rx Coil Design

On the Rx side, we have L_4, which is placed at the bottom of the 3D printed plastic box that houses the headstage electronics and delivers power to the voltage doubler in Figure 3.3b, and L_{31}-L_{34}, which cover all sides of the headstage box while being slanted in four directions toward the bottom edges of the box on the other side. Tx and Rx coils are

symmetrical with respect to the center of the homecage and headstage, respectively. The diameter and number of turns of the wire-wound L_{31}-L_{34} and L_4 were selected by compromising between the headstage size/weight and coupling coefficient between Tx-Rx resonators and Q-factors of L_{31}- L_{34} and L_4, which ultimately affect the PTE, according to the optimization procedure in [31], at the nominal height of H_0 = 7 cm. The result was the choice of 0.4 mm (AWG 26) magnet wire with 3 and 6 turns for L_{31}-L_{34} and L_4.

The coupling between loosely coupled Tx and Rx coils is the dominant factor in determining the PTE of the 4-coil inductive link. Since the size of the headstage is considerably smaller than the homecage, we maximize the effective area of the Rx resonators, through which the Tx magnetic flux passes, to improve their coupling with Tx coils. The maximum effective area of the headstage, which encompass the diagonal planes of the cube, is used to achieve Rx resonators, L_{31}-L_{34}, with the largest possible area. L_{31}-L_{34} then bend the magnetic flux towards L_4 when the headstage is rotated with any arbitrary angle, even in the worst case condition of 90° rotation [111]. For 90° rotation of the headstage, which happens when the rat is sniffing, grooming, resting, or rearing on its hind limbs, L_{31}-L_{34} guide the magnetic flux that passes through the effective area, one of the side faces of the headstage cube, toward L_4.

In [104], we found that the 4-coil link with a single Rx resonator delivers sufficient power to the headstage up to 70° rotation. Therefore, we need Rx resonators with less than 70° rotation, when the headstage is rotated by 70°-90°. This is achieved by tilting at least one Rx resonator at an angle of 25° compared to the horizontal plane in each four directions of the cubical headstage. In Figure 3.5, when the headstage is at maximum 90° rotation, L_{31} is tilted 65° with respect to the horizon, and can bend sufficient flux towards L_4 to

power the headstage. With 65° rotation, however, L_{31} will be tilted 90° with respect to the horizon, and instead, L_{32} is the resonator with less than 65° tilt, bending the flux towards L_4. Similarly, L_{33} and L_{34} play the same role with 90º rotation around the vertical axis.

3.2.3 HFSS Simulation of Poynting vector and SAR

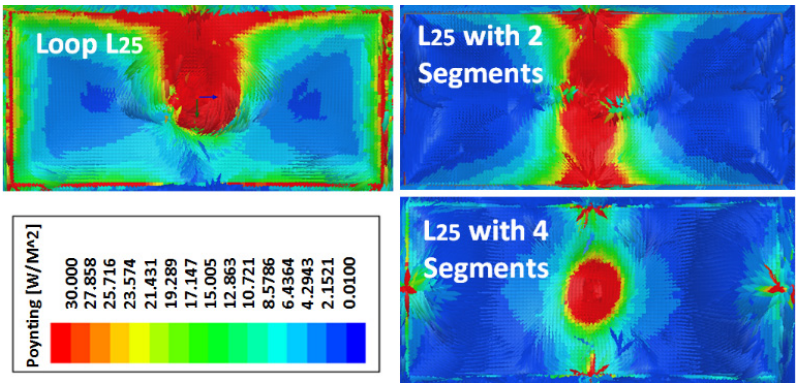

Figure 3.6. Poynting vector simulations in HFSS, showing top view of L_{25} as a complete loop, with two segments, and with four segments, when the headstage is located at the center, 20 cm from the bottom of the homecage.

Figure 3.6 shows the Poynting vectors generated by 3D HFSS model of the 4-coil inductive link. The red areas exhibit the highest directional power flux density, representing the highest rate of power transfer per unit area. Without segmentation, L_{25} strengthens the power transmission toward the headstage, with one activated portion of the loop. With segmentation in two pieces, L_{25} produces a strong and uniform power transmission from two sides of the coil. As we increase the number of segments to four, the directional power flux density distribution becomes more uniform. However, the power transfer density is considerably lower, evident from the smaller red area.

The animal/human body is almost transparent to EM field at frequencies below 20 MHz due to the low body tissue absorption rate [112]. Figure 3.7 presents the SAR simulation result in HFSS for the rat head and body model. For this simulation setup, the

input power is set at 1 W. Since SAR = $\sigma|E|^2/\rho$ is directly related to tissue conductivity, σ, and inversely proportional to density, ρ, we consider the rat model made entirely out of brain tissue with σ = 105 S/m and ρ = 1040 kg/m^3, which generates the worst case for SAR simulation. For the rat model in the EnerCage-HC2 system in Figure 3.7, the maximum simulated SAR value is 0.15 W/kg. A SAR level of 1.6 W/kg has been designated by the FCC as the limit of radio frequency energy that can be safely absorbed by humans while using cellular phones [113]. Therefore, the maximum allowable transmitted power can be found from 1 W × 1.6 (W/kg) / 0.15 (W/kg) = 10.7 W. In the current system, the maximum output power of the PA is limited to 2.5 W, resulting in only a small fraction of power absorbed by the rat body.

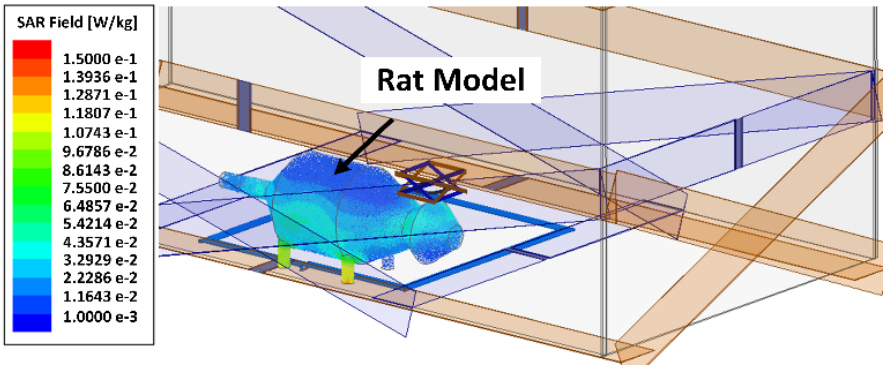

Figure 3.7. SAR simulation in HFSS, presenting the maximum of the average SAR values for the tissue layers with the proposed 4-coil inductive link.

3.3 Experimental Measurements

Figure 3.8 shows the current implementation of Tx and Rx coils. A 46 × 24 × 20 cm^3 standard rodent homecage (Alternative Design, Siloam Springs, AR), was used as a base in this prototype with L_1 and its driver located at the bottom of cage and L_{21}-L_{25} encompassing four sides and the rim on the Tx side. All Tx resonators are covered with Kapton® tape (polyimide film) to improve isolation between resonators. Because of the

strong coupling among L_{21}-L_{25}, only one of them needs a variable capacitor for fine tuning of the entire Tx at 13.56 MHz, while the others have fixed capacitors. On the Rx side, electronics in the form of two stacked PCBs are protected against moisture and mechanical damage in a 3D printed 11 × 20 × 22 mm^3 box with L_4 attached at the bottom, and L_{31}-L_{34} encompassing four diagonal planes. The headstage weighs 7 g, which is suitable for rats. A 1.1 cm 2-pin collar assembly from PlasticsOne (Roanoke, VA) is mounted on the bottom of PCB II to connect the headstage to a pair of implanted electrodes on the rat head.

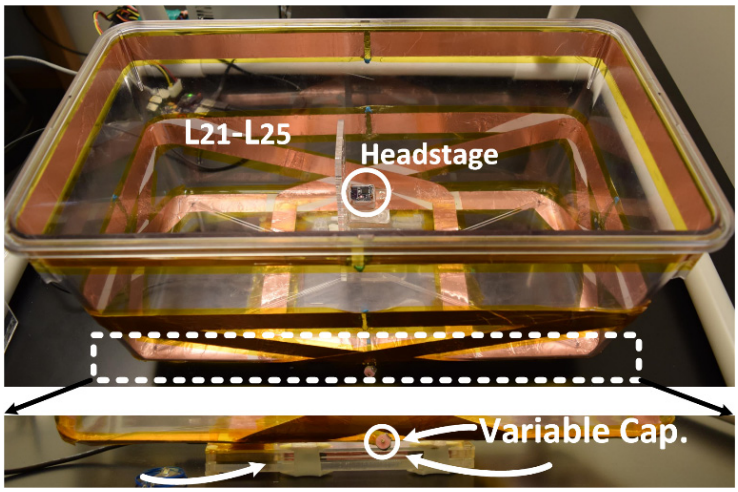

(a)

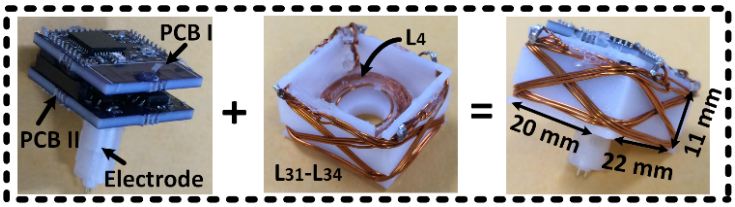

(b)

Figure 3.8. (a) The EnerCage-HC2 proof-of-concept prototype. (b) A close-up view of the headstage and its internal/external components.

To measure the PTE of the 4-coil inductive link with actual load impedance, we measured S_{21} by a Vector Network Analyzer (VNA) in Figure 3.9 configuration. Each LC-tank is tuned at the carrier frequency, and the entire link forms a two-port network including

any configuration of coupled resonators between L_1 and L_4. L_1 is driven by Port-1 of the VNA, which default impedance is 50 Ω. On the load side, 43 mW power consumption of the headstage at 5.5 V, results in R_L = 118 Ω. Therefore, an additional resistor, R_L', was added in series with Port-2 of the VNA to achieve $R_L = R_L' + 50$ Ω. The transmission coefficient under the actual load, S_{21}', and PTE were then calculated from,

$$|S_{21}'|^2 = \frac{{V_2'}^2/(2 \times R_L)}{{V_1}^2/(2 \times 50)} = {S_{12}}^2 \times \frac{R_L}{50} \quad (1)$$

$$PTE = |S_{21}'|^2 \times 100\% \quad (2)$$

where V_1, V_2, and V_2' ($V_2' = V_2 \times (R_L'+50) / 50$) are the voltages across VNA Port-1, Port-2, and load coil.

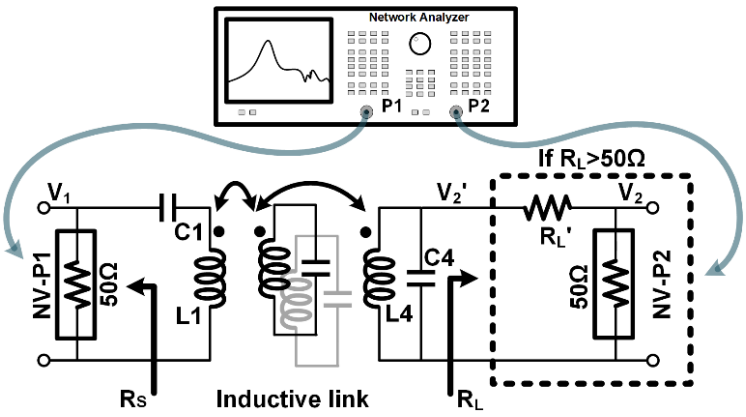

Figure 3.9. PTE measurement setup using a VNA when R_L > 50 Ω.

To measure the PTE distribution across the homecage, the bottom of the cage was marked by an X × Y grid with 2.75 cm spacing and the headstage was swept at various heights, resulting in Figure 3.10a heat maps. Considering the significant size difference between the headstage and homecage, the center of the cage generally has a weaker magnetic flux density, mutual coupling, and PTE compared to its perimeter. At H = 4 cm, PTE slightly drops at the corners of the homecage, which are not covered by Tx resonators,

L_{21}-L_{24}. With proper segmentation, however, L_{21}-L_{25} generate a strong and uniform PTE distribution across the homecage, especially at H = 8 cm, which is close to the nominal height of rats. As H increases, PTE is higher in the center of the cage compared to its perimeter because of the collective effect of L_{21}-L_{24}. The segmented L_{25} further strengthens the magnetic flux density at higher headstage elevations, as demonstrated in Figure 3.10b, which compares the PTE in a vertical plane with and without L_{25}. For H > 14 cm, L_{25} has had a positive effect on increasing the PTE across the homecage. Overall, our measurements showed that the proposed coil/resonator design can guaranty PTE > 6.7% anywhere within the volume of inside the homecage.

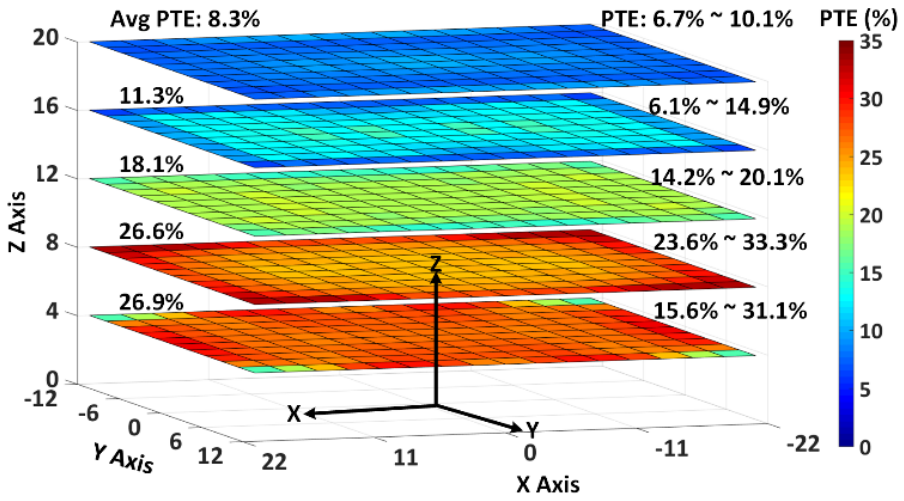

(a)

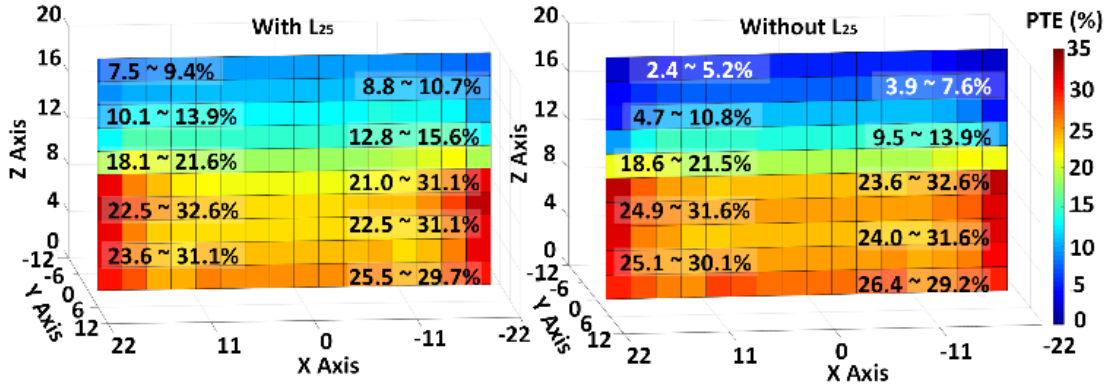

(b)

Figure 3.10. (a) Measured PTE of the 4-coil inductive link when the headstage is swept inside the homecage across XY plane at the heights of 4 cm, 8 cm, 12 cm, 16 cm, and 20 cm. (b) Measured PTE when the headstage is swept across the XZ plane (Y = 0 cm), at a height of 8 cm with and without L_{25}.

Figure 3.11 presents the effects of headstage rotation by showing PTE variations across the XY plane at H = 8 cm with 30°, 60°, and 90°rotations. Slanted Tx and Rx resonators in our design support angular misalignments by shaping the EM field, especially at the corners of the homecage, resulting in higher PTE at the corners. Power transmission is active all the way up to 90° worst case rotation with an average PTE of 1.8% across the homecage. When the headstage is held over the X or Y axes along the center lines of the homecage at 90° rotation, the PTE drops significantly because of the symmetrical Tx resonators along that axis cancelling each other's EM fields. However, the possibility of a rat rotating its head by 90° and holding it exactly on the centerline along the X or Y axes is quite low. Moreover, a small super capacitor following the voltage doubler in the power management block prevents any sudden drop in the headstage supply voltage.

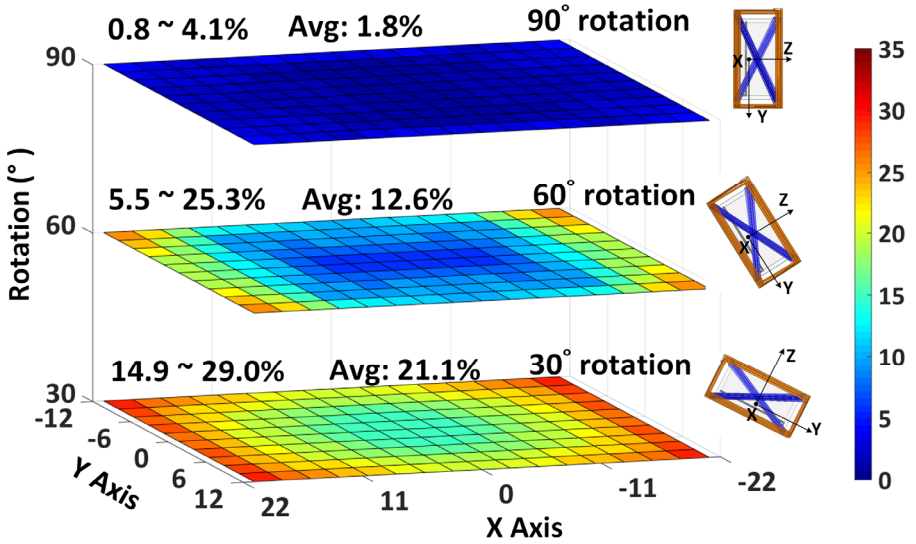

Figure 3.11. Measured PTE of the 4-coil inductive link when the headstage is swept across XY plane in the cage, at H = 8 cm, and rotated by (a) 30°, (b) 60°, and (c) 90° along X axis.

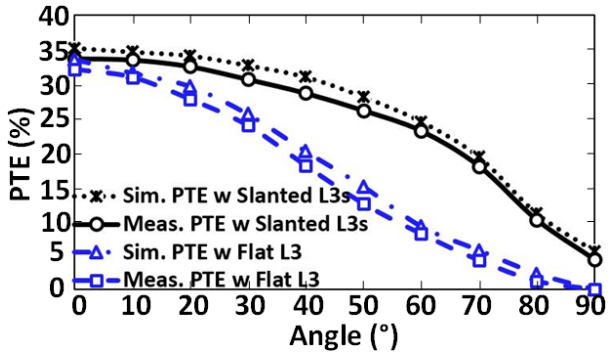

(a)

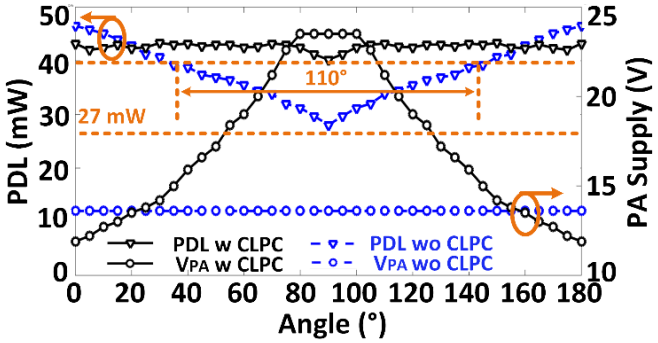

(b)

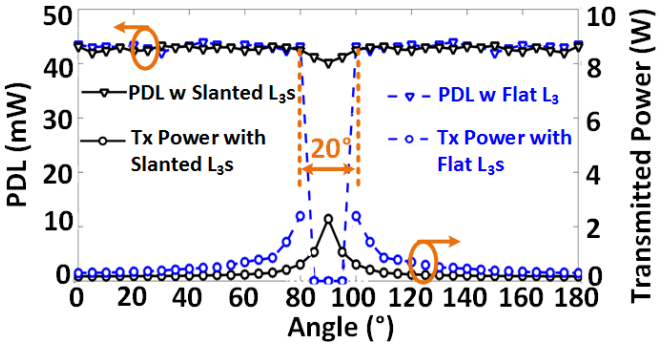

(c)

Figure 3.12. Headstage measurements in the middle of the homecage at H = 8 cm: (a) Comparison between PTE vs. rotation with proposed slanted L_3s and flat L_3 in [104]. (b) Comparison between PDL and PA supply voltage vs. rotation with and without CLPC. (c) Comparison between PDL and Tx power vs. rotation with proposed slanted L_3s and flat L_3 in [104] in CLPC.

To validate the benefits of the proposed slanted Rx resonator design, particularly with respect to angular misalignments, in Figure 3.12a, we have compared simulated and measured PTE results between the new slanted quad Rx resonators and the single flat

resonator design in [104]. The PTE of the proposed 4-coil inductive link is improved for every rotation angle, and the rate of PTE decline vs. angular misalignment has also slowed down. It should also be noted that the simulated and measured results are in very good agreement. In addition to the coil design for homogeneous coverage of the homecage volume, the CLPC dynamically adjusts the Tx power to ensure PDL > 40 mW under any lateral, height, and angular misalignments, below which level the BLE range drops below a minimum reliable data transmission distance of 65 cm. Figure 3.12b presents the measured PDL and PA supply voltage as a function of rotation angular at H = 7 cm, comparing the performance of CLPC vs. open loop. Without CLPC, as the PDL drops under the 40 mW with rotation > 35° or < 145°, and we need to place the controller BLE antenna very close to the headstage to maintain connectivity with no interruption. With CLPC, however, the headstage receives stable power (> 40 mW) within the full range of 0°-180°. In Figure 3.12c we have compared the PDL and Tx power between the new slant coil and flat design in [104] as a function of 0°-180° Rx rotation. The CLPC is active in both cases and delivers sufficient power to the new headstage up to 90° rotation by increasing the Tx power up to 2.3 W. The flat Rx resonator, however, fails to deliver sufficient power to the headstage at rotations > 80º despite the Tx power being maxed out at 2.5 W by the CLPC.

3.4 *In Vivo* Experiments

Figure 3.13 shows the EnerCage-HC2 *in vivo* experimental setup. Our goal was to elicit a well-documented behavioral effect of DBS and observe the consistency of the outcome among three rats as a proof of system functionality in the field. Figure 3.13b shows the EnerCage-HC2 controller implementation, including its custom-designed cape,

which allows the user to control the EnerCage-HC2 system through Wi-Fi connection. Figure 3.13c shows the GUI running on a PC, including a live video stream from a MS-Kinect®, allowing remote control of the EnerCage-HC2 system and behavioral monitoring of the animal [114].

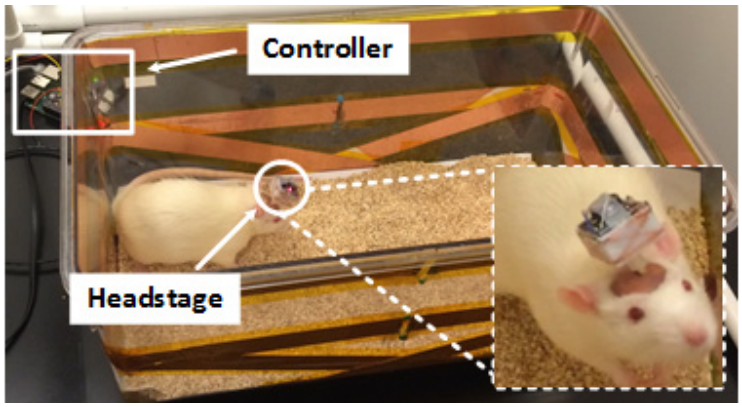

(a)

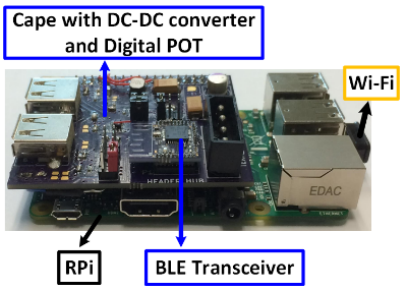

(b)

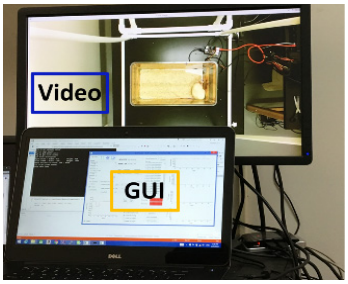

(c)

Figure 3.13. (a) *In vivo* experimental setup for 1-ch DBS in a freely behaving rat. (b) Close-up view of the controller block including a custom-designed cape. (c) GUI running on a PC, including a live video stream from a MS-Kinect® for behavioral monitoring of the animal subject.

In vivo experiments[4] were conducted with prior approval from the IACUC at Emory University. We delivered a unilateral, charge-balanced, electrical stimulation to the GPi of three freely behaving rats. GPi is a major component of the basal ganglia, and is involved in the coordination of movement. Previous studies have reported that head turning behavior is a highly replicable behavioral effect induced by unilateral electrical stimulation of the

[4] I would like to thank Dr. Chia-Chun Hsu for his great collaboration on the *in vivo* experiments.

GPi [115]-[118]. Hence, we expected to observe the same behavior using the EnerCage-HC2 system by stimulating the GPi wirelessly. Three 11-weeks old male Sprague Dawley rats, weighing 330-350 g, were implanted with a pair of monopolar stainless steel stimulating electrodes (MS303/1-AIU, Plastics One) targeting the right GPi (stereotaxic coordinates anteroposterior (AP) -0.8 mm; mediolateral (ML) +3.0 mm; dorsoventral (DV) -6.0 mm), one of which was an uninsulated stainless steel ground wire, wrapped around a skull screw. Impedance of the stimulation electrodes were 12.5 kΩ for rat 1, 7 kΩ for rat 2, and 6.5 kΩ for rat 3. The placement of the electrode tip in GPi was confirmed by subsequent histological processing of the subjects' brain tissue, as shown in Figure 3.14.

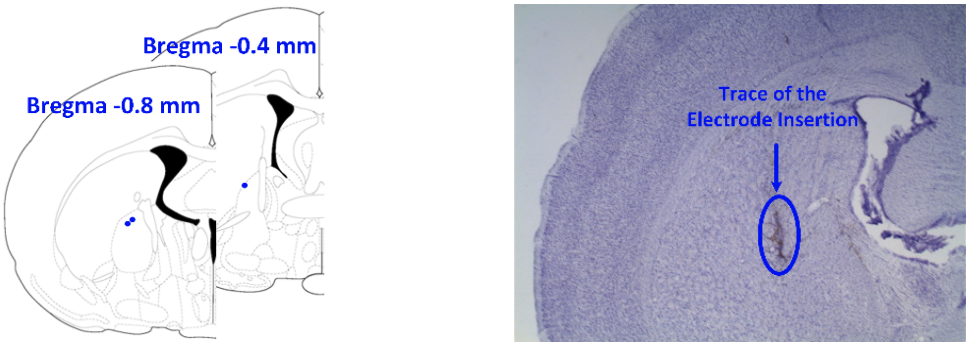

(a) (b)

Figure 3.14. Electrode placement and Histology. (a) The red dots represent placement of the tip of the electrodes, all in the GPi. (b) Sample brain slice, stained with Nissl staining. The dark track in the center of the picture is the trace of the electrode insertion in the brain.

Each stimulation experiment was performed after two weeks of post-surgical recovery. Prior to the start of experiments, the rats were handled for three days to acclimatize them to handling. The rats were habituated in the homecage for 4 minutes, before six 2-minute experiments were conducted. During the first minute of each experiment a sham stimulation was applied at minutes 1, 3, 5, 7, 9, and 11. Within the last 5 s of each experiment, the headstage delivered electrical stimulation to the subject at the

beginning of minutes 2, 4, 6, 8, 10, and 12. We measured the animal head rotation during the first 10 s of each 1-minute segment. Figure 3.15a shows a current-controlled 5 s burst of stimulus pulses that delivers current of 225 µA and 75 µA in cathodic and anodic phases, respectively, at a rate of 40 Hz. To ensure charge balancing, stimulation current in the cathodic phase was 3× larger than the anodic phase, and the pulse width in anodic phase (300 µs) was accordingly 3× longer than the cathodic phase (100 µs), in Figure 3.15b.

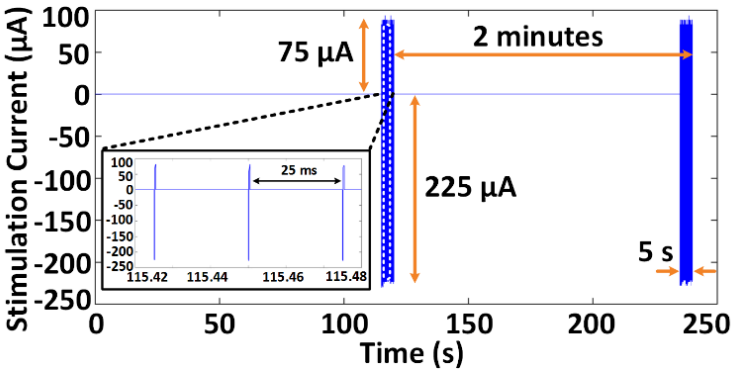

(a)

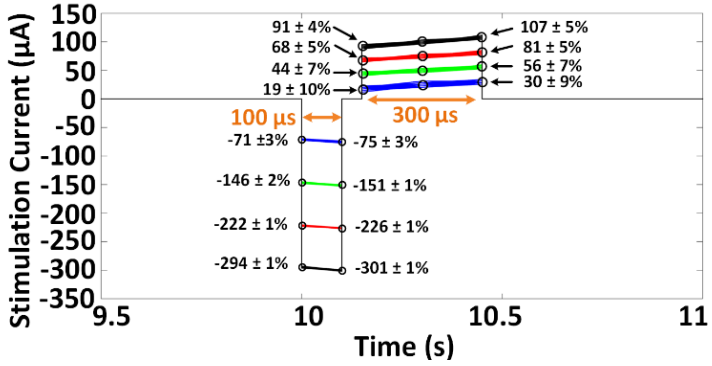

(b)

Figure 3.15. (a) Stimulation pulses in trial # 1 and # 2 of rat #3, acquired by decoding the data transmitted from the headstage via BLE while the animal was freely moving in the homecage. (b) Time-aligned stimulation pulses in trial #1.

To evaluate the accuracy of stimulus pulses in terms of current amplitude, we overlapped the acquired samples from current sensing resistors in Figure 3.3b during the 5 s stimulation period of trial 1. Figure 3.15b shows the acquired samples from time-aligned

stimulation pulses at four current levels over a 1.5 ms window. The mean error between the desired and measured stimulus amplitudes at each sampling point is smaller than 10%, which verifies the stability and accuracy of the stimulation current. Expectedly, minimum stimulation current of 75 µA in the cathodic phase, which generates the lowest current sense voltage detected by the MCU built-in ADC, results in the highest mean error of 10%.

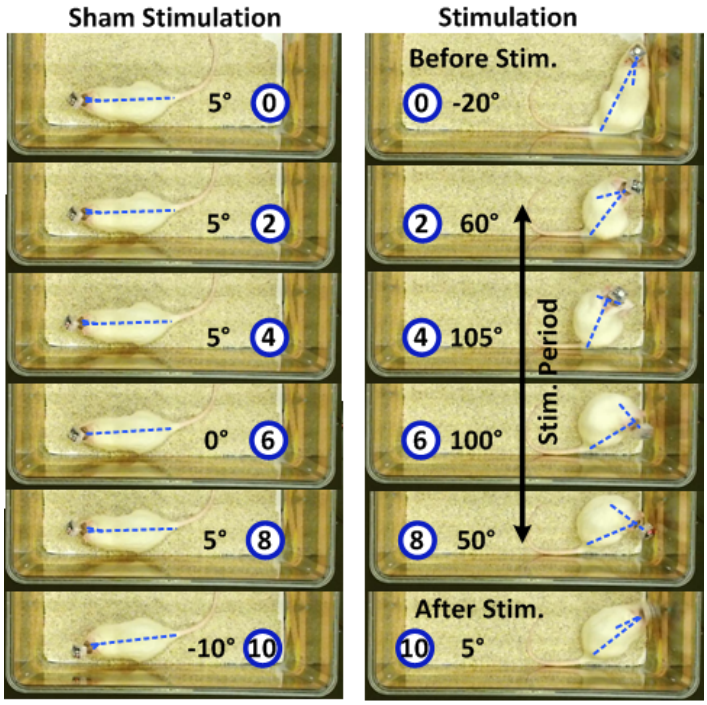

Figure 3.16. Comparing head turning behavior within 10 s between the actual and sham stimulations in rat #3. The relative time before, during, and after stimulation is indicated in seconds in the blue circle in each frame with the measured head turning angle next to it.

Consistent with previous studies [115]-[118], head turning behavior was clearly observed on all three rats during wireless stimulation periods. The head rotation angle (HRA) is defined as the angle between two straight lines, one connecting the base of rat tail to a point between ears to the tip of nose, as shown in Figure 3.16, comparing rat 3 head movements before, during, and after a 5 s episode of the actual and sham stimulations. Figure 3.17a shows the changes in HRA over time, with respect to the baseline angle at

each stimulation onset for each rat for 6 actual and 6 sham stimulations. In Figure 3.17b, a significant effect of stimulation was observed by comparing the maximum rotation angle to sham stimulation using one-tail paired t-test with p = 0.04. The rotation angle of rat 1 during stimulation period was smaller than both rat 2 and rat 3, which could be attributed to the larger impendence value of the stimulation electrode implanted in rat 1, compared to rats 2 and rat 3.

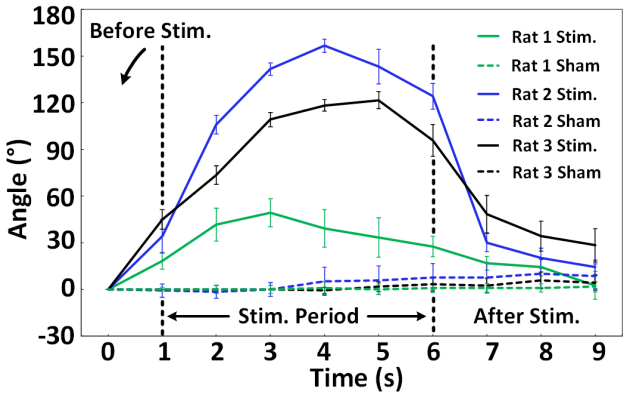

(a)

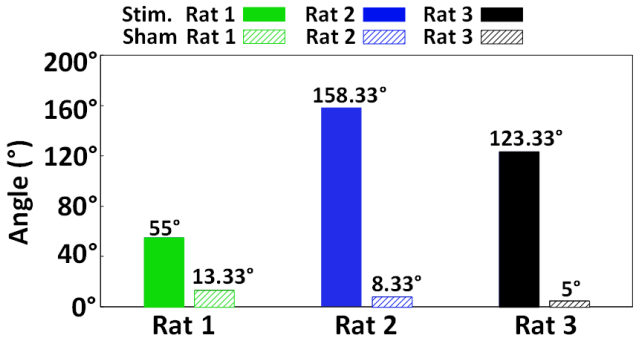

(b)

Figure 3.17. (a) Head rotation angle vs. time during actual stimulation in comparison with 9 s at the end of the 1st minute of a trial as control. (b) The mean maximum head rotations of each rat during actual and sham stimulations.

Figure 3.18 shows the measured V_{DD} and V_{PA} during two trials on rat 3. The EnerCage-HC2 continuously delivers ~43 mW to the headstage by maintaining V_{DD} within a user-defined voltage range, which is made possible by dynamically adjusting V_{PA} and

consequently the PA output power as a result of transmitting V_{DD} samples to the controller at a rate of 100 Hz via BLE. The magnified segments of Figure 3.18 show V_{DD} variations during stimulations, which lead to severe coil misalignments due to animal head rotation. The CLPC mechanism has succeeded in maintaining 5 V < V_{DD} < 5.4 V, indicated by horizontal red lines, by automatically increasing V_{PA} from 12 V up to ~22 V to compensate for the disturbance. Following stimulations, when the subject's head position returns back to normal, V_{PA} is automatically decreased to prevent excessive Tx power transmission. To compensate for the change in the location of the subject's head after stimulation, the V_{PA} voltage has settled at a new level of 17 V.

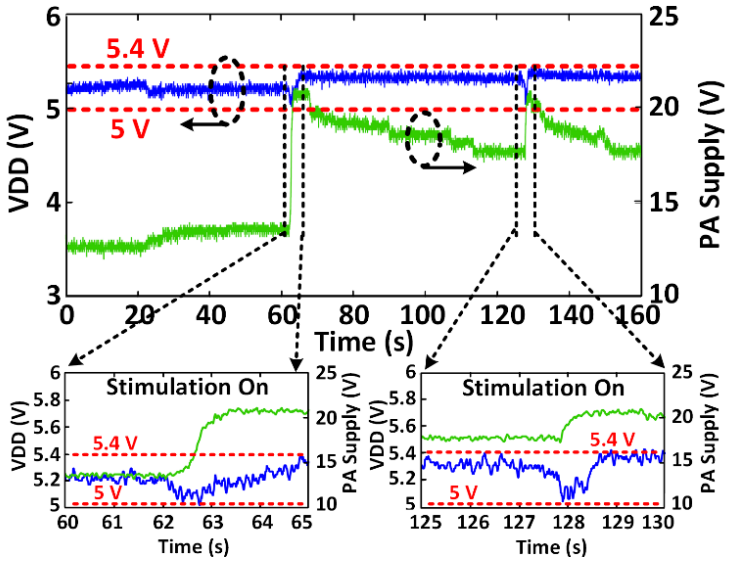

Figure 3.18. V_{DD} and V_{PA} variations during a 5 s stimulation episode in trial #1 and #2, showing the V_{DD} staying within a user-defined window, thanks to CLPC, despite head rotation and load variation during stimulation.

3.5 Summary and Dissuasion

Table 3.2 benchmarks the EnerCage-HC2 against previous versions of smart homecage systems. The proposed EnerCage-HC2 is competitive in terms of PTE and WPT coverage. More importantly, the proposed EnerCage-HC2 with the novel 4-coil inductive

link design together with the CLPC mechanism is able to wirelessly power the headstage within the entire volume of the rodent homecage, while handling any angular misalignments. In addition, the proposed EnerCage-HC doesn't require real-time tracking of the animal subject and additional electronic or mechanical mechanisms to change the position of the active coil, which add to the complexity and cost of the system.

Table 3.2. Benchmarking of the WPT systems for IMDs.

Publication	2014 [36]	2015 [38]	2016 [39]	**2016 [42]**	**This work**
WPT mechanism	Inductive	Inductive	Inductive	Inductive	**Inductive**
Frequency (MHz)	13.56	13.56	13.56	13.56	**13.56**
WPT coverage (cm^3)	3538×12	30×30×17	46×24×20	14×12×7	**46×24×20**
Angular misalignment	-	-	80º	**90º**	**90º**
Rx size (mm^3)	$\pi\times20^2\times20$	40×40×20	20×22×5	10×10×3	**20×22×11**
PTE (%)	5.6-12.6	16.1-36.3	14	2.9-6.4	**23.6-33.3**
Wireless data transmission	LSK/2.4 RF link	LSK/2.4 RF link	BLE	**-**	**BLE**
CLPC	Yes	Yes	Yes	No	**Yes**
Tracking/switching CTRL	Yes	Yes	No	**Yes**	**No**

The scalability is an important aspect of the EnerCage-HC2 system. The proposed 4-coil inductive link implemented in the EnerCage-HC2 is scalable in the size of the headstage and the size of the homecage. Scalability on the size of the headstage, the optimal size of L_1 is directly related to the separation distance (H) and the headstage dimension. H is the dominant parameter to achieve the optimal PTE if $\pi\times H^2 >>$ the area of L_4. The 4-coil inductive link design meet this condition. Therefore, by scaling down the size of the headstage for the mouse application, Tx coils don't need to be scale down. Scalability on the size of the homecage, the key factor in determining geometries of L_{21}-L_{25} is the compatibility with homecage dimensions and maximum overlap with L_1. The rule of thumb in the arrangement of the Tx resonators is to divide the bottom area of the homecage into

smaller subsections with same area as the optimized area of L_1. Optimizing the 4-coil inductive link means increasing the minimum PTE within the homecage to ensure sufficient PDL to keep the headstage on when the CLPC adjusts the Tx power, as opposed to maximizing PTE in the perfectly aligned regions in traditional coil optimization. Therefore, to scale to a larger homecage, same rule can be used to avoid big drops in PTE.

CHAPTER 4. WIRELESSLY-POWERED NEURAL RECORDING AND STIMULATION SYSTEM

In our prior work, the EnerCage-HC2 was successfully used to power a wireless and battery-less headstage, which included a 1-ch stimulator made of COTS components, for DBS in rat model [103]. The EnerCage-HC2 is a general design, which can be used to wirelessly power other types of IMDs for long-term experiments on freely moving rodents.

Lots of applications require IMDs that can interact bi-directionally with the CNS and PNS [6], [8]. For example, DBS, which is an effective neuro-modulation therapy for Parkinson's disease, requires neural recording for closed-loop operation [6]. In the WOENI system, the ECoG data is transferred through BLE link. This is because the recording data is very small, 2-ch ECoG recording with sampling rate of 1 kHz resulting in data rate of 32kpbs [83].

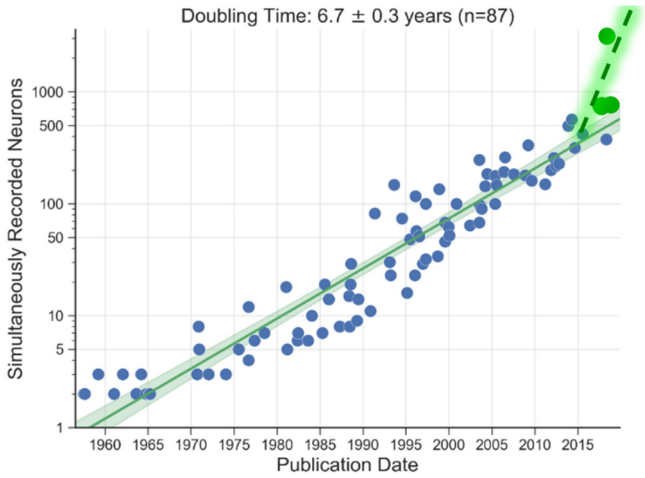

Figure 4.1. The Moore's Law of neuroscience.

In [14] and [119], the Moore's Law of neuroscience tells us that the number of neurons that researchers want to record is increasing. Especially, after 2015, the increasing

speed is much faster (see Figure 4.1). As the number of the recorded neurons increases, the amount of recording data that need to be sent increases correspondingly, may be several Mbps or even more [47]. After addressing the requirement of wireless power transmission to IMDs, a new challenge is developing wireless data link that can transfer a large of amount digitalized recording data from a high density neural interface [47]. Such high data rate is already beyond the capability of the BLE data transmission. Wi-Fi could be an option for transmitting a large amount of recording data. However, it is very power consuming. Considering the limited power budget of a wirelessly-power headstage, we need to consider custom-designed low-power high speed data transmission method.

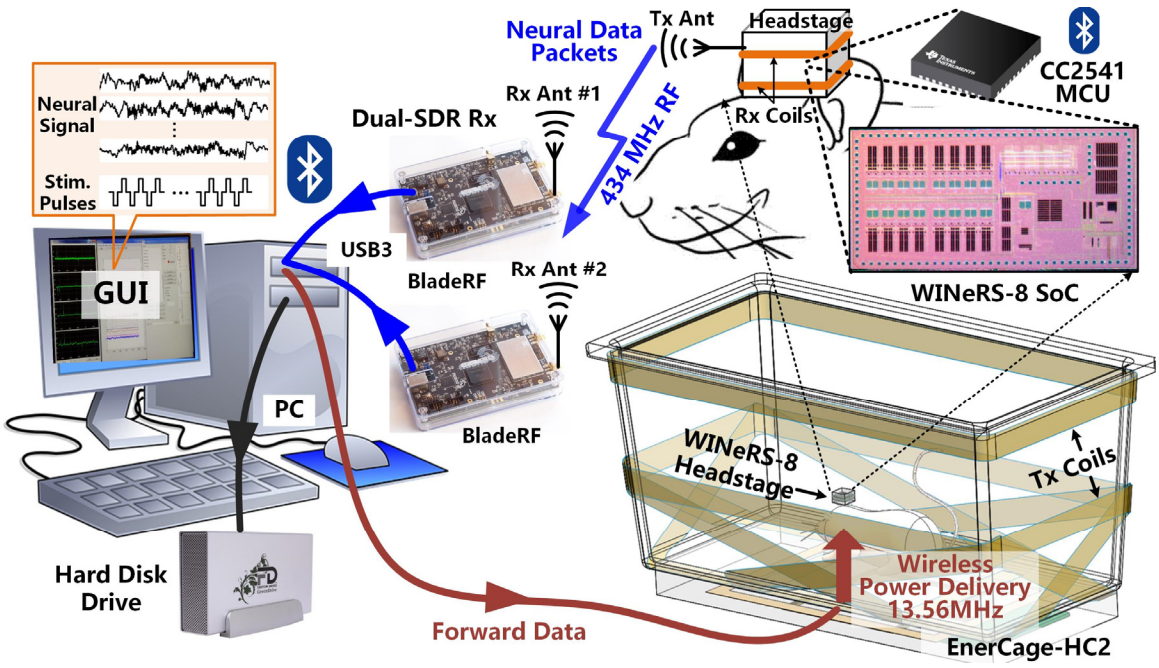

Figure 4.2. A conceptual view of the wirelessly-powered implantable neural recording and stimulation (WINeRS-8) system, which is compatible with EnerCage-HC2 for long-term experiments with small freely behaving animal.

We have developed a wirelessly-powered implantable neural recording and stimulation (WINeRS-8) system[5], which is fully compatible with the EnerCage-HC2 [104], as shown in Figure 4.2 [120]-[122]. On the Tx side, the WINeRS-8 headstage is equipped

[5] I would like to thank Dr. Byunghun Lee for his great collaboration on the WINeRS-8 system development.

with 32-ch neural recording with data rate of 9 Mbps and 4-ch neural stimulation SoC for closed-loop neuromodulation applications. The WINeRS-8 headstage is wirelessly-powered within the EnerCage-HC2 system. Efficient WPT is achieved through a resonance-based 4-coil inductive link. The EnerCage-HC2 also builds bi-directional data communication link with the WINeRS-8 headstage to send recording configuration and stimulation parameters to the headstage and to receive supply voltage information of the headstage for CLPC. There are two implementations of the data link, either data telemetry through the inductive link or a BLE alternative [121]. In the WINeRS-8 system, the wireless data Rx includes two commercial software defined radio (SDR) Rxs (BladeRF x40, Nuand), which are capable of receiving a large amount of digitalized raw data from the custom 434 MHz on-off keying (OOK)-modulated RF link and delivering the data to a PC that is running a custom GUI for data visualization, processing, and storage. We have also demonstrated the performance of the WINeRS-8 system *in vivo* in the rat model.

4.1 Dual-SDR Rx Design

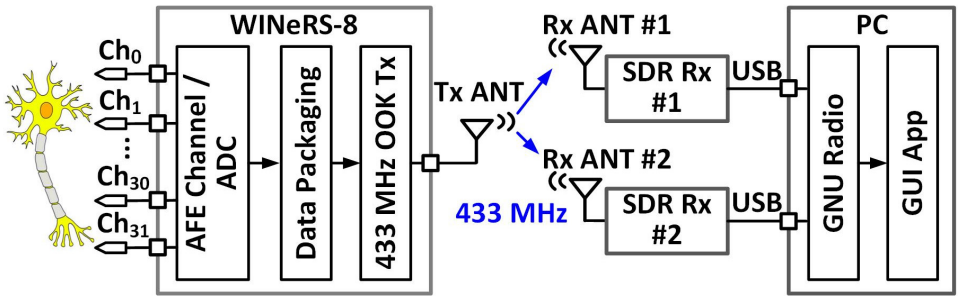

Figure 4.3. Key blocks in the wireless 32-ch neural recording from the WINeRS-8 headstage to the PC, using the proposed wideband dual-SDR Rx.

Figure 4.3 shows the key building blocks of the wideband data telemetry link. Each digitization cycle generates a 176-bit data packet that is serially delivered to the on-chip Tx, which in turn OOK modulates the 434 MHz RF carrier of the PA, followed by a

custom-designed off-chip antenna. The 433MHz OOK data carrier is picked up outside the homecage by a pair of BladeRF SDR Rxs that are designed to create a robust RF data communication link against freely behaving animal movements inside the homecage during the experiment [123]. The LMS6002D front-end (Lime Microsystems, UK) in each BladeRF SDR Rx digitizes and pre-processes the RF signal, before sending it to the GUN radio [124], running on the PC, through their individual USB3 ports, for post-processing. From the two incoming received data streams, the GNU radio picks the one with higher signal strength, and extracts the neural data from data packets before de-multiplexing 32 channels, storing them in the hard disk drive (HDD), and displaying them on the GUI in real time.

4.1.1 Dual-SDR Rx Algorithm Design-I

Figure 4.4a shows the algorithmic block diagram of the dual-SDR Rx design-I[6], in which the SDRs are only in charge of receiving and digitizing the RF signal, while most of the DSP functions are implemented in the GNU radio within the PC. The GNU radio sets the parameters of the SDR RF front-end, such as gain, bandwidth, center frequency, and sampling rate, through the USB port. The RF signal is received, oversampled by a factor of 4, and converted to 12-bit digitalized I & Q samples in each RF front-end, before being sent to the PC through its dedicated USB3 port. The GNU radio converts the two data streams from SDRs to magnitudes, E_{IQ1} and E_{IQ2}, and passes them through 2000-point moving average filters to establish the signal strengths, E_{Avr1} and E_{Avr2}, respectively. In Figure 4.4b example, Rx1 and Rx2 antennas are aligned at 90° and 0°, respectively, with respect to the Tx antenna at the same distance. As expected, $E_{Avr2} > E_{Avr1}$. Once the stronger signal is determined, in this case E_{Avr2}, it is passed through a wideband 3-point moving

[6] I would like to thank Dr. Byunghun Lee for his great contributions for the Dual-SDR Rx design-I.

average filter for noise reduction, E_{IQ}, and compared with the narrow band signal strength, E_{Avr}, for OOK demodulation.

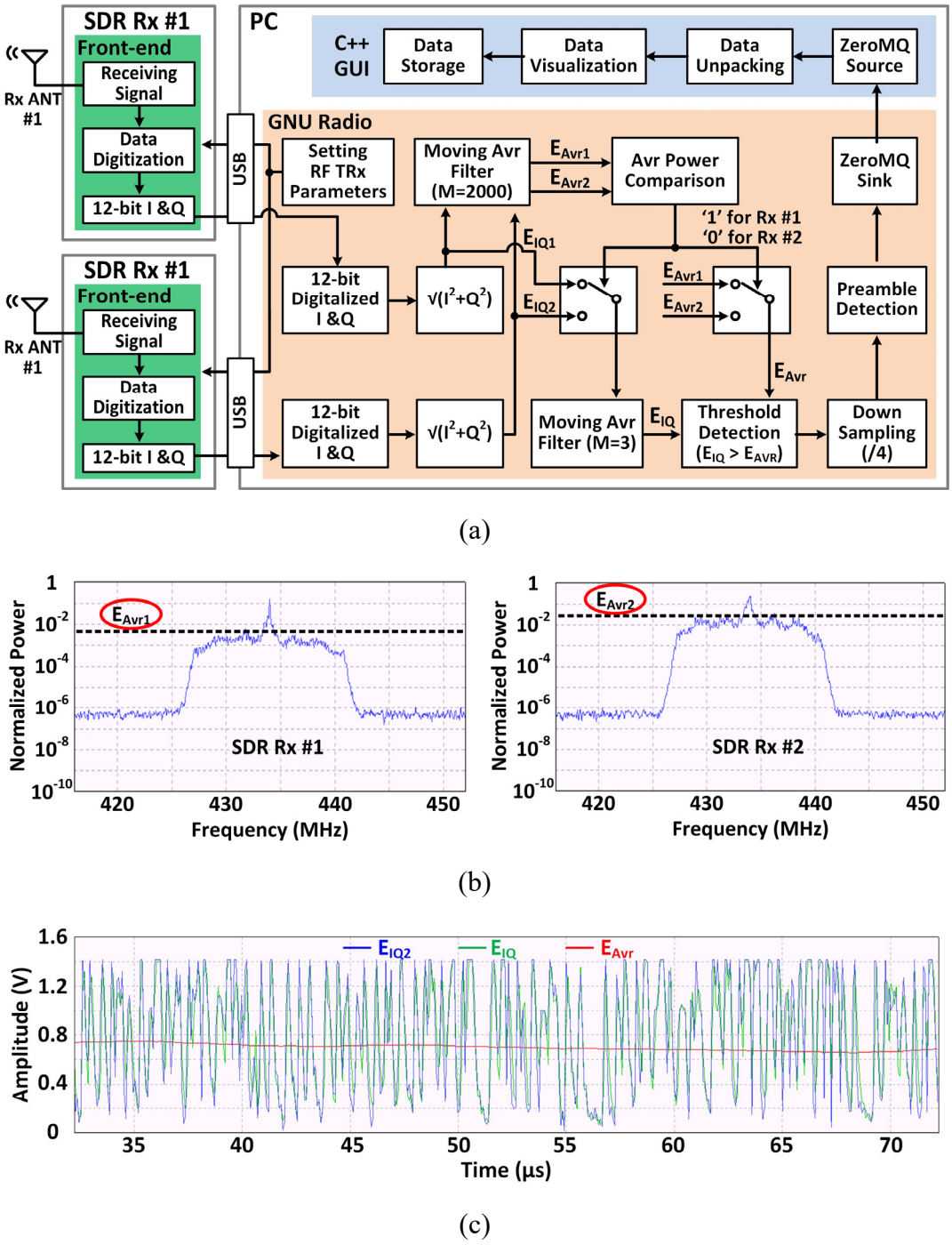

Figure 4.4. (a) Simplified algorithm architecture of the dual-SDR Rx design-I. (b) Signal strength of the data stream from the SDR Rx #1 and the SDR Rx #2. (c) Operation of the adaptive threshold detection.

Since E_{IQ} baseline and E_{Avr} change together, this operation is the equivalent of adaptive thresholding, as shown in Figure 4.4c, which combined with the redundancy provided by dual Rx antennas, ensures robust OOK demodulation and data recovery in the presence of continuous Tx displacements and misalignments due to animal movements within the homecage. The following block is a 4:1 down-sampling module before searching the data stream for a pre-defined 13-bit preamble (1100101000001), which is selected in a way that minimizes the possibility of the overlaps with the recorded data [125]. The data content following each matched preamble is then extracted from the data stream, and sent to the GUI for unpacking and demultiplexing. The GUI is implemented in C++ via ZeroMQ protocol, and extracts the individual 32-ch neural recording data from each data packet. ZeroMQ is a transport layer protocol for exchanging messages between two software platform peers [126]. The GUI code also displays the acquired data in real time and saves it in the PC HDD. The main advantage of the dual-SDR Rx design-I compared to [48] is the use of simple COTS components, flexibility in software-based design, development, and modifications, offered by GNU radio, and ease of use without the need for manual synchronizations among SDRs. On the other hand, it puts a heavy burden on the PC resources, which limits the scalability of this approach.

4.1.2 Dual-SDR Rx Algorithm Design-II

As the number of SDRs increase in an attempt to cover larger experimental arenas, or to facilitate the use of a lower power Tx, it is possible to implement the DSP algorithm front-end within a high-end SDR in a way that the Rx computational resources scale with the number of SDRs. In fact each BladeRF SDR, as well as many other recent SDRs, is equipped with an Altera Cyclone IV (Santa Clara, CA) field programmable gate array

(FPGA) with 115 k logic elements, which can be utilized for this purpose, as shown in Figure 4.5.

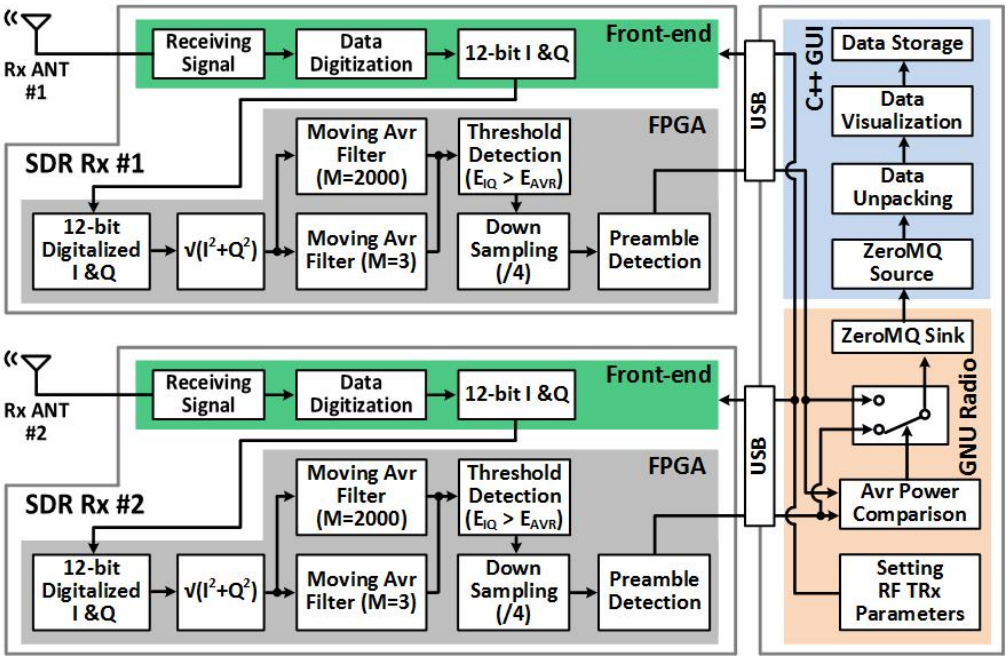

Figure 4.5. Simplified algorithm architecture of the dual-SDR Rx design-II.

In each SDR used in design-II[7], the received RF signal is oversampled, converted to 12-bit digitalized I & Q samples in the RF front-end, and delivered to the FPGA, which calculates the magnitude of the incoming samples. The FPGA then uses 2000-point and 3-point moving average filters to generate E_{Avr} and E_{IQ}, respectively, for adaptive thresholding. The recovered serial data steam is then down-sampled 4:1 before being searched for preambles. The data packets are then extracted from the data stream and sent to the PC via the USB port. The GNU radio running on the PC carries a much lighter load in this design, comparing the two incoming data streams in terms of their signal strengths, and selecting the stronger one for unpacking, plotting, and data storage by the GUI, which is identical to design-I. Since the PC workload, handled by the GNU radio, requires a small amount of resources, several SDRs can be handled by a PC with nominal specs in this

[7] I would like to thank Dr. Shaoping Zeng for his great contributions for the Dual-SDR Rx design-II.

architecture. The SDR in design-II is expected to have sufficient computational resources, often provided by a built-in FPGA.

4.1.3 Experimental Measurements

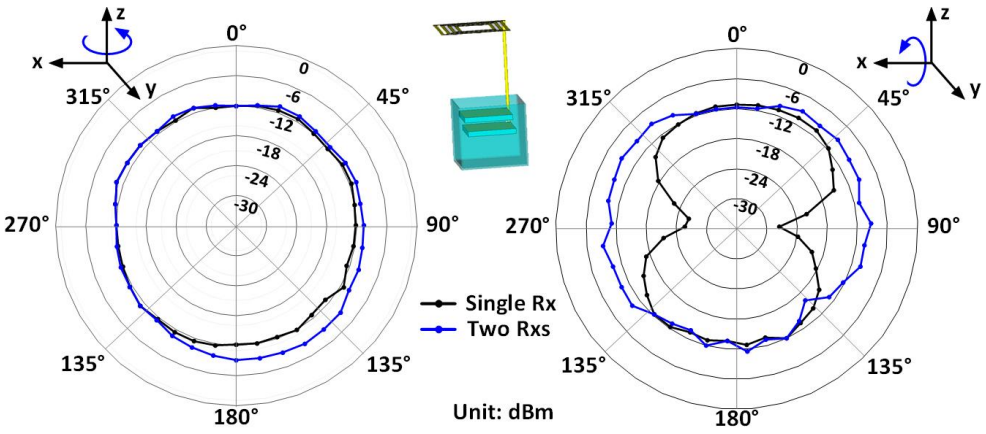

Figure 4.6. Measured relative radiation pattern with a single-SDR Rx vs. a dual-SDR Rx against (a) the horizontal rotation and (b) the vertical rotation of the Tx antenna.

The WINeRS-8 headstage was mounted on a small rotating apparatus at a height of 8 cm in the center of the homecage, which is the nominal height of a rat. Two Rx antennas were placed at 1 m distance from the headstage, facing two adjacent sides at 90º. A pre-recorded neural signal is applied to channel #1 of the AFE with -20 dB attenuation. The headstage then amplifies and digitalizes the input signal and sends out the digitalized data packets, which are picked up and recovered by two SDRs. The following measurement results are obtained by analyzing the recovered data. To measure the relative radiation pattern of the Tx-Rx antennas against angular misalignments, the headstage was manually rotated along the z and x axes from 0º to 360º with 10º increments. In each case, data with higher E_{Avr} is chosen by the Rx and the signal strength was registered and plotted in Figure 4.6. Figure 4.6a compares the relative radiation patterns with a single-SDR Rx vs. a dual-

SDR Rx against horizontal rotation of the Tx antenna, while Figure 4.6b shows similar comparison against Tx vertical rotation. The results show that because of the Tx omnidirectional radiation pattern, dual-SDR Rx performance may not be significantly different from a single-SDR Rx with respect to horizontal rotation. However, relative radiation with a single-SDR Rx can be as much as 15 dBi less than a dual-SDR Rx with vertical rotations, which can maintain E_{Avr} almost constant even under worst-case condition. This is because with two vertically oriented Rx antennas, and the redundancy built-into the dual-SDR Rx architecture, even though the Tx antenna could have worst-case misalignment with one of the Rx antennas, it still maintains sufficient S_{21} with the other Rx antenna. The result is that the proposed dual-SDR Rx removes the RF blind spots, where a single-SDR Rx cannot maintain proper data connectivity due to weak S_{21}.

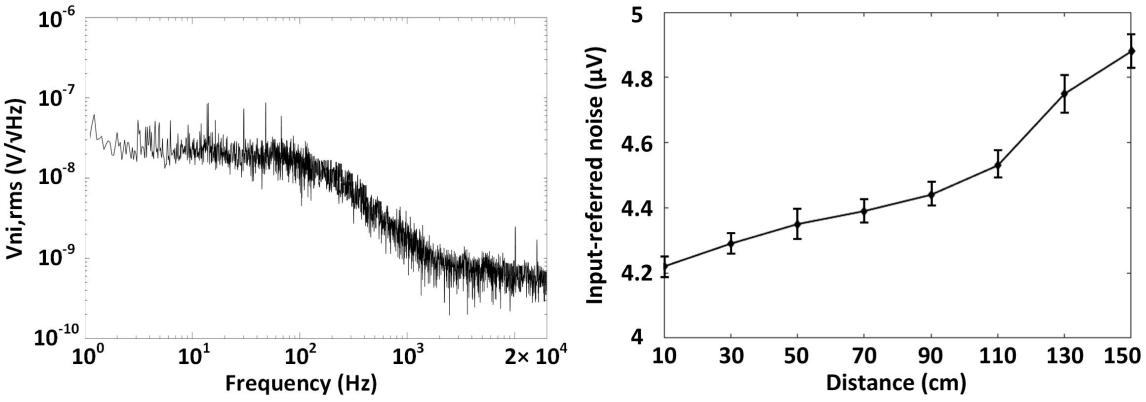

(a) (b)

Figure 4.7. (a) Input-referred power spectral noise density. (b) Input-referred noise versus Tx-Rx distance.

To characterize the noise performance of the entire WINeRS-8 system under wireless powering condition, the AFE was configured for bandwidth of 20 Hz to 15 kHz and gain of 51.5 dB [127], and powered at 13.56 MHz by the EnerCage-HC2 system, while the Tx-Rx distance was sweep from 10 cm to 150 cm with the Rx of design-II. In each

case, recovered data is collected when the AFE inputs are shorted to common node [24], [121]. We applied fast Fourier transform (FFT) to 3-minute periods of recovered data in MATLAB to derive the noise PSD and referred them back to the AFE input. Figure 4.7a shows the input-referred noise PSD at the nominal Tx-Rx distance of 30 cm. Applying square root of the integral under the curve from 10 Hz to 17 kHz yields a RMS noise voltage of 4.68 μVrms for the entire system. Figure 4.7b shows the input-referred noise, with the error bar (95% confidence interval) applied to measurements from 5 samples, at various Tx-Rx distances. As the Tx-Rx separation increases, the input-referred noise voltage significantly increases, because the signal strength on the Rx side drops quadratically, according to the Friis transmission equation [128].

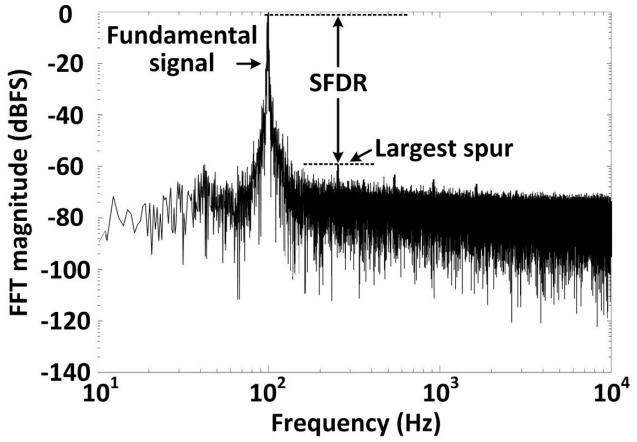

Figure 4.8. Power spectrum of the recovered data for dynamic range measurement.

We also measured the dynamic range of the entire system to evaluate its linearity at Tx-Rx separation of 30 cm. A 1 mV_{PP} sinusoidal waveform at 100 Hz was applied to channel #1 of the AFE. The recovered data on the Rx side over 3 minutes was transferred to frequency domain via FFT to derive its power spectrum. The result in Figure 4.8 shows a spurious-free dynamic range (SFDR) of 58.9 dB, which is the equivalent of 7.9 effective number of bits (ENoB) with the SNR of 49.2 dB [129].

Figure 4.9 shows the measured rate of packet loss in 5 samples in each case. Figure 4.9a presents the rate of packet loss as a result of changing the Tx-Rx distance from 10 cm to 150 cm using the dual-SDR Rx. As expected, when Tx-Rx separation increases, E_{Avr} decreases, resulting in a higher rate of packet loss.

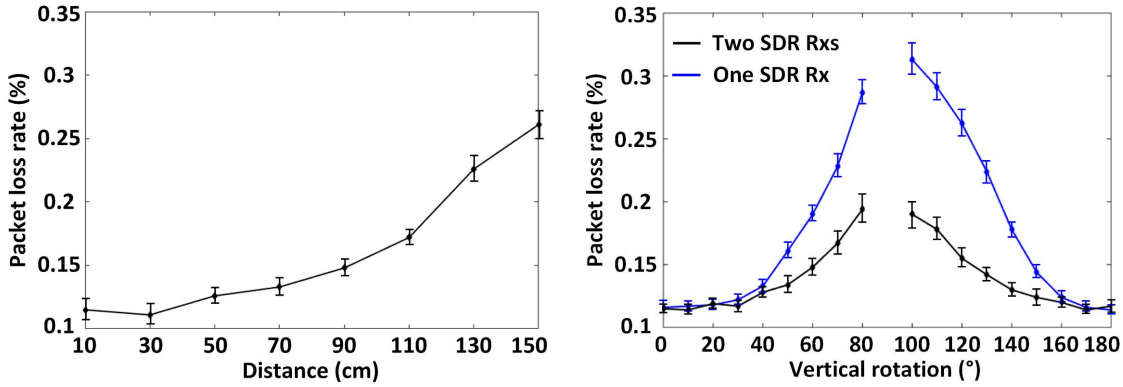

(a) (b)

Figure 4.9. (a) Packet loss vs. Tx-Rx distance with dual-SDR Rx. (b) Comparison between packet loss of a single-SDR Rx and a dual-SDR Rx vs. vertical rotation of the headstage (Tx antenna) at 30 cm Tx-Rx separation.

We also compared the rate of packet loss between a single-SDR Rx and a dual-SDR Rx vs. the Tx vertical misalignment in Figure 4.9b at 30 cm Tx-Rx separation. Using a dual-SDR Rx, the packet loss is significantly reduced, particularly at sharper misalignments thanks to the relatively stable signal strength of the two orthogonal Rx antennas against angular misalignment (see Figure 4.9b). As angular misalignment approaches 90º, the rate of packet loss increases even in dual-SDR Rx. Because the EnerCage-HC2 transmitted power also increases by its CLPC to compensate for the Rx coils angular misalignment and keep the headstage functional [103], resulting in stronger EM interference with the 434 MHz data link. At 90º rotation, the headstage cannot receive enough power even at the highest EnerCage-HC2 output power level, resulting in complete loss of data bit stream. In practice, however, it is unlikely for the headstage to stay at 90º

rotation for a long period. A temporary storage in the headstage, the supercapacitor is considered for this purpose to supply the headstage for up to 25 s when the received power is interrupted for any reason, such as >80° headstage rotation or the animal standing on its hind limbs [24], [121].

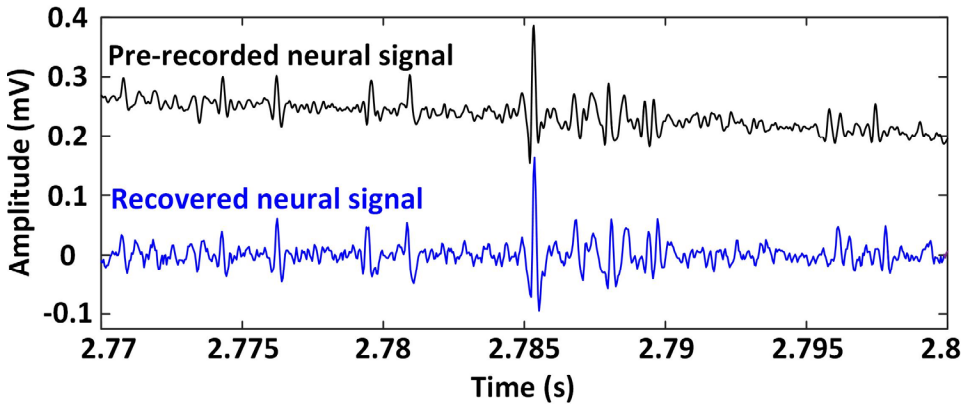

Figure 4.10. Recovered neural signal at 30 cm Tx-Rx separation compared to the pre-recorded neural signal applied to channel #1 of the WINeR-8 AFE.

Table 4.1. Measured specifications of the dual-SDR Rx.

WNeRS-8 Headstage	
Headstage size	2.1×2.1×2.1 cm^3
Headstage weight	5.7 g
Power consumption	18.9 mW (ASIC) + 16.1 mW (BLE)
Data rate	9 Mbps
Tx output power	-3-0.2 dBm, 5 bits
Recording gain	51.6-76 dB, 3 bits
Low cut-off frequency	20-400 Hz, 3 bits
High cut-off frequency	15 kHz
Tx and Rx Antenna	
Center frequency	434 MHz
Data modulation type	OOK
Tx antenna gain	-6 dBi
Tx antenna bandwidth	6.5 MHz
Rx antenna gain	-0.15 dBi
Rx antenna bandwidth	12 MHz
Tx-Rx separation	10-150 cm, 30 cm (nominal distance)
SDR Rx (Nuand BladeRF)	
SDR Rx gain	41 dB
SDR Rx bandwidth	18 MHz
Sampling rate	36 MHz

Input-referred noise	4.22-4.88 $\mu V_{ni,rms}$ (10-150 cm distance)
Dynamic range	59 dB (30 cm distance)
Packet loss rate	0.115%-0.261% (10-150 cm distance) 0.114%-0.194% (0°-180° rotation)
PC & FPGA	
PC computational resources	Dell Inspiron 3650, 16 GB RAM Intel Core i7-6700 CPU @ 3.4 GHz
CPU utilization rate	80% (design-I), 30% (design-II)
FPGA utilization rate	0% (design-I), 45% (design-II)

To emulate a real recording, a pre-recorded neural signal containing spikes in tens of μV_{PP} range plus a 4 Hz sinewave, representing LFP in the background was applied to channel #1 of the AFE. WINeRS-8 AFE was set to filter out the LFPs and extract the spikes. Figure 4.10 shows a short 30 ms interval of the pre-recorded neural signal that was applied to channel #1 (upper trace) and the recovered data on the Rx side (lower trace). It can be seen that the spike is separated from the LFP by high-pass filtering, and can be recovered with high fidelity, which demonstrates the functionality of the dual-SDR Rx system *in vitro*. Table 4.1 summarizes specifications of the dual-SDR Rx prototype.

4.2 WINeRS-8 Headstage

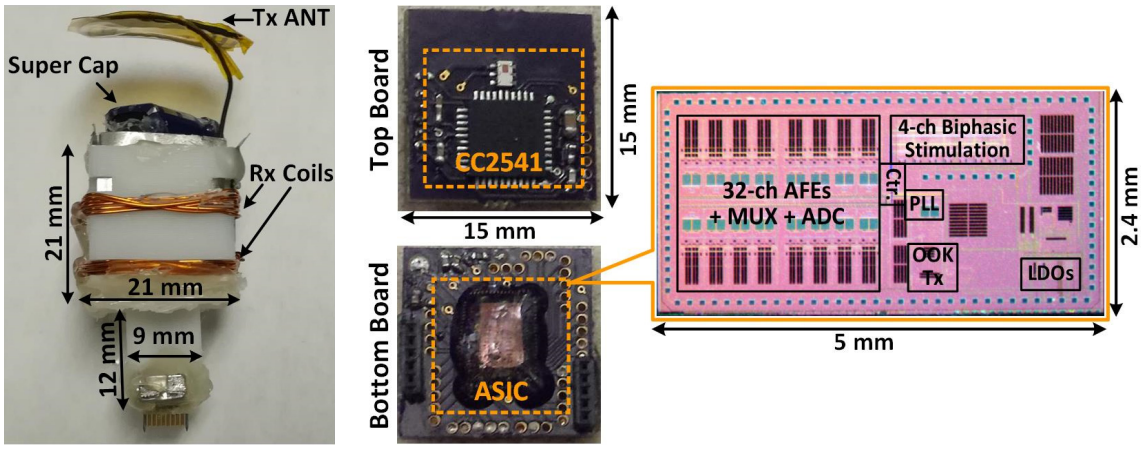

(a) (b)

Figure 4.11. (a) Implementation of the WINeRS-8 headstage with the Tx antenna. (b) Details of the headstage PCBs and the microphage of the WINeRS-8 ASIC.

Figure 4.11a shows the WINeRS-8 headstage[8] equipped with the Tx antenna extending from the top. The headstage includes two stacked PCBs, fitting in a 21×21×21 mm^3 cube, plus a 4×9×12 mm^3 extension at the bottom to provide mechanical supports for a 18-pin Omnetics Nano-strip connector (Minneapolis, MN). The connector is further reinforced with a small magnet, which facilitates mounting the headstage on the animal head. The headstage with a 0.1 F, 5 V supercapacitor (PB-5R0V104-R) weighs 5.7 g. A pair of Rx coils with optimized geometries for maximizing the PTE of the 4-coil inductive link are wound around the 3D-printed cube [103]. Figure 4.11b shows the two headstage PCBs, the upper of which includes an AC-DC converter and a CC2541 MCU. The MCU has a built-in BLE transceiver that can be used for forward data telemetry [103]. The lower board includes the WINeRS-8 SoC and its associated off-chip components. WINeRS-8 SoC was fabricated in a 130-nm standard CMOS process, occupying 2.4×5 mm^2 including pads. The MCU receives user-defined parameters from the PC through its BLE link in order to configure the WINeRS-8 SoC, especially for the 4-ch electrical stimulation function, as well as the 32-ch AFE and on-chip Tx that includes a PA, which output power is 5-bit adjustable from -3-0.2 dBm.

4.2.1 Current-Controlled Stimulation in WINeRS-8 SoC

Figure 4.12 shows a block diagram of the WINeRS-8 SoC[8] that implements 32-ch adaptive averaging AFE, 4-ch current-controlled stimulation (CCS) with stimulus AR, digitization, RF Tx, and control blocks. The rectified voltage is regulated by three low drop-out (LDO) regulators, which provide low analog (V_{DDA} = 1V), low digital (V_{DDL} = 1V), and high analog/digital (V_{DDH} = 2V) supplies for the rest of the SoC. An adaptive averaging method in the 32-ch AFE uses a 32-to-n analog multiplexer (MUX) to further

[8] I would like to thank Dr. Byunghun Lee for his great contributions for the development of the WINeRS-8 SoC and the headstage.

reduce the noise by averaging multiple channels, and each low noise amplifier (LNA) has a dc-coupled structure that maintains high input impedance in the order of 61 MΩ at 1 kHz. Every two channels of the AFE share a 50 kS/s 10-bit successive approximation register (SAR) ADC for digitization depending on 'CH_sel' bit, resulting in 25 kS/s for each individual channel. The digitized data packet includes 13-bit preamble from a preamble generator. A phase-locked loop (PLL) generates a 433MHz data carrier from the 13.56MHz reference clock. Digitized raw data packets are combined with a 13-bit preamble through a parallel-to-series (P2S) conversion block, and control a PA that modulates the 433MHz data carrier at a rate of 9 Mbps with 176-bit data packets to generate the uplink OOK signal, which in turn drives a small Tx antenna through a matching circuit.

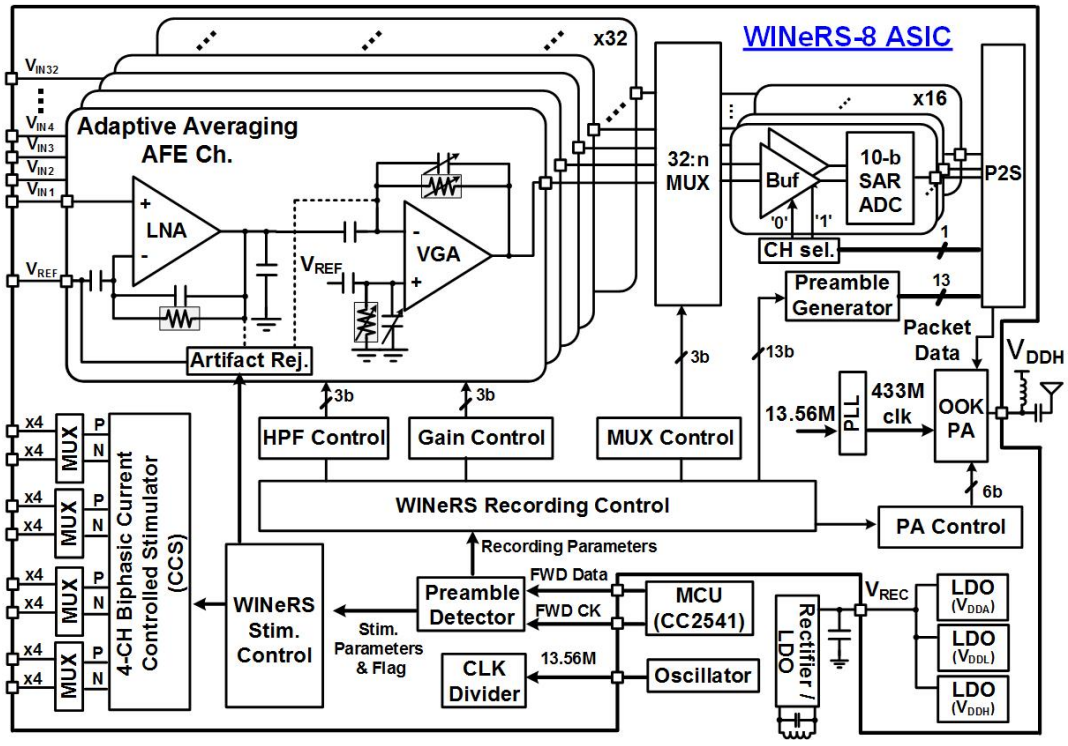

Figure 4.12. The block diagram of the WINeRS-8 SoC.

The downlink data from the BLE link is sent to the stimulation and recording control blocks by serial data (FWD_Data) and synchronized clock (FWD_CK) signals for

setting the recording/RF parameters or performing stimulation, depending on two different preambles. The 4-channel CCS is implemented for the positive (P) and negative (N) stimulations, each equipped with individual two current drivers. The stimulation flag signal is synchronized by the stimulus *AR* signal to prevent the saturation of AFE channels during the stimulation period.

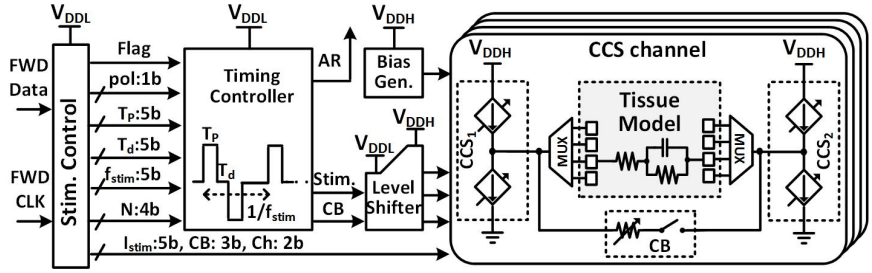

Figure 4.13. Schematic diagram of 4-ch biphasic CCS in WINeRS-8 SoC.

In the WINeRS-8 SoC, what I implemented is the 4-channel biphasic CCS with its adjustable stimulation parameters, as shown in Figure 4.13 [130]. Two stimulation current drivers, CCS_1 and CCS_2 drive four stimulating sites in a complementary fashion with high compliance voltage, increasing the stimulation power efficiency. The stimulation parameters are set by the Stimulation Control block, which follows the preamble detector block. The charge balance (CB) pulse short the selected two stimulating sites to bring the voltage difference between sites within a certain limit to guarantee safe stimulation. A stimulation signal, *Flag*, acting as a stimulation marker, is enabled during the entire stimulation period. Timing controller generates the stimulation *AR* signals to prevent the saturation of the AFEs from large stimulation current and enable the recording to resume right after the stimulation.

Each stimulation current driver has been equipped with a pair of 5-bit current source/sink with binary-weighted, low-dropout transistors, as shown in Figure 4.14.

Feedback loops using AMP_1-AMP_4 set the drain-source voltages of P_1-P_5 and N_1-N_5 at ~60 mV in the triode region. Therefore, the voltage headroom of the output stage, V_{Head}, can drop down to $V_{DS,sat}$ + 60 mV, which is smaller than $2V_{DS,sat}$ of a typical cascode output stage. The two current drivers source and sink at the same time through a pair of 4:1 site selectors, providing a bipolar stimulation compliance voltage of V_{DDH} -$2V_{Head}$.

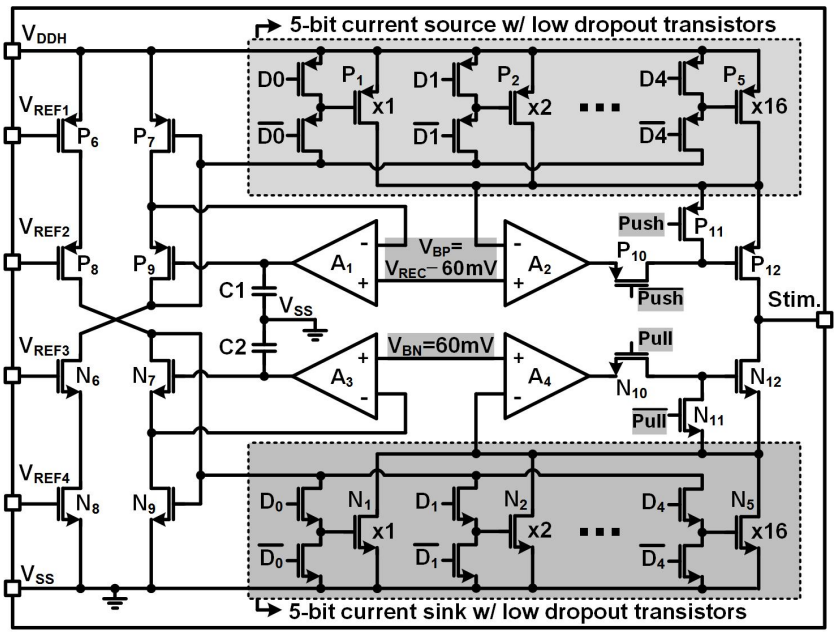

Figure 4.14. Schematic diagram of the current driver with low dropout 5-bit current sources.

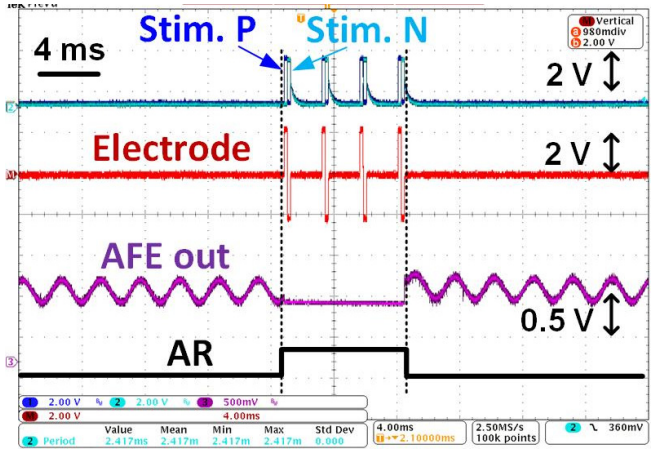

Figure 4.15. Measured waveforms of biphasic stimulation and stimulus *AR* using Randles equivalent tissue model.

Table 4.2. Measured specifications of the 4-ch current-controlled stimulation.

Number of channels	4 channels, 2 bits
Polarity (*Pol*)	Negative/Positive, 1 bit
Pulse width (T_P)	9.5-304 µs, 5 bits
Interval duration (T_D)	9.5-304 µs, 5 bits
Frequency (f_{stim})	13-414 Hz, 5 bits
Number of pulses (N)	1-16, 4 bits
Charging balance	3 bits
Stimulation current (I_{stim})	60-1860 µA, 5 bits

Figure 4.15 shows the measurement waveforms of in-situ stimulation and stimulation *AR* using a Randles equivalent model as the tissue model [131]. Since the generated *AR* signal keeps the AFE channel at the reference voltage during the entire stimulation time period, the AFE output shows the ability to resume recording within 0.2 ms after stimulation, without being saturation, as shown using the sinusoid signal in Figure 4.15. The current stimulation parameters are summarized in Table 4.2.

4.3 *In Vivo* Experiments

In vivo experiments[9] were conducted with prior approval from the IACUC at Emory University to verify the functionality of the dual-SDR Rx system on freely behaving rat model. A Sprague Dawley rat was implanted with a 16-ch MEA from Tucker Davis Technologies (Alachua, FL). Two rows of eight tungsten microwire electrodes with diameter of 50 µm, electrode spacing of 250 µm, and row separation of 500 µm, customized with longer and shorter lengths, targeted the rat hippocampus [132]. The electrodes were approximately placed at 3.5 mm and 2.5 mm ventral from the pia for simultaneous recording from both CA1 (short) and CA3 (long) regions, respectively, as shown in Figure 4.16a. The reference and ground wires were wrapped around the cranial screws, before sealing the surgical opening with dental acrylic. After the surgery, the rat was given pain

[9] I would like to thank Dr. Babak Mahmoudi for his strong support on the *in vivo* experiments.

medication and antibiotics to minimize discomfort and prevent infection until it recovered from the surgery and was able to freely move in the homecage.

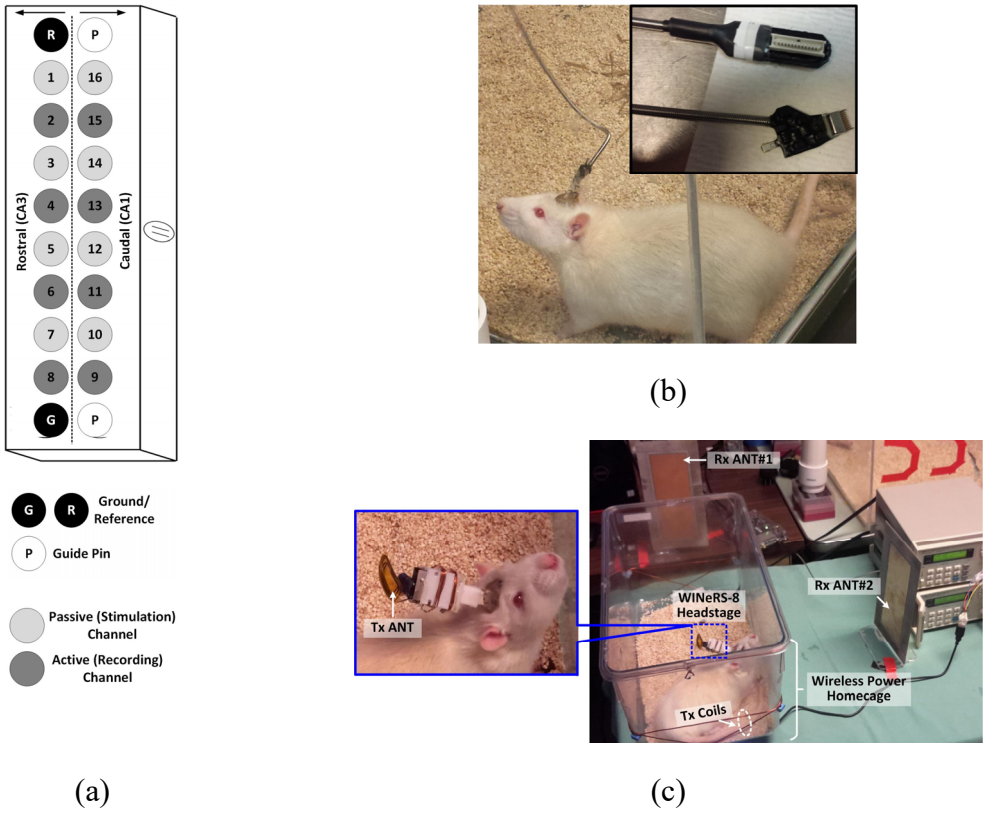

Figure 4.16. (a) Configuration of the electrodes within the MEA. *In vivo* experimental setup for the (b) hardwire recording using RZ2 BioAmp from Tucker-Davis, and (c) WINeRS-8 system.

To evaluate the system performance, we compared the recorded neural signal by a commercial hardwired system, RZ2 BioAmp from Tucker-Davis [133], shown in Figure 4.16b, and the complete WINeRS-8 system (Figure 4.16c). In the latter case, the rat freely moves in the homecage with no tethers, while carrying the WINeRS-8 headstage. The EnerCage-HC2 continuously delivers 35 mW to the headstage with no interruption. Even though the transmitted power from the EnerCage-HC2 increases up to 2.5 W when the headstage is rotated by 90º, magnetic flux density does not surpass the SAR limit at 13.56 MHz [103], [104]. It should be noted that even though in this experiment only 8 channels

were used for neural recording, the data rate did not change, because all 32 channels were still being recorded.

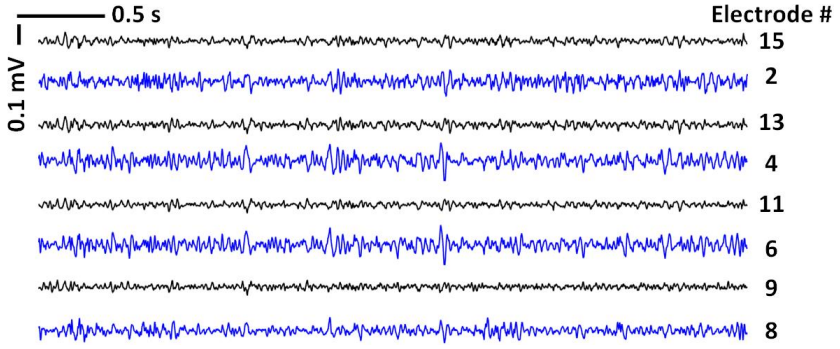

(a)

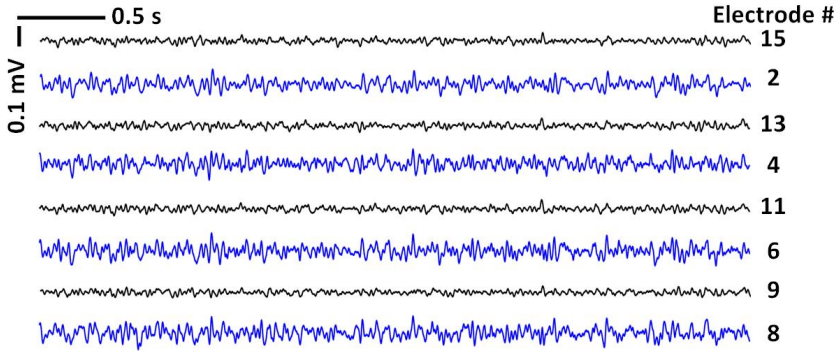

(b)

Figure 4.17. LFP signals recorded back to back from the same rat by the (a) hardwired setup in Figure 4.16b, and (b) WINeR-8 wireless setup in Figure 4.16c.

Both hardwired and wireless recorded data were bandpass filtered between 20 Hz and 200 Hz in MATLAB to extract the LFP from the selected electrodes in the CA1 and CA3 regions. Then the wireless recorded data can be fairly compared with the hardwired data. Figures 4.17a and 4.17b show the hardwired and wireless LFP signals, recorded over 3 s, respectively. In Figure 4.17a, electrodes #9, 11, 13, and 15 record from the CA1 region, while electrodes #2, 4, 6, and 8 record from the CA3 region. The signals from CA3 were highly correlated and typically showed larger variations. One possible reason for the larger LFP amplitude in CA3 region was the shape of the custom-designed electrode array with

different lengths to target both CA1 and CA3 based on the anatomy of the hippocampus. In practice, however, since the relative distance between the electrodes were fixed, once we aimed for recording from CA3, the CA1 electrodes did not end up perfectly within the cell layer. This likely resulted in the lower amplitude recording in the CA1 array. Since the main objective was to compare the hardwired vs. wirelessly recorded data, the results were still viable by observing the same attributes in the wireless and hardwired recordings.

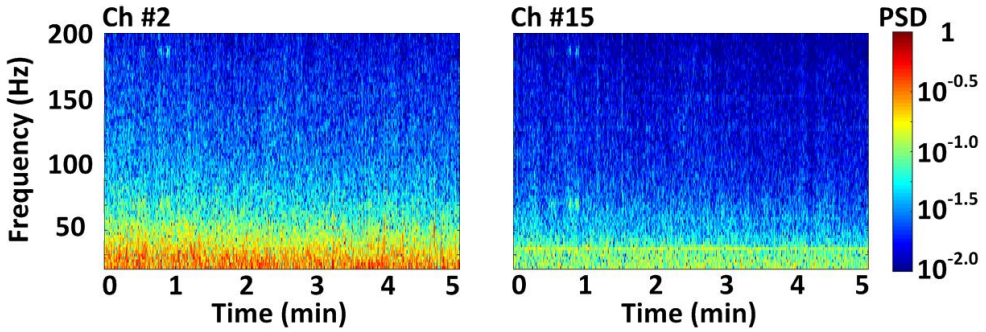

(a)

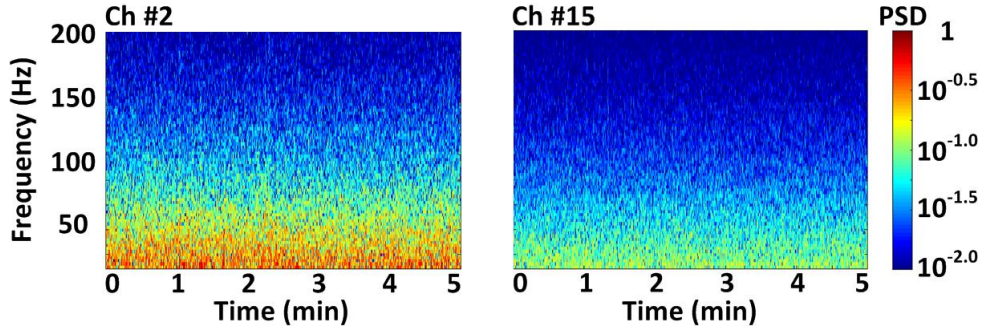

(b)

Figure 4.18. Spectrogram of the normalized LFP recorded from selected CA3 (left) and CA1 (right) electrodes, Ch #2 and Ch#15, using the (a) hardwire recording system shown in Figure 4.16b, and (b) WINeRS-8 system shown in Figure 4.16c.

LFP signals from selected electrodes were mapped onto a spectrogram of normalized PSD over a 5-minute window. In Figures 4.18a and 4.18b, the LFP signals recorded from electrode #2 in the CA3 region, measured by the hardwire recording system and the WINeRS-8 system, show higher PSD within a relatively narrow 20-50 Hz band, as

compared to the PSD of the LFP signals recorded from electrode #15 in the CA1 region in same frequency band.

4.4 WINeRS-9 SoC

Despite significant advances in the development of neural interface capable of neuromodulation and brain, a comprehensive solution is still not available. The main goal is still to develop a fully-integrated, high-channel-count, implantable, wireless tri-modal neural interface system, which can cover the cortical surface to enable selective optical/electrical stimulation and recording of the large-scale cortical networks initially in small freely moving animals.

Yet another key feature, which brings such a trimodal neural interface closer to clinical usability is wireless operation both in terms of power delivery and bidirectional data communication. The trimodal interface system will integrate high-density microelectrodes, individually addressable LEDs, ultra-low-power SoC, and wireless telemetry to form the most comprehensive interface developed for seamless communication with the central nervous system. Successful achievement of the trimodal system will provide unprecedented flexibility for users to select from optical neuromodulation, electrical neurostimulation, and electrical recording.

Therefore, based on WINeRS-8 SoC design, we have embarked upon developing the first completely wireless and battery-less trimodal neural interface SoC, called WINeRS-9, equipped with wireless power/ data links for neural recording, electrical stimulation, and optical stimulation.

4.4.1 WINeRS-9 SoC Overview

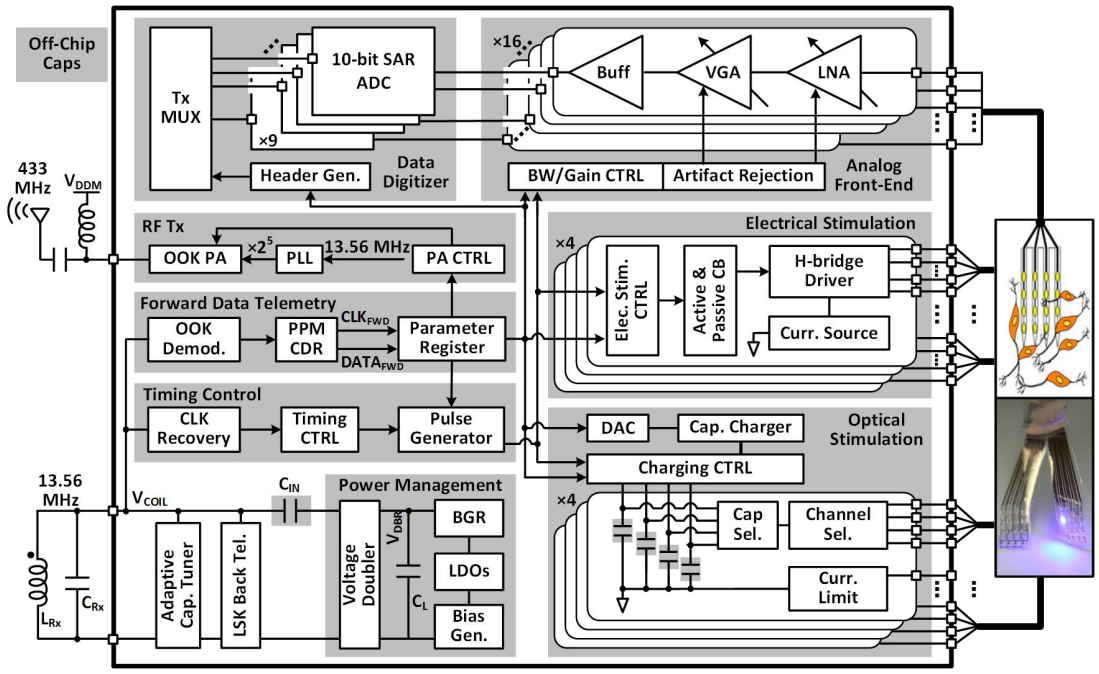

Figure 4.19. Overall block diagram of the trimodal WINeRS-9 SoC.

Figure 4.19 shows the top-level block diagram of the WINeRS-9 SoC[10]. In the power management block, a voltage doubler is in charge of ACDC conversion, and generates V_{DBR} from the 13.56 MHz power carrier, while low dropout regulators and bandgap generator provide supplies and bias voltages/currents for the rest of SoC. The timing control block recovers a 13.56 MHz clock from the power carrier and generates the timing information for stimulation and ADC units. In the forward data telemetry block, a pulse-position-modulated clock/data recovery (PPM-CDR) circuit recovers synchronized data and clock signals from OOK coil voltage, V_{COIL}, to configure stimulation and recording parameters. A Load-shift-keying (LSK) back telemetry is adopted for CLPC by sensing V_{COIL}. Optical stimulation employs a switched-capacitor-based stimulation (SCS) architecture, in which a capacitor charger sequentially charges four storage capacitor banks, while adaptive capacitor tuner compensates the resonance capacitance variation

[10] I would like to thank Dr. Ulkuhan Guler and Yen-Pang Lai for their great collaborations on the WINeRS-9 SoC design.

during charging. The capacitors in each group can be configured to dump their charge into a designated LED through capacitor/ channel selectors, while a current limiter sets an upper bound to the current flowing through the LED. For electrical stimulation, an H-bridge drives stimulating sites with constant current in a biphasic-bipolar fashion, while both active and passive CB circuits can be engaged to ensure the site voltage difference stays within a safe window (± 50 mV) [134].

The WINeRS-9 SoC includes a 16-ch AFE for neural recording. An *AR* circuit changes the AFE gain/bandwidth configuration to prevent saturation during stimulation periods. Every two AFE channels share one 50 kS/s 10-bit SAR ADC, resulting in a sampling rate of 25 kS/s per channel. Each digitization cycle generates a 132-bit data packet, which is serially delivered to the RF Tx block. A PA has a 433 MHz carrier signal, generated by a PLL from the 13.56 MHz power carrier, and ON/OFF keyed by the serial data bit stream to send the modulated data out through a small monopole antenna.

4.4.2 Analog Frond-End for Neural Recording

Each AFE channel includes three stages, as shown in Figure 4.20a: a LNA, a variable gain amplifier (VGA), and an analog buffer. The LNA and VGA employ DC blocking caps, C_1 and C_3, at the input to remove DC offset, while their common-mode voltages are biased at half of the supply voltage, V_{MID}. During the stimulation period, an *AR* pulse pulls the inputs and outputs of LNA and VGA up to V_{MID}. The buffer stage is capable of driving the large switched-capacitor loading of the SAR ADC. The low cutoff frequency of the AFE is set by the LNA at $1/(2\pi \cdot R_1 \cdot C_2)$, while the high cutoff frequency of the AFE is determined by the VGA bandwidth. The mid-band gain of the AFE is

determined by the gains of the LNA and VGA, which are set by C_1/C_2 and C_3/C_4, respectively. C_4 is a 3-bit binary-weighted capacitor array and adjusts the VGA gain, as shown in Figure 4.20b. R_1 in Figure 4.20c is implemented using a cross-coupled pseudo resistor, which prevents DC current flow through P_1 and P_2 [135]. This pseudo resistor and its 3-bit programmable current source sets the AFE low cutoff frequency. R_2 and R_3 in Figure 4.20d are implemented using a non-tunable pseudo resistor.

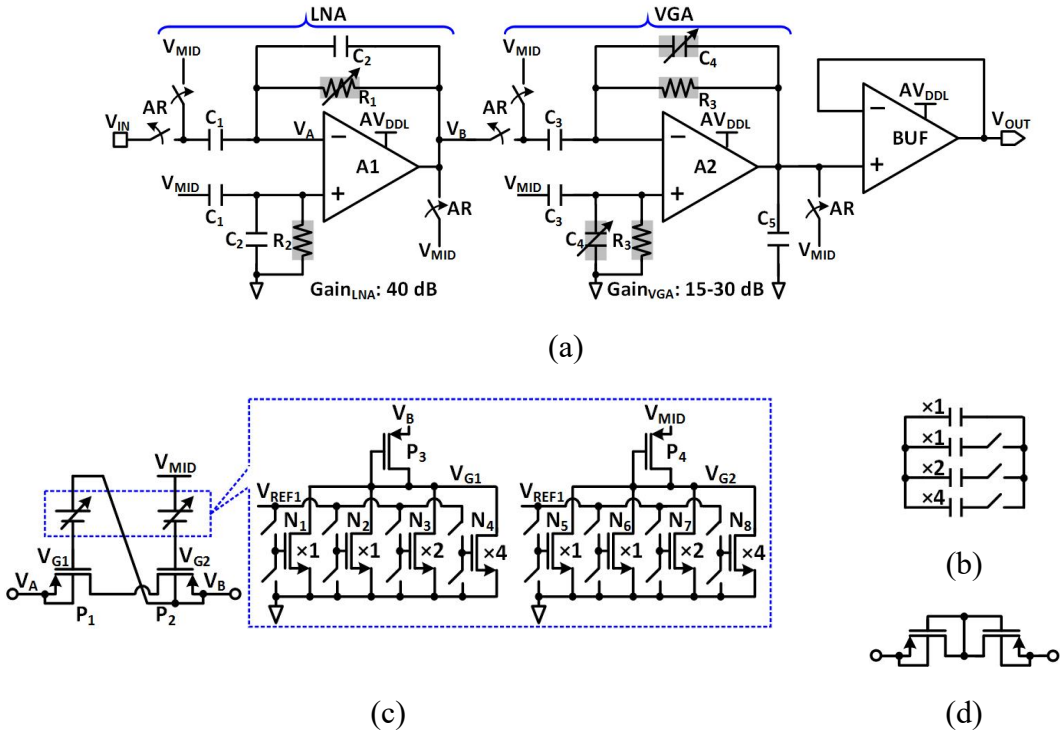

Figure 4.20. (a) Schematic diagram of a single channel AFE. Schematic implementations of (b) C_4, (c) R_1, and (d) R_2 and R_3 in the AFE.

4.4.3 Switch-Capacitor Based Optical Stimulator

Figure 4.21 shows a simplified schematic diagram of the optical stimulation block, which utilizes the SCS architecture [136]. The capacitor charger consists of two switches driven by two high-speed comparators, CMP_N and CMP_P, sequentially charging four off-chip capacitor banks, each including 4 × 1 μF surface-mount device (SMD) caps. The

timing block adjusts the charging interval to control the storage capacitors' charge up to a target voltage, CV_{TG}, set by a 5-bit DAC. The charging cycle continues till a stimulation command arrives. Then in each group, a cap-selector decides which capacitor(s) to be dumped into the LED that is defined by a channel selector for optical stimulation. A current limiter, implemented using a 5-bit current sink with binary-weighted transistors, adjusts the maximum LED current. The stimulation pulses are adjustable in pulse width, TW_{OPTI}, and period, TP_{OPTI}, with four control bits for each of them.

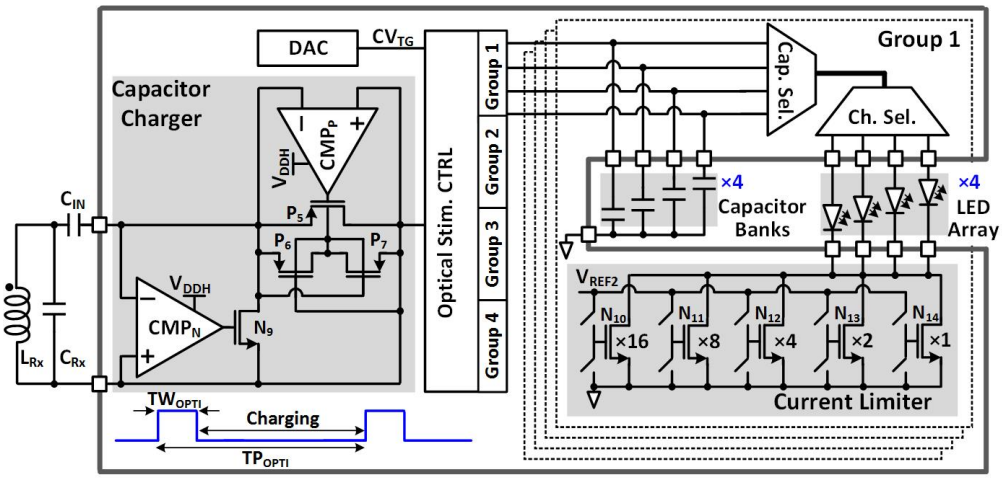

Figure 4.21. Schematic diagram of the optical stimulation block.

4.4.4 Current-Controlled Electrical Stimulation with Active Charge Balance

The electrical stimulation block includes four independent groups, one of which is shown in Figure 4.22. A current stimulator employs four 4:1 MUX with an H-bridge configuration, which interfaces with four active and four return sites. A controller selects the MUXs in pairs to generate anodic and cathodic stimulation phases with a single current driver, which consists of a 5-bit current steering DAC, implemented with low dropout transistors. Using A_3 and A_4 gain stages, feedback loops set the drain-source voltages of N_{17}-N_{21} transistors at ~60 mV in the triode region to reduce the voltage headroom of the

current driver output, while boosting its output impedance. The active CB circuit monitors the voltage difference between active and return stimulating sites during stimulation and active CB periods, when *EN*=1. The site voltage difference is capacitively attenuated before being converted to a single-ended output voltage, V_{DET}. If the site voltage difference goes above a ±50 mV window, V_{DET} will exceed the bounds set by V_{THH} and V_{THL}. In response, a sequence of pulses will be generated to control the stimulator, which will push or pull additional current pulses into the tissue to return the site voltage difference within the safe window. The active CB circuit is then disconnected from the stimulating sites and the passive CB circuit is activated, which further removes the residual charges by shorting the two stimulating sites to ground.

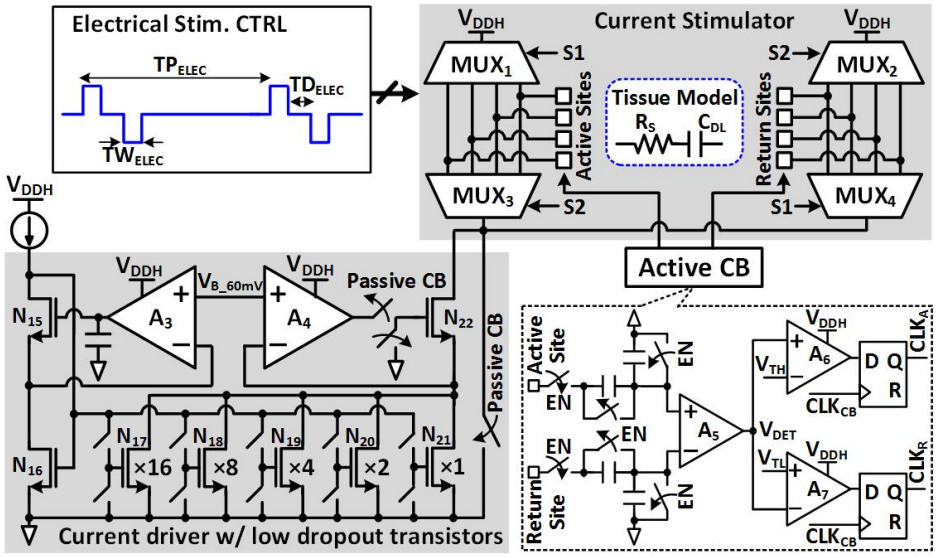

Figure 4.22. Schematic diagram of a single group in the electrical stimulation.

4.4.5 Experimental Measurements

The WINeRS-9 ASIC, shown in Figure 4.23, was fabricated in the TSMC 0.35-µm 4M2P standard CMOS process, and occupies 3×5 mm^2 area. Figure 4.24 shows the experimental setup for testing the optical stimulation function of the WINeRS-9 SoC,

which was wirelessly powered through a 3-coil inductive link. The chip configuration commands were wirelessly sent to the WINeRS-9 SoC via OOK of the power carrier. The same setup was used for testing the electrical stimulation function and the AFE of the neural recording function. The WINeRS-9 SoC was directly wire-bonded on an evaluation PCB, which also includes SMD capacitor banks and LED arrays for testing the optical stimulation function, as well as resistor-capacitor tissue models for testing the electrical stimulation function.

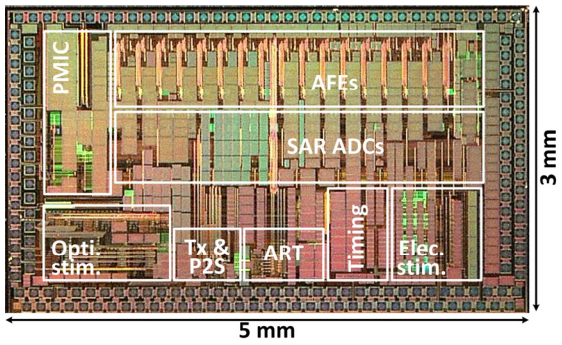

Figure 4.23. Micrograph of the fabricated WINeRS-9 SoC.

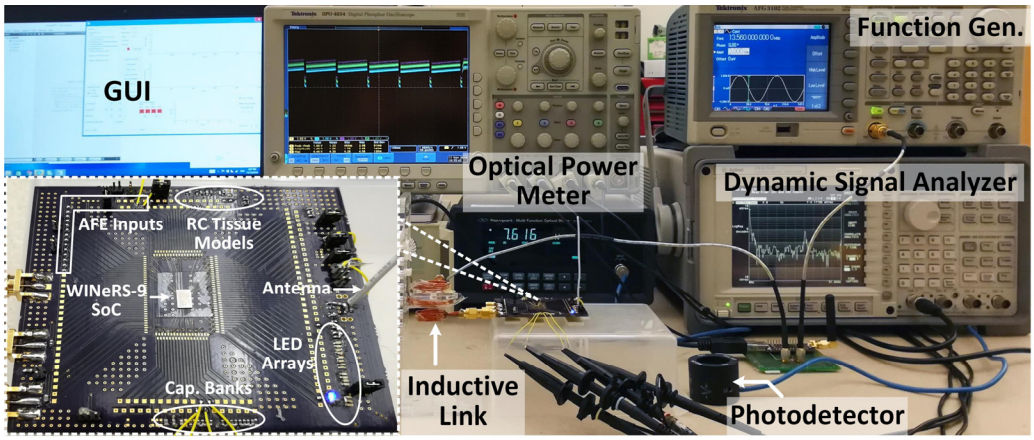

Figure 4.24. Measurement setup for the WINeRS-9 SoC. Inset: One blue LED is selected from the GUI and driven by the WINeRS-9 SoC on evaluation board to demonstrate wireless power/data transmission for optical stimulation.

The AFE was characterized under wireless powering after immersing the electrode in 0.9% saline solution. Figure 4.25a presents the measured AFE input-referred voltage

noise spectrum. The thermal noise level is observed at 10 nV/√Hz and 1/f noise corner occurs at 20 Hz. Integration under this curve from 1 Hz to 50 kHz yields a RMS noise voltage of 3.46 µVrms for the AFE, with a noise efficiency factor (NEF) of 2.95. Figure 4.25b presents the measured frequency response of the AFE. The low cutoff frequency of the AFE is adjustable from 1-100 Hz, while the gain of the AFE is changed from 55-70 dB. The high cutoff frequency of the AFE is constant at 10 kHz. Figure 4.25c shows the input and output transient waveforms of the AFE in 1-s time interval. To emulate a real recording, pre-recorded neural signal applied to the AFE already has background noise and low frequency interference, which should be filtered out to extract the spikes. In the close-up view, the spike was successfully separated from the undesired noise and low frequency interference and amplified by the AFE.

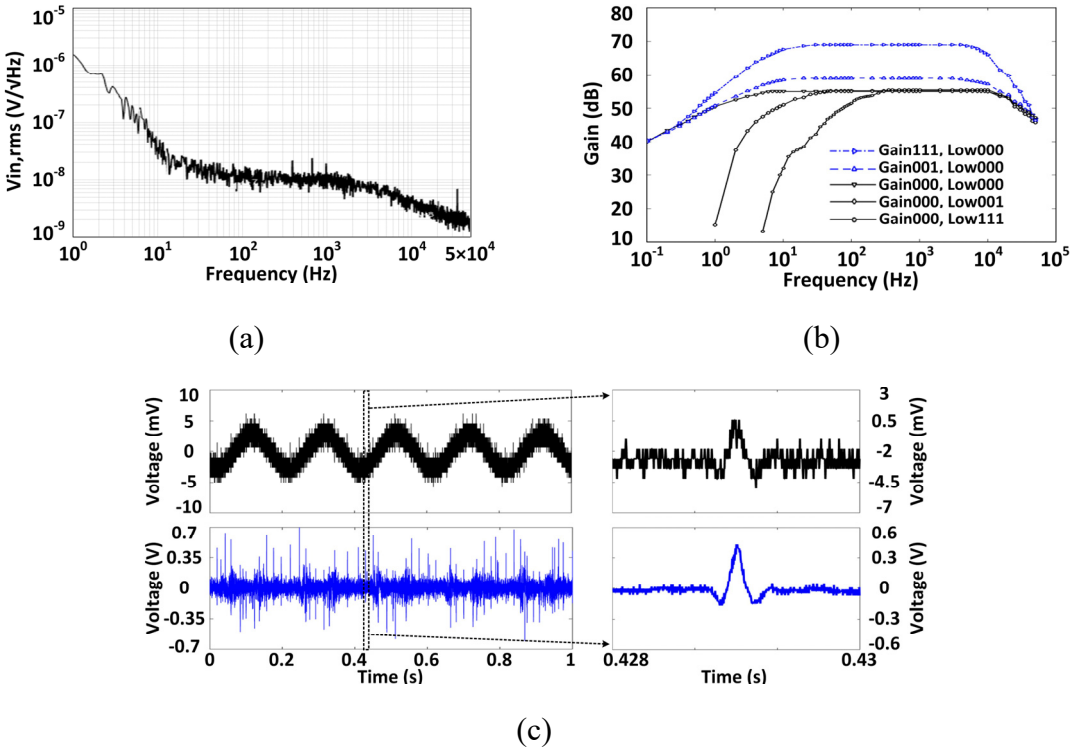

Figure 4.25. (a) Input-referred voltage noise spectrum and (b) frequency response of the AFE. (c) Pre-recorded neural signal given as an input (black) and transient AFE output signal (blue).

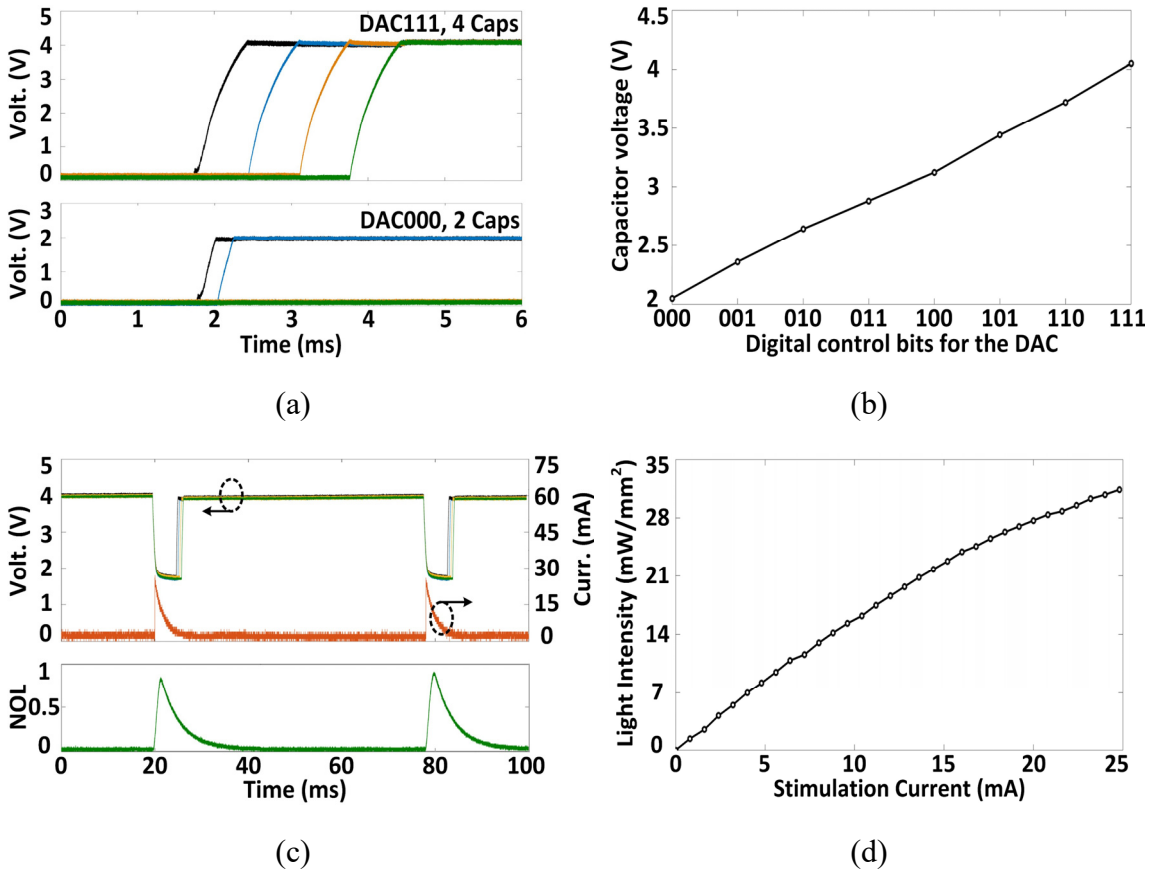

Figure 4.26. Measured results of (a) charging capacitors up to a determined V_{TG} value, (b) capacitor voltage after charging as a function of the DAC digital control bits, (c) discharging capacitors in a selected LED for optical stimulation, and (d) light intensity of the selected LED as a function of LED current.

The upper and lower traces in Figure 4.26a show how all four 1µF capacitors and only two out of four capacitors in a bank are sequentially charged up to V_{TG} = 4 V and V_{TG} = 2 V, respectively. The results illustrate the flexibility of WINeRS-9 in charging different numbers of capacitors up to different V_{TG} levels to control the injected charge into the LED according to $Q = CV$. Figure 4.26b shows the capacitor voltages after being fully charged at different V_{TG} values, set by the DAC control bits. Figure 4.26c presents the overall SCS operation to generate optical stimulation with 5 ms pulse width at 17 Hz. In this case, the LED current is limited to 24.8 mA. In a single group, four capacitors, charged to 4 V, dump their charge simultaneously into a selected LED (LB QH9G, OSRAM), creating an

exponentially decaying current with peak value of 24.8 mA. The emitted light from the LED during stimulation pulse was collected by the photodetector (Newport 883-SL) of an optical power meter (Newport 1835-C). The normalized output light (NOL) expectedly followed the stimulation current variation with a slight delay. After each stimulation, all four capacitors were recharged back to 4 V, as shown in Figure 4.26c. Figure 4.26d shows the light intensity under different current limits with four storage capacitors, which match the LED specifications.

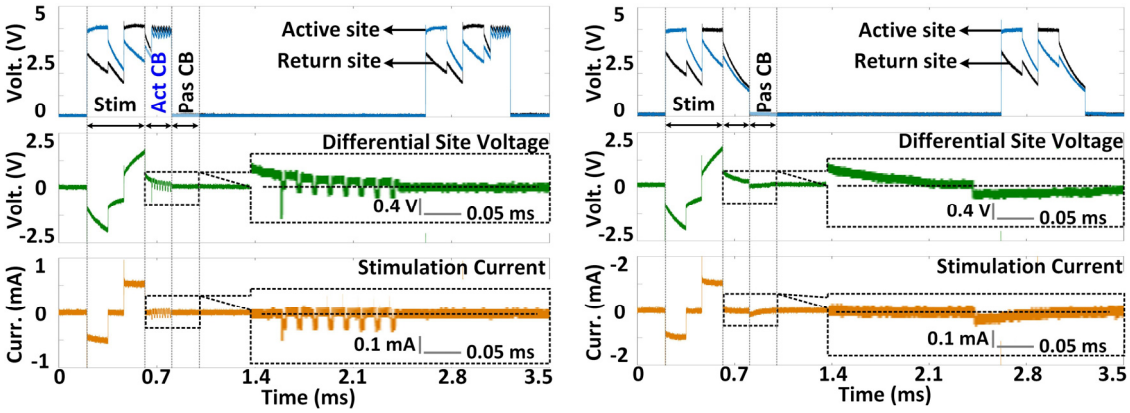

Figure 4.27. Measured stimulation waveforms (a) with and (b) without active CB being activated.

Figure 4.27 presents the electrical stimulation waveforms by delivering ±550 µA to the tissue model consisting of R_S = 2 kΩ and C_{DL} = 500 nF in series. The other stimulation specifications were set as 150 µs pulse width at 400 Hz. In Figure 4.27a, following the biphasic stimulation, the voltage difference between two stimulating sites exceeded the upper bound of the ±50 mV safe window. Accordingly, the active CB circuit injects a series of small cathodic current pulse at a current level of 60 µA and pulse width of 20 µs within 160 µs. The active CB circuit successfully returns the site voltage difference back into the safe window. The active CB circuit was not activated in Figure 4.27b, and instead the

passive CB circuit was engaged to neutralize the residual charges after each stimulation cycle. However, the resulting charge balancing is not as efficient as the active CB in Figure 4.27a.

4.5 Summary and Discussion

We have presented a wirelessly-powered implantable neural recording and stimulation system that is fully compatible with the existing EnerCage-HC2 smart wireless experimental arena for conducting longitudinal electrophysiology and behavioral neuroscience experiments on small freely behaving rodents. The WINeRS-8 headstage supports 32-ch neural spike recording and 4-ch biphasic stimulation capabilities for bidirectional neural interfacing. It has wideband RF data transmission for uplink data and BLE for narrow band downlink data, all powered by the EnerCage-HC2 at 13.56 MHz.

Table 4.3. Benchmarking of data acquisition systems for wireless neural recording.

Publication	2013 [48]	2016 [56]	2017 [52]	2018 [83]	**This work**
# of recording	434 MHz Custom	UWB	LSK/ Wi-Fi	2.4 GHz COTS TRx	**434 MHz Custom**
Data/sampling rate	32	64	16	2	**32**
Data Tx-Rx distance	640 kSps	1.2-45 Mbps	2 Mbps	32 kbps	**9 Mbps**
Power link	Up to 4.2 m	10 cm-10 m	-	3 m	**10 cm-1.5 m**
Backpack	Inductive link	Inductive link	Inductive link	Battery	**Inductive link**
Animal freely behave	No	No	Yes	No	**No**
In vivo arena (cm^3)	Yes	NA	Yes	Yes	**Yes**

Table 4.3 compares the proposed dual-SDR Rx with a few recent data acquisition systems in the literature. In [83], a battery-powered headstage for wireless neural recording and optical stimulation is presented, which use 2.4 GHz COTS transceiver (TRx) to send

data at 32 kbps to PC. The uninterrupted duration of experiment is limited by the battery capacity. In [52], back telemetry via LSK through a transcutaneous inductive link is adopted to send the recorded data to an external relay in the form of a battery-powered backpack, which wirelessly powers and communicates with the IMD. Even though such elegant solution would not face tethering effect compared to hardwired setups [11], [13], the uninterrupted duration of the experiment would still be dependent on the size of the battery embedded in the backpack. In [56], the system using UWB TRx realizes high data rate over the desired range. However, robustness of the system against misalignments and possible blind spots have not been discussed.

Compared to the abovementioned systems, the dual-SDR Rx presented here offers: 1) robust wireless data recovery against spatial and angular misalignments, 2) scalability in terms of the number SDRs operated in parallel in design-II, extending the wireless coverage to the larger arenas, 3) easy implementation and rapid development using software-defined functions either in the FPGA of the SDR or GNU Radio compared to the custom-designed Rx solutions, such as [48], and 4) reasonable workload on the PC, eliminating the need for costly high-end systems. We have demonstrated functionality and robustness of the complete WINeRS-8 system and its compatibility with the EnerCage-HC2 system both *in vitro* and *in vivo*.

We have also presented a trimodal wireless implantable neural recording and stimulation SoC. Table 4.4 benchmarks WINeRS-9 against recently reported neural interfaces, presenting its key advantages over the prior art. WINeRS-9 SoC is wirelessly powered and it receives user commands through the same inductive link. Its AFE can amplify, digitize, and transmit neural signals through a separate link. It can store energy in

capacitor banks and suddenly generate high current levels needed to drive selected LEDs passed optogenetic stimulation threshold. It is capable of safe electrical stimulation with a combination of active and passive CB. Testing and characterization are still ongoing and will be followed by *in vivo* studies on rodents.

Table 4.4. Benchmarking of the state-of-art neural interfaces.

Publications		2017 [57]	2018 [59]	2018 [60]	**This work**
Technology (µm)		0.13	0.18	0.13	**0.35**
Neural Recording	Channel number	64	-	10	**16**
	Power (µW)	0.63	-	11.2	**18.2**
	Noise (μV_{rms})	1.13	-	3.2	**3.46**
	NEF	2.86	-	2.3	**2.95**
Electrical Stimulation	Channel number	64	4	-	**16**
	Current (mA)	0.01-1.35	0.022-5	-	**0.025-0.775**
	Frequency (Hz)	Arbitrary	0-60	-	**25-400**
	TW_{ELEC} (µs)	Arbitrary	14-470	-	**40-640**
	Charge Balance	Passive	Passive	-	**Act+Pass**
Optical Stimulation	Channel number	-	1	4	**16**
	Current (mA)	-	0.022-5	0-35	**0.8-24.8**
	Frequency (Hz)	-	0-60	PWM	**3-50**
	TW_{OPTI} (ms)	-	14-470		**1.25-20**
	Light intensity (mW/mm^2)	-	23	-	**31.5**
Power source		Inductive	Ultrasound	Battery	**Inductive**
Wireless data Tx		UWB	ASK	MCU	**OOK**

CHAPTER 5. MINITURIZED IMPLANTABLE OPTICAL STIMULATION DEVICE

Recently, a few wirelessly-powered optogenetics approaches have been reported, demonstrating significant reduction in the implant size [59], [66]-[69]. In [68] and [69] the proposed optical stimulators, equipped with the energy-harvesting unit, either a coil [69] or a stretchable antenna on board [68], are wirelessly powered in the GHz band. The SAR of EM field in the tissue, which mainly consists of water, at high frequencies is rather high [32]. Moreover, operation in these bands produces considerable radiation, which results in interference with laboratory instruments or wireless devices in the environment [33]-[35].

To circumvent the challenges associated with wireless operation in GHz bands, the carrier frequency in [67] is limited to 13.56 MHz. However, in this case, the Rx coil with a diameter of 9.8 mm becomes the main limiting factor in the device miniaturization. A photovoltaic power transfer strategy is proposed in [66] to wirelessly power the implant using IR light. In this case, the overall PTE is quite low, and additional post-processing steps, needed in microfabrication of the silicon die and separation of the photovoltaic cells, could reduce the yield. In [59], an ultrasonically-powered mm-sized implant enables both optical and electrical stimulations, at the cost of increasing size and weight of the external transmitter, which is too large to be carried by a behaving animal subject. Moreover, even though ultrasonic power transmission is immune to EM interference and offers good PTE in deeper tissues, it is quite sensitive to transducer misalignments and cannot penetrate bone/skull.

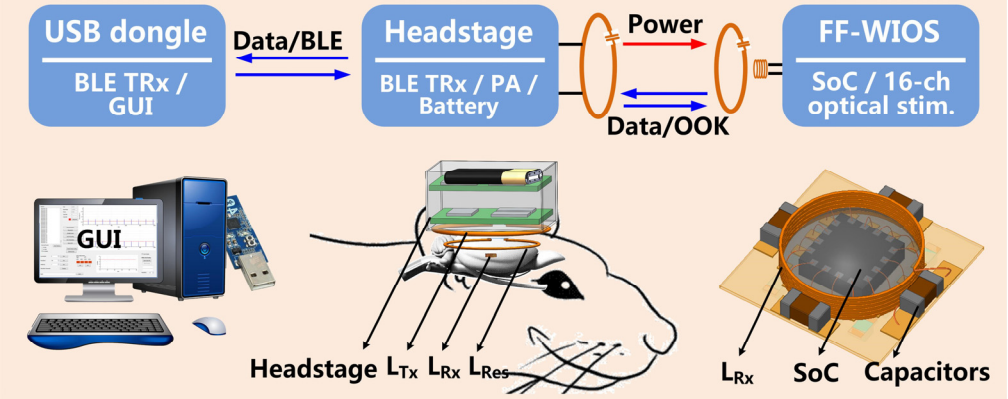

Figure 5.1. A simplified conceptual representation of the FF-WIOS device being wirelessly powered and controlled by a battery-powered headstage, which is in turn controlled via BLE by a PC running the GUI.

We have developed a mm-sized, free-floating, wirelessly-powered, implantable optical stimulation (FF-WIOS) device, building upon our preliminary results in [137], [138], to address the abovementioned limitations. System functionality has been validated *in vivo* on anesthetized rats by observing light-evoked LFPs and immunostained tissue response. The main novelties can be summarized as 1) ensuring sufficient and constant power is delivered to the load at high PTE, while staying well below the SAR limit, 2) assembling the FF-WIOS device with compact size and light weight, 3) designing the FF-WIOS SoC with high-level integration of front-end circuits and wireless power/data transmission related circuits for 16-channel wireless optical stimulation, 4) providing end-users with the accurate control of the optical stimulation patterns.

5.1 System Overview

The conceptual view of the system that wirelessly powers and controls the mm-sized FF-WIOS is shown in Figure 5.1. The FF-WIOS, which includes a SoC, SMD capacitors (0201), Rx coil, and µLEDs, all mechanically supported on a 100 µm-thick polyimide substrate, and hermetically sealed with Parylene-C and polydimethylsiloxane

(PDMS) for acute testing, is designed to be implanted on the surface of the subject's brain. The wire-wound Rx coil, L_{Rx}, which encompasses the SoC, forms a 3-coil inductive link with a Tx coil, L_{Tx}, which is part of the external headstage, and a passive high quality Q-factor resonator, L_{Res}, which encompasses one or more FF-WIOS implants roughly in the same plane. The headstage includes a Class-E PA, controlled by a CC2541 MCU, which delivers power from battery to the FF-WIOS through the 3-coil link at 60 MHz. To wirelessly control the FF-WIOS, stimulation parameters, which are set in a GUI running on a nearby PC, are sent to the headstage MCU via BLE, and then relayed to the FF-WIOS through the 3-coil link by on-off-keying the power carrier signal. The rectified voltage on the FF-WIOS is also digitized, as a measure of the received power on the SoC, and sent back to the headstage via LSK to close the power control loop, and eventually send to the PC via BLE for real-time display.

Figure 5.2 depicts the steps for microassembly of the FF-WIOS. In the current prototype, 18 µm of copper is patterned on both sides of the polyimide substrate with the diameter of 2.5×2.5 mm^2 to form interconnections between the wire-bonded SoC die, µLED pads, and SMD caps. The µLEDs (220×270×50 μm^3, TR2227TM, Cree) were mounted on their pads using low melting point solder (144 Alloy Field's Metal) and then encapsulated using Parylene-C [86]. The µLEDs are separated by 700 µm to ensure enough illumination field distinction. The FF-WIOS SoC was fixated in the center of the substrate for wire bonding, following which it was protected with ultraviolet-cured medical grade epoxy, while capacitors were mounted on the periphery of the SoC die using silver conductive epoxy (MG Chemicals 8331). The wire-wound Rx coil was then mounted around the SoC die and its terminals were connected to one of the SMD capacitors by silver

conductive epoxy to form the $L_{Rx}C_{Rx}$-tank, resonating at the power carrier frequency. Finally, the FF-WIOS device is sealed with Parylene-C and PDMS.

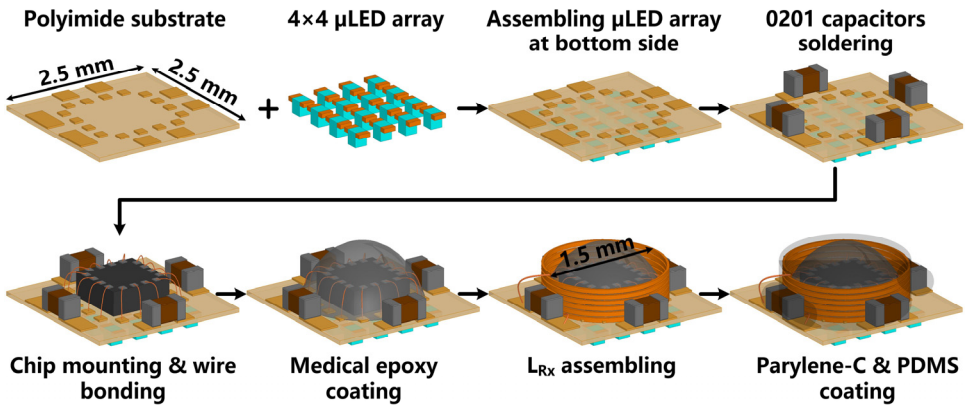

Figure 5.2. The fabrication and micro-assembly process of the FF-WIOS device.

5.1.1 Circuit Details

The overall block diagram of the FF-WIOS SoC is shown in Figure 5.3. Major challenges in the design of FF-WIOS circuitry include small input power from L_{Rx} due to its weak couplings with L_{Tx} and L_{Res}, and safety limit on the SAR [32]. On the other hand, instantaneous output power to µLEDs needs to be large enough for the resulting light intensity to surpass the optogenetic stimulation threshold [61]. High efficiency should also be maintained at every step from the PA to the µLED array to minimize heat generation. To address the issues, we adopted the wireless SCS architecture in [136], and modified it for this particular application. A built-in charger of a voltage double periodically charges a storage capacitor, C_{LED}, from the inductive link. A charge control unit sets the target charging voltage at 5 V. During stimulation, C_{LED} is detached from the charging cell and delivers its stored charge to the selected µLED through positive and negative terminal selector without loading the inductive link. A current limiter is added to limit the maximum current flowing through the target µLED. To control the timing of C_{LED}

charging/discharging, a timing control block is designed based on the Schmitt trigger in [139] and utilized for generating reference clocks, *CLKs*, and a stimulation enable signal, Stim, which pulse width and frequency are adjustable [137]. In the power management, the voltage doubler, following $L_{Rx}C_{Rx}$-tank, generates a DC voltage, V_{DBR}, while the other sub-blocks generate supply voltage, V_{DD}, and reference voltages and currents [137]. In the forward data telemetry, a PPM-CDR circuit recovers synchronized clock/data from the OOK modulated coil voltage, V_{COIL}, setting a 12-bit shift register through a serial-to-parallel (S2P) converter with 10-bit pre/post-amble data [136], [137]. LSK back telemetry is adopted for CLPC of the FF-WIOS by sensing V_{DBR} [24], [136].

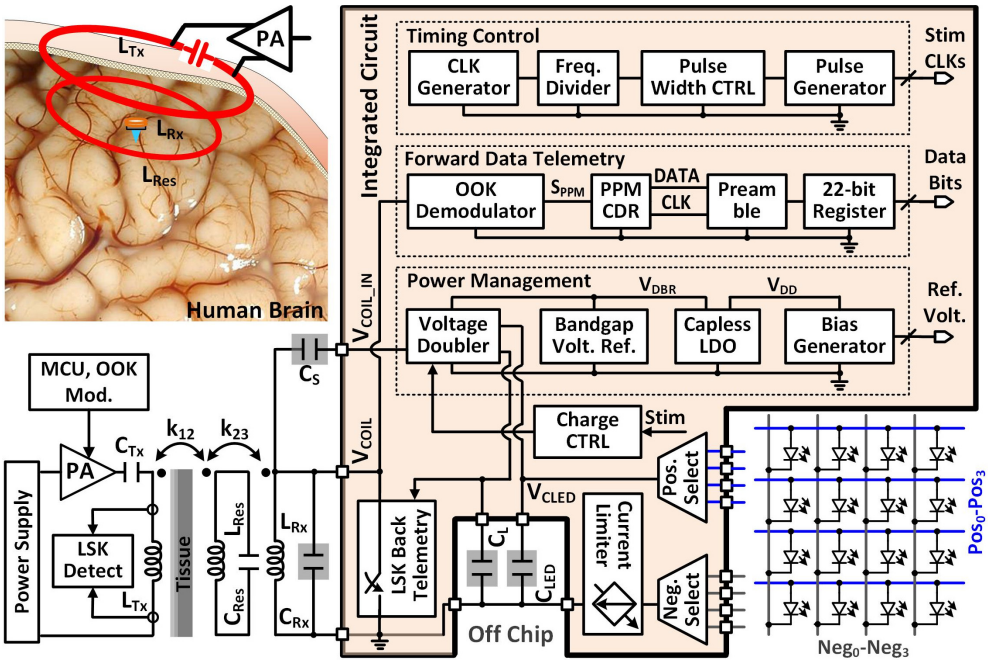

Figure 5.3. A simplified system architecture of the FF-WIOS SoC.

The 60 MHz power carrier induces a V_{COIL} across the $L_{Rx}C_{Rx}$-tank, which is rectified and regulated by the voltage doubler and cap-less LDO blocks, respectively, as shown in Figure 5.4a. The built-in charger is controlled by the Stim input, which turns P_4 on and N_2 off when it is lowered. During stimulation, *Stim* = '1', the charger is disabled to avoid V_{DD}

drop, while C_{LED} is connected to the stimulation sites. We adopt dynamic body biasing with two pairs of auxiliary transistors, automatically connecting the body voltage of P_1 and P_5 to the highest potential [136]. To reduce the number of off-chip components, a cap-less LDO is utilized to generate a stabilized V_{DD} = 1.8 V for the rest of SoC.

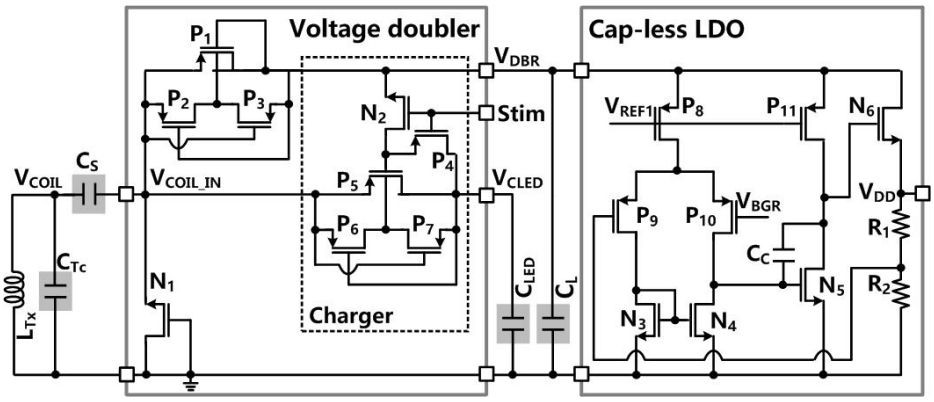

(a)

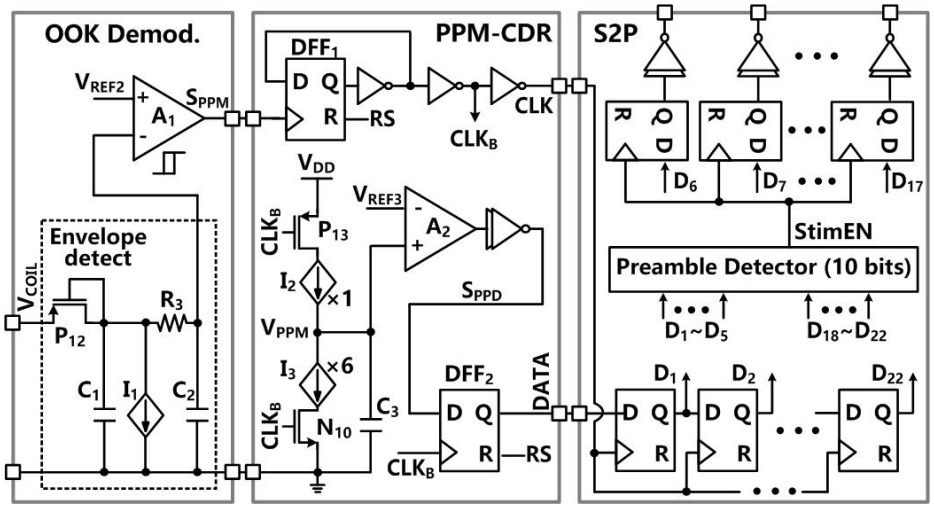

(b)

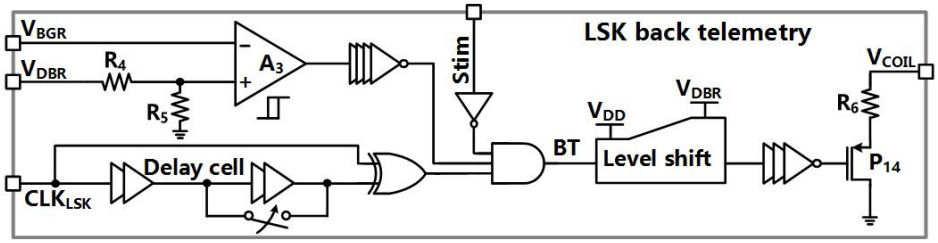

(c)

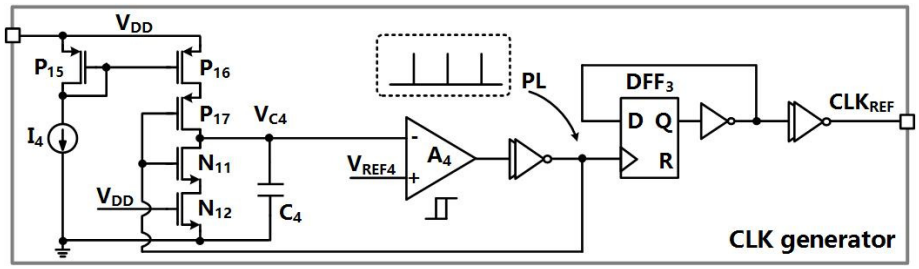

(d)

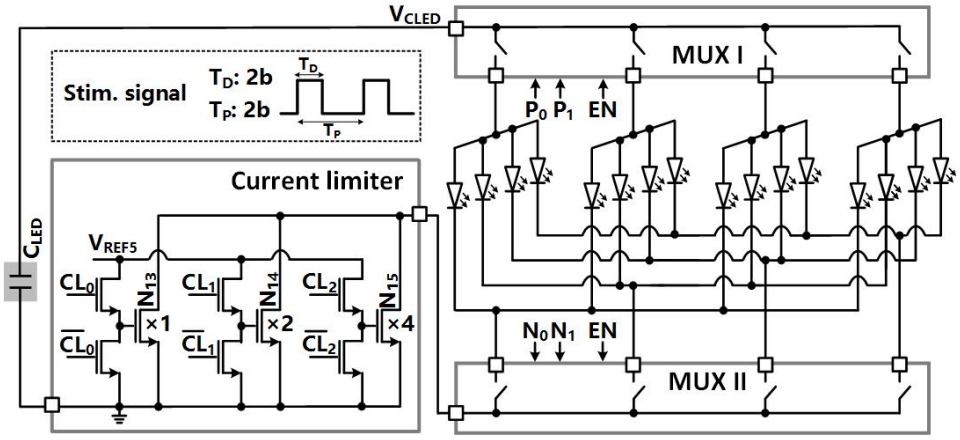

(e)

Figure 5.4. Schematic diagrams of (a) voltage doubler with built-in charger and cap-less LDO, (b) forward data telemetry with OOK modulation, (c) LSK back telemetry, (d) clock generator, (e) current limiter and stimulation output stage.

Figure 5.4b shows the schematic diagram of the OOK-based forward data telemetry block, adopted from [136]. In the OOK demodulator, V_{COIL} is low-pass filtered by an envelope detector, following which OOK pulses are recovered by a hysteresis comparator, A_1, when compared with V_{REF2}, to provide the PPM signal, S_{PPM}. In the PPM-CDR block, S_{PPM} is converted to clock, *CLK*, using a frequency divider. *CLK* controls the charging and discharging of C_3, which generates a triangular waveform, V_{PPM}. If positioning ratio among three consecutive S_{PPM} pulses is 4:1, V_{PPM} exceeds V_{REF3} during *CLK* = '1', leading to *DATA* = '1'. Otherwise, *DATA* = '0', if the positioning ratio is 1:4. In the S2P, the recovered data, *DATA*, is shifted by *CLK* into a buffer. Once the pre/post-amble data bits (D_1-D_5, D_{18}-

D_{22}) are matched with a pre-defined 10-bit value, a flag, $Stim_{EN}$, will be raised and then the data bits (D_6-D_{17}) will be saved in registers to set the stimulation parameters.

LSK back telemetry is adopted for CLPC of the FF-WIOS. This is a key mechanism for practical implementation in the face of headstage (basically L_{Tx}) and brain motion artifacts, as well as uneven brain surface morphology, e.g. gyri and sulci, in larger species. Considering requirements for the CLPC stability in [107], [140], we have chosen a 160 Hz clock, CLK_{LSK}, to control the timing of back telemetry pulse, *BT*, which results in a *BT* data rate of 160 bps.

In Figure 5.4c, the pulse width of *BT* (1 µs or 2 µs) is decided by the number of delay cells that are engaged in generating this pulse. The resistive divider, R_4 and R_5, sets the maximum V_{DBR} at 4.2 V. When the divided V_{DBR} exceeds the bandgap reference voltage, V_{BGR}, *BT* pulses are generated to short L_{Rx} by closing P_{14} switch, resulting in increasing L_{Rx} Q-factor, as well as the voltage across and current through L_{Tx}.

Figure 5.4d shows the schematic diagram of the clock generator for the timing of charging and stimulation. A control signal, *PL*, at the output of a hysteresis comparator, A_4, controls the timing and amplitude of V_{C4} by charging C_4, in the phase of *PL* = '0'. Once V_{C4} reaches V_{REF4}, *PL* is set to '1' to discharge C_4 in a short period, generating a single narrow *PL*, which is converted to a reference clock, CLK_{REF}, through a frequency divider.

In Figure 5.4e, a µLED is selected from the 4×4 µLED array by specifying the positive/ negative terminals of the µLED through a pair of 4:1 MUXs. The current limiter, consisting of a pair of 3-bit current sinks with binary-weighted transistors, can adjust the maximum current limit and the light output of the activated µLED.

5.1.2 3-Coil Inductive Link Design

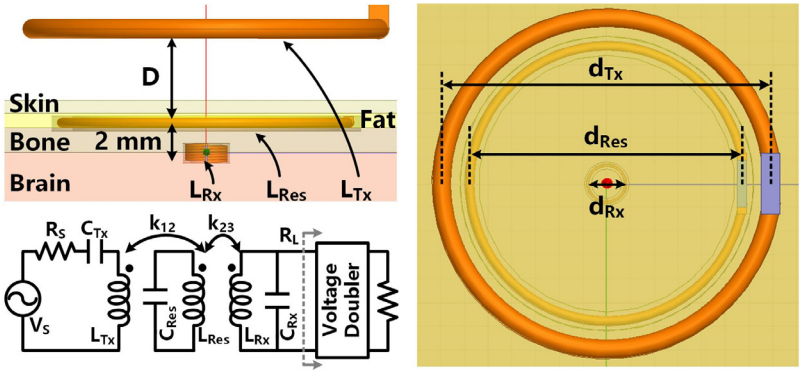

Figure 5.5. The model of the 3-coil inductive link with tissue layers in HFSS and the circuit equivalent model

A 3-coil inductive link[11] model with surrounding tissue layers of a rodent model was constructed in HFSS for the coil optimization. In Figure 5.5, L_{Tx} is placed above the head, while L_{Res} and L_{Rx} are implanted above and under the skull, respectively. Using a high Q-factor L_{Res} can significantly improve and homogenize the EM field over the area encompassed by L_{Res}. To complete the HFSS model, L_{Res} and L_{Rx} are coated with 50 µm PDMS and 5 µm Parylene-C for bio-compatibility. A simplified equivalent circuit model of the inductive link is shown in Figure 5.5 as well. The power conversion efficiency (PCE) of passive AC-DC converters, such as rectifiers and voltage doublers, which use diode-connected transistors, degrades at higher frequencies due to the parasitic capacitance [141], [142].

Considering the effects of surrounding tissue and PCE of the voltage doubler that loads L_{Rx} [27]-[31], Figure 5.6 shows an algorithm, which generates the optimized coil specifications and operating frequency that would maximize PTE×PCE. Because PTE is obtained by taking into account the loading effect of the voltage doubler, which is reflected through the PCE, it is fine to simply multiply PTE and PCE at each frequency.

[11] I would like to thank Dr. Abdollah Mirbozorgi for the stimulating discussions about the 3-coil inductive link design and optimization.

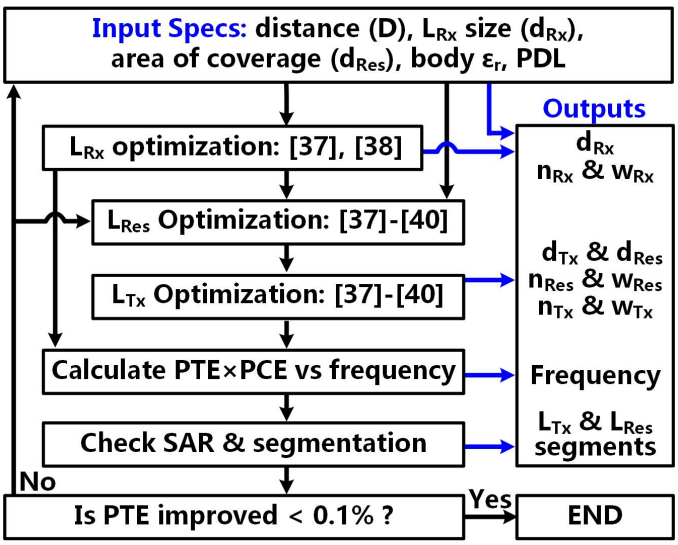

Figure 5.6. The flowchart of algorithm for the 3-coil inductive link optimization.

Other considerations are the application and fabrication constraints, which are the input parameters to the algorithm, including the distance between L_{Tx} and L_{Res}, D, L_{Rx} diameter, d_{Rx}, L_{Res} diameter, d_{Res}, and PDL. The equivalent load, R_L, was set to 4.6 kΩ based on a maximum PDL of 2.7 mW at 5 V_{peak} across L_{Rx}, which is imposed by the process. Based on [27] and [28], L_{Rx} optimization corresponds to maximizing the efficiency of L_{Rx} power reception under a given magnetic field exposure. We maximize the effective area of L_{Rx} to increase magnetic flux passing through it. Implementation of L_{Rx}, however, should not enlarge the size of FF-WIOS. As a result, L_{Rx}, made by AWG 34 magnet wire, encompasses the silicon die, resulting in d_{Rx} of 1.6 mm, wire thickness, w_{Rx}, of 0.16 mm, and n_{Rx} = 6 number of turns. In our application, we expect to observe light-evoked neural activities from V1 following the optical stimulation performed by the FF-WIOS. According to [143], approximately 0.5-5 mm lateral of skull midline overlays V1 in one side lobe. L_{Res} was designed to encompass the V1 area in both left and right lobes. Considering a margin, $d_{Res} \geq 11$ mm was selected. The wire thickness, w_{Res}, and the number of turns, n_{Res}, were selected considering the limited space for L_{Res}, its Q-factor, and coupling

coefficient between L_{Res} and L_{Rx}. The result was a single-turn coil made of 0.4 mm (AWG 26) magnet wire.

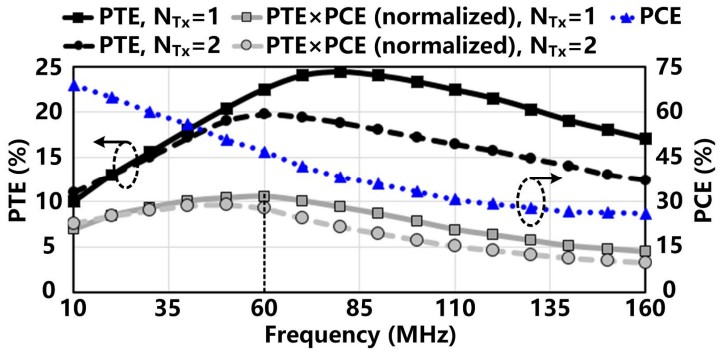

Figure 5.7. HFSS simulation results for PTE of the 3-coil inductive link vs. power carrier frequency and n_{Tx}, simulated PCE of the voltage doubler as a function of frequency, and normalized PTE×PCE vs. frequency and n_{Tx}.

The distance between L_{Tx} and L_{Res}, D, is determined by the thickness of various tissue layers, depending on the anatomical position of the FF-WIOS. For the rodent model, we considered the thickness of skin and fat to be 5 mm at most. The optimal size of L_{Tx} is directly related to D and is calculated for maximum coupling between L_{Tx} and L_{Res} using equation (4) in [28]. L_{Tx} is made of 0.8 mm (AWG 20) magnet wire for high Q-factor. It is relatively easier to fine-tune L_{Tx} parameters compared to those of L_{Rx} and L_{Res}. To find the best the number of turns, n_{Tx}, PTE of the 3-coil link is simulated from 10 MHz to 160 MHz for 1- and 2-turn L_{Tx} in Figure 5.7. The PTE with 2-turn L_{Tx} is lower across the entire frequency range, and its peak occurs at lower frequency. As a result, L_{Tx} is designed as a single-turn coil. The PCE of the voltage doubler is yet another key factor in determining the overall efficiency of the power delivery path. In Figure 5.7, the PCE of the voltage doubler drops sharply as the frequency increases because of parasitic capacitors of the diode-connected transistors. The best operating frequency was decided based on the peak value of PTE×PCE, which appears at 60 MHz with the 1-turn L_{Tx}.

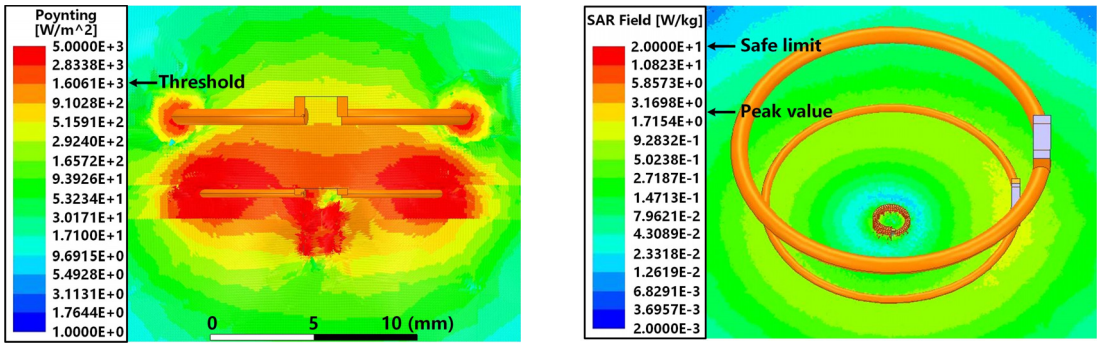

(a) (b)

Figure 5.8. (a) Poynting vector and (b) local SAR simulations in HFSS.

Figure 5.8a shows the directional power flux density, i.e. the rate of power transfer per unit area, using Poynting vectors. The power density varies from 1 to 5×10^3 W/m^2 when the input power level is set at 12.86 mW to deliver a target PDL of ~2.7 mW to the FF-WIOS. The threshold marked on the vertical column indicates the required power flux density to deliver PDL ≥ 2.7 mW. The area where L_{Rx} is to be located is above the threshold, indicating sufficient received power. L_{Res} and L_{Rx} are concentrically aligned with L_{Tx} in this model. In terms of PTE vs. horizontal misalignment, this arrangement is considered the worst-case scenario for L_{Rx}, as demonstrated in [28]. Since the 3-coil inductive link provides sufficient PDL in the worst-case scenario, and the Poynting vector in Figure 5.8a shows higher EM power density close to the perimeter of L_{Res}, the entire area within L_{Res} is indeed covered with sufficient PDL. Concerning the exposure to EM field and heat generation in the tissue, Figure 5.8b presents the HFSS simulation of the local SAR for different tissue layers under the same power source setting. Simulation results show that the maximum local SAR is ~2.78 W/kg, which is well below the safety limit of 20 W/kg.

5.2 Experimental Measurements

5.2.1 3-Coil Inductive Link Implementation

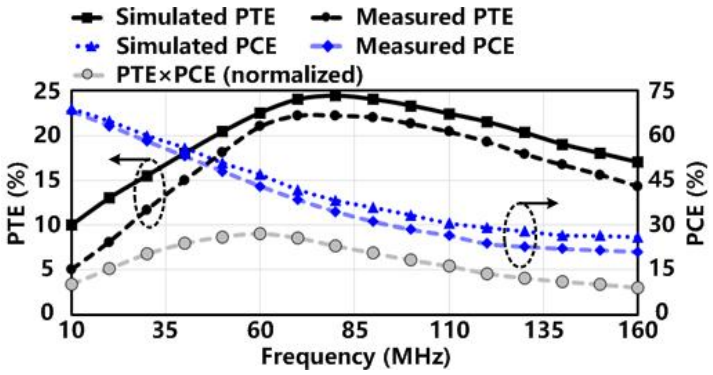

Figure 5.9. PTE of the 3-coil inductive link and PCE of the voltage doubler in both simulation and measurement as a function of frequency, and normalized PTE×PCE based on the measurement results.

Table 5.1. Measured specifications of the 3-coil inductive link at 60 MHz.

Coil	Tx	Resonator	Rx
Inductance (nH)	26	21.2	50.1
Resistance (Ω)	0.04	0.1	0.85
Quality factor (Q)	246	79	22
Diameter (mm)	14.3	11.6	1.6
Number of turns	1	1	6
Wire gauge	AWG 20	AWG 26	AWG 34
Separation (mm)	$D_{Tx\text{-}Res} = 5$		$D_{Res\text{-}Rx} = 2$
PTE		21%	
Carrier frequency (f)		60 MHz	

A 3-coil inductive link was implemented using the optimized geometries from Section IV. The PTE of the inductive link and the PCE of the voltage doubler were measured, respectively, and compared with simulations in Figure 5.9, as a function of frequency. The PTE×PCE was also calculated, normalized, and added in Figure 5.9. Measurements have good agreement with simulation results. The lower PTE in measurements can be attributed to the tissue effect on L_{Res}. Its high Q-factor is affected by the large contact area with the surrounding tissue and makes it sensitive to detuning. The difference between the measured and simulated PCEs could be due to process variation and parasitic effects of the measurement instruments. The parasitic inductance and capacitance from the probes cause distortion in the measured waveforms at higher

frequencies, resulting in further reduction in the measured PCE. The key point here is that the optimal carrier frequency to achieve maximum PTE×PCE is still at 60 MHz, as expected from simulations and design target. After fine tuning the optimal inductive link parameters *in vitro* using fresh tissue from sheep head, they were determined and summarized in Table 5.1.

5.2.2 Bench-top Characterization

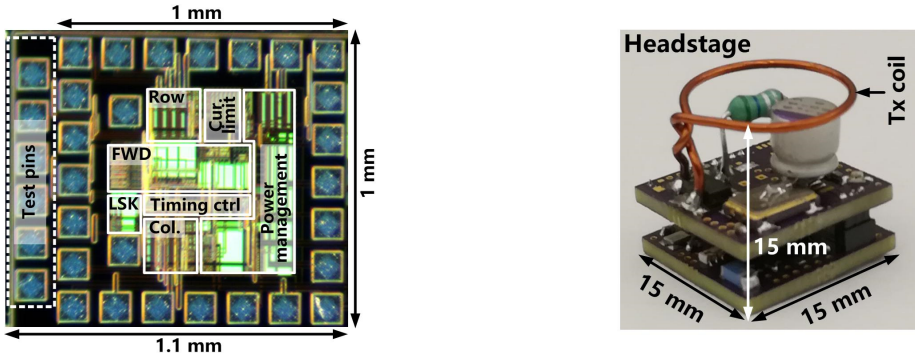

(a) (b)

Figure 5.10. (a) The micrograph of the FF-WIOS SoC and (b) implementation of the prototype headstage with the Tx coil.

The FF-WIOS SoC was fabricated in the TSMC 0.35-µm 4M2P standard CMOS process, occupying a 1×1 mm^2 footprint including pads, as shown in Figure 5.10a. With additional test pins, the die area is 1.1×1 mm^2.

Figure 5.10b shows a prototype headstage, which consists of two stacked PCBs, together with L_{Tx}, fitting in a 15×15×15 mm^3 cube. The headstage, made of COTS components, not only drives L_{Tx} by its PA but also operates the CLPC [144]. The envelop detector block in the headstage, which has been explained in [144], is used to recover the *BT* pulses. The resulting signal is then detected by the headstage MCU. Similar to [107], [140], the headstage decreases the PA supply voltage, V_{PA}, when it detects the *BT* pulses.

Otherwise, V_{PA} is continually increased by default at an adjustable rate. In steady state, V_{PA} bounces within a range to stabilize V_{DBR}.

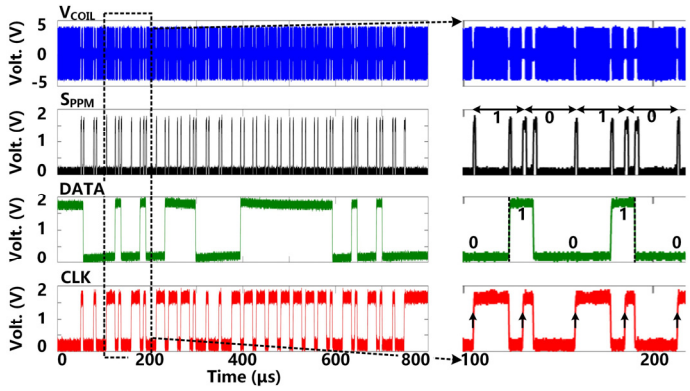

(a)

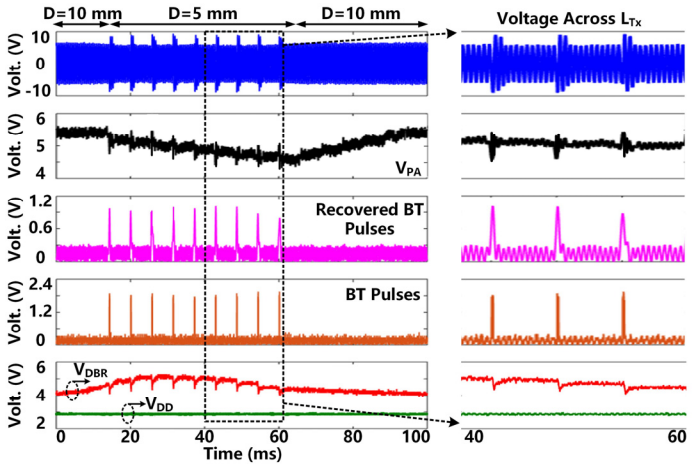

(b)

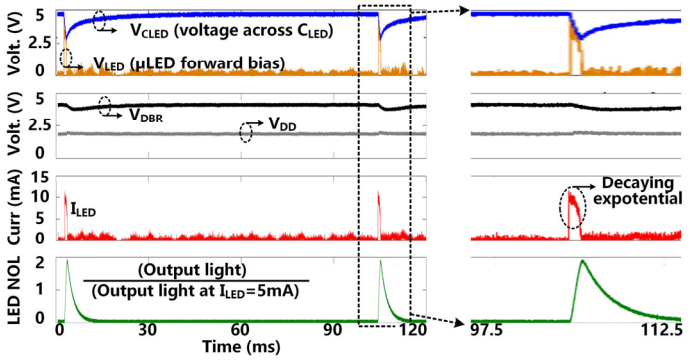

(c)

Figure 5.11. Measured results of (a) forward data telemetry, (b) back telemetry for CLPC, and (c) charging and stimulation.

Figure 5.11a shows the measurement results of the forward data telemetry. V_{COIL} is OOK-demodulated to generate S_{PPM}, which is converted to synchronized 50 kbps *CLK* and *DATA* by PPM-CDR. In the close-up view, S_{PPM} with pulse position ratio of 4:1 generates *DATA* = '1'. On the contrary, when the positioning ratio is 1:4, *DATA* = '0'.

Figure 5.11b shows the CLPC operation when the headstage is moved manually from D = 10 mm to 5 mm and then back to 10 mm. As the headstage gets closer to the FF-WIOS, *BT* pulses are generated when V_{DBR} is larger than a certain threshold, indicating that there is more than enough power available to the FF-WIOS. In response, voltage across L_{Tx} increases, and the CLPC starts reducing V_{PA} to compensate for this perturbation. V_{PA} decreases by 1 V in 8 steps, resulting in the step size of 0.125 V. It takes ~60 ms for V_{DBR} to return back to 4.2 V. As the headstage moves back to its original location, V_{PA} starts to increase in the absence of *BT* pulses. During the short switching period of L_{Rx}, the FF-WIOS SoC is powered by the stored charge in C_L, and V_{DD} remains stable at 1.8 V.

Figure 5.11c shows the charging and discharging of the 10 µF C_{LED} to generate optical stimulation with 2 ms pulse width at 10 Hz. The µLED current, I_{LED}, is limited to 10 mA. Once stimulation starts, C_{LED} discharges in the target µLED with a decaying exponential current. V_{DBR} shows a slight drop (0.45 V), which is much less than V_{CLED} (voltage across C_{LED}), and remains above the minimum level (2.6 V) required for V_{DD} not to be affected by its variations. The emitted light from µLED (0.5×1×0.4 mm^3, LB QH9G, OSRAM) during stimulation pulse was collected by the photodetector (Newport 883-SL) of an optical power meter (Newport 1835-C). The NOL expectedly follows the stimulation current variation but with a slight delay. After each stimulation, C_{LED} is recharged back to the target voltage within 30 ms.

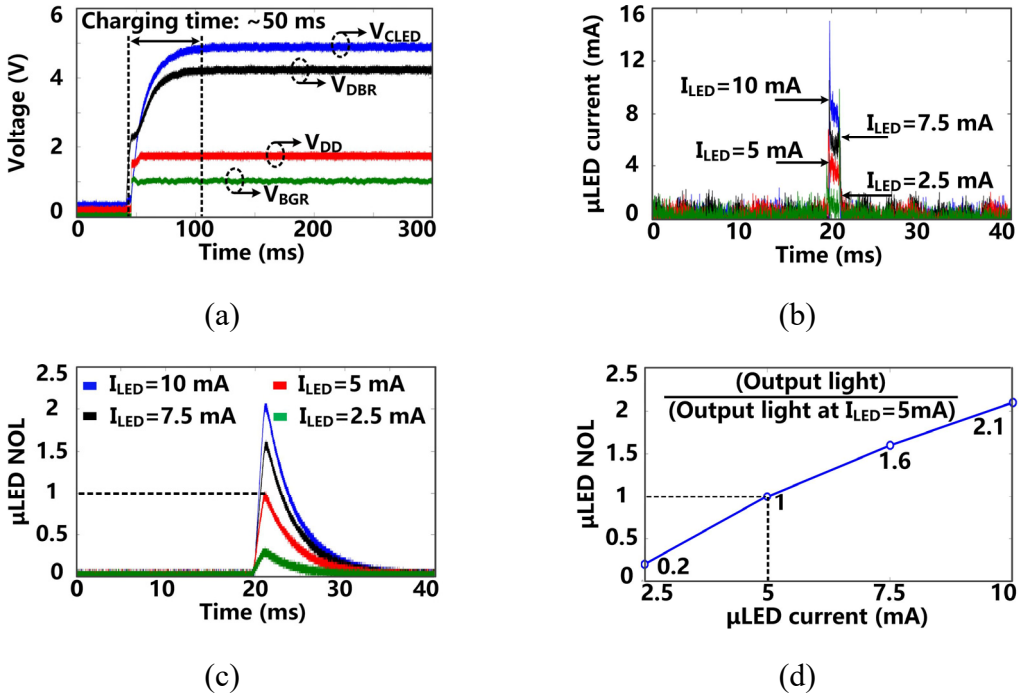

Figure 5.12. (a) Starting up transients of the power management block, (b) measured µLED current at 4 stimulation current settings, and NOL as a function of (c) time and (d) µLED current.

Following startup, as shown in Figure 5.12a, it takes ~50 ms for V_{DBR} and V_{CLED} to stabilize at their steady-state target voltages. Before this, V_{DD} and V_{BGR} have already been stabilized within 20 µs at 1.8 V and 1.2 V, respectively. The µLED current under 4 different settings was measured from the voltage across a 10 Ω current-sensing resistor in series with the µLED. In Figure 5.12b, I_{LED} increases from 2.5 mA to 10 mA in a 2.5 mA step according to the design specifications. The µLED output light during a stimulation pulse is also measured at each current level with 2 ms pulse width at 10 Hz, as shown in Figure 5.12c. To validate measurement results with the µLED datasheet, we normalized the output light by the peak value of the light intensity (4.8 mW/mm^2) under 5 mA current. Figure 5.12d shows that NOL intensities under different currents match with specifications of the µLED [145]. FF-WIOS SoC characterizations are summarized in Table 5.2.

Table 5.2. Measured specifications of the FF-WIOS SoC.

Overall system	
ASIC area	ASIC area
Power with stimulation	Power with stimulation
Power without stimulation	Power without stimulation
Voltage doubler efficiency	Voltage doubler efficiency
Switch capacitor-based stimulation	
Target voltage	Target voltage
Charging efficiency	Charging efficiency
Charging time	Charging time
C_S / C_{LED} / C_L	C_S / C_{LED} / C_L
Optical stim. efficiency	Optical stim. efficiency
Stimulation parameters	
Stimulation frequency	Stimulation frequency
Pulse width	Pulse width
Current limiter	Current limiter
Forward and back data telemetry	
Data bits	Data bits
Pre/post-amble bits	Pre/post-amble bits
PPM data rate	PPM data rate
LSK data rate	LSK data rate
BT pulse width	*BT* pulse width

5.3 *In Vivo* Experiments

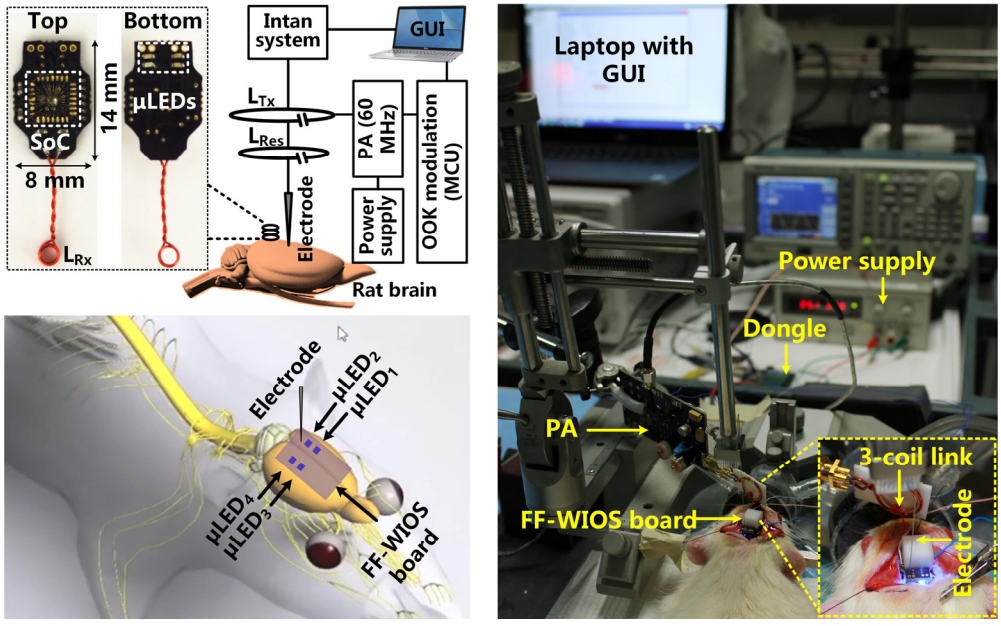

Figure 5.13. *In vivo* experimental setup with its block diagram and anatomical location of the FF-WIOS board, electrode, and μLEDs on the rat brain.

In vivo experiments[12] were conducted to verify the efficacy of the FF-WIOS to optically evoke neural activities in the V1 of anesthetized rats. One male and one female adult rat (Sprague Dawley, 600-650 g) were tested based on our established protocols approved by the IACUC at Michigan State University [83]. Using the stereotaxic surgery protocol in [83], adeno-associated virus (AAV) that carries optogenetics opsin (AAV-hSyn-hChR2 (H134R)-mCherry; UNC Vector Core) was injected bilaterally into the rat's V1. Post injection, the rats were housed in the animal facilities for 4 weeks till the V1 neurons express ChR2 [83]. Then the animals were subjected to *in vivo* experiments. A modified FF-WIOS system was used in these experiments to facilitate the acute animal studies. The FF-WIOS board (14×8 mm^2), shown in Figure 5.13, consisted of an FF-WIOS SoC bonded on the top side, a 2×2 μLED array (0.5×1×0.4 mm^3, LB QH9G, OSRAM) assembled on the bottom side, and LRx soldered at the back-end. A Class-E PA delivered power wirelessly to the FF-WIOS board through the optimized 3-coil inductive link at 60 MHz. The FF-WIOS board was placed over the skull of the rats with two μLEDs aligned over each side of V1 lobe. More specifically, μLED_1 and μLED_2 were above the left V1, while μLED_3 and μLED_4 were above the right V1. Under anesthesia, unilateral optical stimulation was performed on the left V1 by selectively driving μLED_1 with user-defined parameters, while LFPs were simultaneously recorded through a tungsten electrode, which penetrated into the left V1 cortical layers. The LFP recordings were amplified and digitalized through a commercial 32-ch Intan system (RHD2132), and then uploaded to a PC for data analysis using a MATLAB Chronux toolbox.

Figure 5.14 shows LFPs recorded at the depths of 100 μm, 500 um, and 1 mm, following light stimulation directed with a pulse train of 2 ms pulse width, 2.5 Hz

[12] I would like to thank Dr. Wen Li, Dr. Arthur Weber, and Wasif Khan for their great collaborations on the *in vivo* experiments.

frequency, and 10 mA stimulation current. Clear light-evoked LFPs were observed at the ~100 µm depth, in response to the optical stimulation, whereas the LFP variation decreases as the recording depth increases. This result reveals that the optical stimulation applied by the FF-WIOS can evoke the neurons in superficial layers.

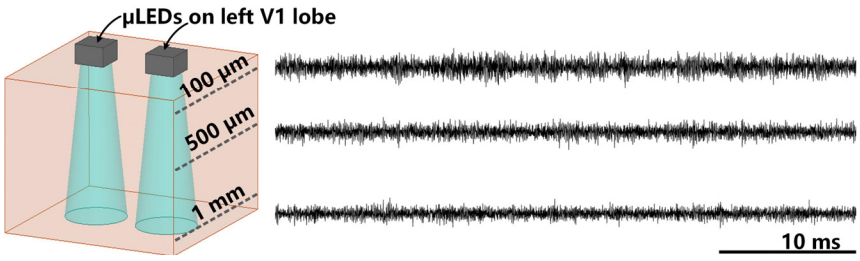

Figure 5.14. LFP recordings at different depths through the tungsten electrode.

At the effective stimulation depth of 100 µm, LFPs were measured when the µLED light intensity is above and below the threshold of 1 mW/mm^2 [61]. The stimulation pulses have 2 ms pulse width at 2.5 Hz with 10 mA and 2.5 mA current limits, corresponding to the light intensity of ~10 mW/mm^2 and ~0.95 mW/mm^2, respectively. Spontaneous LFPs were also recorded as a baseline when µLEDs were completely off. We expected to observe light-evoked LFPs, i.e. synchronized with above-threshold stimulation, being distinguishable from the LFPs uncorrelated with below-threshold stimulation.

LPF recordings recorded at different light intensity are compared in Figure 5.15a over a time span of 50 s. The stimulation flags in the close-up view of 1 s long LFP recordings indicate the occurrence of a stimulation pulse. Photoelectric artifacts induced from light stimulation came along with the LFPs [7], [8]. The recorded LFPs with below-threshold stimulation is not evoked as compared to the spontaneous LFPs, while with 10 mA stimulation current, the recorded LFPs show significantly larger variations, suggesting that the above-threshold stimulation can effectively evoke neural activity.

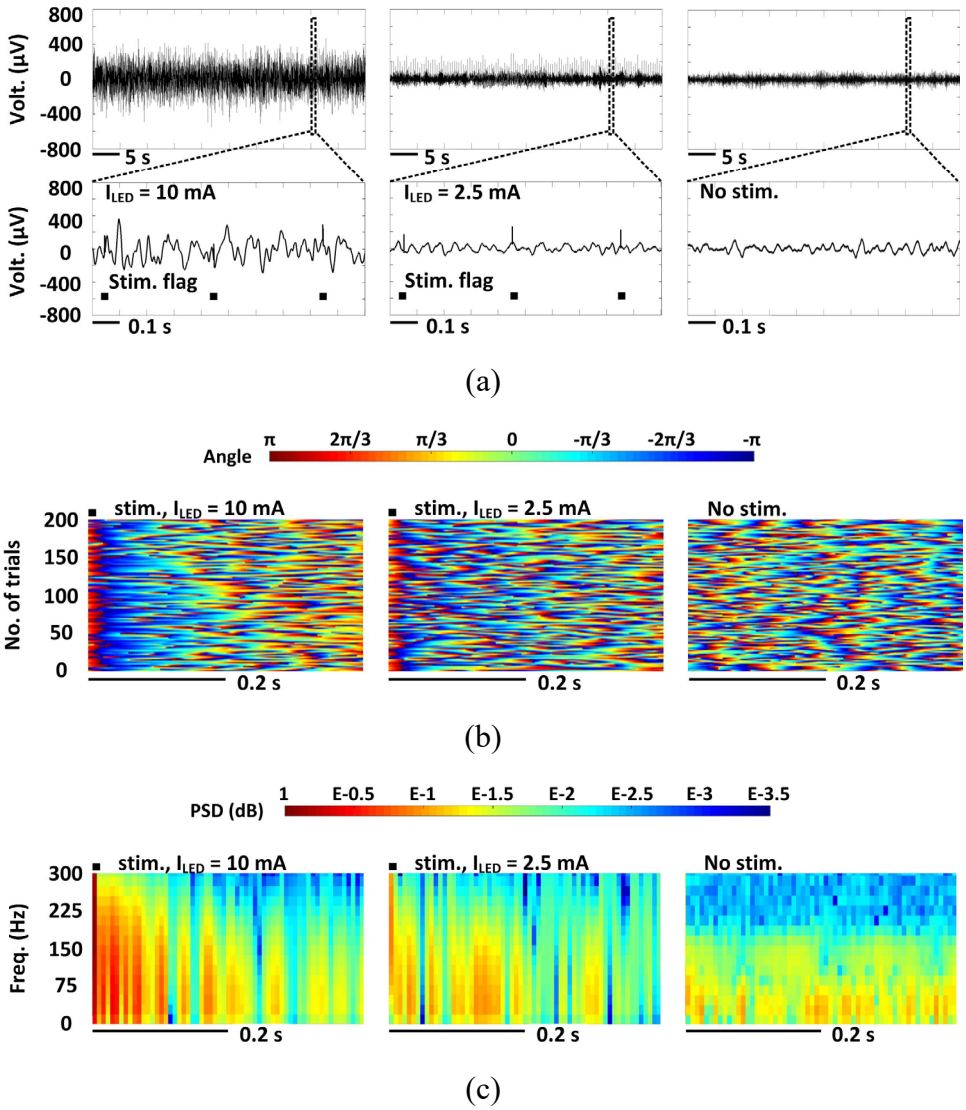

Figure 5.15. LFP analysis in terms of (a) amplitude variation, (b) instantaneous phases, and (c) normalized PSD with above threshold stimulation (left), below threshold stimulation (middle), and no stimulation (right).

The Hilbert transformation was applied to extract the instantaneous phases of 200 trials of LFP recordings within a frequency range of 1-25 Hz [83], [91]. The instantaneous phase of individual trial is color coded, aligned to the concurrence of the stimulus, and stacked as shown in Figure 5.15b. Expectedly, the spontaneous LFPs with random phases did not show phase synchrony. Very short phase synchrony was observed at the 2.5 mA stimulation current, which could be the effect of photoelectric artifacts. In contrast, strong

and reliable phase-locked synchronization was observed across 200 trials within a time window of ~100 ms following the optical stimulation at 10 mA current ($p < 0.05$, Wilcoxon signed rank test).

Furthermore, 200 trial LFPs were averaged and mapped onto a time-frequency graph of color-coded, normalized PSD distribution [83], [90]. Figure 5.15c shows the PSD results in a 1-300 Hz frequency range, where a significant increase in PSD was observed in a short time window of ~100 ms following the optical stimulation of 10 mA. In contrast, stimuli at 2.5 mA only caused a slight increase in PSD as compared to the PSD of the spontaneous LFPs, which can be mainly attributed to the photoelectric artifacts.

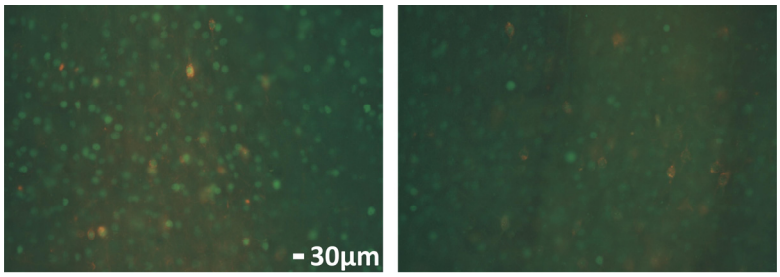

(a)

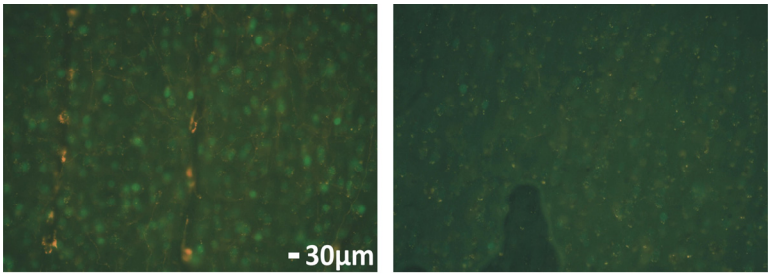

(b)

Figure 5.16. C-Fos expression in left and right V1 lobes of (a) rat #1 and (b) rat #2.

In addition to LFPs, immunochemical analysis was performed to identify the increased expression of c-Fos as an indirect measure of light-evoked neuronal activity induced by optical stimulation [83], [146]. In this experiment, the left V1 lobes of both rat

#1 and #2 were stimulated optically for 45 mins, with 2 ms pulse width, 2.5 Hz pulse rate, and 10 mA stimulation current, while the right V1 was untouched as a control. Figure 5.16 shows the fluorescent microscope images of the post-processed brain tissue with a thickness of 50 µm. Green fluorescence spots indicate cells expressing c-Fos, while orange spots are m-cherry stained cells that are expressing optogenetic opsins (ChR2). The tissue analysis results show a significant increase in the c-Fos expression under 10 mA stimulation, implying elevated neural activity. In contrast, only a slight increase in the c-Fos expression was observed at the 2.5 mA current, most likely representative of background activity since both of the rats' eyes were open during testing [83]. Moreover, the overlapping of the cells expressing both m-cherry and c-Fos reveals that the same transfected cells express increased activities induced by the above-threshold optical stimulation.

5.4 *In Vitro* Experiments

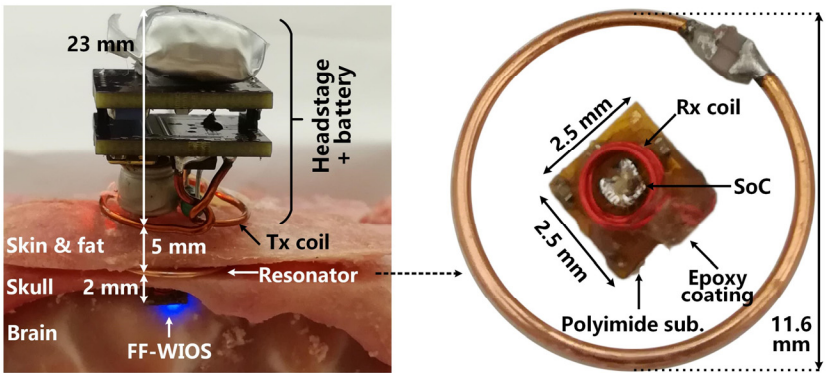

Figure 5.17. *In vitro* measurement setup using the sheep model with a close-up view of the FF-WIOS and the resonator.

Figure 5.17 shows the *in vitro* setup using tissue layers in a cube cut out of a sheep head, including brain, skull, fat, and skin for preliminary evaluation of the system operation. The headstage, powered by a 100 mAh rechargeable LiPo battery, weights 4.2

g. The assembled FF-WIOS and L_{Res} are encapsulated with 5 µm Parylene-C and ~50 µm PDMS before implantation. The FF-WIOS implant, with dimensions and weight of 2.5×2.5×1.5 mm^3 and 15 mg, respectively, is placed on the surface of the brain, while L_{Res} is placed above the skull but under the scalp, well aligned with and 2 mm away from the FF-WIOS implant. Between L_{Tx} and L_{Res} is the skin and fat layers of scalp with a total thickness of 5 mm. The headstage is placed above the skin and concentrically aligned with L_{Res}. In this setup, the headstage delivered sufficient power to operate the FF-WIOS by driving a selected µLED (blue color), while the MCU established BLE link with PC and OOK modulated the power carrier, resulting in 97.6 mW drawn from the 3.7 V battery.

5.5 FF-WIOS2 SoC

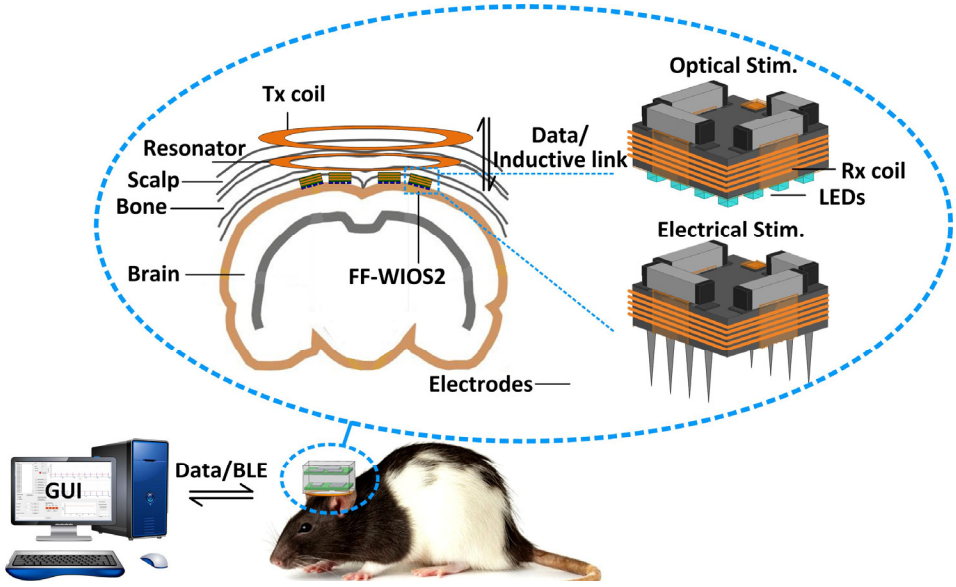

Figure 5.18. Conceptual view of the system setup for operating multiple FF-WIOS2 devices, distributed on a freely moving rat brain.

Generally speaking, the main constrains for the tiny IMDs in the distributed architecture are space, power budget, and functionality. New architectures should be explored to reach the best compromise among the conflicting space-power-functionality

trade-offs. Building upon our previous work in [137], we are demonstrating a SoC design as the next step in our quest towards a mm-sized free-floating wirelessly-powered implantable opto-electro stimulation (FF-WIOS2) device. It can support a total of 16-ch optical stimulation and 4-ch electrical stimulation, which to the best of our knowledge, is the most comprehensive mm-sized neuromodulation device ever reported. Figure 5.18 shows the conceptual view of the wirelessly-powered multiple FF-WIOS2 devices distributed on the surface of a freely behaving rat brain. Figure 5.18 presents two variations of the FF-WIOS2, one for optical and the other one for electrical stimulation. The FF-WIOS2 employs the silicon die as a substrate to carry four off-chip SMD capacitors. A polyimide film, which carriers either a μLED array for optical stimulation or a MEA for electrical stimulation, is attached to the back side of the silicon die, and folded over to connect to the pads on top of the silicon die.

5.5.1 FF-WIOS 2 SoC Overview

The FF-WIOS2 SoC block diagram is shown in Figure 5.19. The FF-WIOS2 SoC operation involves charging, delay, and stimulation. A voltage doubler periodically charges a storage capacitor, C_S, from the inductive link up to a voltage that is set by the back telemetry. At the onset of stimulation, C_S is detached from the charger, and dumps its charge through four MUXs that form an H-bridge to pass the current through a designated μLED or a pair of electrodes, while a current limiter sets an upper bound to the stimulus amplitude. The stimulation pulses are adjustable in pulse width and frequency with two control bits for each parameter. An active CB circuit measure the amount of charge injected in each direction by observing the voltage drop across C_S, and dynamically changing the stimulus pulse width to neutralize the residual charge in the tissue. A passive CB switch

shorts the selected pair of electrodes after stimulation to further eliminate any residual charge.

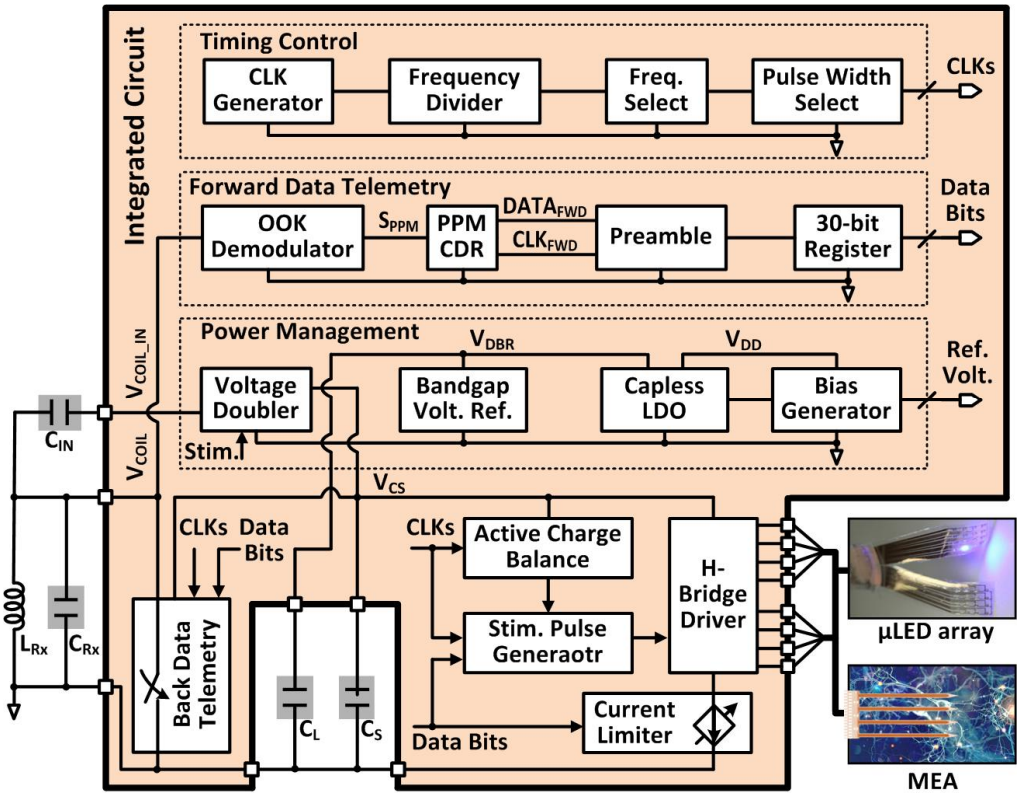

Figure 5.19. Block diagram of the FF-WIOS2 SoC architecture.

The stimulus driver, shown in Figure 5.20, employs four 4:1 MUXs in an H-bridge configuration with a current limiter. The MUXs select a pair out of four active and four return sites by control signals AC_1-AC_2 and RE_1-RE_2, respectively. In optical stimulation mode, current flows only in one direction by MUX_1-MUX_4 group. In electrical stimulation mode, however, both pairs of MUXs are utilized alternatively to generate anodic and cathodic stimulation phases in opposite directions. A µLED or a pair of electrodes is selected out in row-column format. The current limiter, consisting of a 3-bit programmable current sink with binary-weighted transistors, is controlled by CL_0-CL_2. The switch, S_{CB}, is utilized for passive CB after stimulation.

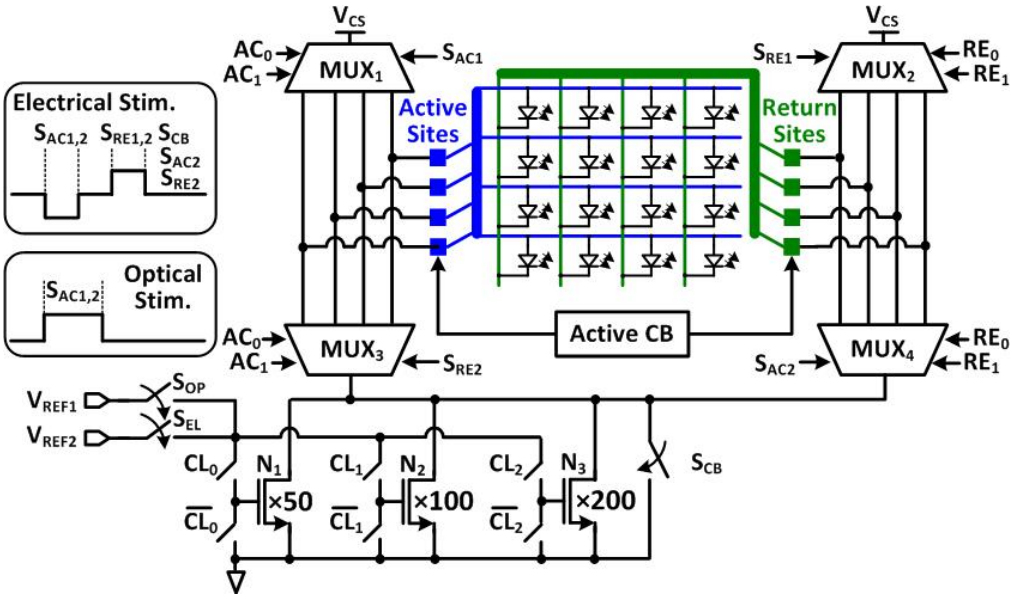

Figure 5.20. Schematic diagram of the stimulation driver in H-bridge configuration.

Figure 5.21 shows the active CB circuit, which is utilized to ensure charge-balanced biphasic stimulation. The storage capacitor, C_S, is alternately connected to the selected active and return sites to supply stimulus current. The active CB circuit uses a capacitive-feedback amplifier to integrate the discharge voltage waveform of V_{CS} to detect the amount of negative and positive injected charge into the tissue. A charge monitoring signal, S_{CM}, stays at "0" before stimulation, while amplifiers A_1 and A_2 operate as buffers, which are biased at the half supply voltage, V_{MID}. When the negative stimulation starts with a predefined duration, T_N, A_1 becomes a capacitive-feedback amplifier, and A_2 operates as a comparator. The sensing voltage across C_3, V_{NN}, increases as V_{CS} decreases during T_N, and stays at its final value until the end of the positive stimulation period, T_P. During the intermediate delay period, T_{IN}, A_1 operates as a buffer to reset its output voltage at V_{MID}. When C_S discharges for positive stimulation, the sensing voltage across C_4, V_{PP}, starts increasing. When the amounts of V_{PP} and V_{NN} increments are equal, S_{CM} = "0" again, and the positive stimulation stops to ensure that the net injected charge is zero.

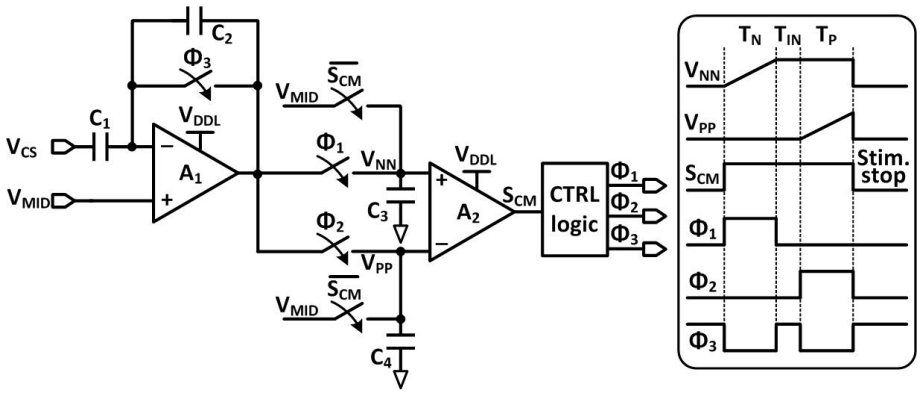

Figure 5.21. Schematic diagram of the active charge balancing circuit.

5.5.2 Experimental Measurements

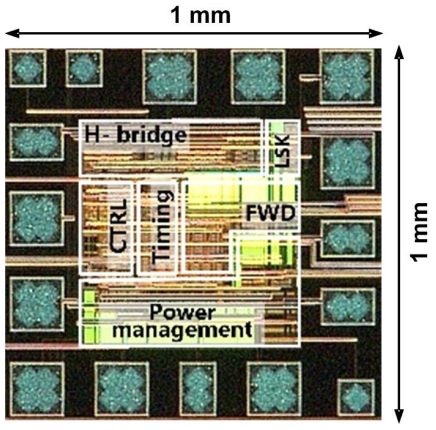

Figure 5.22. Micrograph of the fabricated FF-WIOS2 SoC prototype.

The FF-WIOS SoC was fabricated in the TSMC 0.35-μm 4M2P standard CMOS process, occupying a 1×1 mm^2 footprint including pads, as shown in Figure 5.22. The experimental setup of testing the FF-WIOS2 SoC is shown in Figure 5.23. The FF-WIOS2 SoC was directly wire-bonded onto an evaluation board, which also included L_{Rx}, L_{Res}, off-chip capacitors, and μLED arrays for testing the optical stimulation function, as well as resistor-capacitor tissue model [131] for testing the electrical stimulation function. A Class-E PA, made of COTS components, delivers power to the FF-WIOS2 SoC through an optimized 60 MHz 3-coil inductive link, which coil specifications are presented in [137].

A USB dongle applies OOK to the power carrier, delivering stimulation parameters through the power carrier to the FF-WIOS2 SoC.

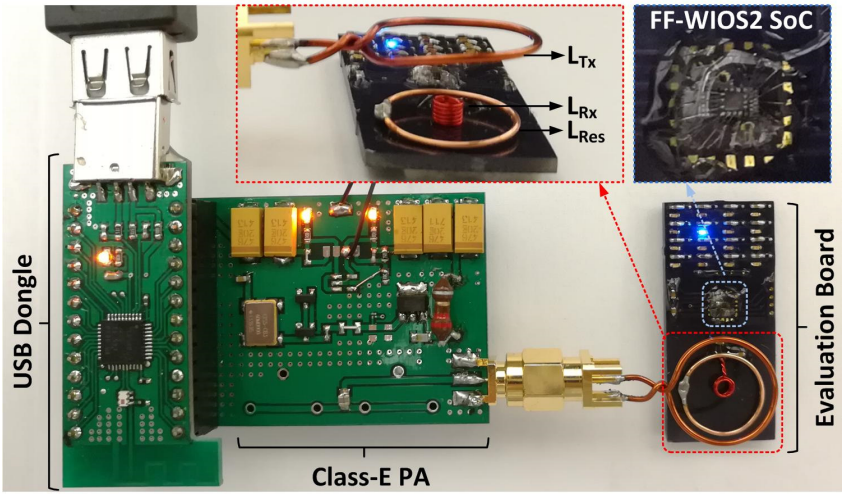

Figure 5.23. Benchtop experimental setup of the FF-WIOS2 SoC prototype for demonstrating wireless optical and electrical stimulation.

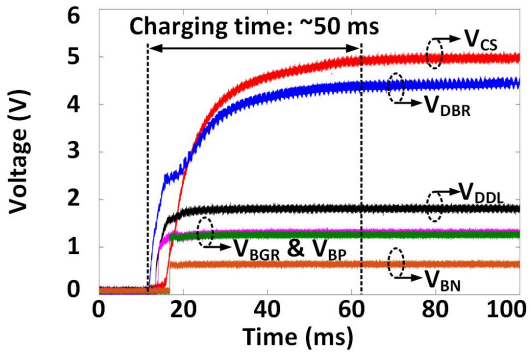

Figure 5.24. Transient waveforms of the power management block at starting up.

Following startup, it takes ~50 ms for V_{CS} and V_{DBR} to stabilize at their steady-state target voltages of 5 V and 4.2 V, respectively, as shown in Figure 5.24. V_{DD} and V_{BGR} have already been stabilized at 1.8 V and 1.2 V, respectively, at this point, and so do, V_{BP} and V_{BN} references at 1.2 V and 0.6 V, respectively.

Figure 5.25a shows the charging and discharging of the C_S = 10 µF to generate optical stimulation with 6.4 ms pulse width at 5 Hz. The µLED current is limited to 12 mA.

Once stimulation starts, C_S discharges in the target µLED with a decaying exponential current, resulting in a drop of ~2.5 V in V_{CS}, while V_{DBR} remains above the minimum level of 2.6 V, required for maintain V_{DD} unaffected. The emitted light from the µLED (0.5×1×0.4 mm^3, LB QH9G, OSRAM) during stimulation pulse was collected by the photodetector (Newport 883-SL) of an optical power meter (Newport 1835-C). As expected, the NOL follows the stimulation current variation. After each stimulation, C_S is recharged to the target voltage within 30 ms.

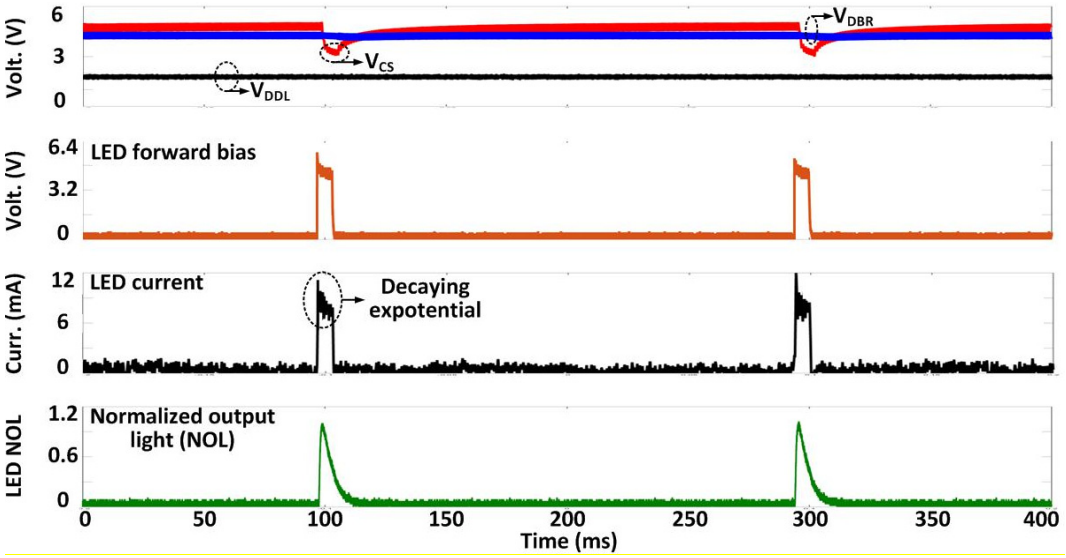

(a)

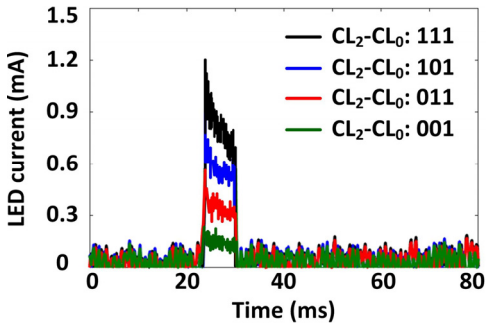

(b)

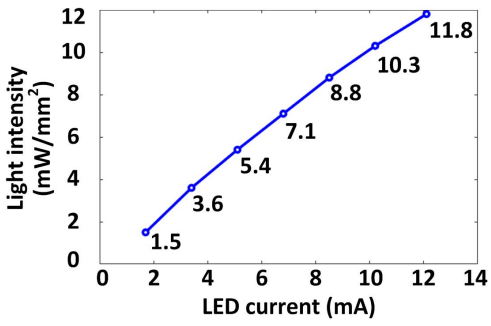

(c)

Figure 5.25. (a) Measured optical stimulation waveforms. (b) Measured µLED current at different stimulation current setting. (c) NOL intensity as a function of the µLED current.

The μLED current under four different settings (CL_0-CL_2) was measured from the voltage across a 10 Ω current-sensing resistor in series with the μLED. In Figure 5.25b, the peak value of the μLED current increases from 1.7 mA to 12 mA with 3.4 mA steps, according to the design specifications. We also measured the light intensity at each current level to validate measurement results with the μLED datasheet. In Figure 5.25c, the peak value of the light intensity under 12 mA current is 11.8 mW/mm^2. At the minimum μLED current of 1.7 mA, the light intensity is 1.5 mW/mm^2, which is above the 1 mW/mm^2 threshold for effective optical modulation of neural activities [61].

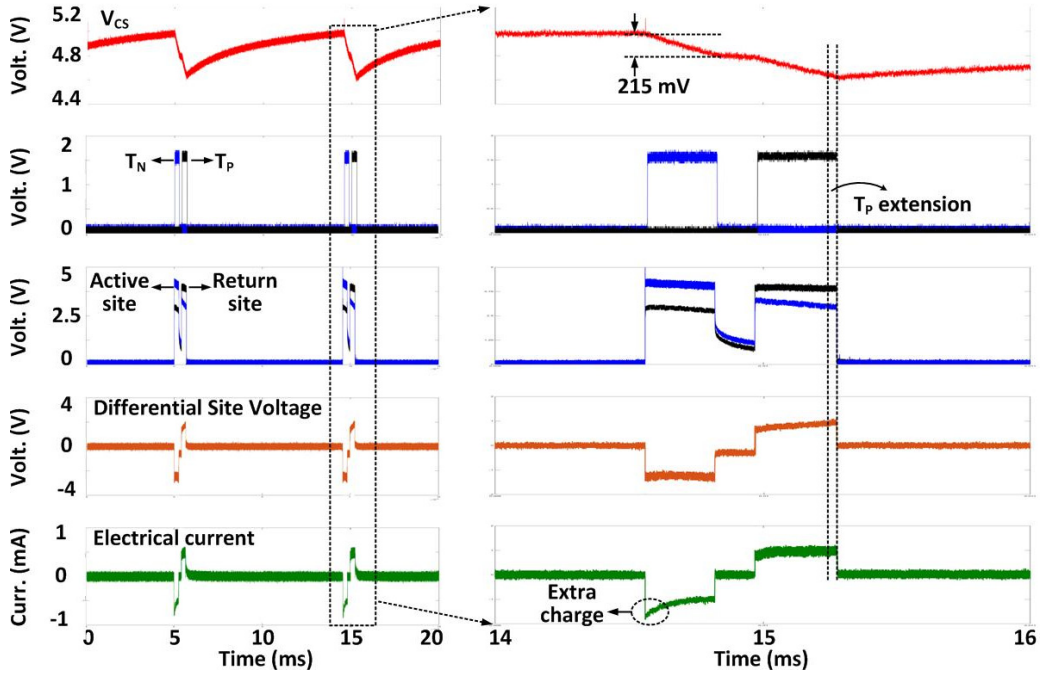

Figure 5.26. Measured electrical stimulation waveforms with active charge balancing.

Figure 5.26 presents the charge-balanced electrical stimulation waveforms with C_S = 1 μF, delivering cathodic and anodic charge stimuli to a tissue model, consisting of R_S = 2 kΩ and C_{DL} = 500 nF in series, and current limited to ±700 μA. The cathodic stimulation, T_N, is applied for a predefined duration of 350 μs, discharging V_{CS} by 215 mV. Since the

stimulation current shows a slight drop during anodic stimulation, T_P is dynamically adjusted to 420 µs by the charge monitoring circuit, discharging V_{CS} by the same amount to ensure that injected charges are neutralized. After stimulation, both sites are shorted to ground for a predefined period of 100 µs for additional charge balancing. Measured specifications of the current FF-WIOS2 SoC prototype are summarized in Table 5.3.

Table 5.3. Measured specifications of the FF-WIOS2 SoC.

Overall system		
ASIC area		1 mm^2
Power without stimulation		320 µW
Voltage doubler efficiency		43 %
Switched-capacitor based stimulation		
Target voltage		5 V
Charging efficiency		37 %
Charging time		50 ms
C_S / C_{IN} / C_L		10 µF or 1 µF / 10 µF / 10 µF
Optical stim. efficiency		62.5 %
Stimulation	**Electrical**	**Optical**
Frequency	20-200 Hz, 2 bits	1-10 Hz, 2 bits
Pulse width	50-350 µs, 2 bits	1.6-6.4 ms, 2 bits
Current limiter	100-700 µA, 3 bits	1.7-12 mA, 3 bits
Light intensity	NA	1.5-11.8 mW/mm^2
Forward and back telemetry		
Data bits		20 bits
Pre/post-amble bits		10 bits
PPM data rate		50 kbps
LSK data rate		160 Hz-1280 Hz, 2 bits
Back telemetry pulse width		1 or 2 µs, 1 bit

5.6 Summary and Discussion

Table 5.4 benchmarks the FF-WIOS against state-of-art optical implants in the literature. The FF-WIOS is competitive in terms of implant size, weight, and stimulation capability. The near-field 3-coil link combined with SCS charge storage is a safe and efficient strategy that can offer sufficient PDL for optical stimulation. Moreover, CLPC can handle misalignments much better than ultrasound and focused EM field at high

frequencies. The FF-WIOS also benefits from high-level integration of 16-ch stimulation and provides the end user with full control over the stimulation parameters. The FF-WIOS prototype used *in vitro* is built on polyimide substrate, which is flexible and biocompatible. It is an important step towards the free-floating distributed neural interface concept. It is also possible to couple a fiber onto the µLED to further focalize LED light onto a specific brain area at the cost of being more invasive.

Table 5.4. Benchmarking of mm-sized wirelessly powered optogenetic interfaces.

Publication		2017 [67]	2018 [68]	2018 [66]	2018 [59]	**This work**
Technology		COTS	COTS	0.35 µm	0.18 µm	**0.35 µm**
WPT mechanism, Freq.		RF, 13.56 MHz	RF, 2.9 GHz	Photovoltaic	Ultrasound, 1.314 MHz	**Inductive 60 MHz**
# of stimulation		1	4	1	5	**16**
Max. I_{LED} (mA)		20	-	5	5	**10**
Light intensity (mW/mm^2)		1-50	30	15	1.4-23	**Up to 10**
Stim. eff.	Power eff.** %	-	-	10.7	50.3	**37.5**
	Optical eff.*** %	-	-		30.7	**62.5**
Device size (mm^3)		9.8 mm diameter	125	1.3×1.3×(0.6-1.0)	2×3×6.5	**2.5×2.5×1.5**
Device weight (mg)		30	220	2.3	78	**15**
Stim. proper Ctrl		No	No	No	Yes	**Yes**
In vivo experiments		Yes	Yes	No	No	**Yes**

From the neuroscience perspective of alignment with a particular target in the brain, a combination of multiple FF-WIOS distributed within the region of interest, and each FF-WIOS being capable of driving a 4×4 µLED array with 700 µm pitch, give the neuroscientist sufficient flexibility, redundancy, and leeway to try multiple adjacent channels or nearby devices to find the optimal target. In rodents, surgery procedure involves creating small holes in the skull that match the size of FF-WIOS at the target

locations. After placing the device, the hole will be sealed by dental cement. This approach would preserve key feature of the FF-WIOS to be free-floating with no anchor onto the skull or brain tissues, and minimize damage to the surrounding tissue. Due to small intracranial space and thinness of the skull bone, L_{Res} will be placed above the skull but under the scalp to power the FF-WIOS devices underneath through the bone. L_{Res} is stationary and covers the target brain area. Therefore, no accurate alignment is needed when one or more FF-WIOS are to be located within L_{Res}, and as we have demonstrated before [28], every one of them can receive sufficient power regardless of their position.

We have also presented the FF-WIOS2 SoC. The circuit topology for each block is chosen for power/area efficiency and design simplicity to achieve a compact and reliable system. The SCS architecture of the FF-WIOS2 SoC allows it to generate high current levels needed to drive the μLEDs and pass the minimum threshold needed for optogenetic stimulation despite weak inductive link of a mm-sized device. It is also capable of safe electrical stimulation with a combination of active and passive charge balancing. FF-WIOS2 is effectively powered through an optimized 3-coil inductive link, which also carriers the stimulation parameters via forward telemetry and received power information via back telemetry. The FF-WIOS2 allows for high-level integration of up to 16-ch optical and 4-ch electrical stimulation, providing the end user with flexibility to specify the type and patterns of stimulation.

CHAPTER 6. DUAL-BAND WIRELESS POWER TRANSMISSION SYSTEM FOR EVALUATING MINITURIZED IMPLANTS

We have developed the FF-WIOS device [106], [107]. A resonance-based 3-coil inductive link ($link_{3\text{-}coil}$) powers the FF-WIOS. The $link_{3\text{-}coil}$ includes a resonator that is implanted above or below the skull in rodents or larger hosts, respectively, for increasing the magnetic field intensity within the area that is encompassed by the resonator. In general, when a small IMD is immersed in the tissue environment, its Rx coil tends to have its Q-factor maximized at tens to hundreds of MHz [147]. The $link_{3\text{-}coil}$ in FF-WIOS is designed based on the algorithm presented in [106] for the optimal operating frequency of 60 MHz.

We have also developed the EnerCage-HC2 [103], [104]. This system, built around a standard-sized rodent homecage, can wirelessly power a headstage regardless of the position and orientation of the headstage within the cage, through a resonance-based 4-coil inductive link ($link_{4\text{-}coil}$). The operating frequency of $link_{4\text{-}coil}$ is chosen 13.56 MHz for four reasons: 1) Large dimensions of the Tx resonators, which are imposed by the size of the homecage, tend to reduce the coils' SRF, which should be kept about an order of magnitude above the power carrier; 2) Compatibility with the ISM band and readily existing high frequency RFID technology with commercially available COTS chipsets; 3) Safety considerations of the personnel exposure to EM radiation, which are more relaxed at lower frequencies, and lower risk of interference with adjacent devices; 4) Low EM power absorption in the tissue, preventing elevation of the animal subject body temperature. 13.56 MHz is already close to the resonators' SRF.

Building upon these two systems, the focus of this work is to enable wireless powering of the FF-WIOS anywhere within the standard homecage continuously in the presence of all Tx-Rx misalignments, such that the animal can freely move without any tethers or bulky payload. Misalignments in link$_{4\text{-coil}}$ result in significant variations in its PTE and consequently the amount of power delivered to FF-WIOS.

The headstage in this case operates as a power relay and temporary energy storage to support continuous operation of the FF-WIOS. However, there is a mismatch between the optimal operating frequencies of link$_{4\text{-coil}}$ and link$_{3\text{-coil}}$ because of the difference in the sizes of headstage and FF-WIOS. Operating both links at the same frequency results in degradation in the overall PTE. This optimal frequency gap increases either in larger experimental arenas or with smaller IMDs, resulting in the PTE degradation become even worse [27]-[31]. Since the headstage functions are needed in this application, it is beneficial to operate the two links at their optimal frequencies.

We have developed a new dual-band EnerCage-HC system, in which two inductive links are operating simultaneously at their optimal frequencies to wirelessly deliver sufficient PDL to FF-WIOS within the entire homecage. This system has a headstage, as an intermediate power converter and buffer, which receives power from the EnerCage via link$_{4\text{-coil}}$ at 13.56 MHz and delivers it to the FF-WIOS via link$_{3\text{-coil}}$ at 60 MHz. CLPC mechanism is established to deal with such misalignments and minimize power fluctuations due to animal movements in the FF-WIOS. Nonetheless, the headstage can use its stored energy to support continuous operation of the FF-WIOS in the case of severe misalignments in link$_{4\text{-coil}}$.

6.1 System Overview

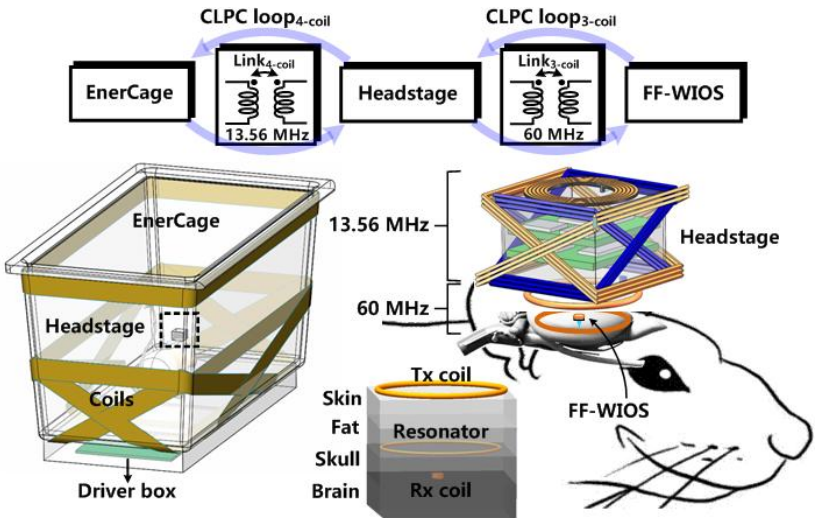

Figure 6.1. A conceptual representation of the dual-band EnerCage-HC system.

Figure 6.1 shows the conceptual view of the entire system. $Link_{4\text{-}coil}$, delivers power from the EnerCage-HC to the headstage at 13.56 MHz, while $link_{3\text{-}coil}$ delivers power from the headstage to the FF-WIOS at 60 MHz. The EnerCage-HC has multiple coils made of copper foil wrapped around the homecage, plus one in the driver box, which also acts as a homecage pedestal without any electrical contact between them. The cm-sized headstage includes small wire-wound coils optimized for both 13.56 MHz and 60 MHz. Since a rat model is considered for preliminary evaluation of the system, the Tx coil of $link_{3\text{-}coil}$ is placed at the bottom of the headstage, as close as possible to the resonator and FF-WIOS Rx coil, which are implanted above and below the skull, respectively. The CLPC mechanism that compensates for coil misalignments in this system, includes two control loops, $loop_{4\text{-}coil}$ and $loop_{3\text{-}coil}$, which adjust PDLs of $link_{4\text{-}coil}$ and $link_{3\text{-}coil}$ at designated levels, respectively. $Loop_{3\text{-}coil}$ stabilizes the FF-WIOS received power, P_L, by adjusting the headstage output power, P_{o_HS}, which is in turn supported by $loop_{4\text{-}coil}$ to adjust the headstage input power, P_{i_HS}, by adjusting the EnerCage-HC output power, P_{o_HC}.

6.1.1 Circuit Details

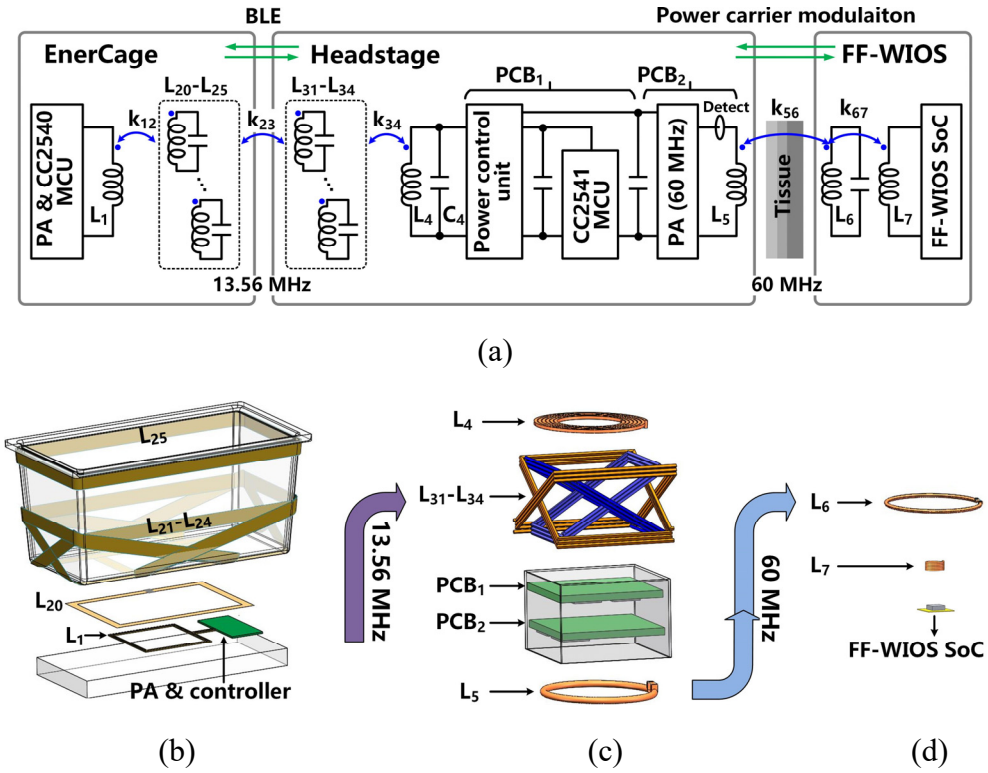

Figure 6.2. (a) Block diagram of key components involved in the dual-band WPT. The 3D model of key components in the (b) EnerCage-HC, (c) headstage, and (d) FF-WIOS.

Figure 6.2 shows the key components involved in the WPT and their 3D models. A Tx coil, L_1, in the driver box, six Tx resonators, L_{20}-L_{25}, around the homecage, four Rx resonators, L_{31}-L_{34}, around the headstage, and an Rx coil, L_4, inside it form the $\text{link}_{4\text{-coil}}$. L_1 is driven by a 13.56 MHz Class-E PA, $PA_{13.56MHz}$, also in the driver box. The headstage circuitry includes two PCBs, which are housed in a small 3D-printed plastic enclosure. The power management unit generates supply voltages from the 13.56 MHz power carrier for the entire headstage, while a 60 MHz Class-E PA, PA_{60MHz}, delivers power to $\text{link}_{3\text{-coil}}$. An Rx coil, L_7, wrapped around the FF-WIOS chip, a Tx coil, L_5, at the bottom of the headstage, and a resonator, L_6, implanted under the scalp and encompassing one or more

FF-WIOS devices, form the link$_{3\text{-coil}}$. The CLPC is established by a BLE link between a CC2540 MCU in the EnerCage-HC and a CC2541 MCU in the headstage, as well as a bidirectional OOK forward telemetry and LSK back telemetry link between the headstage and FF-WIOS.

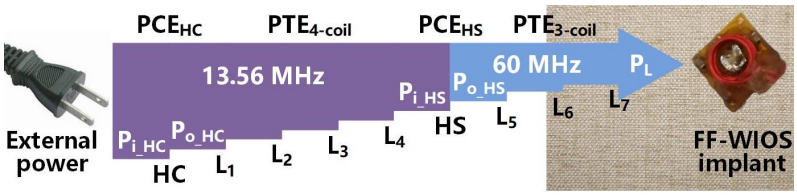

Figure 6.3. Power flow from the external power source to the FF-WIOS.

Figure 6.3 shows the power flow from the external power source, which passes through the EnerCage-HC, link$_{4\text{-coil}}$, headstage, and link$_{3\text{-coil}}$ to be eventually delivered to the FF-WIOS. The PCEs of the EnerCage-HC (PCE$_{HC}$) and the headstage (PCE$_{HS}$) are defined as P_{i_HC}/P_{o_HC} and P_{i_HS}/P_{o_HS}, respectively. The PTEs of the 4-coil (PTE$_{4\text{-coil}}$) and 3-coil (PTE$_{3\text{-coil}}$) links are defined as P_{o_HC}/P_{i_HS} and P_{o_HS}/P_{i_HS}, respectively. Then, the PTE of the entire dual-band WPT path, PTE$_{total}$, can be calculated from PCE$_{HC}$ × PTE$_{4\text{-coil}}$× PCE$_{HS}$ × PTE$_{3\text{-coil}}$.

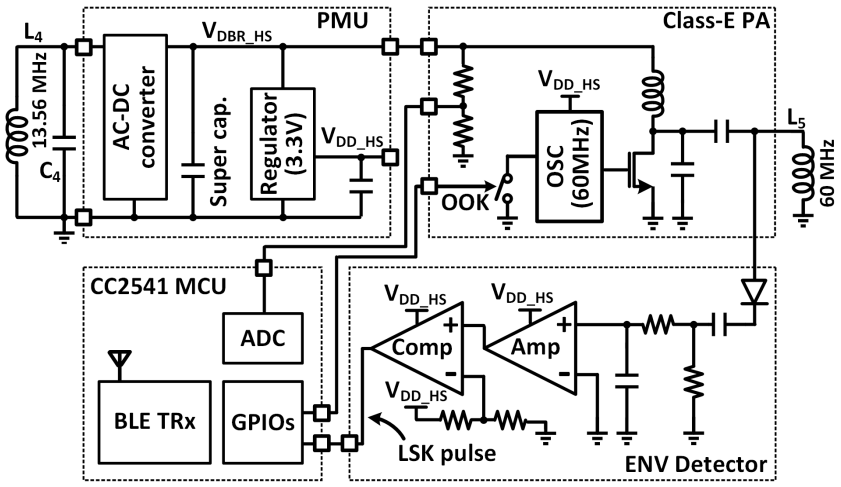

Figure 6.4. Simplified schematic diagram of the dual-band headstage.

Figure 6.4 shows the headstage simplified schematic diagram, which includes the power management unit and CC2541 MCU modules housed in PCB_1 and the PA_{60MHz} and envelop detector circuits housed in PCB_2. In the power management unit, a voltage doubler made of HSMS-2822 Schottky diodes follows L_4 and generates a DC voltage, V_{DBR_HS}, from the EnerCage-HC 13.56 MHz power carrier to supply the PA_{60MHz}. A voltage regulator (TPS79901) generates V_{DD_HS} = 3.3 V from V_{DBR_HS} for the rest of the headstage.

A divided version of V_{DBR_HS} is sampled by the built-in ADC of the headstage MCU and sent out via BLE to the driver box to calculate P_{i_HS}. A 60 MHz oscillator (CB3LV) drives PA_{60MHz}, which is also on-off keyed to implement the OOK forward telemetry link. The LSK back telemetry link uses an envelope detector to monitor the voltage variations across L_5, which is extracted by a band-pass filter before being amplification (AD8603). The resulted signal is then compared (TLV3491) with $V_{DD\_HS}/2$ to recover the back telemetry data, which are detected by the headstage MCU.

Referring to the FF-WIOS SoC design in [137], the LSK back telemetry schematic is involved in the $loop_{3\text{-}coil}$ for the CLPC. Based on our earlier studies on the CLPC stability [107], [140], a 160 Hz clock, CLK_{LSK}, is selected to control the timing of back telemetry pulses, BT_{FF}, which pulse width is adjusted at either 1 μs or 2 μs by the number of delay cells. The output of the on-chip voltage doubler, V_{DBR_FF}, is divided by the resistive divider and then compared with the on-chip bandgap reference voltage, V_{BGR_FF}. When the divided V_{DBR_FF} exceeds V_{BGR_FF}, BT_{FF} pulses are generated along with CLK_{LSK} and level-shifted up to V_{DBR_FF}. The level shifted BT_{FF} then control P_1 transistor to switch L_7. Shorting L_7 will increase its Q-factor, resulting in the voltage across L_5 to increase, sampling which delivers back telemetry data from the FF-WIOS to the headstage.

6.1.2 Data Communication Algorithm

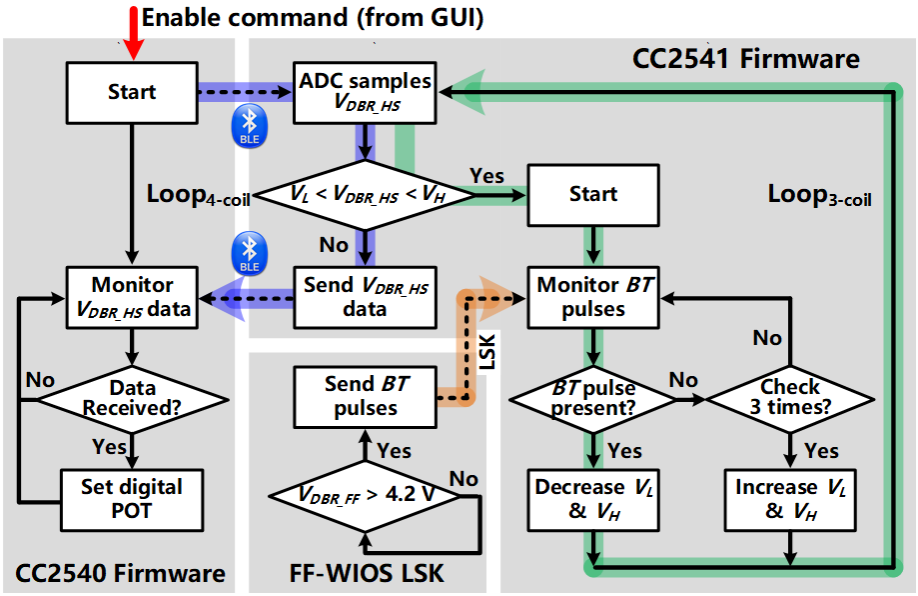

Figure 6.5. Simplified flowchart of the CLPC algorithm, which is implemented in the firmware of the EnerCage CC2540 MCU and headstage CC2541 MCU.

Figure 6.5 depicts the CLPC flowchart, including $loop_{4\text{-}coil}$ and $loop_{3\text{-}coil}$, which operate sequentially, the BLE link between the EnerCage-HC and headstage MCUs, and the LSK back telemetry between the headstage and the FF-WIOS. $Loop_{4\text{-}coil}$ is activated first and aims at stabilizing V_{DBR_HS} within a dynamically-adjusted window, with upper/lower boundaries of V_H and V_L, respectively, by adjusting V_{PA_HC}, the supply voltage of the EnerCage $PA_{13.56MHz}$. Upon receiving the CLPC enable command from the user, and associated parameters from the GUI that is running on a PC, $loop_{4\text{-}coil}$ starts from sampling V_{DBR_HS} in the headstage MCU, and determines if it is within the V_H-V_L window. If not, the headstage MCU sends V_{DBR_HS} samples to the EnerCage-HC MCU via BLE, which in turn adjusts V_{PA_HC} by setting a POT that changes P_{o_HC} and eventually P_{i_HS}.

Once V_{DBR_HS} returns back within the V_H-V_L window, $loop_{3\text{-}coil}$ starts monitoring V_{DBR_FF}. In order to keep the FF-WIOS chip as small and low power as possible, $loop_{3\text{-}coil}$

control logic is kept quite simple. V_H and V_L in this loop increase by default at a constant, but firmware-adjustable, rate as long as there is no BT_{FF} pulses detected across L_5 during 3 consecutive cycles through the envelope detector shown in Figure 6.4. BT_{FF} pulses are generated if $V_{DBR\_FF} > 4.2$ V. In the presence of BT_{FF} pulses, $\text{loop}_{3\text{-coil}}$ changes V_H and V_L direction and decreases them at a constant rate until BT_{FF} pulses disappear. This trend continues while monitoring whether $V_H > V_{DBR\_HS} > V_L$ is still true. If V_{DBR_HS} falls out of the dynamic V_H-V_L window, then $\text{loop}_{3\text{-coil}}$ stops and $\text{loop}_{4\text{-coil}}$ restarts its operation. Since $\text{loop}_{4\text{-coil}}$ needs to respond to V_{DBR_HS} variations quickly by adjusting V_{PA_HC} before the next adjustment of V_H and V_L values by $\text{loop}_{3\text{-coil}}$, its sampling and operating rate is set at 1 kHz, much faster than $\text{loop}_{3\text{-coil}}$ sampling rate of 160 Hz. Once CLPC reaches steady state, V_H and V_L maintain their up/down cycle, and V_{DBR_HS} bounces in between, while being mirrored by V_{PA_HC} to stabilize V_{DBR_FF}.

6.2 Design of Multi-Coil Inductive Links

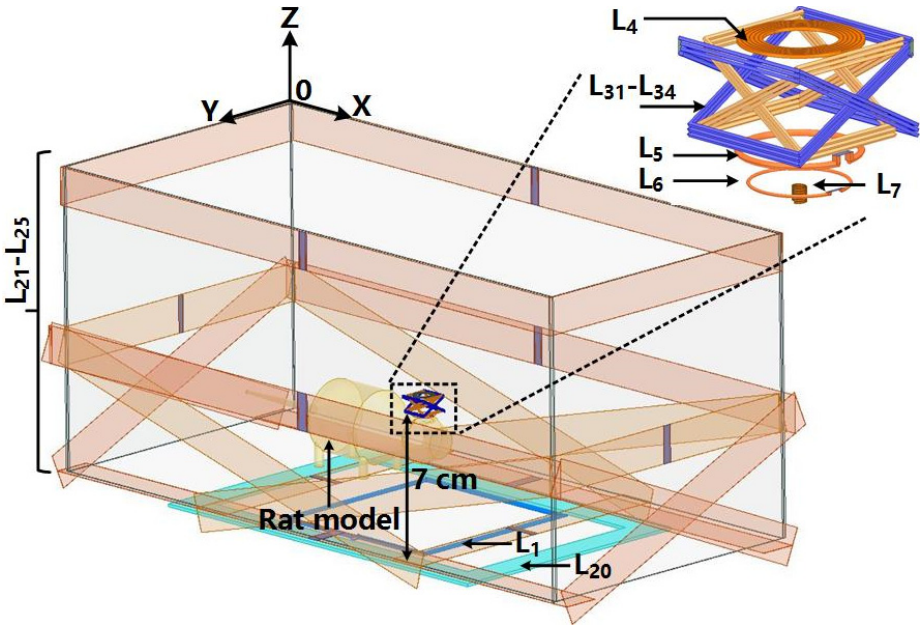

Figure 6.6. The model of two inductive links with tissue layers in HFSS.

Figure 6.6 shows the geometrical arrangement of the two multi-coil inductive links responsible for dual-band WPT to mm-sized FF-WIOS, modeled in HFSS. To design and optimize the multi-coil inductive links, we have used finite element method (FEM) in HFSS environment, instead of theoretical calculations. This is because of the complexity of the coil arrangements, rendering the FEM model as the only practical solution with sufficient accuracy not only for calculating the mutual coupling among the overlapping L_{20}-L_{25} and L_{31}-L_{34} in link$_{4\text{-coil}}$ but also the effects of tissue surrounding link$_{3\text{-coil}}$, as well as computing the magnetic field distribution in the tissue to evaluate the SAR limits.

Figure 6.6 should be compared with Figure 6.2 to observe the role of each coil from circuit perspective. L_1 and L_{20} are in the driver box and centrally aligned with the homecage. L_{21}-L_{24} cover four sides of the homecage, while being elevated by 7 cm (the nominal height of the headstage on the rat head) from the bottom of the homecage on one side and extend onto the other side of the homecage to fully overlap with L_1 and L_{20}. L_{25} wraps around the top rim of the homecage to extend WPT coverage along the z-axis when the animal stands on its rear limbs. Thanks to strong coupling among L_{20}-L_{25}, only L_{20} needs to be equipped with a variable capacitor for fine tuning of the resonance frequency of the entire EnerCage-HC at 13.56 MHz. L_{31}-L_{34} cover four sides of the headstage, being slanted by 40º to compensate for rotational misalignments. L_4 and L_5 are placed at the top and bottom sides of the headstage, respectively, to minimize their cross-coupling, while allowing L_5 to be as close as possible to the FF-WIOS. Finally, L_6 and L_7, which are coated with 5 μm parylene-C and 50 μm PDMS [83], are concentrically aligned with L_5 in this model. In terms of PTE, this arrangement is considered the worst-case scenario for L_7, as we have shown in [28] that PTE$_{3\text{-coil}}$ is higher when L_7 is placed anywhere else within L_6.

The resonators in link$_{4\text{-coil}}$ and link$_{3\text{-coil}}$, with their high Q-factors form narrow-band and sharp bandpass filters at 13.56 MHz and 60 MHz, respectively, which can attenuate out-band noise. Therefore, the interference between the two links, i.e. the undesired cross-coupling between their coils, can be ignored during geometrical optimization of the coils, at least at the theoretical level. These small cross-couplings are, however, considered in the HFSS simulations using Figure 6.6 model.

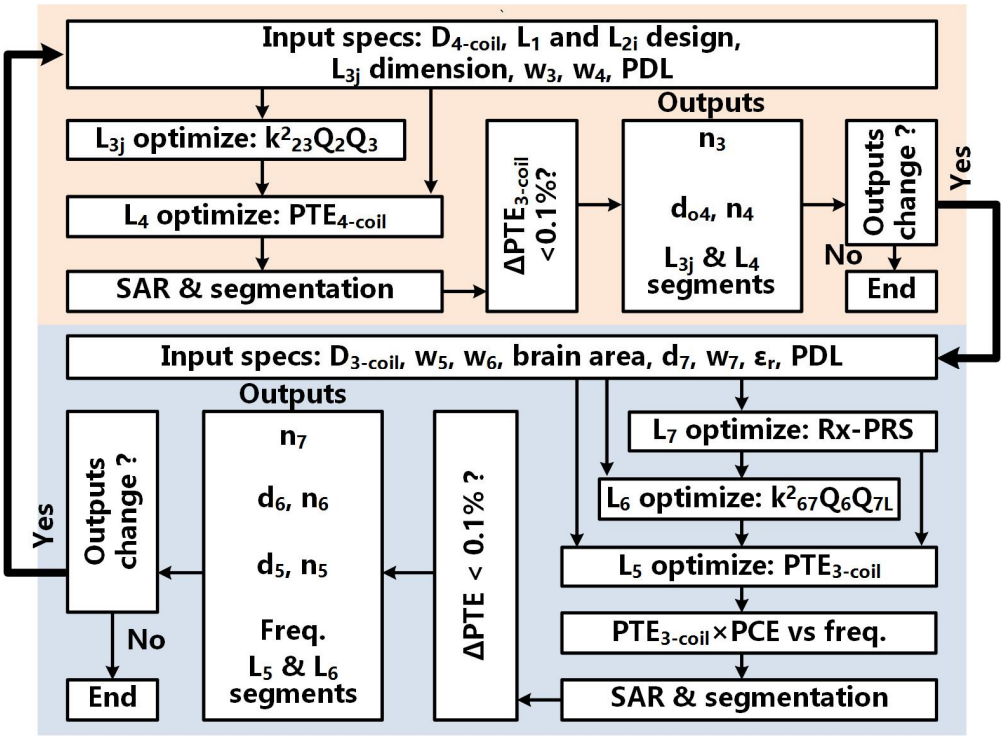

Figure 6.7. The flowchart of optimization algorithm for the two inductive links used in dual-band EnerCage-HC system.

Figure 6.7 shows the recursive optimization algorithm[13] that we have devised for this purpose based on [27]-[31]. The flowchart has two parts, alternating between the optimization of the two multi-coil links. The nominal loadings in this prototype were $R_{4\text{-}coil}$ = 148 Ω based on P_{i_HS} = 122 mW at 6 V_{peak} across L_4, and $R_{3\text{-}coil}$ = 4.6 kΩ based on P_L = 2.7 mW at 5 V_{peak} across L_7 for link$_{4\text{-coil}}$ and link$_{3\text{-coil}}$, respectively.

[13] I would like to thank Pengcheng Zhang for the technical support on the optimization of the inductive links.

6.2.1 4-Coil Inductive Link Design

Without changing the existing coil design on the Tx side of EnerCage-HC [103], [104], we optimized L_{31}-L_{34} and L_4, at the nominal height of 7 cm for link$_{4\text{-coil}}$. Since the headstage (18×18×15 mm^3) is much smaller than the homecage, the coupling between loosely coupled L_{2i} (i = 0~5) and L_{3j} (j = 1~4) is the dominant factor in determining PTE$_{4\text{-coil}}$. To improve L_{3j} and L_{2i} coupling, we need to maximize the effective area of L_{3j}. Based on power delivery studies in [103], L_{3j} are required to tilt ≥25º.

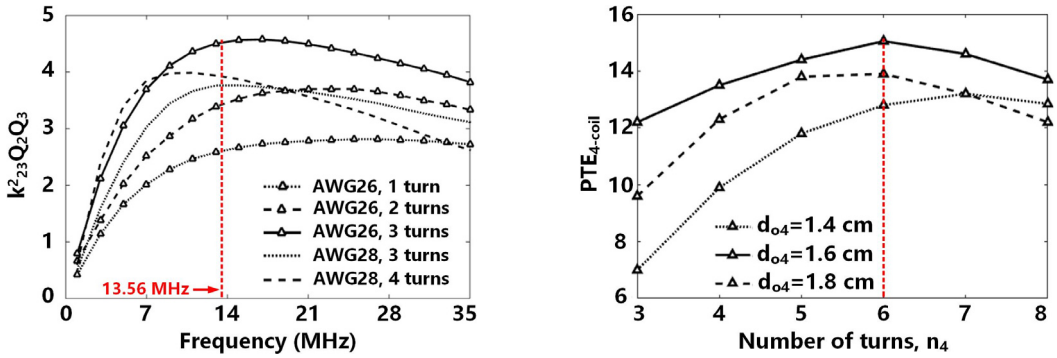

(a) (b)

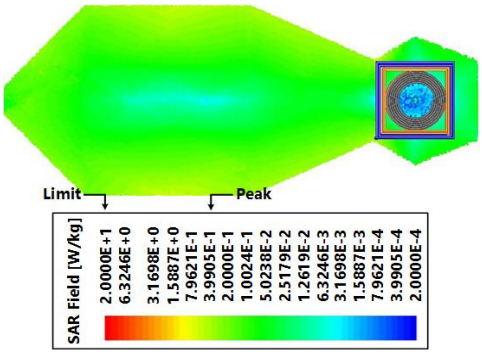

(c)

Figure 6.8. (a) $k^2_{23}Q_2Q_3$ versus n_3 when using AWG26 and AWG28 magnetic wires (b) PTE$_{4\text{-coil}}$ versus d_{o4} and n_4. (c) Local SAR simulation at 13.56 MHz.

Therefore, the diagonal planes of the headstage cube are used to implement L_{3j}, resulting in the tilting angle of ~40°. L_{3j} are made of AWG26 magnetic wire with a

thickness of w_3 = 0.4 mm. According to [31], with this type of wire, the number of turns, n_3, for L_{3j} is optimal when $k^2_{23}Q_2Q_3$ is maximized, where k_{23} is the coupling coefficient between L_{2i} and L_{3j}, and Q_2 and Q_3 are Q-factors of L_{2i} and L_{3j}, respectively. To strike a balance between the optimal n_3 and the resulting headstage size/weight, we simulated $k^2_{23}Q_2Q_3$ with n_3 = 1, 2, and 3 (using AWG26) and n_3 = 3 and 4 (using AWG28) in HFSS. Using thinner wire for L_{3j} allows to have higher n_3, but shifts the peak of $k^2_{23}Q_2Q_3$ towards lower frequencies. The results of this simulation, shown in Figure 6.8a, confirmed that using AWG26 magnetic wire with n_3 = 3 would be the best choice.

The outer dimension of L_4, d_{o4}, should be selected to fit on one face of the headstage cube. The optimal number of turns for L_4, n_4, is determined by optimizing its cross-coupling with L_{3j} in a way that $PTE_{4\text{-coil}}$ is maximized [31]. In Figure 6.8b, $PTE_{4\text{-coil}}$ is simulated in HFSS by sweeping n_4 from 3 to 8 turns, with d_{o4} = 1.8 cm, 1.6 cm, and 1.4 cm. From these simulation results, $PTE_{4\text{-coil}}$ is maximized at d_{o4} = 1.6 cm and n_4 = 6. Figure 6.8c presents the local SAR simulation for the rat head and body model at 13.56 MHz. The input power at L_1 is set at its maximum value of 5.6 W, while the input power at L_5 is set at 15 mW to deliver P_L = ~2.7 mW. This simulation shows that the maximum local SAR is ~0.4 W/kg, which is well below the 20 W/kg limit [32].

6.2.2 3-Coil Inductive Link Design

Unlike $link_{4\text{-coil}}$, in optimization of $link_{3\text{-coil}}$ and its operating frequency, the surrounding tissue plays a significant role [30]. According to [141] and [142], the PCE of the on-chip voltage doubler, PCE_{VD}, degrades at higher frequencies due to parasitic capacitance of its diode-connected transistors. Therefore, PCE_{VD} should also be considered

in determining the overall efficiency of the power delivery path. Hence, the optimal carrier frequency of link$_{3\text{-coil}}$ is selected to maximize PTE$_{3\text{-coil}}$ × PCE$_{VD}$.

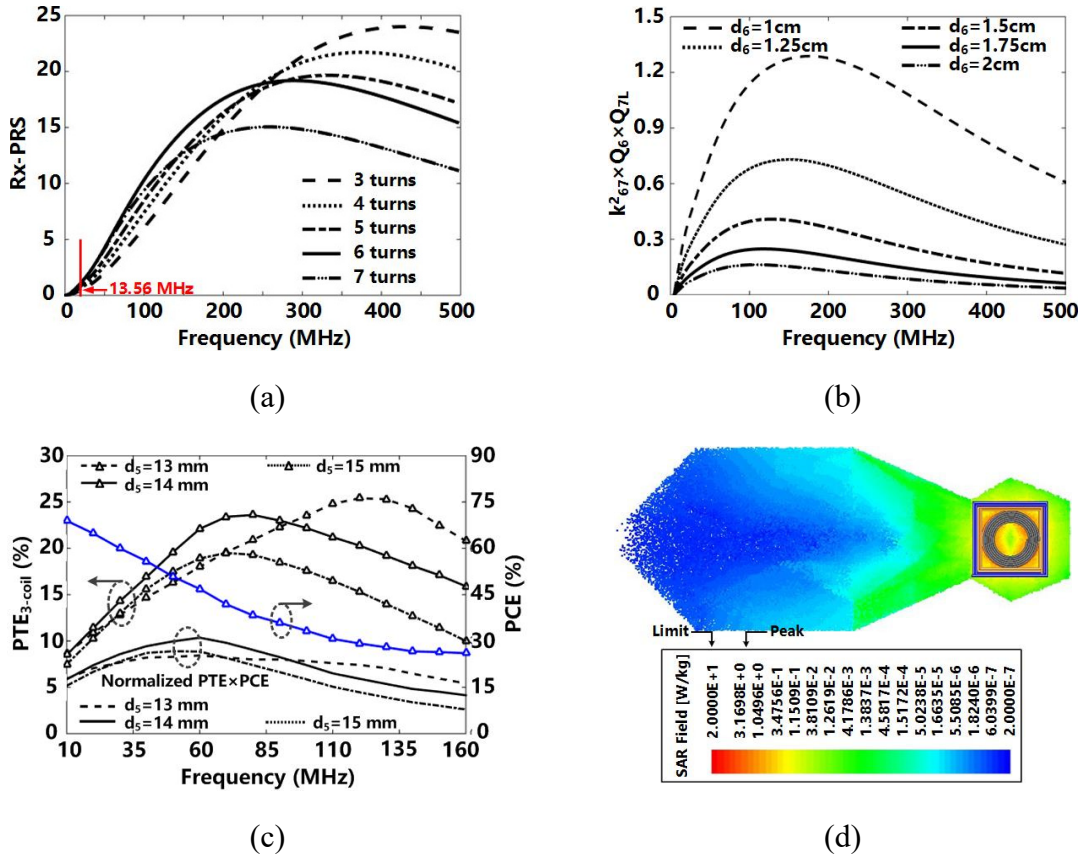

Figure 6.9. (a) Rx-PRS vs. n_7. (b) $k^2_{67}Q_6Q_{7L}$ vs. $d6$. (c) PTE$_{3\text{-coil}}$, PCE$_{VD}$, and normalized PTE$_{3\text{-coil}}$×PCE$_{VD}$ vs. d_5 and carrier frequency (d) Local SAR simulation at 60 MHz.

Design procedure starts with L_7 optimization considering the geometrical, electrical, and fabrication constraints. L_7 is wire wound around the FF-WIOS die, using AWG34 magnetic wire (w_7 = 0.16 mm), resulting in the outer diameter of d_7 = 1.6 mm. L_7 optimization corresponds to maximizing the receiver power reception susceptibility, Rx-PRS, which indicates the efficiency of L_7 power reception under a given EM field exposure [27], [28]. Figure 6.9a presents the simulation results of Rx-PRS as a function of frequency while changing n_7. As n_7 increases, the peak of Rx-PRS shifts towards lower frequencies. To determine n_7, we need to strike a balance between Rx-PRS and geometrical parameters

of L_5 and L_6 as a function of frequency to maximize $PTE_{3\text{-}coil}$. Therefore, n_7 is chosen after determining the carrier frequency for $link_{3\text{-}coil}$. It should be noted in Figure 6.9a that the Rx-PRS at 13.56 MHz is very small, indicating the need to move $link_{3\text{-}coil}$ operation to higher frequencies, and justifying the dual-band design.

The diameter of L_6, d_6, is a design input based on a trade-off between the cortical area of interest, where L_7 is to be located, and $PTE_{3\text{-}coil}$, which is determined by the loose coupling between L_6 and L_7. In our target application for the FF-WIOS, L_6 is designed to encompass the V1 lobes of rats [137]. Since each V1 lobe covers an area approximately from 0.5 mm to 5 mm lateral of the skull midline in rats [143], d_6 should be more than 1 cm for proper coverage. L_6 is made of AWG26 magnetic wire to achieve high Q-factor while fitting in the limited space on the rat skull. The number of turns for L_6, n_6, is minimized to a single turn to ensure that its SRF is at least 4× higher than $link_{3\text{-}coil}$ carrier frequency [28]. According to [29] and [31], d_6, is optimized by maximizing $k^2_{67}Q_6Q_{7L}$, in which k_{67} is the coupling coefficient between L_6 and L_7, Q_6 is the Q-factor of L_6, and Q_{7L} is the loaded Q-factor of L_7. In Figure 6.9b, d_6 is swept from 1 cm to 2 cm with a step size of 2.5 mm. As d_6 increases, $k^2_{67}Q_6Q_{7L}$ reduces. With a certain margin of error, d_6 = 11.6 mm is selected.

The thickness of various tissue layers, depending on the anatomical position of the FF-WIOS, determines the distance between L_5 and L_6, $D_{3\text{-}coil}$. For a rodent model, $D_{3\text{-}coil} \leq$ 5 mm, considering the thicknesses of skin and fat between L_5 and L_6. Like L_6, the number of turns for L_5, n_5, is selected as one to achieve the highest SRF [28]. A thicker AWG20 magnetic wire (w_5 = 0.8 mm) was chosen, though, to increase its Q-factor without any considerable increase in the headstage weight.

In Figure 6.9c, $PTE_{3\text{-}coil}$ is simulated as a function of frequency under different L_5 diameters, d_5. Compared to $PTE_{3\text{-}coil}$ at d_5 = 14 mm, $PTE_{3\text{-}coil}$ at d_5 = 15 mm drops across the entire frequency sweep with its peak shifted to lower frequencies, while $PTE_{3\text{-}coil}$ at d_5 = 13 mm has its peak appeared at high frequencies. To optimize d_5, we also need to consider PCE_{VD}, which is plotted on the right axis of Figure 6.9c as a function of frequency. As expected, PCE_{VD} decreases at higher frequencies. $PTE_{3\text{-}coil} \times PCE_{VD}$ at three options for d_5 are normalized and plotted in Figure 6.9c also, which is maximized at 60 MHz with d_5 = 14 mm. Thus, 60 MHz is selected as the carrier frequency for $link_{3\text{-}coil}$, and $n_7 = 6$ is selected based on the simulation results in Figure 6.9a. Figure 6.9d presents the local SAR stimulation at 60 MHz under the same power source setting in Figure 6.8c. The maximum local SAR value is ~2.96 W/kg, which is well below the safety limit [32].

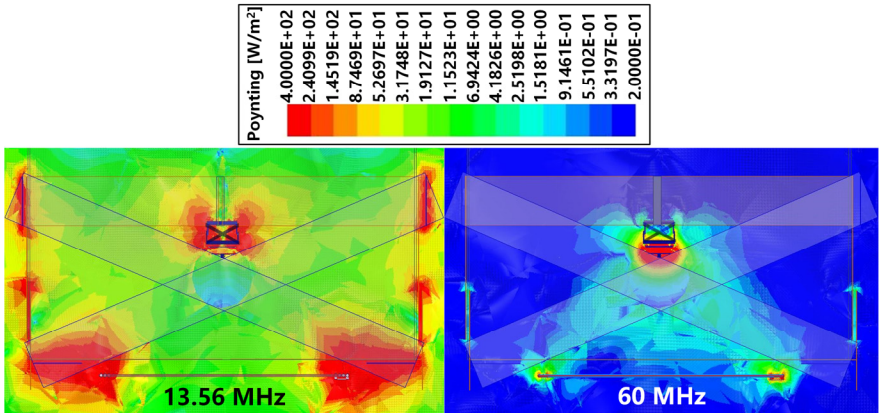

Figure 6.10. Poynting vector simulation in HFSS for $link_{4\text{-}coil}$ and $link_{3\text{-}coil}$ operating at 13.56 MHz and 60 MHz, respectively.

Figure 6.10 shows the Poynting vector simulations in HFSS, which indicate the directional power flux density, i.e. the rate of power transfer per unit area. The red areas exhibit the highest directional power flux density. Two inductive links are activated simultaneously under the same power source setting for the local SAR simulation. At 13.56

MHz, the red area is mainly distributed around L_{3j} and L_4, while at 60 MHz, they are mainly around L_5 and L_6. This simulation also supports the initial assumption for negligible interference between the two inductive links, which are separately optimized.

6.3 Experimental Measurements

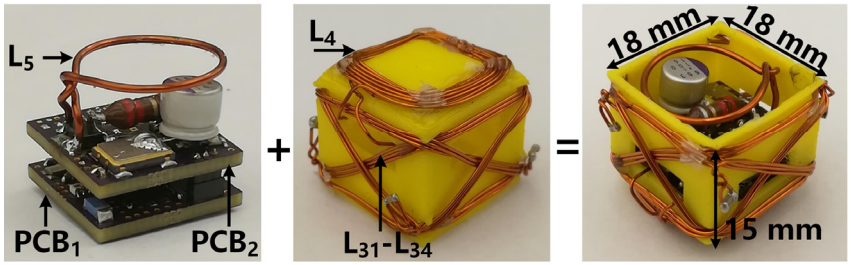

(a)

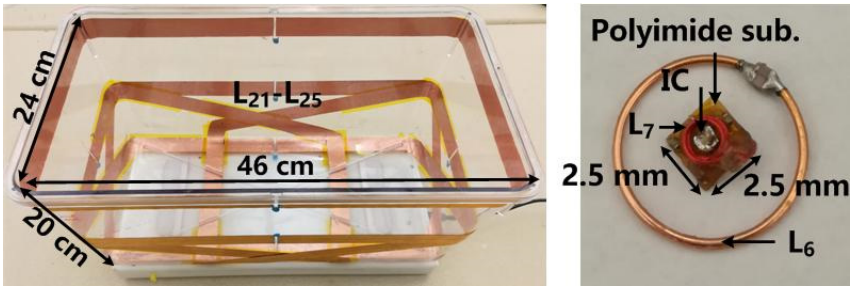

(b) (c)

Figure 6.11. Implementation of (a) the dual-band headstage, which houses L_{31}-L_{34}, L_4, and L_5, (b) EnerCage-HC prototype, which houses L_1, L_{20}-L_{25}, and the driver box underneath, (c) L_6 resonator and the FF-WIOS, which houses L_7.

Figure 6.11 shows implementation of the dual-band EnerCage-HC prototype. In Figure 6.11a, the headstage electronics in the form of two stacked PCBs are enclosed in a 3D-printed box for protection against moisture and damage, while providing mechanical support for L_{3j} coils, resulting in an 18×18×15 mm^3 cube, weighting 4.8 g. In Figure 6.11b, a 46×24×20 cm^3 standard rat homecage (Alternative Design, Siloam Springs, AR), is used as mechanical support for L_{2i} coils, which are also covered with Kapton® tape (polyimide film) to improve insulation. The FF-WIOS is a 2.5×2.5×1.5 mm^3 device, shown in Figure

6.11c, weighing only 15 mg. Figure 6.11c also shows the implantable L_6 and its resonance capacitor. Dual-band coils' specifications, which are optimized according to the steps described in Figure 6.7, are summarized in Table 6.1.

Table 6.1. Measured specifications of the dual-band inductive links.

Coils*	L_{31}-L_{34}	L_4	L_5	L_6	L_7
Frequency	13.56 MHz			60 MHz	
Inductance (nH)	0.59	0.92	26	21.2	50.1
Q-factor	120	139	246	79	22
d_o, d_i (mm)	-	16, 11	-	-	-
d (mm)	-	-	14.5	11.6	1.6
Width (mm)	18	-	-	-	-
Length (mm)	18	-	-	-	-
Distance	Height = 7 cm			$D_{3\text{-}coil}$ = 5 mm	
Number of turns	3	6	1	1	6
Wire type	AWG 26	AWG 26	AWG 20	AWG 26	AWG 34
PTE	14.9%-22.7%			18%	

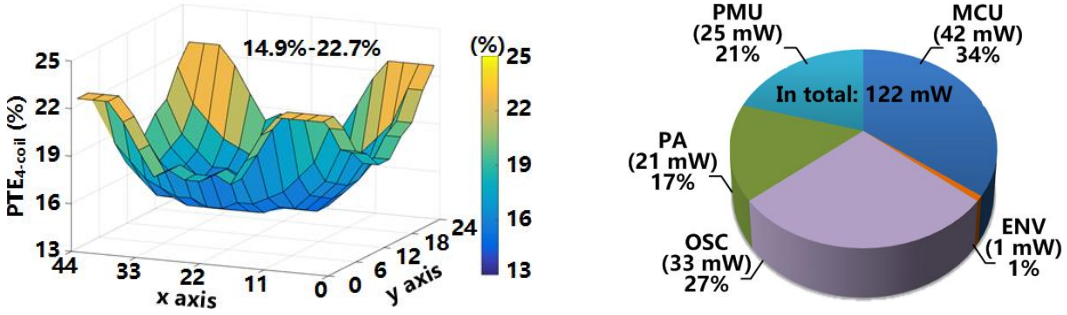

(a) (b)

Figure 6.12. (a) $PTE_{4\text{-}coil}$ measurement by sweeping the Rx in the homecage across XY plane at 7 cm height. (b) Power consumption of each block in the headstage.

Figure 6.12a presents the $PTE_{4\text{-}coil}$ distribution across the homecage at 7 cm above the bottom of the homecage, measured by moving the headstage horizontally across the XY plane. Due to the significant difference between the sizes of headstage and homecage, center of the homecage generally has weaker mutual coupling with the headstage compared to its perimeter, resulting in the lower end of 14.9%-22.7% range in $PTE_{4\text{-}coil}$. Thus, to consider the worst-case scenario, the following measurements were conducted with the

entire Rx apparatus, referred to the headstage, link$_{3\text{-coil}}$, and FF-WIOS, initially placed in the center of the homecage, at the height of 7 cm from the bottom, with $D_{3\text{-}coil}$ = 5 mm.

Figure 6.12b pie-chart shows the 122 mW power distribution among headstage building blocks, measured when V_{DBR_HS} was set at 4.2 V. The headstage MCU has the highest power consumption at 42 mW, followed by the 60 MHz oscillator, at 33 mW. The power management unit and envelope detector also consume 25.1 mW and 1 mW, respectively. The rest of the received power at the headstage (21.4 mW) is consumed by the Class-E PA$_{60MHz}$, part of which is delivered to FF-WIOS through link$_{3\text{-coil}}$. This power distribution shows that there is considerable room in improving the headstage overall power efficiency.

6.4 *In Vitro* Experiments

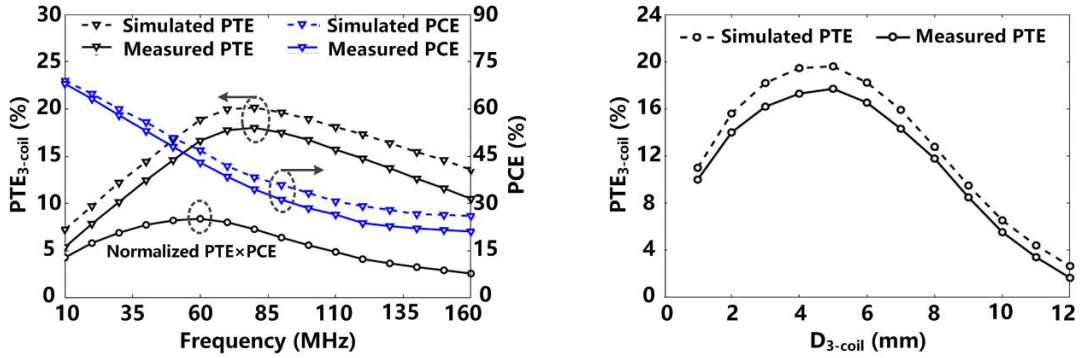

(a) (b)

Figure 6.13. (a) PTE$_{3\text{-coil}}$ and PCE$_{VD}$ in simulation and measurement and normalized PTE$_{3\text{-coil}}$×PCE$_{VD}$ vs. frequency (b) simulated and measured PTE$_{3\text{-coil}}$ vs. $D_{3\text{-}coil}$.

To characterize the system specifications in the presence of real tissue layers, we conducted *in vitro* experiments and used tissue layers of brain, skull, fat, and skin, which are cut from a fresh sheep head, to surround the link$_{3\text{-coil}}$ and the FF-WIOS. Figure 6.13a shows a good agreement between the measured and simulated results of PTE$_{3\text{-coil}}$ and

PCE_{VD} in the frequency range of 10 MHz to 160 MHz. Measured $PTE_{3\text{-}coil} \times PCE_{VD}$ is normalized and presented on the same graph also. The lower $PTE_{3\text{-}coil}$ in measurements is mainly attributed to the effect of tissue on L_6 because of its large contact area with the surrounding tissue, and the resulting detuning. Fabrication tolerances could be another reason for the difference. For the PCE_{VD}, the difference could be due to process variations and parasitic effects of the measurement instruments, which have not been fully considered in simulations. A key finding, however, is verifying that the optimal carrier frequency for $link_{3\text{-}coil}$ to maximize $PTE_{4\text{-}coil} \times PCE_{VD}$ is indeed at 60 MHz. Figure 6.13b shows the comparison between the measured and simulated $PTE_{3\text{-}coil}$, while sweeping $D_{3\text{-}coil}$ from 1 mm to 12 mm. Expectedly, the maximum $PTE_{3\text{-}coil}$ is achieved at the designated $D_{3\text{-}coil}$ = 5 mm. It should also be noted that in the range of 3 mm to 7 mm, around the nominal $D_{3\text{-}coil}$ = 5 mm, the $PTE_{3\text{-}coil}$ has less than 10% drop from its peak, indicating the insensitivity of $link_{3\text{-}coil}$ to small $D_{3\text{-}coil}$ variations. Based on P_{i_HS} = 122 mW and $PTE_{4\text{-}coil}$ is 14.9% at the center of the homecage, the homecage output power, P_{o_HC}, at 13.56 MHz can be calculated as 819 mW. The measured input DC power of the EnerCage-HC under this condition was 1.14 W, resulting in PCE_{HC} to be 72%. Similarly, with $PTE_{3\text{-}coil}$ = 18% and P_L = 2.7 mW, the P_{o_HS} is calculated to be 15 mW at 60 MHz. Since PA_{60MHz} consumes 21.4 mW, its efficiency is 70%, while headstage PCE_{HS} is calculated to be 12.3%. Under these conditions, dual-band PTE_{total} is 0.24%-0.36%, which is small but sufficient for indefinitely operating the FF-WIOS while staying well below the SAR limits.

The CLPC is in charge of improving the system robustness against three types of disturbances in the two inductive links: 1) movements of the entire Rx in terms of height, position, and orientation along with the behaving animal head motion with respect to the

stationary EnerCage-HC, 2) changes in the headstage position with respect to the rodent head, resulting in variations in $D_{3\text{-}coil}$ and the concentric alignment between L_5 and L_6, 3) changes in the position and orientation of the FF-WIOS due to uneven brain surface (gyri and sulci) and its migration or micromotions. All of these disturbances affect P_L, in response to which, the CLPC adjusts P_{o_HC} to ensure that the minimum required P_{i_HS} is always available to the headstage.

Figure 6.14a compares the measured P_{i_HS} with and without CLPC when the Rx was swept across the XY-plane at 7 cm height. With the CLPC on, P_{o_HC} was dynamically adjusted to maintain P_{i_HS} within a desired window around 122 mW across the entire homecage. In contrast, P_{i_HS} varies significantly in open loop operation when P_{o_HC} is constant at 0.7 W. Near corners of the homecage, coupling is too strong, and P_{i_HS} could result in unsafe overvoltage in the headstage, if it is not protected, while P_{i_HS} is insufficient near the center, and may cause the headstage to shut down.

In Figure 6.14b, the Rx was moved manually from the bottom to top of the homecage at the center of the cage with a step size of 2 cm. Since this movement had little effect on the $\text{link}_{3\text{-coil}}$, the required P_{i_HS} to power up the FF-WIOS remained stable. However, as the Rx is elevated, $\text{PTE}_{4\text{-coil}}$ reduces, and P_{o_HC} is forced to increase by the CLPC to stabilize P_{i_HS}. Once the headstage is mounted on the animal head with dental cement, glue, or permanent magnets, L_6 maintains its relative position with respect to the headstage along with the animal head.

Figure 6.14c presents the variations of P_{i_HS} and P_{o_HC}, caused by either the headstage rotation (angular misalignment) relative to the homecage, $\theta_{HC\text{-}HS}$, or the FF-

WIOS rotation relative to the headstage, $\varphi_{HS\text{-}FF}$. In particular, $\varphi_{HS\text{-}FF}$ decides the required P_{i_HS} of the headstage to power up the FF-WIOS due to the disturbance in link$_{3\text{-coil}}$, while $\theta_{HC\text{-}HS}$ decides how much P_{o_HC} is needed to provide the required P_{i_HS} due to the disturbance in link$_{4\text{-coil}}$. This means that P_{i_HS} is not influenced by $\theta_{HC\text{-}HS}$, within the range of P_{o_HC}. Therefore, in Figure 6.14c we have only plotted P_{i_HS} vs. $\varphi_{HS\text{-}FF}$ at $\theta_{HC\text{-}HS} = 0^{\circ}$. As expected, the required P_{i_HS} increases as $\varphi_{HS\text{-}FF}$ increases. Moreover, the curves in blue show P_{o_HC} variations as a function of $\varphi_{HS\text{-}FF}$ under four $\theta_{HC\text{-}HS}$ values. As $\theta_{HC\text{-}HS}$ increases, P_{o_HC} variations are elevated, while still responding to $\varphi_{HS\text{-}FF}$ variations. For example, when $\theta_{HC\text{-}HS} = 0^{\circ}$, P_{o_HC} can compensate for the misalignment of $\varphi_{HS\text{-}FF}$ up to 50º, however, for $\theta_{HC\text{-}HS} = 70^{\circ}$, P_{o_HC} can only support the required P_{i_HS} for $\varphi_{HS\text{-}FF}$ up to 20º.

Figure 6.14d and 6.14e show the automatic changes in P_{i_HS} and P_{o_HC} in response to various misalignments between L_5 and L_6. In Figure 6.14d, $D_{3\text{-}coil}$ changes from 1 mm to 12 mm due to movement of the FF-WIOS together with L_6. As $D_{3\text{-}coil}$ deviates from the designated value of 5 mm distance between L_5 and L_6, PTE$_{3\text{-coil}}$ decreases. To compensate for the PTE$_{3\text{-coil}}$ drop, P_{o_HC} is forced to increase by the CLPC to provide additional P_{i_HS}. The CLPC can compensate for the $D_{3\text{-}coil}$ variations up to 12 mm, beyond which the EnerCage-HC and headstage would not be able to power up the FF-WIOS.

In Figure 6.14e, the horizontal shifts happen along with the horizontal movements of the FF-WIOS together with L_6 with respect to L_5. Since PTE$_{3\text{-coil}}$ decreases, extra P_{i_HS} is required to stabilize P_L. CLPC has increased P_{o_HC} to provide the extra P_{i_HS}. For FF-WIOS horizontal misalignments >7 mm, PTE$_{3\text{-coil}}$ drops to a level that the EnerCage-HC can no longer provide sufficient P_{o_HC} to activate the FF-WIOS though the headstage. The measurements in Figure 6.14 collectively indicate that the CLPC can keep the headstage

and FF-WIOS functional by stabilizing P_{i_HS} and P_L in the entire volume of the homecage. The measured specifications of the proposed system are summarized in Table 6.2.

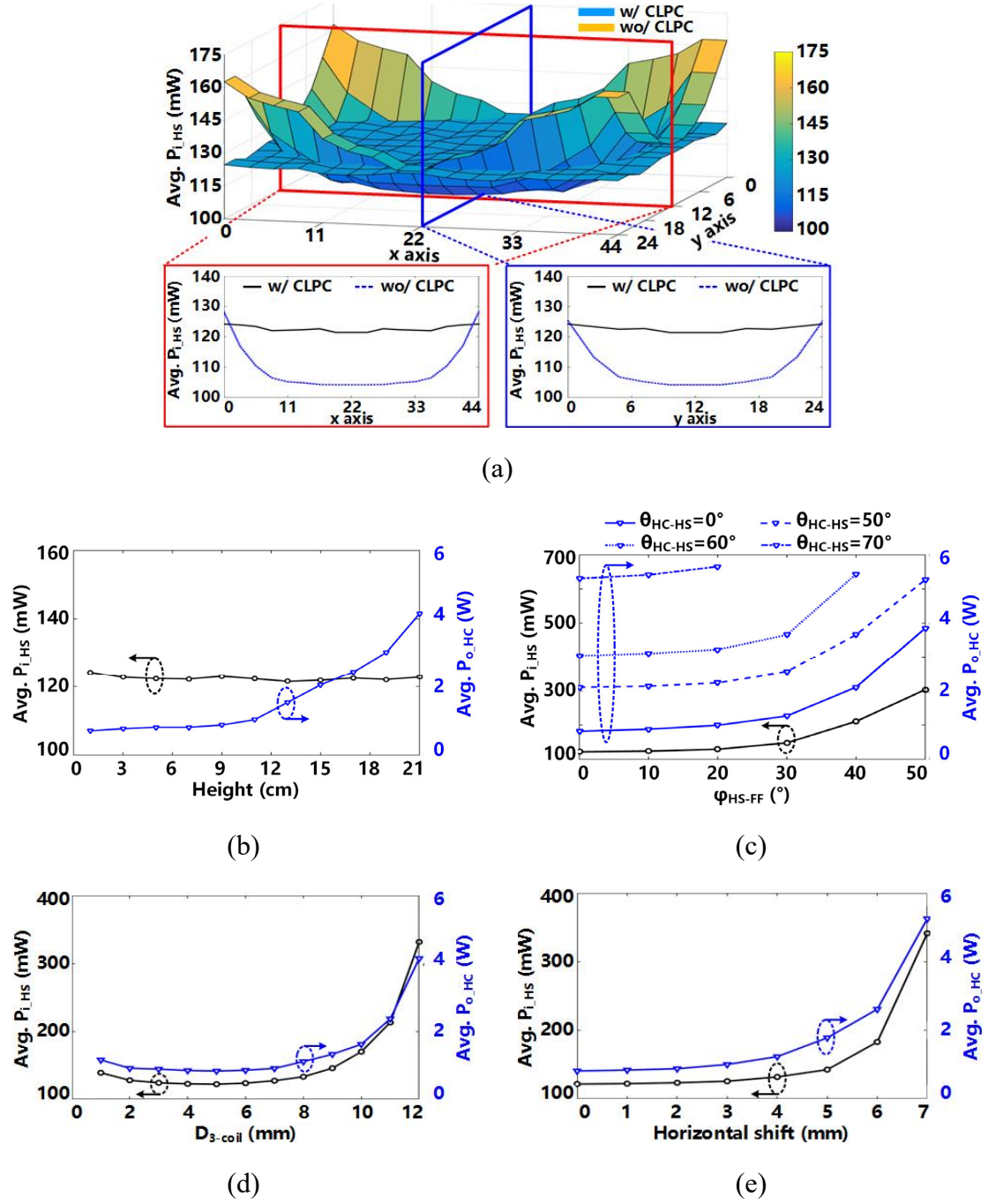

Figure 6.14. (a) Measured P_{i_HS} when the entire Rx is swept across the XY-plane at 7 cm height with and without CLPC. Measured P_{i_HS} and P_{o_HC} as a function of (b) headstage height, (c) $\theta_{HC\text{-}HS}$ and $\theta_{HS\text{-}FF}$, (d) $D_{3\text{-}coil}$, and (e) horizontal misalignment between L_5 and L_6.

Table 6.2. Measured specifications of the dual-band EnerCage-HC system.

EnerCage-HC		FF-WIOS	
Size	46×24×20 cm^3	Size	46×24×20 cm^3
P_{o_HC}	Up to 5.6 W	P_{o_HC}	Up to 5.6 W
PCE_{HC}	72%	PCE_{HC}	72%
Headstage		CLPC	
Size	18×18×15 mm^3	Size	18×18×15 mm^3
Weight	4.8 g	Weight	4.8 g
P_{i_HS}	122-341 mW	Wireless Data Transmission	
PCE_{HS}	12.3%	BLE	32 kbps @ 2.4 GHz
PA_{60MHz} Eff.	70%	FT/BT	50 kbps/160 Hz @ 60 MHz

In Figure 6.15, the CLPC transient response is presented in three disturbance scenarios. In the steady state phase, V_{PA_HC} fluctuates within 17-18 V window according to the CLPC mechanism, and the headstage keeps V_{DBR_HS} within 4.5-5.5 V to maintain V_{DBR_FF} fluctuating around 4.2 V, depending on the presence or absence of BT_{FF} pulses. In Figure 6.15a, the FF-WIOS is manually moved at ~7 s to increase $D_{3\text{-}coil}$ from 5 mm to 10 mm, which leads to $PTE_{3\text{-}coil}$ reduction. As a result, V_{DBR_FF} initially drops slightly, while CLPC starts to compensate by increasing the V_{DBR_HC} variation window, and V_{PA_HC} to oppose this perturbation. It takes ~0.6 s for the V_{PA_HC} and V_{DBH_HS} to settle in their new fluctuation windows. Once the FF-WIOS is returned back to its original distance from the headstage at ~13 s from the beginning of the recording, V_{PA_HC} and V_{DBH_HS} return back to their original voltage windows as well. In Figure 6.15b, the FF-WIOS was gradually rotated starting at ~2 s to increase $\varphi_{HS\text{-}FF}$ from 0° to 30°, while maintaining $\theta_{HC\text{-}HS}$ = 0°. Because of the drop in $PTE_{3\text{-}coil}$, the V_{DBR_FF} variation is slightly decreased, while the fluctuation windows for V_{PA_HC} and V_{DBR_HC} are elevated by the CLPC to compensate for the higher power demand to keep FF-WIOS operational. At the steady state of $\varphi_{HS\text{-}FF}$ = 30°, V_{PA_HC} and V_{DBR_HS} are bounded within 19-21 V and 5.5-6.2 V, respectively. After returning back to $\varphi_{HS\text{-}FF}$ = 0° at ~12 s, V_{PA_HC} and V_{DBR_HC} return back to original ranges.

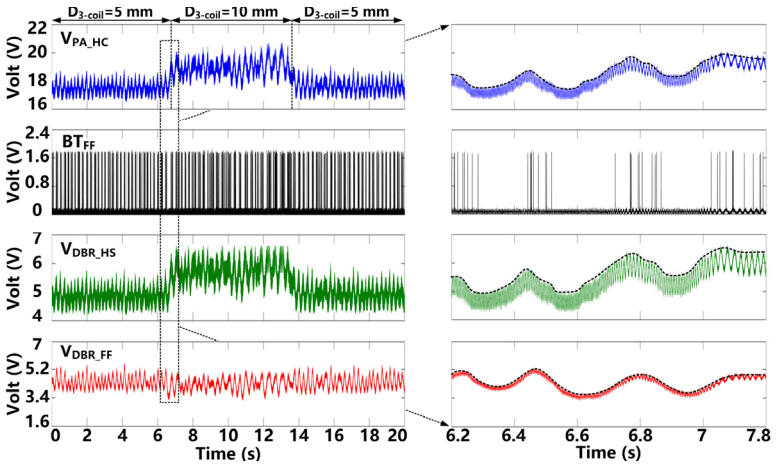

(a)

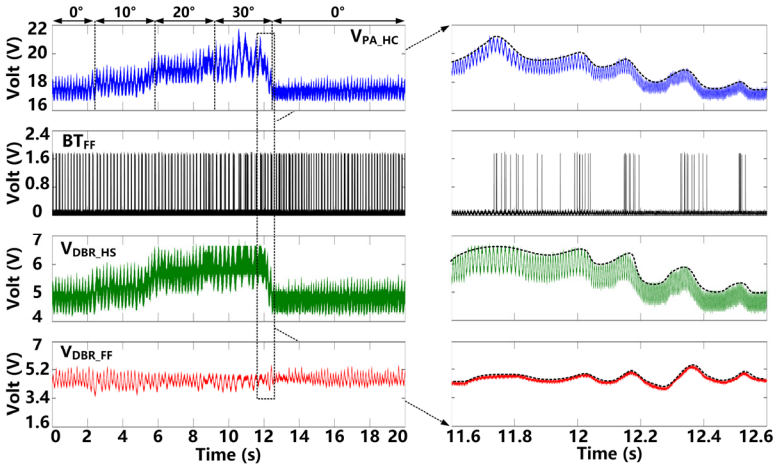

(b)

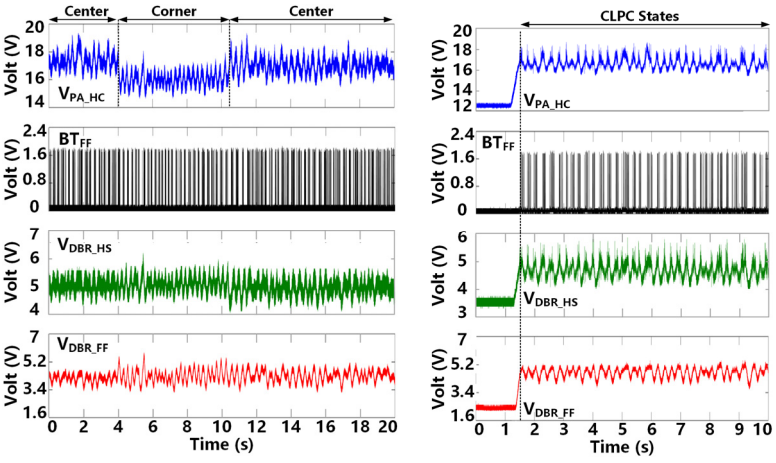

(c) (d)

Figure 6.15. Transient waveforms of V_{PA_HC}, BT_{HS}, V_{DBR_HS}, and V_{DBR_FF} under CLPC operation, when (a) moving the FF-WIOS to change $D_{3\text{-}coil}$ from 5 mm to 10 mm and

back to 5 mm, (b) rotating the FF-WIOS to increase $\varphi_{HS\text{-}FF}$ up to 30° and return it back to 0°, and (c) moving the entire Rx from the center of the homecage to the corner and back to the center. (d) CLPC startup transients.

In Figure 6.15c, the entire Rx was moved from the center of the homecage to the corner at ~4 s, resulting in increased $PTE_{4\text{-coil}}$. It can be seen that V_{DBR_HS} fluctuations increase, followed by that of V_{DBR_FF}. With the CLPC operation, the V_{PA_HC} variations are lowered to 14.3-15.6 V to reduce the power delivered via the $link_{4\text{-coil}}$, stabilize V_{DBR_HS} within 4.5-5.5 V range, and keep the same amount of power delivered to the FF-WIOS. Once the Rx is moved back to its original location, V_{PA_HC} also returns to its original window of variations. In Figure 6.15d, with the entire Rx apparatus at the center of the homecage, the initial value of V_{PA_HC} is 12 V, when the system is powered on, resulting in V_{DBR_HS} of 3.6 V and V_{DBE_FF} of 2.5 V, which are just sufficient to operate the headstage and the FF-WIOS, respectively. To meet the target V_{DBR_FF} = 4.2 V, V_{PA_HC} and V_{DBR_HS} are increased in response to the CLPC operation, and settled after ~0.5 s within the windows of 16.2-17.8 V and 4.4-5.2 V, respectively.

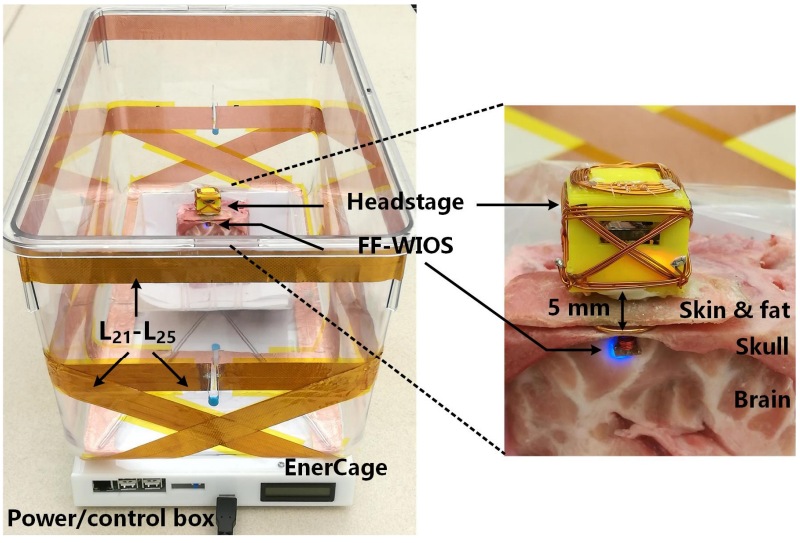

Figure 6.16. The final *in vitro* measurement setup using the sheep head layers with a close-up view of the headstage and the FF-WIOS.

Figure 6.16 shows the final *in vitro* measurement setup for enabling optical stimulation in the proposed system. We cut out a 6×6×7 cm^3 cube from a fresh sheep head, including brain, skull, fat, and skin, and placed the cube in the center of the cage. The headstage was mounted on top of the tissue cube by facing L_5 downward onto the skin layer. L_6 was placed above the skull but under the scalp, well aligned with L_5, while the FF-WIOS was concentrically aligned with L_6 and placed ~2 mm under the skull. At the end, we had 5 mm distance between L_5 and L_6 filled with scalp, fat, and air layers. The headstage was then wirelessly powered with active CLPC. Both the orange LED that is an indicator of the headstage receiving sufficient power at 13.56 MHz and the selected blue LED, driven by the FF-WIOS that is powered at 60 MHz are on. These measurements demonstrate the feasibility of dual-band WPT and FF-WIOS assembly/packaging and overall functionality of FF-WIOS and EnerCage-HC systems at *in vitro* level.

6.5 Summary and Discussion

We have studied several state-of-art WPT solutions for neural interfacing application and summarized them in Table 6.3. To facilitate comparison among multiple key factors in this application, we have defined a new figure of merit (FoM) as,

$$FoM = PTE_{total} \times D_{Tx-Rx} \times \frac{U_{Tx}}{U_{Rx}} \quad (3)$$

where $D_{Tx\text{-}Rx}$ is the total WPT distance, U_{Tx} is the volume covered with sufficient PDL, and U_{Rx} is the volume of the Rx device.

Compared to the abovementioned WPT systems for small IMDs, the proposed system is competitive in terms of both PTE_{total} and IMD size. More importantly, it is able to wirelessly power the mm-sized IMDs within a large rodent homecage, resulting in the

best FoM. However, achieving this dual-band WPT method requires the addition of an extra headstage. As long as the size and weight of the headstage are below certain limits, established by the norms of behavioral research on small animal subjects, to make them manageable by the animal species, the headstage is not affecting the subject behavior. In addition, the headstage is positioned outside the animal body and does not make the device any more invasive. Moreover, not all the power that is consumed by the headstage should be considered wasted because first of all, part of it is stored in its super capacitor (or rechargeable battery) to help with continuous operation of the FF-WIOS.

Table 6.3. Benchmarking of the WPT system for small mm-sized IMDs.

Publication	2015 [69]	2016 [42]	2017 [76]	2018 [68]	**This work**
WPT mechanism	Resonant cavity	Inductive	Inductive/ ultrasound	RF (antenna)	**Dual-band Inductive**
Frequency (MHz)	1.5 GHz	13.56	1.1 / 1.1	1.8/2.9 GHz	**13.56/60**
WPT coverage (cm^3)	$\pi\times10.5^2\times15$	14×12×7	$\pi\times5^2\times6$	$4/3\times\pi\times10^3$	**46×24×20**
Rx size (mm^3)	10	10×10×3	1	125	**2.5×2.5×1.5**
PTE_{total} (%)	0.18-0.49	2.9-6.4	0.16	0.5-0.9	**0.24-0.36**
Wireless data transmission	Tx PWM	-	-	Tx PWM	**OOK/LSK/ BLE**
CLPC	No	-	No	No	**Yes**
FoM ($\times10^9$)	1.41-3.83	0.09-0.18	0.45	0.17-0.3	**11.3-16.96**
Intermediate device (mm^3)	No	No	Yes, 31×17×2	No	**Yes, 18×18×15**

Even though the presented system is focusing on wireless operation of the FF-WIOS, as an exemplar IMD for a high power application, such as optogenetic stimulation, the high PTE and stable PDL capabilities of the proposed approach makes it a suitable choice for other types of IMDs and WPT applications where extreme size and harsh environment are key challenges.

CHAPTER 7. CONCLUSIONS AND FUTURE WORK

This dissertation focuses on developing innovative circuit- and system-level techniques for the development of various IMDs with wireless power transmission and data communication. The WOENI device has been proven as a versatile tool in the studies that involve long-term optogenetic neuromodulation and ECoG recording. The EnerCage-HC2 system, which takes advantage of the novel 4-coil inductive link design and the CLPC mechanism, can wirelessly power a variety of sensors, actuators, and other electronic devices that are attached to or implanted in the animal body, irrespective of the position and orientation of the Rx within the entire volume of the rodent homecage, while creating an enriched environment close to their natural habitat.

The WINeRS-8 device, which is wirelessly powered in the EnerCage-HC2, can apply neural recording and electrical stimulation. For the wireless data communication with the WINeRS-8, the dual-SDR data Rx is developed to pick up the recording data signal outside of the homecage, while maintaining wireless data integrity and continuity, in the presence of any misalignments between the Tx and Rx antennas. The FF-WIOS device, with compact size and light weight, as well as high-level integration of front-end circuits and wireless power/data transmission related circuits, can apply 16-ch wireless optical stimulation. Correspondingly, the first near-field WPT approach that selects two optimal bands based on the sizes of the headstage and the tiny implant is proposed for wireless power delivery to the tiny implant, regardless of misalignments caused by the headstage and the tiny implant within the rodent homecage. This chapter summarizes the results and scientific contributions of this dissertation, followed by future work.

7.1 Conclusions

7.1.1 Battery-Powered Neural Interface Devices

The WOENI device, equipped with optical stimulation and ECoG recording for bi-directional neuromodulation, has been presented. The wireless data transmission link between the headstage and a USB dongle, ensures remote control of the headstage, resulting in an untethered system with a low risk of biasing the animal behavior. The functionality of the WOENI device has been demonstrated *in vivo* by applying cortical optical stimulation and visual stimulation on freely behaving rats. Moreover, the consistency of *in vivo* results observed in four consecutive experiments, evenly distributed over 21-days post-implantation, can validate the stability and utility of the WOENI device.

7.1.2 Wireless Power Transmission Systems

The EnerCage-HC2, a wireless research instrument for conducting behavioral research on freely moving rodents, has been presented. It is robust and fully compatible with dimensions of standard homecage used in animal research facilities. To be more specific, it benefits from: 1) a novel geometrically-optimized array of Rx coils for harvesting EM power for the headstage at any arbitrary positions or orientations within the homecage, 2) an array of strategically positioned high-Q segmented Tx coils that create a homogeneously EM powered space across the entire homecage, 3) a robust communicating network based on Wi-Fi, UART, and BLE links, realizing remote control of and data acquisition from the headstage, and 4) a CLPC mechanism ensuring sufficient and stable power delivery to the headstage. We have verified the functionality of the EnerCage-HC2 *in vivo* for wireless DBS by targeting the right GPi in three freely moving rats, eliciting a

distinct, well-documented, and very consistent behavior, involving quantified head rotation, while recording the actual stimulus current and measures of Tx and Rx power.

Based on the EnerCage-HC2, we have also demonstrated that the proposed dual-band EnerCage-HC system accommodates robust WPT to mm-sized IMDs within the standard rat homecage in the presence of various misalignments. The devised dual-loop sequential CLPC mechanism has further improved the system robustness by adjusting the EnerCage-HC transmitted power to stabilize the PDL for the FF-WIOS, which is an example of the tiny implants used for high power applications. The two-stage wireless data transmission also enables remote control of the FF-WIOS, which has been tested *in vitro*.

7.1.3 Wirelessly Powered Neural Interface

The WINeRS-8 device that is compatible with both the EnerCage-HC2 for battery-less operation and the dual-SDR Rx for wireless recording data acquisition has been presented for long-term neuroscience experiments on freely moving rodents. The WINeRS-8 SoC includes front-end circuits for 32-ch neural recording, 4-ch electrical stimulation, as well as wireless power Rx circuits, and wireless data Rx and Tx circuits for untethered and battery-free operation. For the, the recording and stimulation parameters are sent through either BLE link or OOK modulation of the power carrier. The narrowband downlink data transmission is implemented by both OOK-PPM of the power carrier and BLE link to deliver user-defined parameters to the SoC. The wideband uplink data transmission uses a 433 MHz RF Tx to send neural recording data out. The RF signal is then picked up outside the homecage by a pair of BladeRF SDR Rxs, which extend the wireless coverage of the experimental arena and eliminate any blind spots caused by the

Tx antenna directivity. The entire WINeRS-8 system forms bidirectional wireless and battery-less neural interface within a standard homecage. The system has been verified *in vivo* on rat animal model. Real-time stimulation and recording demonstrated the system's potential for supporting longitudinal neuroscience experiments in an enriched environment.

Based on the WINeRS-8 SoC design, the first trimodal wireless implantable neural interface SoC capable of neural recording, electrical stimulation, and optical stimulation has been designed. This SoC, which we call WINeRS-9, is also designed to be compatible with the EnerCage-HC2. The WINeRS-9 SoC includes front-end circuits for 16-ch neural recording, 16-ch electrical stimulation, and 16-ch optical stimulation, as well as wireless powering and communication circuits for untethered and battery-free operation.

7.1.4 SDR Data Rx for Wideband Data Acquisition

A scalable dual-SDR Rx system for wideband and robust wireless data acquisition as part of the WINeRS-8 system has been presented. The current prototype can achieve a data rate of 9 Mbps with WINeRS-8 headstage via OOK of a 434 MHz RF carrier, while the headstage is wirelessly powered in the EnerCage-HC2 at 13.56 MHz. Measurement results show that the dual-SDR Rx system can eliminate RF blind spots with the redundancy offered by two orthogonal directional Rx antennas. The presented system overcomes the inflexibility of custom hardware implementation without imposing too much workload on the back-end computing resources in real-time operation. The functionality of the system has been verified both *in vitro* and *in vivo* on a freely behaving rat model in comparison with a commercial hardware system as the gold standard.

7.1.5 Fully Implantable Tiny Implants

A wirelessly powered free-floating implantable optical stimulation device has been presented. With its compact size and light weight, the FF-WIOS is expected to minimize tissue damage and therefore enable efficient chronic wireless optical stimulation. Thanks to the 3-coil inductive link design, the FF-WIOS is efficiently powered, while staying well below the SAR limit. Wireless data transmission between the headstage and FF-WIOS is established with OOK modulation of the power carrier. The CLPC mechanism is also utilized to ensure stable power delivery to the FF-WIOS. The SCS architecture implemented in the FF-WIOS SoC provides high instantaneous current for effective optical stimulation without putting too much burden on the inductive link. The circuit topology for each block is chosen for power/area efficiency and design simplicity to achieve a compact and reliable SoC design. It is possible to further reduce power consumption using ultra-low power circuit designs. We have verified the functionality of the entire system *in vitro* and *in vivo* on sheep head and rat models, respectively. We targeted the left V1 of two anesthetized rats with wireless optical stimulation, while observing light-evoked LFPs and immunostained tissue responses.

Based on the FF-WIOS SoC design, the most comprehensive mm-sized neuromodulation SoC, FF-WIOS2, has been designed. This SoC is designed to have 16-ch optical stimulation and 4-ch electrical stimulation. In addition, this SoC also integrates wireless powering and communication circuits to be compatible with the dual-band EnerCage-HC for untethered and battery-free operation.

7.2 Future Work

The EnerCage-HC2 system, built around the standard homecage, compatible with racks in large animal facilities is scalable from a single EnerCage-HC2 system to a large

rack of multiple EnerCage-HC2 systems, called multi-EnerCage-HC system. The multi-EnerCage-HC system, which runs in parallel for high throughput experiments, while controlled with only one computer (PC station) via Wi-Fi connection, is our next goal. However, in the multi-EnerCage-HC system, high-quality resonators are used to build every single EnerCage-HC2 system. The resonators of one single EnerCage-HC2 system have mutual inductance with the resonators in the adjacent EnerCage-HC2 systems if the gap between them is less than 20 cm. This mutual inductance shifts the resonance frequency of the entire multi-EnerCage-HC system and must be avoided to prevent decrement of PTE or PDL of each EnerCage-HC2 system. Therefore, it is necessary to develop an auto-tuning mechanism in each EnerCage-HC2 system to re-turn its resonance frequency considering the EM interference from adjacent EnerCage-HC2 systems if the gap between multiple of EnerCage system is less than 20 cm.

Based on the WINeRS-8 SoC design, a trimodal neural interface SoC, which we call WINeRS-9 has been designed and fabricated in TSMC 0.35-µm standard CMOS process. The WINeRS-9 SoC is capable of neural recording, electrical stimulation, and optical stimulation has been designed. The next step is to build the WINeRS-9 headstage and test it *in vivo*, first on anesthetized rats and then on freely behaving subjects with EnerCage-HC2 system and the dual-SDR data Rx system.

The future work about the dual-SDR data Rx system includes closed-loop neuromodulation with real-time distributed signal processing of the recorded data using the embedded FPGA in each SDR Rx. As scaling up the number of BladeRF SDR Rxs to increase the wireless coverage, the proposed system prototype can also be utilized for experiments involving non-human primates (NHP), which are often housed in larger cages.

The FF-WIOS prototype used for *in vitro* experiments is the miniaturized version of the FF-WIOS prototype used *in vivo*. By the miniaturized version of FF-WIOS, we are referring to the prototype built on a polyimide substrate. We are now working towards testing this miniaturized version *in vivo*, first on anesthetized rats and then on freely behaving subjects within the EnerCage-HC2 environment [33], [34]. Since the miniaturized version has smaller Cree μLEDs assembled, the resolution of optical stimulation applied using this prototype can be improved.

For the dual-band EnerCage-HC system, the next step is to conduct *in vivo* experiments to further evaluate the performance of the entire dual-band EnerCage-HC system. Efforts are already ongoing for developing the next version of the headstage. The CC2541 MCU will be replaced with an ultra-low power alternative, e.g., nRF52x family, which reduces the power consumption of that stage roughly by half, even before applying any power management routines. The new headstage will use an ASIC, which integrates some of the blocks on the headstage, such as the power management unit and PA_{60MHz}. It will result in further improvement in the headstage efficiency. These efforts will result in more relaxed power requirement from the EnerCage-HC2 driver box to the extent that it will be USB-powered. With today's computationally-powerful and yet low power MCUs, FPGAs, and custom ASIC solutions, a considerable amount of processing can be performed within the headstage itself to conduct important functions, such as pre-processing and compression to reduce the volume of data before it is wirelessly transmitted or close the neuromodulation loop locally and reduce the latency and possible interruptions that may occur if all the processing is implemented in the backend PC.

As a proof of concept, the abovementioned devices and systems to be developed or improved in the plan will be evaluated with *in vivo* experiments. The next step is to use these fully-evaluated devices and systems for neuroscience studies, such as visual prosthesis, traumatic brain injury, and seizure prediction.

REFERENCES

[1] Global perspective human stories, UN News. Available: https://news.un.org/en/story/2007/02/210312-nearly-1-6-worlds-population-suffer-neurological-disorders-un-report

[2] Neurological disorders public health challenges, World Health Organization. Available:https://www.who.int/mental_health/neurology/neurological_disorders_report_web.pdf

[3] M. M. Maharbiz, R. Muller, E. Alon, J. M. Rabaey, and J. M. Carmena, "Reliable next-generation cortical interfaces for chronic brain-machine interfaces and neuroscience," *Proceedings of the IEEE*, vol. 105, no. 1, pp. 73-82, Jan. 2017.

[4] J. Rivnay *et al.*, "Next-generation probes, particles, and proteins for neural interfacing," *Science Advances*, vol. 3, no. 6, p. 1601649, June 2017.

[5] S. B. Goncalves *et al.*, "Design and manufacturing challenges of optogenetic neural interfaces: a review," *J. Neural Eng.*, vol. 14, no. 4, p. 041001, May. 2017.

[6] S. Santaniello, G. Fiengo, L. Glielmo, and W. M. Grill, "Closed-loop control of deep brain stimulation: a simulation study," *IEEE Trans. Neural Syst. Rehabil. Eng.*, vol. 19, no. 1, pp. 15-24, Feb. 2011.

[7] B. Fan and W. Li, "Miniaturized optogenetic neural implants: a review," *Lab on a Chip*, vol. 15, pp. 3838-3855, Aug. 2015.

[8] R. Pashaie *et al.*, "Closed-loop optogenetic brain interface," *IEEE Trans. Biomed. Eng.*, vol. 62, no. 10, pp. 2327-2337, Oct. 2015.

[9] W. M. Grill, S. E. Norman, and R. V. Bellamkonda, "Implanted neural interfaces: biochallenges and engineered solutions," *Annu. Rev. Biomed. Eng.*, vol. 11, pp. 1-24, Aug. 2009.

[10] J. P. Donoghue, "Bridging the brain to the world: a perspective on neural interface systems," *Neuron*, vol. 60, pp. 511-521, Nov. 2008.

[11] R. Shulyzki *et al*, "320-channel active probe for high-resolution neuromonitoring and responsive neurostimulation," *IEEE Trans. Biomed. Circuits Syst.*, vol. 9, no. 1, pp. 34-49, Feb. 2015.

[12] Z. Luo and M. D. Ker, "A high-voltage-tolerant and power-efficient stimulator with adaptive power supply realized in low-voltage CMOS process for implantable biomedical applications," *IEEE J. Emerg. Sel. Topic Circuits Syst.*, vol. 8, no. 2, pp. 178-186, June 2018.

[13] J. Wang *et al.*, "Integrated device for combined optical neuromodulation and electrical recording for chronic in vivo applications," *J. Neural Eng.*, vol. 13, no. 3, p. 039501, May 2016.

[14] J. J. Jun *et al.*, "Fully integrated silicon probes for high-density recording of neural activity," *Nature*, vol. 551, no. 7679, p. 232, Nov. 2017.

[15] W16 system, Triangle BioSystems International (TBSI). Available: https://www.trianglebiosystems.com/w-series-systems.html

[16] G. Gagnon-Turcotte *et al.*, "A wireless headstage for combined optogenetics and multichannel electrophysiological recording," *IEEE Trans. Biomed. Circuits Syst.*, vol. 11, no. 1, pp. 1-14, Feb. 2017.

[17] M. A. Rossi *et al.*, "A wirelessly controlled implantable LED system for deep brain optogenetic stimulation," *Front. Integr. Neurosci.*, vol. 9, no. 8, Feb. 2015.

[18] S. T. Lee *et al.*, "A miniature, fiber-coupled, wireless, deep-brain optogenetic stimulator," *IEEE Trans. Neural Syst. Rehabil. Eng.*, vol. 23, no. 4, pp. 655-664, July 2015.

[19] J. W. Jeong *et al.*, "Wireless optofluidic systems for programmable in vivo pharmacology and optogenetics," *Cell*, vol. 162, no. 3, pp. 662-674, July 2015.

[20] Thomas Dual Stimulator, TREC. Available: https://www.thomasrecording.com/products/neuroscience-products/chronic-recording-devices/small-animal/thomas-dual-stimulator-tds.html#tab3726

[21] HELIOS wireless optogenetic system, Plexon. Available: https://plexon.com/products/helios-wireless-optogenetic-system/#helios-resources

[22] Optogenetics, EiCom, [Online] Available: https://www.eicomusa.com/teleopto/

[23] W2100-HS4-opto, Multichannel Systems. Available: https://www.multichannelsystems.com/products/w2100-hs4-opto

[24] B. Lee *et al.*, "An implantable peripheral nerve recording and stimulation system for experiments on freely moving animal subjects," *Scientific Reports*, vol. 8, no. 1, p. 6115, Apr. 2018.

[25] S. B. Lee, B. Lee, M. Kiani, B. Mahmoudi, R. Gross, and M. Ghovanloo, "An inductively-powered wireless neural recording system with a charge sampling analog front-end," *IEEE Sens. J.*, vol. 16, no. 2, pp. 475-484, Jan. 2016.

[26] Inductive power accessory, Triangle Biosystems Inc. Available: http://www.trianglebiosystems.com/inductive-power.html

[27] D. Ahn and M. Ghovanloo, "Optimal design of wireless power transmission links for millimeter-sized biomedical implants," *IEEE Trans. Biomed Circuits Syst.*, vol. 10, no. 1, pp. 125-137, Feb. 2016.

[28] S. A. Mirbozorgi, P. Yeon, and M. Ghovanloo, "Robust wireless power transmission to mm-sized free-floating distributed implants," *IEEE Trans. Biomed. Circuits Syst.*, vol. 11, no. 3, pp. 692-702, June 2017.

[29] P. Yeon, S. A. Mirbozorgi, J. Lim, and M. Ghovanloo, "Feasibility study on active back telemetry and power transmission through an inductive link for millimeter-sized biomedical implants," *IEEE Trans. Biomed. Circuits Syst.*, vol. 11, no. 6, pp. 1366-1376, Dec. 2017.

[30] U. M. Jow and M. Ghovanloo, "Modeling and optimization of printed spiral coils in air, saline, and muscle tissue environments," *IEEE Trans. Biomed. Circuits Syst.*, vol. 3, no. 5, pp. 339-347, Oct. 2009.

[31] M. Kiani, U. M. Jow, and M. Ghovanloo, "Design and optimization of a 3-coil inductive link for efficient wireless power transmission," *IEEE Trans. Biomed. Circuits Syst.*, vol. 5, no. 6, pp. 579-591, Dec. 2011.

[32] IEEE Standard for Safety Levels with Respect to Human Exposure to Radio Frequency Electromagnetic Fields, 3 kHz to 300 GHz, IEEE Standard C95.1-2005. 2005.

[33] A. Ibrahim, M. Meng, and M. Kiani, "A comprehensive comparative study on inductive and ultrasonic wireless power transmission to biomedical implants," *IEEE Sensors J.*, vol. 18, no. 9, pp. 3813-3826, Mar. 2018.

[34] A. B. Amar, A. B. Kouki, and H. Cao, "Power approaches for implantable medical devices," *Sensors*, vol. 15, no. 11, pp. 28889-28914, Nov. 2015.

[35] H. J. Kim, H. Hirayama, S. Kim, K. Han, R. Zhang, J. Choi, "Review of near-field wireless power and communication for biomedical applications," *IEEE Access*, vol. 5, no. 11, pp. 21264-21285, Sept. 2017.

[36] U. Jow, P. McMenamin, M. Kiani, and M. Ghovanloo, "EnerCage: a smart experimental arena with scalable architecture for behavioral experiments," *IEEE Trans. Biomed. Eng.*, vol. 61, no. 1, pp. 139-148, Jan. 2014.

[37] E. Kilinc *et al.*, "A system for wireless power transfer of micro-systems in-vivo implantable in freely moving animals," *IEEE Sensors Journal*, vol. 14, no. 2, pp.522-531, Feb. 2014.

[38] B. Lee, M. Kiani, and M. Ghovanloo, "A smart wirelessly powered homecage for long-term high-throughput behavioral experiments," *IEEE Sensors Journal*, vol. 15, no. 9, pp. 4905-4916, Sept. 2015.

[39] S. A. Mirbozorgi, H. Bahrami, M. Sawan and B. Gosselin, "A smart cage with uniform wireless power distribution in 3D for enabling long-term experiments with freely moving animals," *IEEE Trans. Biomed. Circuits Syst.*, vol. 10, no. 2, pp. 424-434, Apr. 2016.

[40] R. E. Millard and R. K. Shepherd, "A fully implantable stimulator for use in small laboratory animals," *J. Neurosci. Methods*, vol. 166, pp. 168-177, Nov. 2007.

[41] X. Li *et al.*, "A new omnidirectional wireless power transmission solution for the wireless endoscopic micro-ball," *IEEE International Symposium of Circuits and Systems (ISCAS)*, Rio de Janeiro, Brazil, pp. 2609-2612, 2011.

[42] B. Lee, D. Ahn, and M. Ghovanloo, "Three-phase time-multiplexed planar power transmission to distributed implants," *IEEE J. Emerg. Sel. Topics Power Electron*, vol. 4, no. 1, pp. 263-272, Mar. 2016.

[43] B. H. Choi *et al.*, "Six degrees of freedom mobile inductive power transfer by crossed dipole Tx and Rx coils," *IEEE Trans. Power Electron.*, vol. 31, no. 4, pp. 3252-3272, Apr. 2016.

[44] P. Cong, "Neural interfaces for implantable medical devices: circuit design considerations for sensing, stimulation, and safety," *IEEE Solid-State Circuits Mag.*, vol. 8, no. 4, pp. 48-56, Nov. 2016.

[45] C. M. Lopez *et al.*, "A neural probe with pp to 966 Electrodes and up to 384 configurable channels in 0.13 μm SOI CMOS," *IEEE Trans. Biomed. Circuits Syst.*, vol. 11, no. 3, pp. 510-522, June 2017.

[46] S. Park, J. Cho, K. Na, and E. Yoon, "Modular 128-channel Δ-ΔΣ analog front-end architecture using spectrum equalization scheme for 1024-channel 3-D neural recording microsystems," *IEEE J. Solid-State Circuits*, vol. 53, no. 2, pp. 501-514, Feb. 2018.

[47] T. Wu, W. Zhao, H. Guo, H. H. Lim, and Z. Yang, "A streaming PCA VLSI chip for neural data compression," *IEEE Trans. Biomed. Circuits Syst.*, vol. 11, no. 6, pp. 1290-1302, Dec. 2017.

[48] S. B. Lee, M. Yin, J. R. Manns, and M. Ghovanloo, "A wideband dual-antenna receiver for wireless recording from animals behaving in large arenas," *IEEE Trans. Biomed. Eng.*, vol. 60, no. 7, pp. 1993-2004, July 2013.

[49] H. Mei, K. A. Thackston, R. A. Bercich, J. G. R. Jefferys, and P. P. Irazoqui, "Cavity resonator wireless power transfer system for freely moving animal experiments," *IEEE Trans. Biomed. Eng.*, vol. 64, no. 4, pp. 775-785, Apr. 2017.

[50] Y. Lin *et al.*, "A battery-less, implantable neuro-electronic interface for studying the mechanisms of deep brain stimulation in rat models," *IEEE Trans. Biomed. Circuits Syst.*, vol. 10, no. 1, pp. 98-112, Feb. 2016.

[51] X. Liu *et al.*, "A fully integrated wireless compressed sensing neural signal acquisition system for chronic recording and brain machine interface," *IEEE Trans. Biomed. Circuits Syst.*, vol. 10, no. 4, pp. 874-883, Aug. 2016.

[52] Y. Lo, Y. Kuan, S. Culaclii, B. Kim, P. Wang, C. Chang, J. A. Massachi, M. Zhu, K. Chen, P. Gad, V. R. Edgerton, and W. Liu, "A fully integrated wireless SoC for motor function recovery after spinal cord injury," *IEEE Trans. Biomed. Circuits Syst.*, vol. 11, no. 3, pp. 497-509, June 2017.

[53] A. Borna and K. Najafi, "A low power light weight wireless multichannel microsystem for reliable neural recording," *IEEE J. Solid-State Circuits*, vol. 49, no. 2, pp. 439-451, Feb. 2014.

[54] H. Rhew, J. Jeong, J. A. Fredenburg, S. Dodani, P. G. Patil and M. P. Flynn, "A fully self-contained logarithmic closed-loop deep brain stimulation SoC with wireless telemetry and wireless power management," *IEEE J. Solid-State Circuits*, vol. 49, no. 10, pp. 2213-2227, Oct. 2014.

[55] S. Brenna, F. Padovan, A. Neviani, A. Bevilacqua, A. Bonfanti, and A. L. Lacaita, "A 64-channel 965-μW neural recording SoC with UWB wireless transmission in 130-nm CMOS," *IEEE Trans. Circuits Syst. II*, vol. 63, no. 6, pp. 528-532, June 2016.

[56] H. Kassiri *et al.*, "Battery-less tri-band-radio neuro-monitor and responsive neurostimulator for diagnostics and treatment of neurological disorders," *IEEE J. Solid-State Circuits*, vol. 51, no. 5, pp. 1274-1289, May 2016.

[57] H. Kassiri *et al.*, "Rail-to-rail-input dual-radio 64-channel closed-loop neurostimulator," *IEEE J. Solid-State Circuits*, vol. 52, no. 11, pp. 2793-2810, Nov. 2017.

[58] C. Cheng *et al.*, "A fully integrated 16-channel closed-loop neural-prosthetic CMOS SoC with wireless power and bidirectional data telemetry for real-time efficient human epileptic seizure control," *IEEE J. Solid-State Circuits*, vol. 53, no. 11, pp. 3314-3326, Nov. 2018.

[59] J. Charthad *et al.*, "A mm-sized wireless implantable device for electrical stimulation of peripheral nerves," *IEEE Trans. Biomed. Circuits Syst.*, vol. 12, no. 2, pp. 257-270, Apr. 2018.

[60] G. Gagnon-Turcotte, M. N. Khiarak, C. Ethier, Y. D. Koninck, and B. Gosselin, "A 0.13-µm CMOS SoC for simultaneous multichannel optogenetics and neural recording," *IEEE J. Solid-State Circuits*, vol. 53, no. 11, pp. 3087-3100, Nov. 2018.

[61] E. Stark, T. Koos, and G. Buzsaki, "Diode probes for spatiotemporal optical control of multiple neurons in freely moving animals," *J. Neurophysiol.*, vol. 108, no. 2, pp. 349-363, July 2012.

[62] G. C. McConnell, H. D. Rees, A.I. Levey, C.A. Gutekunst, R.E. Gross, and R.V. Bellamkonda, "Implanted neural electrodes cause chronic, local inflammation that is correlated with local neurodegeneration," *J. Neural Eng.*, vol. 6, no. 5, p. 056003, Aug. 2009.

[63] J. C. Barrese, N. Rao, K. Paroo, C. Triebwasser, C. Vargas-Irwin, L. Franquemont, and J. P. Donoghue, "Failure mode analysis of silicon-based intracortical microelectrode arrays in non-human primates," *J. Neural Eng.*, vol. 10, no. 6, p. 066014, Nov. 2013.

[64] D. Seo, R. M. Neely, K. Shen, U. Singhal, E. Alon, J. M. Carmena, M. M. Maharbiz, "Wireless recording in the peripheral nervous system with ultrasonic neural dust," *Neuron*, vol. 91, no. 3, pp. 529-539, Aug. 2016.

[65] D. K. Piech, B. C. Johnson, K. Shen, M. M. Ghanbari, K. Li, R. M. Neely, J. E. Kay, J. M. Carmena, M. M. Maharbiz, and R. Muller, "StimDust: A 2.2 mm^3, implantable wireless precision neural stimulator with ultrasonic power and communication," *arXiv Preprint arXiv: 1807.07590*, 2018.

[66] T. Tokuda, T. Ishizu, W. Nattakarn, M. Haruta, T. Noda, K. Sasagawa, M. Sawan, and J. Ohta, "1 mm^3-sized optical neural stimulator based on CMOS integrated photovoltaic power receiver," *AIP Advances*, vol. 8, no. 4, p. 045018, Apr. 2018.

[67] G. Shin *et al*., "Flexible near-field wireless optoelectronics as subdermal implants for broad applications in optogenetics," *Neuron*, vol. 93, no. 3, pp. 509-521, Feb. 2017.

[68] K. N. Noh *et al.*, "Miniaturized, battery-free optofluidic systems with potential for wireless pharmacology and optogenetics," *Small*, vol. 14, no. 4, p. 1702479, Jan. 2018.

[69] K. L. Montgomery *et al*., "Wirelessly powered, fully internal optogenetics for brain, spinal and peripheral circuits in mice," *Nat. Methods*, vol. 12, no. 10, pp. 969-974, Aug. 2015.

[70] A. Alivisatos *et al*., "The brain activity map," *Science*, vol. 339, pp. 1284-1285, Mar. 2013.

[71] A. Alivisatos, M. Chun, G. Church, R. Greenspan, M. Roukes, and R. Yuste, "The brain activity map project and the challenge of functional connectomics," *Neuron*, vol. 74, pp. 970-974, June 2012.

[72] N. Mano, "A 280 microW cm-2 biofuel cell operating at low glucose concentration," *Chem. Commun.*, no.19, pp. 2221-3, May 2008.

[73] J.A. Paradiso and T. Starner, "Energy scavenging for mobile and wireless electronics," *IEEE Pervasive Computing*, vol. 4, no. 1, pp. 18-27, Jan. 2005.

[74] E. K. Reilly and P. K. Wright, "Modeling, fabrication and stress compensation of an epitaxial thin film piezoelectric microscale energy scavenging device," *J. Micromech. Microeng.*, vol. 19, no. 9, p. 095014, Sept. 2009.

[75] R. Vullers, R. Schaijk, H. Visser, J. Penders, and C. Hoof, "Energy harvesting for autonomous wireless sensor networks," *IEEE Solid-State Circuits Magazine*, vol. 2, no. 2, pp. 29-38, Feb. 2010.

[76] M. Meng and M. Kiani, "A hybrid inductive-ultrasonic link for wireless power transmission to millimeter-sized biomedical implants," *IEEE Trans. Circuits Syst. II*, vol. 64, no. 10, pp. 1137-1141, Oct. 2017.

[77] Y. LeChasseur *et al*., "A microprobe for parallel optical and electrical recordings from single neurons in vivo," *Nat. Methods*, vol. 8, no. 4, pp. 319-325, Apr. 2011.

[78] S. Dufour *et al*., "A multimodal micro-optrode combining field and single unit recording, multispectral detection and photolabeling capabilities," *PloS One*, vol. 8, no. 2, p. e57703, Feb. 2013.

[79] J. Wang *et al*., "Integrated device for combined optical neuromodulation and electrical recording for chronic in vivo applications," *J. Neural Eng.*, vol. 9, no. 1, p. 016001, Dec. 2011.

[80] K. Tamura *et al*., "A glass-coated tungsten microelectrode enclosing optical fibers for optogenetic exploration in primate deep brain structures," *J. Neurosci. Methods*, vol. 211, no. 1, pp. 49-57, Oct. 2012.

[81] S. K. Mohanty and N. V. Thakor. "Optogenetics: optical methods for cellular control." *Optogenetics: Optical Methods for Cellular Control*, vol. p. 8586. Mar. 2013.

[82] J. G. McCall *et al.*, "Fabrication and application of flexible, multimodal light-emitting devices for wireless optogenetics," *Nature Protocols* vol. 8, pp. 2413-2428, Nov. 2013

[83] Y. Jia *et al.*, "Wireless opto-electro neural interface for experiments with small freely moving animals", *J. Neural Eng.*, vol. 15, no. 4, p. 046032, June 2018.

[84] Y. Jia, Z. Wang, S. A. Mirbozorgi and M. Ghovanloo, "A closed-loop wireless homecage for optogenetic stimulation experiments," *IEEE Biomedical Circuits and Systems Conference (BioCAS)*, Atlanta, GA, pp. 1-4, 2015.

[85] G. Gagnon-Turcotte *et al.*, "A wireless optogenetic headstage with multichannel electrophysiological recording capability," *Sensors*, vol. 15, no. 9, pp. 22776-22797, Sept. 2015.

[86] K. Y. Kwon *et al.*, "Opto-μECoG array: a hybrid neural interface with transparent μECoG electrode array and integrated LEDs for optogenetics," *IEEE Trans. Biomed. Circuits Syst.*, vol. 7, no. 5, pp. 593-600, Oct. 2013,

[87] Parylene conformal coating specifications & properties, Specialty Coating Systems. Available: http://scscoatings.com

[88] Y. S. Jeong, B. Ratier, A. Moliton, and L. Guyard, "UV-visible and infrared characterization of poly(p-xylylene) films for waveguide applications and OLED encapsulation," *Synthetic Metals*, vol. 127, no. 1-3, pp. 189-193, Mar. 2002.

[89] E. Castagnola, A. Ansaldo, E. Maggiolini, T. Ius, M. Skrap, D. Ricci, and L. Fadiga, "Smaller, softer, lower-impedance electrodes for human neuroprosthesis: a pragmatic approach," *Front. Neuroeng.*, vol. 7, no. 8, Apr. 2014.

[90] E. C. Leuthardt, G. Schalk, J. R. Wolpaw, J. G. Ojemann, and D. W. Moran, "A brain-computer interface using electrocorticographic signals in humans," *J. Neural Eng.*, vol. 1, no. 2, pp. 63-71, June 2004.

[91] M. L. V. Quyen *et al.*, "Comparison of Hilbert transform and wavelet methods for the analysis of neuronal synchrony," *J. Neurosci. Methods*, vol. 111, no. 2, pp. 83-98, Oct. 2004.

[92] D. H. Hubel, "Eye, brain, and vision," *Scientific American Library/Scientific American Books*, 1995.

[93] Chonux, Chronux Analysis Software. Available at: http://chronux.org/

[94] J. Subbaroyan, D. C. Martin, and D. R. Kipke, "A finite-element model of the mechanical effects of implantable microelectrodes in the cerebral cortex," *J. Neural Eng.*, vol. 2, no. 4, pp. 103, Oct. 2005.

[95] V. S. Polikov, P. A. Tresco, and W. M. Reichert, “Response of brain tissue to chronically implanted neural electrodes,” *J Neurosci. Methods*, vol. 148, no. 1, pp. 1-18, Oct. 2005.

[96] J. P. Harris *et al*, “Mechanically adaptive intracortical implants improve the proximity of neuronal cell bodies,” *J. Neural Eng.*, vol. 8, no. 6, p. 066011, Nov. 2011.

[97] J. Simpson and J. Kelly, “The impact of environmental enrichment in laboratory rats-behavioural and neurochemical aspects,” *Behavioural Brain Research,* vol. 222, pp. 246-264, Sept. 2011.

[98] G. Kempermann, H.G. Kuhn, and F.H. Gage, “More hippocampal neurons in adult mice living in an enriched environment,” *Nature,* vol. 386, pp. 493-495, Apr. 1997.

[99] A. Belayev *et al.*, “Enriched environment delays the onset of hippocampal damage after global cerebral ischemia in rats,” *Brain research,* vol. 964, pp. 121-127, Feb. 2003.

[100] A. Brauner, D. Kurjiaka, A. Ibragimov, and A. Baldwin, “Imapct of cage size and enrichment (tube and shelf) on heart rate variability in rats,” *Science,* vol. 37, 2010.

[101] H. Wurbel, “Ideal homes? housing effects on rodent brain and behaviour,” *Trends Neurosci.,* vol. 24, pp. 207-211, Apr. 2001.

[102] Alternative Design Manufacturing & Supply, Rat Plastic Cage. Available at: http://www.altdesign.com/products/animals/rat/rat-plastic-cage/

[103] Y. Jia, S. A. Mirbozorgi, Z. Wang, C. Hsu, T. E. Madsen, D. Rainnie, and M. Ghovanloo, “Position and orientation insensitive wireless power transmission for EnerCage-Homecage system,” *IEEE Trans. Biomed. Eng.*, vol. 64, no. 10, pp. 2439-2449, Oct. 2017.

[104] S. A. Mirbozorgi, Y. Jia, D. Canales, and M. Ghovanloo, “A wirelessly-powered homecage with segmented copper foils and closed-loop power control,” *IEEE Trans. Biomed. Circuits Syst.*, vol. 10, no. 5, pp. 979-989, Oct. 2016.

[105] S. A. Mirbozorgi, Y. Jia, and M. Ghovanloo, “Power efficiency and power delivery measurement in inductive links with arbitrary source and load impedance values,” *IEEE Life Sciences Conference (LSC)*, Montreal, QC, pp. 25-28, 2018.

[106] Y. Jia *et al.*, “A wirelessly-powered homecage with animal behavior analysis and closed-loop power control,” *IEEE Engineering in Medicine and Biology Society (EMBC)*, Orlando, FL, 2016, pp. 6323-6326, 2016.

[107] M. Kiani and M. Ghovanloo, “An RFID-based closed-loop wireless power transmission system for biomedical applications,” IEEE Trans. *Circuits* Syst., *II*, Exp. Briefs, vol. 57, no. 4, pp. 260-264, Apr. 2010.

[108] J. T. Vaughan and J. R. Griffiths, *RF coils for MRI*: John Wiley & Sons, 2012.

[109] A. Sharma, I. J. G. Zuazola, J. C. Batchelor, and A. Perallos, “Dual purpose near-and far-field UHF RFID coil antenna with non-uniformly distributed-turns,” *IEEE Antennas Wirel. Propag. Lett.,* vol. 14, pp. 1342-1345, Feb. 2015.

[110] S. C. Tang and N. J. McDannold, “Power loss analysis and comparison of segmented and unsegmented energy coupling coils for wireless energy transfer,” *IEEE J. Emerg. Sel. Topics Power Electron*., vol. 3, no. 1, pp. 215-225, Mar. 2015.

[111] W. Zhong, C. K. Lee, and S. R. Hui, “General analysis on the use of Tesla's resonators in domino forms for wireless power transfer,” *IEEE Trans. Ind. Electron.,* vol. 60, no. 1, pp. 261-270, Jan. 2013.

[112] S. Gabriel, R.W. Lau, and C. Gabriel, “The dielectric properties of biological tissues: II. measurements in the frequency range of 10 Hz to 20 GHz,” *Phys. Med. Biol*., vol., 41, pp. 2251-2269, 1996.

[113] W Federal Communications Commission, Specific Absorption Rate for Cellular Telephones. Available at: https://www.fcc.gov/general/specific-absorption-rate-sar-cellular-telephones.2013

[114] Z. Wang, S. A. Mirbozorgi, and M. Ghovanloo, "Towards a Kinect-based behavior recognition and analysis system for small animals," *IEEE Biomedical Circuits and Systems Conference (BioCAS)*, Atlanta, GA, pp. 683-686, 2015.

[115] M. D. Kelland, D. Asdourian, and D. Z. Kelland, "Inhibition and excitation of neck and shoulder muscles during unilateral electrical stimulation of the rat neostriatum," *Behav. Brain Res.*, vol. 30, no. 1, pp. 1-13, Sept. 1988.

[116] Y. Aiko, S. Hosokawa, F. Shima, M. Kato, and K. Kitamura, "Alterations in local cerebral glucose utilization during electrical stimulation of the striatum and globus pallidus in rats," *Brain Res.*, vol. 442, no. 1, pp. 43-52, Feb. 1988.

[117] D. Asdourian, S. Lentz, and M. Kelland, "Motor effects of globus pallidus stimulation in the rat: lesions to corticofugal fibers block the motor effects," *Behav. Brain Res.*, vol. 44, no. 2, pp. 185-193, Aug. 1991.

[118] L. Lee and P. Slater, "Role of globus pallidus and substantia nigra efferent pathways in striatally evoked head turning in the rat," *Exp. Brain Res.*, vol. 44, no. 2, pp. 170-176, Oct. 1981.

[119] I. H. Stevenson and K. P. Kording, "How advances in neural recording affect data analysis," *Nat. Neurosci.*, vol. 14, pp. 139-142, Jan. 2011.

[120] Y. Jia, B. Lee, F. Kong, Z. Zeng, M. Connolly, B. Mahmoudi, and M. Ghovanloo, "A software-defined radio receiver for wireless recording from freely-behaving animals," submitted to *IEEE Trans. Biomed*. Eng., 2019.

[121] B. Lee *et al.*, "An inductively powered wireless neural recording and stimulation system for freely-behaving animals," *IEEE Trans. Biomed. Circuits Syst.*, vol. 13, no. 2, pp. 413-424, Apr. 2019.

[122] B. Lee, Y. Jia, F. Kong, M. Connolly, B. Mahmoudi, and M. Ghovanloo, "Toward a robust multi-antenna receiver for wireless recording from freely-behaving animals," *IEEE Biomedical Circuits and Systems Conference (BioCAS)*, Cleveland, OH, 2018.

[123] BladeRF X40, Nuand, San Francisco, CA, Aug. 2018. Available: https://www.nuand.com/product/bladerf-x40/.

[124] GNURadio: Learn About GNU Radio, Oct. 2018. Available: http://gnuradio.org.

[125] MathWorks, PN Sequence Generator, Sept. 2018. Available: https://www.mathworks.com/help/comm/ref/pnsequencegenerator.html.

[126] GNU Radio Manual and C++ API Reference: ZeroMQ, Aug. 2011. Available: https://www.gnuradio.org/doc/doxygen/page_zeromq.html.

[127] B. Lee and M. Ghovanloo, "An adaptive averaging low noise front-end for central and peripheral nerve recording," *IEEE Trans. Cir. and Syst. II*, vol. 65, no. 7, pp. 839-843, July 2018.

[128] C. A. Balanis, *Antenna Theory: Analysis and Design*, 3th ed. Hoboken, NJ, USA: Wiley, 2016.

[129] R. J. Baker, *Circuit Design, Layout, and Simulation*, 4th ed. Hoboken, NJ, USA: Wiley, 2010.

[130] H. Lee, H. Park, and M. Ghovanloo, "A power-efficient wireless system with adaptive supply control for deep brain stimulation," *IEEE J. Solid-State Circuits*, vol. 48, no. 9, pp. 2203-2216, Sept. 2013.

[131] X. F. Wei and W. M. Grill, "Impedance characteristics of deep brain stimulation electrodes in vitro and *in vivo*," *J. Neural Eng*., vol. 6, no. 4, July 2009.

[132] Omnetics Based Electrodes, Tucker-Davis Technologies, Alachua, FL, Jan. 2018. Available: https://www.tdt.com/omnetics-based-electrodes.html.

[133] RZ2 BioAmp Processor, Tucker-Davis Technologies, Alachua, FL, Jan. 2018. Available: https://www.tdt.com/rz2-bioamp-processor.html.

[134] D. R. Merrill, M. Bikson, and J. G. R. Jefferys, "Electrical stimulation of excitable tissue: design of efficacious and safe protocols," *J Neurosci Methods*, vol. 141, no. 2, pp. 171-198, Feb. 2005.

[135] H. Rezaee-Dehsorkh, N. Ravanshad, R. Lotfi, K. Mafinezhad, and A. M. Sodagar, "Analysis and design of tunable amplifiers for implantable neural recording applications," *IEEE J. Emerg. Sel. Topic Circuits Syst.*, vol. 1, no. 4, pp. 546-556, Dec. 2011.

[136] H. Lee *et al.*, "A power-efficient switched-capacitor stimulating system for electrical/optical deep brain stimulation," *IEEE J. Solid-State Circuits*, vol. 50, no. 1, pp. 360-374, Jan. 2015.

[137] Y. Jia *et al*., "A mm-sized free-floating wirelessly-powered implantable optical stimulation device," *IEEE Trans. Biomed. Circuits Syst*., *May* 2019.

[138] W. Khan, Y. Jia, F. Madi, A. Weber, M. Ghovanloo and W. Li, "Inductively coupled, mm-sized, single channel optical neuro-stimulator with intensity enhancer," *Microsyst. Nanoeng.*, vol. 5, no. 1, p. 23, June 2019.

[139] R. J. Baker, "Special purpose CMOS circuits," in *CMOS circuit design, layout, and simulation*, 3nd ed. Hoboken, NJ, U.S.: John Wiley & Sons, Inc., 2010, pp. 523-529.

[140] B. Lee, M. Kiani, and M. Ghovanloo, "A triple-loop inductive power transmission system for biomedical applications," *IEEE Trans. Biomed. Circuits Syst.*, vol. 10, no. 1, pp. 138-148, Feb. 2016.

[141] U. Guler, Y. Jia, and M. Ghovanloo, "A reconfigurable passive RF-to-DC converter for wireless IoT applications," *IEEE Trans. Circuits Syst. II: Express Briefs*, Jan. 2019.

[142] U. Guler, Y. Jia, and M. Ghovanloo, "A reconfigurable passive voltage multiplier for wireless mobile IoT Applications," *IEEE Trans. Circuits Syst. II: Express Briefs*, June 2019.

[143] C. Gias, N. Hewson-Stoate, M. Jones, D. Johnston, J. E. Mayhew, and P. J. Coffeya, "Retinotopy within rat primary visual cortex using optical imaging," *NeuroImage*, vol. 24, no. 1, pp. 200-206, Jan. 2005.

[144] Y. Jia, S. A. Mirbozorgi, P. Zhang, O. T. Inan, W. Li, and M. Ghovanloo, "A dual-band wireless power transmission system for evaluating mm-sized implants," *IEEE Trans. Biomed. Circuits Syst*., *May* 2019.

[145] "CHIPLED 0402 Datasheet," Osram. Munich, Germany. Version 1.2 LT QH9G, Sept. 2005. Available: https://www.osram.com/media/resource/hires/osram/LT%20QH9G.pdf

[146] T. Kawashima, H. Okuno, and H. Bito, "A new era for functional labeling of neurons: activity-dependent promoters have come of age," *Front.* Neural Circuits, vol. 8, no. 37, Apr. 2014.

[147] M. Mark, "Powering mm-size wireless implants for brain-machine interfaces," Ph.D. dissertation, Electrical Engineering and Computer Sciences, University of California at Berkeley, Dec. 2011.